

UCLA

UCLA Electronic Theses and Dissertations

Title

Seismic Performance, Modeling, and Failure Assessment of Reinforced Concrete Shear Wall Buildings

Permalink

<https://escholarship.org/uc/item/3c96x2qn>

Author

Tuna, Zeynep

Publication Date

2012

Peer reviewed|Thesis/dissertation

UNIVERSITY OF CALIFORNIA

Los Angeles

Seismic Performance, Modeling, and Failure Assessment
of Reinforced Concrete Shear Wall Buildings

A dissertation submitted in partial satisfaction of the
requirements for the degree Doctor of Philosophy
in Civil Engineering

by

Zeynep Tuna

2012

ABSTRACT OF THE DISSERTATION

Seismic Performance, Modeling, and Failure Assessment of Reinforced Concrete Shear Wall Buildings

by

Zeynep Tuna

Doctor of Philosophy in Civil Engineering

University of California, Los Angeles, 2012

Professor John W. Wallace, Chair

Reinforced concrete structural (shear) walls are commonly used as lateral load resisting systems in high seismic zones because they provide significant lateral strength, stiffness, and deformation capacity. Understanding the response and behavior of shear walls is essential to achieve more economical and reliable designs, especially as performance-based design approaches for new buildings have become more common. Results of a case study of 42-story RC dual system building, designed using code-prescriptive and two different performance-based design approaches, are presented to assess expected performance. Median values and dispersion of the response quantities are, in general, well-below acceptable limits and the overall behavior of the three building designs are expected to be quite similar. However, the ability to define shear failure and collapse proved difficult and provided motivation to conduct additional studies.

For both design of new buildings and evaluation/rehabilitation of existing structural wall buildings, an accurate assessment of median (expected) and dispersion of wall shear strength and deformation capacity are needed. A wall test database (124 specimens) was assembled to investigate the influence of various parameters on wall shear strength and deformation capacity, and to recommend alternative relations for strength and deformation capacity depending on expected wall behavior. Test results indicated that ACI 318-11 underestimates the shear strength of the shear-controlled walls. Mean curvature ductility ratios were obtained as about 3 and 7 for shear- and flexure-controlled walls, respectively. The new relations will allow improved damage and failure assessment of buildings utilizing structural walls for lateral load resistance.

Failure assessment of RC shear walls also was conducted for the 15-story Alto Rio building which collapsed in the 2010 Chile earthquake. Possible reasons for collapse were identified using post-earthquake observed damage, structural drawings, and nonlinear static and dynamic response analyses. Analysis results indicate that collapse was likely influenced by various factors, including compression failure at the web boundary of T-shaped walls on the east side of the building, large shear demands at the filled-in corridor walls at the first level, and tensile fracture and splice failures at the west side of the building.

Nonlinear modeling and analysis of the four-story RC building that was tested on E-Defense shaking table (2010) was investigated to assess current modeling approaches and assumptions, and to identify issues that require additional study. Including concrete tension strength, stiffness degradation, and strength degradation significantly improved the correlation between the analytical and test results.

The dissertation of Zeynep Tuna is approved.

Thomas A. Sabol

Scott J. Brandenburg

Jian Zhang

Jack P. Moehle

John W. Wallace, Committee Chair

University of California, Los Angeles

2012

My dissertation is dedicated to my dear parents.

TABLE OF CONTENTS

| | |
|---|----|
| Chapter 1 Introduction | 1 |
| 1.1. Objectives and Scope | 1 |
| 1.1.1. Seismic performance of tall buildings..... | 1 |
| 1.1.2. Shear Strength and Deformation Capacity of Reinforced Concrete Shear Walls | 2 |
| 1.1.3. Collapse Assessment of Torre Alto Rio | 3 |
| 1.1.4. 2010 E-Defense Four-Story Reinforced Concrete and Post-Tensioned Buildings | 4 |
| 1.2. Organization | 5 |
| Chapter 2 Case Study of a 42-story Reinforced Concrete Dual System Building..... | 6 |
| 2.1. Introduction | 6 |
| 2.2. Design..... | 8 |
| 2.2.1. Building Properties..... | 8 |
| 2.2.2. Design of Building 2A (Code Design)..... | 12 |
| 2.2.3. Design of Building 2B (Performance Based Design) | 15 |
| 2.2.4. Design of Building 2C (Enhanced Performance Based Design)..... | 20 |
| 2.2.5. Design Summary | 21 |
| 2.2.6. Modeling | 22 |
| 2.2.7. Modeling of Building 2A | 23 |
| 2.2.8. Modeling of Building 2B | 32 |
| 2.2.8.1. Core wall modeling..... | 32 |
| 2.2.8.4. Damping..... | 33 |
| 2.3. Non-linear Dynamic Earthquake Analyses Results..... | 33 |
| 2.3.1. Overall Behavior | 34 |

| | | |
|---|---|-----|
| 2.3.2. | Core Shear Wall Behavior..... | 44 |
| 2.3.3. | Frame Behavior..... | 65 |
| 2.3.4. | Comparison of two buildings..... | 71 |
| 2.4. | Cost Analysis Results..... | 76 |
| 2.4.1. | Initial construction cost..... | 76 |
| 2.4.2. | Annual repair cost..... | 77 |
| 2.5. | Summary and Conclusions..... | 78 |
| Chapter 3 Shear Strength and Deformation Capacity of Reinforced Concrete Shear Walls..... | | 82 |
| 3.1. | Introduction..... | 82 |
| 3.1.1. | Shear strength..... | 86 |
| 3.1.2. | Deformation capacity..... | 88 |
| 3.2. | Description of the database..... | 90 |
| 3.3. | Definition of failure..... | 93 |
| 3.4. | Statistical Analyses..... | 99 |
| 3.4.1. | Regression analyses for shear strength..... | 99 |
| 3.4.2. | Regression analysis for the normalized deformation capacity..... | 107 |
| 3.5. | ACI 318-11 compliant walls..... | 116 |
| 3.5.1. | Shear strength for the ACI 318-11 compliant walls..... | 117 |
| 3.5.2. | Normalized deformation capacity for the ACI 318-11 compliant walls..... | 122 |
| 3.6. | Summary and conclusions..... | 127 |
| Chapter 4 Collapse Assessment of the Alto Rio Building in the 2010 Chile Earthquake..... | | 132 |
| 4.1. | Introduction..... | 132 |

| | | |
|---|---|-----|
| 4.2. | The February 27, 2010 Earthquake – A brief overview | 135 |
| 4.3. | Building Code Provisions in Chile | 138 |
| 4.4. | Building Description | 139 |
| 4.5. | Building Damage..... | 142 |
| 4.6. | Preliminary Studies | 148 |
| 4.7. | Nonlinear Analytical Studies..... | 150 |
| 4.8. | Analysis Results | 158 |
| 4.8.1. | Nonlinear Static (Pushover) Analyses..... | 160 |
| 4.8.2. | Nonlinear Response History Analyses..... | 161 |
| 4.9. | Sensitivity Studies | 168 |
| 4.10. | Failure Assessment Using Ductility Approach..... | 170 |
| 4.11. | Summary and Conclusions | 170 |
| | | |
| Chapter 5 2010 E-Defense Four-Story Reinforced Concrete Building - Comparative Study of Experimental and Analytical Results..... | | 174 |
| | | |
| 5.1. | Introduction | 174 |
| 5.2. | Description of the test..... | 176 |
| 5.3. | Conventional reinforced concrete building (RC Building) | 178 |
| 5.4. | Assessment of RC Building using ASCE 7-05 and ACI 318-08..... | 182 |
| 5.4.1. | Strength Requirements for Walls | 183 |
| 5.4.2. | Capacity Design Checks..... | 184 |
| 5.4.3. | Drift Requirements in the Wall | 186 |
| 5.4.4. | Detailing Requirements for the Wall | 186 |

| | | |
|--|---|-----|
| 5.5. | Collapse Mechanism | 188 |
| 5.6. | Test plan, Ground (Table) Motions, and Instrumentation | 189 |
| 5.6.1. | Test plan | 189 |
| 5.6.2. | Instrumentation | 189 |
| 5.6.3. | Ground (Table) Motions..... | 191 |
| 5.7. | Test Results | 192 |
| 5.8. | Preliminary Modeling and Analysis Results | 194 |
| 5.8.1. | Shear Wall Modeling | 195 |
| 5.8.2. | Beam and column modeling..... | 198 |
| 5.8.3. | Damping and masses..... | 198 |
| 5.8.4. | Comparisons of the preliminary analytical results with test results | 199 |
| 5.9. | Enhanced Modeling and Analysis Results | 203 |
| 5.9.1. | Additional properties..... | 203 |
| 5.9.2. | Comparisons of the enhanced analytical results with test results..... | 209 |
| 5.10. | Sensitivity Studies..... | 213 |
| 5.10.1. | Slip/extension behavior | 214 |
| 5.10.2. | Reinforcing steel behavior..... | 216 |
| 5.10.3. | Cyclic degradation parameters | 218 |
| 5.11. | Summary and Conclusions | 220 |
| Chapter 6 Summary and Conclusions..... | | 223 |
| 6.1. | Summary | 223 |
| 6.2. | Conclusions | 225 |
| Appendix A..... | | 230 |

| | |
|--|-----|
| Appendix B | 231 |
| Summary of the range of parameters | 251 |
| Regression Analysis Results | 256 |
| Appendix C | 259 |
| References | 260 |

LIST OF FIGURES

| | |
|---|----|
| Figure 2-1. Three dimensional building view [Ghodsi, et al., 2009]..... | 9 |
| Figure 2-2. Elevation views of the building..... | 9 |
| Figure 2-3. Typical plan view for basement and tower levels [Ghodsi, et al., 2009]..... | 11 |
| Figure 2-4. 5% damped code and site specific design response spectra [Ghodsi, et al., 2009].... | 12 |
| Figure 2-5. Schematic of typical frame beam and column cross-sections..... | 15 |
| Figure 2-6. Serviceability level spectra | 16 |
| Figure 2-7. Target acceleration response spectra at MCE level | 19 |
| Figure 2-8. 25 and 43 years return period response spectrum with 2.5% of critical damping | 21 |
| Figure 2-9. Concrete stress-strain relationship | 24 |
| Figure 2-10. Inelastic shear stress-strain relationship..... | 25 |
| Figure 2-11. Inelastic steel stress-strain relationship..... | 26 |
| Figure 2-12. Typical coupling beam modeling..... | 26 |
| Figure 2-13. Shear displacement hinge backbone curve | 27 |
| Figure 2-14. Typical beam modeling..... | 28 |
| Figure 2-15. Moment-rotation hinge backbone curve | 29 |
| Figure 2-16. Typical column modeling | 30 |
| Figure 2-17. Rayleigh damping as defined in Perform 3D..... | 31 |
| Figure 2-18. Mass modeling..... | 32 |
| Figure 2-19. Story displacements under various hazard levels..... | 36 |
| Figure 2-20. Inter-story drift ratios under various hazard levels | 38 |
| Figure 2-21. Floor accelerations under various hazard levels | 39 |
| Figure 2-22. Story displacements under various hazard levels..... | 41 |

| | |
|--|----|
| Figure 2-23. Inter-story drifts under various hazard levels..... | 42 |
| Figure 2-24. Floor accelerations under various hazard levels | 44 |
| Figure 2-25. Core wall shear forces under various hazard levels..... | 46 |
| Figure 2-26. Average shear stress profiles of the core wall..... | 46 |
| Figure 2-27. Core wall moments under various hazard levels..... | 48 |
| Figure 2-28. Locations of nodes used in strain calculations..... | 49 |
| Figure 2-29. Elevation view of deformed wall segment..... | 49 |
| Figure 2-30. North and South wall strains under OVE level..... | 50 |
| Figure 2-31. East and West wall strains under OVE level | 51 |
| Figure 2-32. Coupling beam locations..... | 52 |
| Figure 2-33. Coupling beam rotations under various hazard levels | 53 |
| Figure 2-34. Fragility curves for diagonally reinforced concrete coupling beams at high aspect ratio [Naish, 2010] | 54 |
| Figure 2-35. Core wall shear forces under various hazard levels..... | 56 |
| Figure 2-36. Average shear stress profiles of the core wall..... | 56 |
| Figure 2-37. Core wall moments under various hazard levels..... | 58 |
| Figure 2-38. North and South wall strains under OVE level..... | 59 |
| Figure 2-39. East and West wall strains under OVE level | 60 |
| Figure 2-40. Coupling beam rotations under various hazard levels | 61 |
| Figure 2-41. Elevation view of a core wall portion | 63 |
| Figure 2-42. Shear failure criterion for structural walls | 63 |
| Figure 2-43. Representative shear failure (at the circle)..... | 64 |
| Figure 2-44. Representative shear-flexure failure (at the circle)..... | 64 |

| | |
|---|----|
| Figure 2-45. Frame beam rotations under OVE level..... | 66 |
| Figure 2-46. Absolute and normalized column axial forces under OVE level..... | 67 |
| Figure 2-47. P-M interaction diagram for South-West column at (a) ground floor, (b) 15 th floor..... | 67 |
| Figure 2-48. Frame column rotations under OVE level | 68 |
| Figure 2-49. Frame beam rotations under OVE level..... | 69 |
| Figure 2-50. Absolute and normalized axial forces under OVE level..... | 69 |
| Figure 2-51. Frame column rotations under OVE level | 70 |
| Figure 2-52. Distribution of shear forces in the system under OVE level..... | 71 |
| Figure 2-53. Comparison of inter-story drifts (a) under OVE level, (b) under SLE25 level..... | 72 |
| Figure 2-54. Comparison of core shear stresses (a) under OVE level, (b) under SLE25 level | 72 |
| Figure 2-55. Comparison of core wall strains under OVE level..... | 74 |
| Figure 2-56. Comparison of coupling beam rotations (a) OVE level, (b) MCE level..... | 75 |
| Figure 2-57. Comparison of frame beam rotations under OVE level..... | 75 |
| Figure 2-58. Comparison of normalized column axial forces under OVE level | 76 |
| Figure 3-1. Failure criterion for shear walls | 84 |
| Figure 3-2. Wall shear strength versus ductility relation (Corley et al., 1981)..... | 85 |
| Figure 3-3. ASCE 41-06 (2007) Column Shear Strength – Demand Relation (PEER/ATC 72-1, 2010)..... | 86 |
| Figure 3-4. Summary of the experimental tests included in the study..... | 92 |
| Figure 3-5. Force-deformation response of a reinforced concrete shear wall [Massone, 2006] .. | 94 |
| Figure 3-6. Normalized force-deformation response of the shear-controlled walls (47 specimens) – displacement ductility | 96 |

| | |
|--|-----|
| Figure 3-7. Normalized force-deformation response of the transition walls (25 specimens) – displacement ductility | 96 |
| Figure 3-8. Normalized force-deformation response of the flexure-controlled walls (52 specimens) – displacement ductility | 97 |
| Figure 3-9. Normalized force-deformation response of the shear-controlled walls (47 specimens) – curvature ductility | 97 |
| Figure 3-10. Normalized force-deformation response of the transition walls (25 specimens) – curvature ductility | 98 |
| Figure 3-11. Normalized force-deformation response of the flexure-controlled walls (52 specimens) – curvature ductility | 98 |
| Figure 3-12. Correlation between the fitted (with ACI 318-11 parameters) and measured shear stress for the shear-controlled walls..... | 103 |
| Figure 3-13. Correlation between the best fitted and measured shear stress for the shear-controlled walls..... | 103 |
| Figure 3-14. Correlation between the fitted (with ACI 318-11 parameters) and measured shear stress for the transition walls..... | 104 |
| Figure 3-15. Correlation between the best fitted and measured shear stress for the transition walls | 104 |
| Figure 3-16. Correlation between the fitted (with ACI 318-11 parameters) and measured shear stress for the flexure-controlled walls..... | 105 |
| Figure 3-17. Correlation between the best fitted and measured shear stress for the flexure-controlled walls..... | 105 |

| | |
|---|-----|
| Figure 3-18. Correlation between the best fitted and calculated μ_{ϕ_1} for the shear-controlled walls | 110 |
| Figure 3-19. Correlation between the simplified and calculated μ_{ϕ_1} for the shear-controlled walls | 110 |
| Figure 3-20. Correlation between the best fitted and calculated μ_{ϕ_1} for the transition walls | 111 |
| Figure 3-21. Correlation between the simplified and calculated μ_{ϕ_1} for the transition walls.... | 111 |
| Figure 3-22. Correlation between the best fitted and calculated μ_{ϕ_1} for the flexure-controlled walls | 112 |
| Figure 3-23. Correlation between the simplified and calculated μ_{ϕ_1} for the flexure-controlled walls | 112 |
| Figure 3-24. Correlation between the best fitted and calculated μ_{δ_1} for the shear-controlled walls | 115 |
| Figure 3-25. Correlation between the simplified and calculated μ_{δ_1} for the shear-controlled walls | 116 |
| Figure 3-26. Correlation between the fitted (with ACI 318-11 parameters) and measured shear strength for the shear-controlled walls..... | 119 |
| Figure 3-27. Correlation between the best fitted and measured shear strength for the shear- controlled walls..... | 119 |
| Figure 3-28. Correlation between the fitted (with ACI 318-11 parameters) and measured shear strength for the transition walls..... | 120 |
| Figure 3-29. Correlation between the best fitted and measured shear strength for the transition walls | 120 |

| | |
|--|-----|
| Figure 3-30. Correlation between the fitted (with ACI 318-11 parameters) and measured shear strength for the flexure-controlled walls..... | 121 |
| Figure 3-31. Correlation between the best fitted and measured shear strength for the flexure-controlled walls..... | 121 |
| Figure 3-32. Dispersion of shear strength using: (a) ACI 318-11 equation, (b) derived equation with ACI 318-11 parameters..... | 122 |
| Figure 3-33. Correlation between the best fitted and calculated μ_{ϕ_1} for the shear-controlled walls..... | 124 |
| Figure 3-34. Correlation between the simplified and calculated μ_{ϕ_1} for the shear-controlled walls..... | 125 |
| Figure 3-35. Correlation between the best fitted and calculated μ_{ϕ_1} for the transition walls | 125 |
| Figure 3-36. Correlation between the simplified and calculated μ_{ϕ_1} for the transition walls.... | 126 |
| Figure 3-37. Correlation between the best fitted and calculated μ_{ϕ_1} for the flexure-controlled walls..... | 126 |
| Figure 3-38. Correlation between the simplified and calculated μ_{ϕ_1} for the flexure-controlled walls..... | 127 |
| Figure 4-1. Torre Alto Rio (a) before, (b) after the earthquake [(a) Bonelli, 2010; (b) Wallace, 2010]..... | 132 |
| Figure 4-2. (a) Plan view (1st floor) and (b) Plan view (2st floor). (Figures taken from ftp://atc94:chile-concrete@ftp.atcouncil.org .)..... | 134 |
| Figure 4-3. Location of the 2010 Chilean Earthquake [USGS, 2010]..... | 135 |
| Figure 4-4. Ground acceleration histories recorded in Concepción | 135 |

| | |
|--|-----|
| Figure 4-5. (a) Displacement spectra: Code ($A_0 = 0.4$), (b) Acceleration spectra, Elastic, and Inelastic | 137 |
| Figure 4-6. Effective force reduction factor R_{eff}^* (Lagos et al., 2012) | 138 |
| Figure 4-7. Typical detailing at wall boundaries in Chile (constructed in 2008) | 139 |
| Figure 4-8. Elevation views of the walls (after Uribe, 2010) | 141 |
| Figure 4-9. Typical cross-sectional view of the walls in Axes 11 and 13 (@ 1st floor) (after Uribe, 2010) | 142 |
| Figure 4-10. Specimen TW1 [Thomsen and Wallace, 2004] | 144 |
| Figure 4-11. Lateral load vs. top displacement relation for specimen TW1 [Thomsen and Wallace, 2004] | 144 |
| Figure 4-12. Damage at the transverse walls after the earthquake (Uribe, 2010) | 146 |
| Figure 4-13. T-shaped wall strain gradients | 146 |
| Figure 4-14. Collapsed building Torre Alto Rio..... | 147 |
| Figure 4-15. Damage illustration | 148 |
| Figure 4-16. Moment-curvature relation of the T-shaped cross section..... | 149 |
| Figure 4-17. Examples for wall crushing: (a) Macul, Santiago [Wallace, 2010]; (b) Santiago [Moehle, 2010]..... | 150 |
| Figure 4-18. Views of the structural model in Perform 3D | 151 |
| Figure 4-19. Material stress-strain relationships: (a) Concrete, b) Reinforcing Steel, (c) Shear material | 153 |
| Figure 4-20. Analytical meshing of the model | 157 |
| Figure 4-21. Pushover curves in positive and negative H1 directions..... | 161 |
| Figure 4-22. Compressive strain demands at the east-side walls and failure assessment..... | 162 |

| | |
|--|-----|
| Figure 4-23. Base shear response history | 163 |
| Figure 4-24. Maximum strain demands at the transverse walls..... | 163 |
| Figure 4-25. Moment-rotation relationship for the top floor slab in Axis 13 | 164 |
| Figure 4-26. Comparison of the models with and without slabs | 165 |
| Figure 4-27. Strut and tie model and assessment of shear demands in the filled-in corridor walls (Axis 13) | 168 |
| Figure 4-28. (a) Alternative meshing for sensitivity studies and (b) comparisons of strains for six different cases | 169 |
| Figure 4-29. Roof drift comparisons for six different cases | 169 |
| Figure 5-1. E-Defense shaking table..... | 177 |
| Figure 5-2. Overview of test set up on the shaking table..... | 177 |
| Figure 5-3. Plan and elevation views of the test specimens | 177 |
| Figure 5-4. Equivalent lateral loads on the shear wall system..... | 185 |
| Figure 5-5. P-M interaction diagram for the wall..... | 185 |
| Figure 5-6. Inter-story drift demands for the wall | 186 |
| Figure 5-7. Collapse mechanism assessment-influence of wall yielding level | 188 |
| Figure 5-8. Controlling collapse mechanism in the wall direction a) triangular load, (b) uniform load..... | 189 |
| Figure 5-9. Instrumentation of the RC shear walls..... | 190 |
| Figure 5-10. LVDT layout in the RC Building (South Wall)..... | 191 |
| Figure 5-11. Acceleration spectra of the Kobe records | 192 |
| Figure 5-12. Displacement spectra of the Kobe records..... | 192 |
| Figure 5-13. Roof drift history of the RC Building | 193 |

| | |
|---|-----|
| Figure 5-14. (a) Base shear vs. roof drift; (b) Base moment vs. roof drift | 193 |
| Figure 5-15. Overall damage of the RC Building (a) 50% Kobe, (b) 100% Kobe [Nagae et. al., 2012] | 194 |
| Figure 5-16. Damage on the RC shear walls (Axis A) at (a) 50%, (b) 100% Kobe record..... | 194 |
| Figure 5-17. Views of the structural model in Perform 3D | 195 |
| Figure 5-18. (a) Unconfined concrete stress-strain relationship (Floor 1), (b) Confined concrete stress-strain relationship (Floor 1) | 196 |
| Figure 5-19. Reinforcement material stress-strain relationships | 197 |
| Figure 5-20. Shear material stress-strain relationship..... | 198 |
| Figure 5-21. Comparisons at 25% Kobe: (a) roof drifts, (b) base overturning moments | 200 |
| Figure 5-22. Comparison of global response at 25% Kobe | 200 |
| Figure 5-23. Comparisons at 50% Kobe record: (a) roof drifts, (b) base overturning moments | 201 |
| Figure 5-24. Comparison of global response at 50% Kobe record..... | 201 |
| Figure 5-25. Comparisons at 100% Kobe record: (a) roof drifts, (b) base overturning moments | 202 |
| Figure 5-26. Comparison of global response at 100% Kobe record..... | 202 |
| Figure 5-27. Enhanced model at 25% Kobe record – effect of including concrete tension behavior..... | 203 |
| Figure 5-28. Enhanced model at (a) 25%, (b) 50%, (c) 100% Kobe records – effects of modeling slip/extension effects explicitly..... | 206 |
| Figure 5-29. Enhanced model at (a) 25%, (b) 50%, (c) 100% Kobe records – effects of cyclic degradation..... | 208 |
| Figure 5-30. Enhanced model at 100% Kobe record – effects of strength degradation | 209 |

| | |
|---|-----|
| Figure 5-31. Comparisons at 25% Kobe: (a) roof drifts, (b) base shears, (c) base overturning moments, (d) base rotations over 550 mm..... | 210 |
| Figure 5-32. Comparisons at 25% Kobe: (a) Base shear vs roof drift, (b) Base moment vs roof drift..... | 210 |
| Figure 5-33. Comparisons at 50% Kobe: (a) roof drifts, (b) base shears, (c) base overturning moments, (d) base rotations over 550 mm..... | 211 |
| Figure 5-34. Comparisons at 50% Kobe: (a) Base shear vs roof drift, (b) Base moment vs roof drift..... | 212 |
| Figure 5-35. Comparisons at 100% Kobe: (a) roof drifts, (b) base overturning moments, (c) base shears, (d) base rotations..... | 213 |
| Figure 5-36. Comparisons at 100% Kobe: (a) Base moment vs roof drifts, (b) Base shear vs roof drifts | 213 |
| Figure 5-37. Slip/extension moment-rotation hinge properties | 214 |
| Figure 5-38. Enhanced model at (a) 25%, (b) 50%, (c) 100% Kobe records – sensitivity of the slip/extension behavior | 216 |
| Figure 5-39. Alternative steel behaviors for sensitivity studies (example for D19 bars) | 217 |
| Figure 5-40. Enhanced model at 100% Kobe record – sensitivity of the descending portion of the steel material | 217 |
| Figure 5-41. Enhanced model at 100% Kobe record – sensitivity of the cyclic degradation parameters used in the steel material | 219 |
| Figure 5-42. Enhanced model at 100% Kobe record – sensitivity of the cyclic degradation parameters used in the steel material | 219 |
| Figure B-1. Four points defined to obtain backbone curves..... | 250 |

| | |
|---|-----|
| Figure B-2. Range of height, length, thickness in three failure regions | 251 |
| Figure B-3. Range of concrete strength, shear span ratio, spacing to boundary bar diameter ratio in three failure regions | 252 |
| Figure B-4. Range of axial load ratio, yield strength of transverse boundary reinforcement, transverse boundary reinforcement ratio in three failure regions | 253 |
| Figure B-5. Range of yield strength of longitudinal boundary reinforcement, longitudinal boundary reinforcement ratio, yield strength of longitudinal web reinforcement in three failure regions..... | 254 |
| Figure B-6. Range of yield strength of longitudinal web reinforcement ratio, yield strength of transverse web reinforcement, transverse web reinforcement ratio in three failure regions | 255 |
| Figure B-7. Distribution of correlation coefficient of key parameters with respect to the shear strength..... | 257 |
| Figure B-8. Distribution of correlation coefficient of key parameters with respect to the normalized deformation capacity (curvature ductility)..... | 258 |
| Figure C-1. Concrete properties from the test results | 259 |

LIST OF TABLES

| | |
|--|-----|
| Table 2-1. Linear dynamic site specific response spectrum analysis parameters [Ghodsi, et al., 2009] | 13 |
| Table 2-2. Period and mass participation summary | 13 |
| Table 2-3. Load criteria [Ghodsi, et al., 2009]..... | 14 |
| Table 2-4. Design acceptance criteria for serviceability level [Ghodsi, et al., 2009] | 17 |
| Table 2-5. Design acceptance criteria for collapse prevention level [Ghodsi, et al., 2009] | 18 |
| Table 2-6. Period and mass participation summary | 19 |
| Table 2-7. Stiffness assumptions | 22 |
| Table 2-8. Cyclic degradation parameters | 27 |
| Table 2-9. Damping parameters for Building 2A | 31 |
| Table 2-10. Damping parameters for Building 2B | 33 |
| Table 2-11. Initial structural and content costs, in million U.S. dollars | 77 |
| Table 2-12. Annual repair costs | 78 |
| Table 3-1. Expected behavior and failure modes of the walls | 83 |
| Table 3-2. Summary of the specimens included in the study | 91 |
| Table 3-3. Range of the parameters in each of the category..... | 92 |
| Table 3-4. Comparisons of nominal and measured normalized shear stress values..... | 100 |
| Table 3-5. Correlation coefficients of key parameters with respect to the shear strength..... | 101 |
| Table 3-6. Summary of the shear strength equations and the corresponding correlation coefficients and standard deviation with respect to the original data | 102 |
| Table 3-7. Comparisons of alternative equations of shear strength..... | 106 |

| | |
|---|-----|
| Table 3-8. Correlation coefficients of key parameters to the normalized deformation capacity (μ_{ϕ_1})..... | 107 |
| Table 3-9. Summary of the normalized deformation capacity equations and the corresponding correlation coefficients and standard deviation with respect to the original data..... | 109 |
| Table 3-10. Average normalized deformation capacities (μ_{ϕ_1}) | 109 |
| Table 3-11. Summary of the normalized deformation capacity equations and the corresponding correlation coefficients and standard deviation with respect to the original data..... | 115 |
| Table 3-12. Summary of the shear strength equations and the corresponding correlation coefficients and standard deviation with respect to the original data | 118 |
| Table 3-13. Comparisons of alternative equations of shear strength..... | 118 |
| Table 3-14. Summary of the normalized deformation capacity equations for the ACI 318 compliant walls | 123 |
| Table 3-15. Average normalized deformation capacities (μ_{ϕ_1}) | 124 |
| Table 4-1. Period and mass participation summary..... | 159 |
| Table 4-2. Normalized displacements based on modal analysis results | 159 |
| Table 5-1. Reinforcement details of columns, walls, and slabs..... | 179 |
| Table 5-2. Reinforcement details of beams and girders | 180 |
| Table 5-3. Weight of the RC Building..... | 181 |
| Table 5-4. Design material properties..... | 182 |
| Table 5-5. Actual material properties | 182 |
| Table 5-6. Cyclic degradation parameters for the reinforcing steel..... | 218 |
| Table 5-7. Cyclic degradation parameters for the beam moment-rotation hinges..... | 218 |
| Table B-1. Specimen Geometry Data | 231 |

| | |
|---|-----|
| Table B-2. Specimen Concrete and Web Reinforcement Details..... | 236 |
| Table B-3. Specimen Boundary Reinforcement Details..... | 241 |
| Table B-4. Specimen Load and Displacement Data | 246 |

ACKNOWLEDGMENTS

First of all, I would like to express my sincere thanks and gratitude to my advisor, Professor John W. Wallace, for his guidance and support throughout the course of my graduate study and the research work. Thanks are also extended to the members of the doctoral committee, Professors Thomas Sabol, Scott Brandenburg, Jian Zhang, and Jack P. Moehle for their invaluable advice and insightful comments. I would like to thank Professor Moehle in particular for sharing information and ideas throughout my research.

I would like to acknowledge Assistant Professor Tony Yang at the University of British Columbia for his valuable collaboration while working closely on my research presented in Chapters 2 and 3. His support and encouragement also is greatly appreciated. Thanks are extended to Assistant Professor Leonardo Massone at the University of Chile, for providing information and valuable comments on Chapter 4.

I would also like to thank Dr. Alberto Salamanca for his contribution to my teaching experience. Thanks also go to Dr. Robert L. Nigbor and Erica Eskes for their friendly assistance anytime I needed some help.

My special thanks go to fellow doctoral student Camille Marodon for being a wonderful friend to me and for her continuous support over the last four years. Thanks are extended to my coworkers, Thien Tran, Kristijan Kolozvari, Christopher Motter, and Christopher Hilson, for their help and encouragement; particularly to Sofia Gavridou for her great friendship and collaboration on the E-Defense related studies. My exceptional thanks are also given to Emel Seyhan, Kamil Afacan, and Salih Tileylioglu for their invaluable friendship and encouragement during my graduate studies, as well as to my dear friends back from Middle East Technical University: Beliz Ugurhan, Nazli Aslican Yilmaz, and Tolga Tonguc Deger.

Last but not the least; I would like to especially thank my family, particularly to my parents Hulya-Ahmet Tuna and my brothers Mehmet and Mahmut, for being continuously supportive of me throughout my education, and for enduring years of distance to let me achieve my goals.

VITA

- 2008
B.S., Civil Engineering
Middle East Technical University
Ankara, Turkey
- 2009
M.S., Civil and Environmental Engineering
University of California, Los Angeles
Los Angeles, CA
- 2009-2012
Teaching Assistant
Dept. of Civil and Environmental Engineering
University of California, Los Angeles
- 2009-2012
Graduate Student Research Assistant
Dept. of Civil and Environmental Engineering
University of California, Los Angeles

SELECTED PUBLICATIONS AND PRESENTATIONS

- Moehle, J.P., Bozorgnia, Y., Jayaram, N., Jones, P., Rahnama, M., Shome, N., Tuna, Z., Wallace, J.W., Yang, T.Y., Zareian, F., (2011). "Case studies of the seismic performance of tall buildings designed by alternative means," Task 12 Report for the Tall Buildings Initiative, PEER 2011/05, Pacific Earthquake Engineering Research Center, University of California, Berkeley.
- Nagae, T., Tahara, K., Matsumori, T., Shiohara, H., Kabeyasawa, T., Kono, S., Nishiyama, M., Wallace, J., Ghannoum, W., Moehle, J., Sause, R., Keller, W., Tuna, Z., (2011). "Design and Instrumentation of the 2010 E-Defense Four-Story Reinforced Concrete and Post-Tensioned Concrete Buildings," PEER Report 2011/104, Pacific Earthquake Engineering Research Center, University of California, Berkeley.
- Tuna Z., Wallace J. W., Yang T. Y., and Moehle, J.P., "*Seismic safety evaluation of the RC shear walls in high-rise buildings*," The Young Researcher Session and Poster Reception, PEER Annual Meeting, September 30 – October 1, 2011., Berkeley, CA, USA.
- Tuna Z., Wallace J. W., "Preliminary Collapse Assessment of the Torre Alto Rio Building In The Mw = 8.8 February 27, 2010 Chile Earthquake," ACI Spring Convention, April 3-7, 2011, Tampa, FL, USA.
- Tuna Z., Wallace J. W., "Preliminary Collapse Assessment of the Torre Alto Rio Building In The Mw = 8.8 February 27, 2010 Chile Earthquake," 8th International Conference on Urban Earthquake Engineering, Tokyo Institute of Technology, March 7-8, 2011, Tokyo, Japan.
- Tuna Z., Wallace J. W., "Analysis of Dual System Building," Los Angeles Tall Buildings Structural Design Council: Tall Building Design Showcase, May 7, 2010, Los Angeles, CA, USA.

Chapter 1 Introduction

1.1. Objectives and Scope

The studies presented focus on examining the behavior, response, and modeling of shear walls, with the objective of improving our ability understand failure/collapse of reinforced concrete shear wall buildings under earthquake loading. Separate studies were conducted, two of which were aimed at assessing and improving modeling of conventional reinforced concrete (RC) buildings that utilize structural walls for lateral load resistance: one study focused on seismic performance of a RC dual system tall building (core wall and moment frames) designed following different design approaches, whereas the other study focused on modeling and behavior of a four-story RC building tested on the E-Defense shake table in 2010. Two other studies were conducted to investigate and understand failure of shear walls: one that concentrated on defining shear strength and deformation capacity of the structural walls by developing a comprehensive test database, and another that focused on possible reasons for collapse of a 15-story shear wall building (Torre Alto Rio) in the 2010 Chile earthquake.

1.1.1. Seismic performance of tall buildings

Use of performance-based design for design of new tall buildings has become very common in recent years because the process allows designers to bypass certain prescriptive code requirements, such as height limits. Guidelines for non-prescriptive design have been published by Los Angeles Tall Buildings Structural Design Council for the Los Angeles area. However, it was unclear whether a building designed using a performance-based designed approach produces a design that actually performs better than a building designed using prescriptive code-based procedures. To address this issue, a study of three tall buildings was initiated by the Pacific

Earthquake Engineering Research (PEER) Center Tall Buildings Initiative to analyze and quantify building performances using engineering demand parameters (EDPs) at five different levels of ground shaking intensities for code-designed and two different performance-based designed tall buildings.

This dissertation focuses on one of the three tall buildings considered: a 42-story reinforced concrete dual system (Building 2) which consisted of core walls and moment frames. The building was designed using three different design approaches. Approach A follows the traditional code design approach (e.g. IBC 2006), approach B follows the performance-based design procedure published by the LATBSDC, and approach C follows an enhanced performance-based design approach published by the Pacific Earthquake Engineering Center (a draft version of the PEER TBI Guidelines). Nonlinear dynamic responses of differently designed buildings were analyzed at five hazard levels using CSI Perform3D. Seismic performance of the different designs were assessed and compared for various response quantities at each level of ground shaking intensity by post-processing the nonlinear response history analysis results. The results of the design study were used to assess and compare construction costs, whereas results of the analyses (EDPs) were used to assess repair costs by a professional cost estimator. Failure of the shear walls was also assessed using the analysis results and a failure envelope which was obtained using previous test results.

1.1.2. Shear Strength and Deformation Capacity of Reinforced Concrete Shear Walls

Reinforced concrete structural (shear) walls are commonly used in lateral load resisting systems as they provide significant lateral strength and stiffness under earthquake loading. Therefore, a good understanding of wall shear strength and deformation capacity is necessary to be able assess failure of the shear walls and shear wall buildings. Previous studies (Orakcal et al, 2009),

which were conducted using a limited test database, was used to define a shear strength failure criteria for structural walls that was used in the case study of the 42-story reinforced concrete dual system building. However, because the number of tests in the database was very limited, there was insufficient data to assess and verify the failure criteria used in the PEER TBI study; therefore, additional studies were conducted to investigate the potential to improve the definition of failure.

To address this need, a detailed wall test database (consisting of 124 specimens) was developed and used to determine the influence of various parameters on wall shear strength and deformation capacity. The database also was used to assess the validity of the ACI 318-11(S21.11.9) equation used to compute wall shear strength. Alternative relations were recommended for wall shear strength and deformation capacity depending on expected wall behavior; these expressions are valuable in that they can be used by engineers to provide more reliable designs by assessing demand-to-capacity ratios for both strength and ductility. Design variables with the greatest impact can then be adjusted to improve safety. An important component of this study was to determine median values and dispersions of wall shear strength associated with different wall failure modes, as well as impacts of various parameters on wall deformation capacity for the various failure modes. Another advantage of this study is that nonlinear deformation capacity of the walls that are expected to have brittle failure modes (shear-controlled walls) can be assessed and used for safety evaluation/rehabilitation of existing buildings to achieve more economical designs.

1.1.3. Collapse Assessment of Torre Alto Rio

The $M_w = 8.8$ February 27, 2010 earthquake in Chile subjected thousands of modern reinforced concrete buildings to strong shaking. The 15-story, residential, Torre Alto Rio building (located

in Concepcion) was one of the few, modern RC buildings over ten stories to collapse. Since the concrete building code used in Chile is based on ACI 318-95, and includes seismic design approaches similar to those in ASCE 7-10, assessing the performance of this building and identifying possible reasons for the collapse is a valuable exercise. Reasons for the collapse were studied using post-earthquake observed damage, structural drawings, and nonlinear static and dynamic response analyses. The aim was to assess nonlinear response using the ground motions recorded in Concepcion and to understand the behavior of the building as well as potential factors that caused collapse, using state-of-the-art nonlinear modeling approaches.

1.1.4. 2010 E-Defense Four-Story Reinforced Concrete and Post-Tensioned Buildings

A series of shaking table tests were conducted on two, full-scale, four-story buildings on the NIED E-Defense shake table in December 2010. The buildings were almost identical in geometry and configuration; one building utilized a conventional reinforced concrete (RC) structural system with shear walls in one direction and moment frames in the other direction, whereas the other building utilized the same systems constructed with post-tensioned (PT) members. The buildings were simultaneously subjected to increasing intensity shaking until large deformations were reached to assess performance in service, design, and maximum considered earthquake shaking. Nonlinear modeling and analysis of the reinforced concrete building was investigated as a means to assess current modeling approaches and assumptions. The model was developed using Perform 3D (CSI, 2011) because this software is commonly used in engineering practice in the United States, and similar programs are used worldwide. Response history analyses were conducted in the shear wall direction, to compare analytical and experimental results. The results of this study helped guide the study related to the Alto Rio building discussed in 1.1.3.

1.2. Organization

This dissertation is organized into six chapters. The introduction (Chapter 1) is followed by the 42-story reinforced concrete dual system case study in Chapter 2. This chapter includes design and performance information for the building, including the design of the structural system, analytical modeling, summary of response results, as well as failure assessment of shear walls. Chapter 3 provides a statistical study to reassess the failure criteria for shear walls as well as to define wall shear strength and deformation capacity. Chapter 4 presents collapse assessment of the Torre Alto Rio building in the 2010 Chile Earthquake. Chapter 5 provides an overview of the full-scale testing of four-story reinforced concrete and post-tensioned concrete buildings, as well as nonlinear modeling of the reinforced concrete building and comparisons of test results and analytical results. Conclusions to the research are provided in Chapter 6.

Chapter 2 Case Study of a 42-story Reinforced Concrete Dual System Building

2.1. Introduction

Until fairly recently, tall buildings have typically been designed following building code requirements using linear analysis procedures, such as a linear response spectrum approach; use of nonlinear analysis was rare. However, since the early 2000's, use of performance-based design and non-linear analysis for specified ground motions has become more common. Use of a performance-based design approach has led engineers to seek more economical lateral-force-resisting-systems, systems or components of these systems may be allowed within the prescriptive requirements of current codes. Probably the most common exception that arises for new tall building construction is the case of a central core wall as the only lateral-force-resisting-system in a building that exceeds 160 ft, whereas the code would require the use of a dual system. To design such systems, project specific design criteria are established and peer-review is required.

In recent years, consensus documents have been developed in an attempt to provide for a more uniform peer-review process for tall buildings, such as San Francisco Department of Building and Inspection AB-083 (Seismic Design and Review of Tall Buildings Using Non-Prescriptive Procedures), 2005 LATBSDC guidelines, and subsequent versions in 2008 and 2011 (Los Angeles Tall Buildings Structural Design Council), and PEER-TBI (Pacific Earthquake Engineering Research Center-Tall Building Initiative). Since studies have not been conducted to compare the expected performance of code designed versus performance-based designed buildings, it was generally unknown if buildings designed according to a performance-based

approach actually are likely to perform equivalent to, or better than, buildings designed using current prescriptive code requirements. Systematic studies at various hazard levels were needed to investigate this issue.

To accomplish this task, a multi-campus study was undertaken to analyze three building systems, a 42-story reinforced concrete core wall (Building 1), a 42-story reinforced concrete dual system (Building 2), and a 40-story steel buckling restrained braced frame (Building 3), each located in Los Angeles, CA. The buildings were designed to: (A) satisfy current code requirements (IBC 2006, which adopts ACI 318-08 and ASCE 7-05), (B) satisfy serviceability level criteria and to comply with the collapse prevention criteria under the Maximum Considered Earthquake (MCE) as described in Los Angeles Tall Building Structural Design Council “An Alternative Design Approach for Tall Buildings” (LATBSDC 2008), with minimal exceptions (e.g. definition of serviceability level and minimum base shear requirement are ignored.), (C) achieve a better performance with an enhanced performance-based design approach following the performance-based design procedures published the Pacific Earthquake Engineering Research Center Tall Building Initiative (PEER/TBI 2010)).

To investigate responses, five levels of ground shaking intensity were selected: Serviceability with 25 years return period (70%/30 years), Serviceability with 43 years return period (50%/30 years), Life-Safety with 475 years return period (10%/ 50 years), Collapse Prevention with 2475 years return period (2%/50 years) and a higher intensity than Collapse Prevention with 4975 years return period (1% in 50 years). They were named as SLE25, SLE43, DBE, MCE, and OVE, respectively. Each building design was analyzed for 15 ground motions for each hazard level. Response quantities such as floor accelerations, floor displacements, inter-story drifts, and core wall forces and strains, commonly referred to as EDPs (engineering

demand parameters), were obtained for each ground motion and median and dispersion were determined for each hazard level. Results for all hazard levels provide information necessary to develop fragility relations for the various EDPs. Collections of these data enable a systematic review of the relative merits associated with the two performance-based design approaches.

Results presented in this chapter focus on the 42-story reinforced concrete dual system (Building 2). The building description, three different designs, and modeling assumptions for primary components, as well as response history analysis results and comparisons based on cost analyses of the building, are presented in the following sections.

2.2. Design

2.2.1. Building Properties

The dual system building had 42 stories above the ground and 4 stories below the ground with a typical story height of 10.5 ft and a 20 ft tall penthouse (Figure 2-1, Figure 2-2). The lateral-force-resisting system consists of a core wall and four-bay Special Moment Frames along all four sides of the building perimeter. The core walls were composed of L-shaped walls connected with coupling beams which were typically 30" deep. The core wall continues through the podium and basement levels to the foundation and exterior 16" thick basement walls exist around the perimeter of the 4 story podium below grade. At ground level, a diaphragm exists to transfer loads to the perimeter basement walls. Typical plan views for basement levels and the tower levels are presented in Figure 2-3.

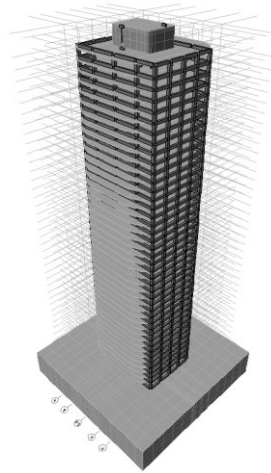


Figure 2-1. Three dimensional building view [Ghods, et al., 2009]

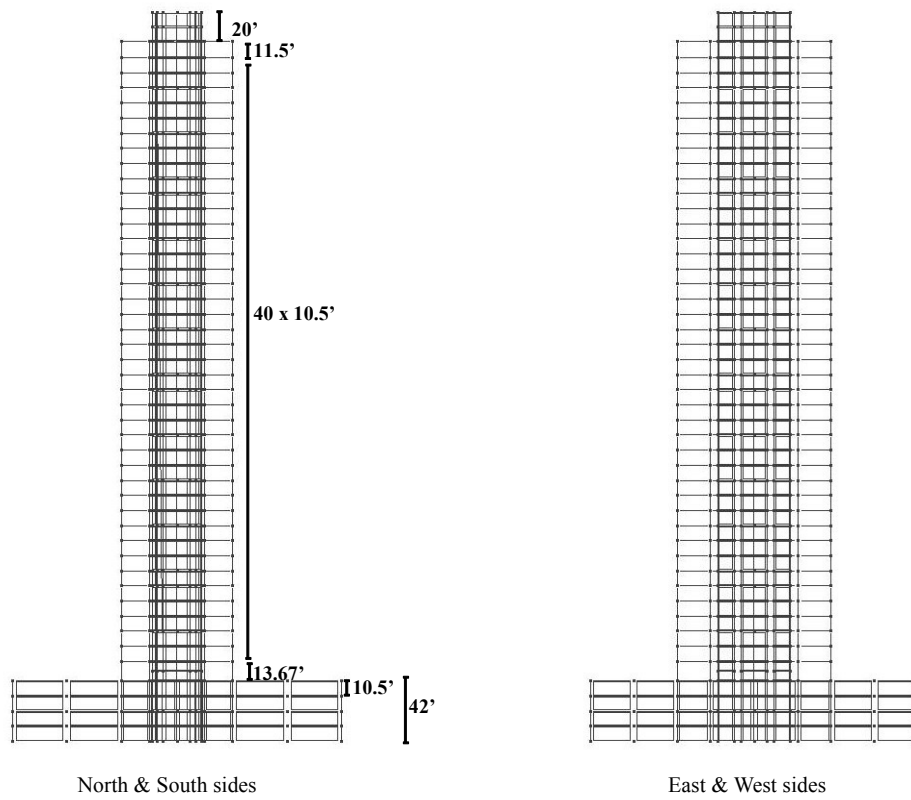
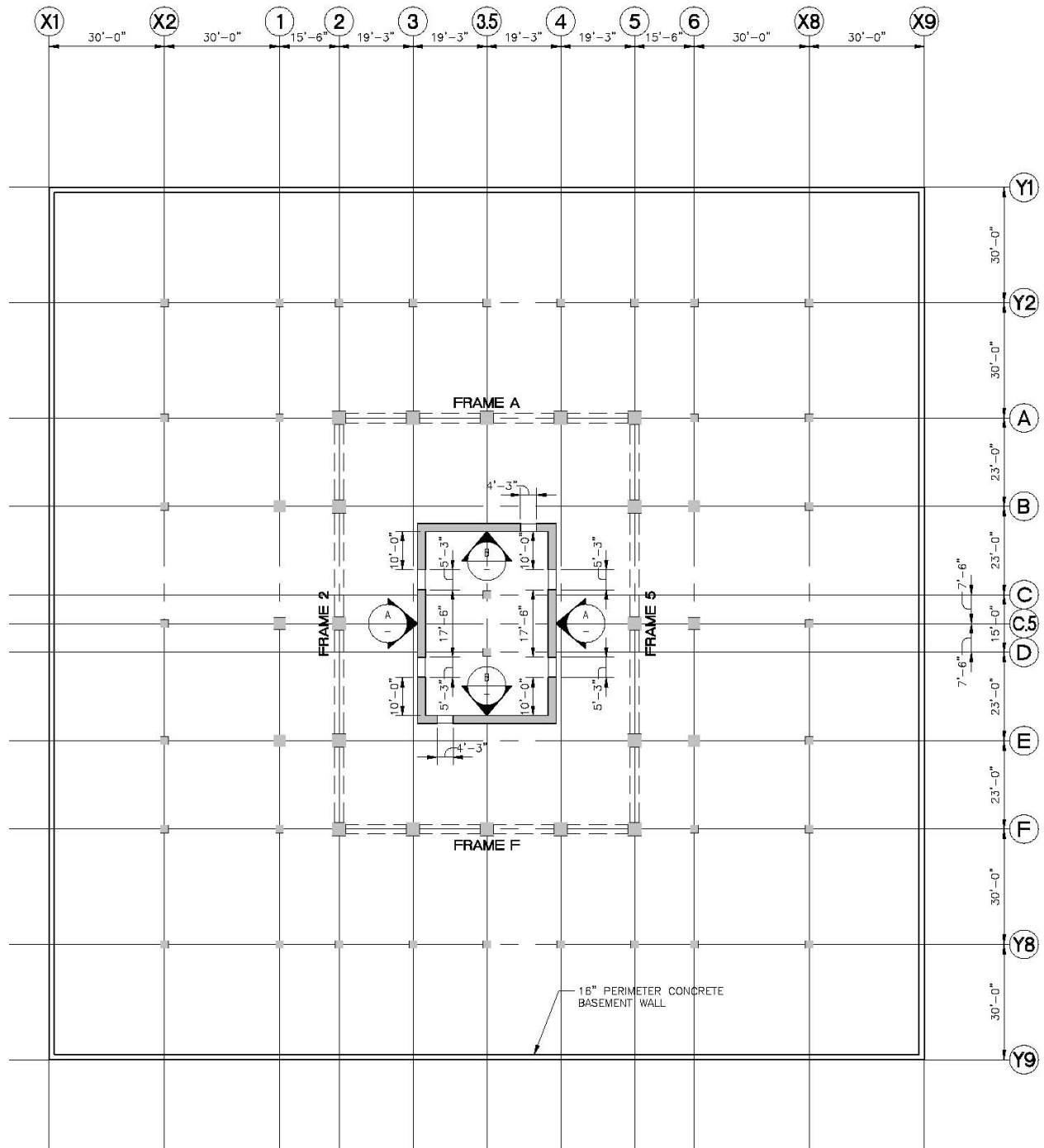
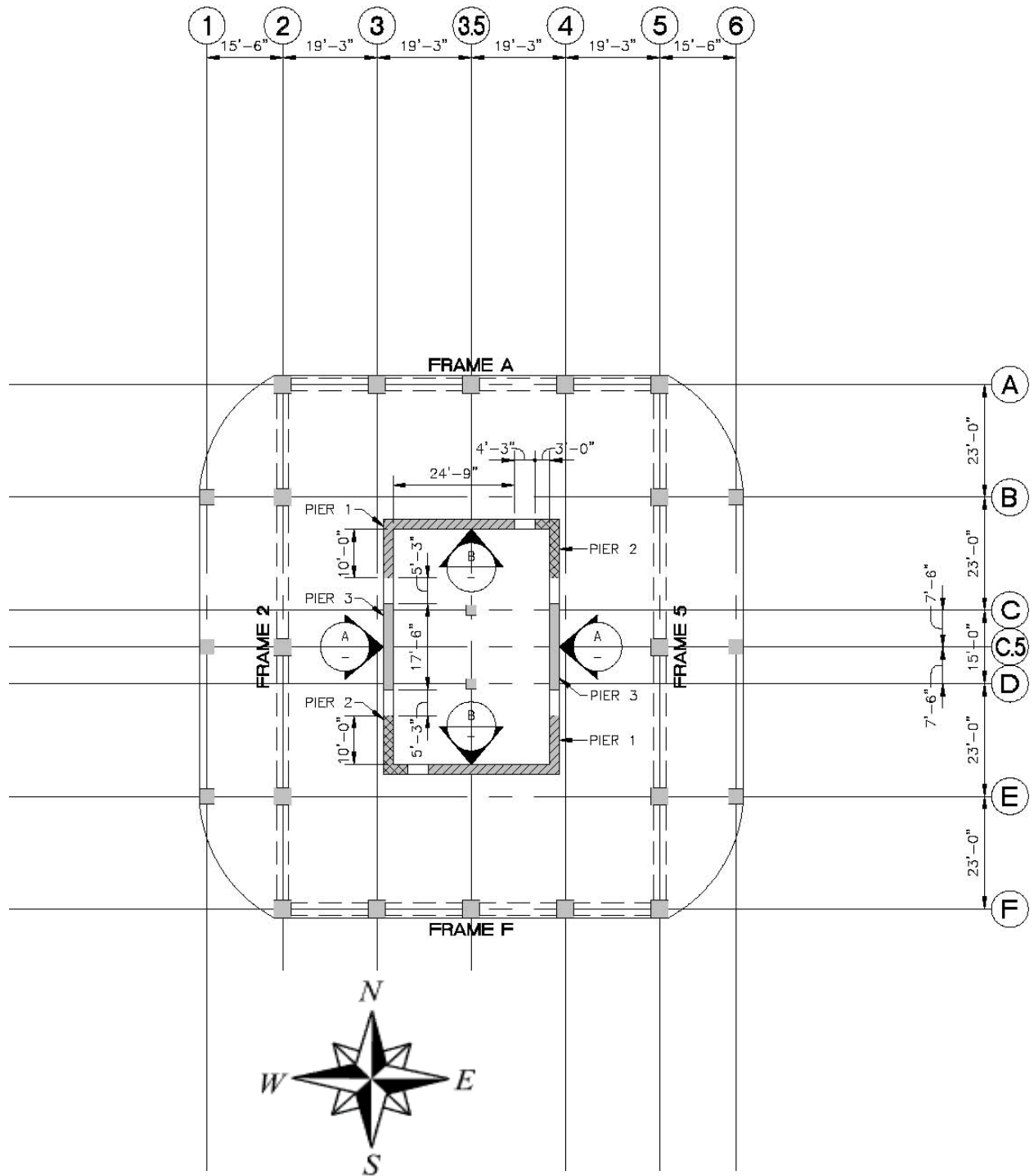


Figure 2-2. Elevation views of the building



(a) Basement levels



(b) Tower levels

Figure 2-3. Typical plan view for basement and tower levels [Ghodsi, et al., 2009]

In the overall study, which included three tall buildings; the dual system was designated as Building 2 and was designed by Englekirk Partners Inc (EPI). Three designs were completed for Building 2 using: (A) current building code requirements, (B) performance-based, and (C) an enhanced performance-based design. The designs are summarized in the following sections.

2.2.2. Design of Building 2A (Code Design)

Building 2A was designed according to building code provisions in IBC 2006, which requires the use of the ASCE 7-05 and ACI 318-08. Although a height limit of 160 ft exists for core-wall only systems, the code does not specify a height limit for dual systems; therefore, the code was followed prescriptively. A modal response spectrum analysis was used for site-specific response spectra for 5% damping in accordance with ASCE 7-05, (Figure 2-4). Associated spectra parameters and period summary are provided in Table 2-1 and Table 2-2 respectively.

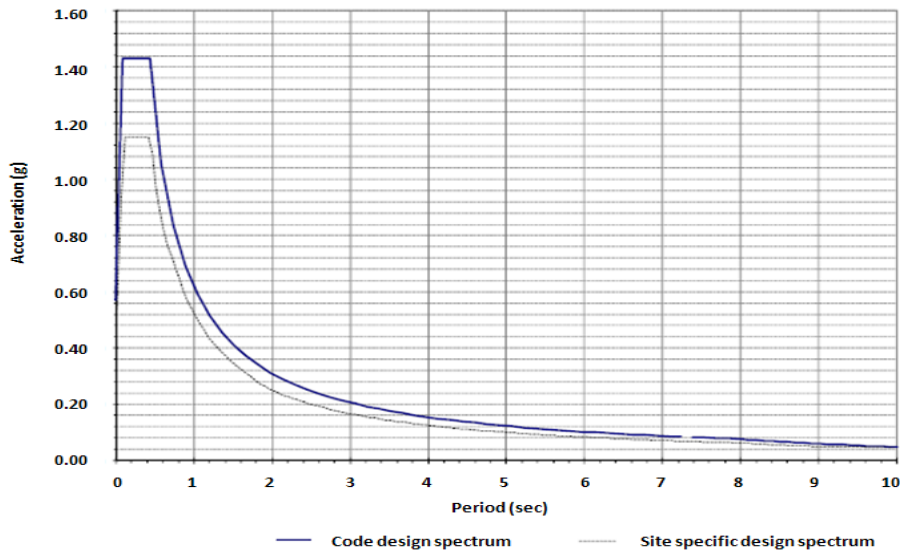


Figure 2-4. 5% damped code and site specific design response spectra [Ghodsii, et al., 2009]

Table 2-1. Linear dynamic site specific response spectrum analysis parameters [Ghods, et al., 2009]

| | |
|---|--|
| S_s | 1.725 g |
| S_1 | 0.602 g |
| F_a | 1 |
| F_v | 1.3 |
| S_{Ms} | 1.718 g |
| S_{M1} | 0.782 g |
| S_{DS} | 1.145 g |
| S_{D1} | 0.521 g |
| R | 7.0 |
| Site Class | C |
| C_d | 5.5 |
| C_s | 0.051 |
| Seismic Weight (W) | 102000 kips |
| Modal combination method | Complete quadratic combination (CQC) |
| Redundancy factor (ρ) | 1.0 |
| Accidental eccentricity | 5% |
| Base shear "V" | 5202 kips |
| Modal Base shear " V_t " | $V_{tx}=11436/R=1634$ kips $V_{ty}=11760/R=1680$ kips |
| Modal base shear scaled to match 0.85 V | $0.85 \times 5202=4421$ kips |

Table 2-2. Period and mass participation summary

| Vibration Mode | Period (sec) | Mass Participation | | Dominant Direction |
|----------------|--------------|--------------------|---------------------|----------------------------------|
| | | H1 (East-West) | H2 (North-South) | |
| 1 | 4.456 | 70.70% | 0.02% | Translation mode on H1 direction |
| 2 | 4.026 | 0.01% | 71.12% | Translation mode on H2 direction |
| 3 | 2.478 | 0% | 5.92 e-5% | Torsion mode |

In addition to the self-weight of the structure, the loads listed in Table 2-3 were used for the calculation of design loads.

Table 2-3. Load criteria [Ghodsi, et al., 2009]

| Use | Location | Superimposed dead load (psf) | Live Load (psf) |
|--------------------------|----------------------------|------------------------------|---------------------|
| Parking | 4 stories below ground | 3 | 50 (Reducible) |
| Retail | Ground Level inside area | 110 | 100 (Non-Reducible) |
| Cladding | Perimeter of tower | 15 psf per elevation | |
| Outside Plaza | Ground level outside area | 350 | 100 (Non-Reducible) |
| Corridors and Exit Areas | Inside elevator core | 28 | 100 (Non-Reducible) |
| Residential | 2nd floor up to 42nd floor | 28 | 40 (Reducible) |
| Mechanical | At roof floor only | 100 kip | 25 (Reducible) |
| Roof | Roof floor | 28 | 20 (Reducible) |

For the core wall, specified concrete strength f'_c was taken as 6000 *psi* for the floors from the foundation to the 20th floor (24" wall thickness) and as 5000 *psi* above the 20th floor (18" wall thickness). The core wall consisted of L-shaped sections connected by 30" deep coupling beams over doorways that provide access to elevators and stairs. For the Special Moment Frame design, all beams had cross-section dimensions of 30"x36" with $f'_c = 5000$ *psi*, and all North and South columns (frames A and F) were 36"x36" with f'_c varying from 10,000 *psi* to 5000 *psi* along the height. East and West columns (frames 2 and 5) varied both in size (from 46"x46" to 36"x36") and f'_c (from 10,000 *psi* to 5000 *psi*) along the height. Typical frame beam and column cross-sections are presented in Figure 2-5. All reinforcement was A706 Grade 60. The reinforcement details of the coupling beams and the frame members are available in

Ghodsi et al., (2009). Floor slabs were 10 in. thick at basement levels, 12" thick at the ground level, 8" thick in the tower, and 10" thick at the roof level. Slabs in the tower were post-tensioned. A 16" thick basement wall existed below grade.

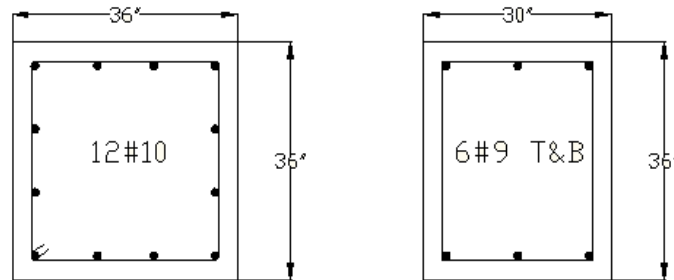


Figure 2-5. Schematic of typical frame beam and column cross-sections

2.2.3. Design of Building 2B (Performance Based Design)

Building 2B, which has the same layout and floor plan as Building 2A, was designed and checked using 2008 LATBSDC guidelines for two performance levels: serviceability and collapse prevention. Each of these levels is described in more detail in the following sections.

2.2.3.1. Serviceability Level

The design forces were obtained using an elastic site-specific response spectrum analysis, where the spectrum represents a mean recurrence interval of 25 years, (Figure 2-6).

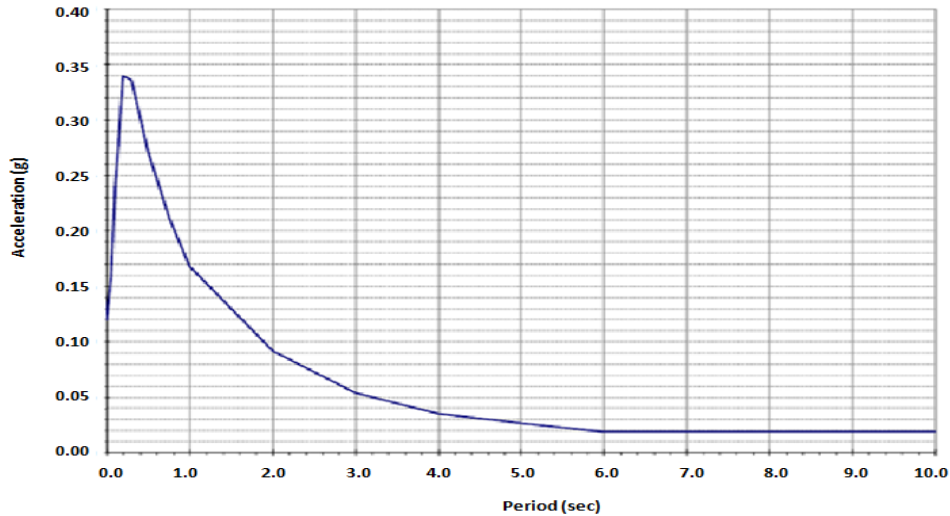


Figure 2-6. Serviceability level spectra

Design acceptance criteria were summarized as follows:

- The overall inter-story drift of the structure should not exceed $0.005h_n$. (LATBSDC (2008) §3.3.6.)
- The following load combination was used: $D+0.25L \pm E_{service}$, where D is dead load, L is live load which is factored by 0.25 (expected live load) and E is earthquake demand at service level.
- Based on the classification of elements and action types (Table 2-4), 20% of the elements with ductile actions are allowed to have a demand to capacity ratio between 1.0 and 1.5 when checking against the load combinations. The remaining elements should have a demand to capacity ratio of 1.0 or less. All elements with brittle actions should have a demand to capacity ratio of 1.0 or less.
- For both ductile and brittle actions, strengths should be calculated using a strength reduction factor in accordance with current material codes. For brittle actions, strength is

calculated using specified material properties. For ductile actions, expected material properties are used.

- Accidental eccentricity is not considered for serviceability checks per LATBSDC recommendations.

Table 2-4. Design acceptance criteria for serviceability level [Ghodsi, et al., 2009]

| Element | Action Type | Classification |
|------------------------------------|---------------------------------------|-----------------------|
| Reinforced Concrete Frame Beam | Flexure Shear | Ductile Brittle |
| Reinforced Concrete Frame Column | Axial-Flexure interaction Shear | Ductile Brittle |
| Reinforced Concrete Shear Walls | Flexure Shear | Ductile Brittle |
| Reinforced Concrete Coupling Beams | Shear | Ductile |

2.2.3.2. Collapse Prevention Level

Building 2B, which was initially designed for serviceability level forces, was then analyzed for MCE level actions. For this purpose, a non-linear 3-D model was created in Perform 3D (CSI, 2006), details of which are discussed in Section 2.2.6. The components were checked using a non-linear response history analysis based on collapse prevention acceptance criteria (Table 2-5). Consistent with requirements in ASCE 7-05, seven pairs of spectrum-matched ground motions with a mean return period of 2475 years were derived using the target acceleration response spectrum shown in Figure 2-7; more information on the selection of ground motions is available

in Moehle et al., 2011 (PEER report). A summary of the periods for different vibration modes is provided in and Table 2-6.

Table 2-5. Design acceptance criteria for collapse prevention level [Ghodsi, et al., 2009]

| Element | Action Type | Classification | Expected behavior | Acceptance limit for non-linear behavior |
|------------------------------------|---------------------------|-----------------------|--------------------------|--|
| Reinforced Concrete Frame Beam | Plastic hinge rotation | Ductile | Non-linear | Hinge rotation ≤ 0.045 rad |
| | Beam Shear | Brittle | Linear | N/A |
| Reinforced Concrete Frame Column | Axial-Flexure interaction | Ductile | Non-linear | Axial compression $\leq 0.40 f_{cexp} A_g$ Hinge rotation ≤ 0.025 rad |
| | Shear | Brittle | Linear | N/A |
| Reinforced Concrete Shear Walls | Axial-Flexure interaction | Ductile | Non-linear | Concrete compression strain ≤ 0.015 Reinforcing rebar tension strain ≤ 0.05 Axial compression force $\leq 0.35 f_{cexp} A_g$ |
| | Shear | Brittle | Linear | N/A |
| Reinforced Concrete Coupling Beams | Shear | Ductile | Non-linear | 0.06 rad chord rotation |

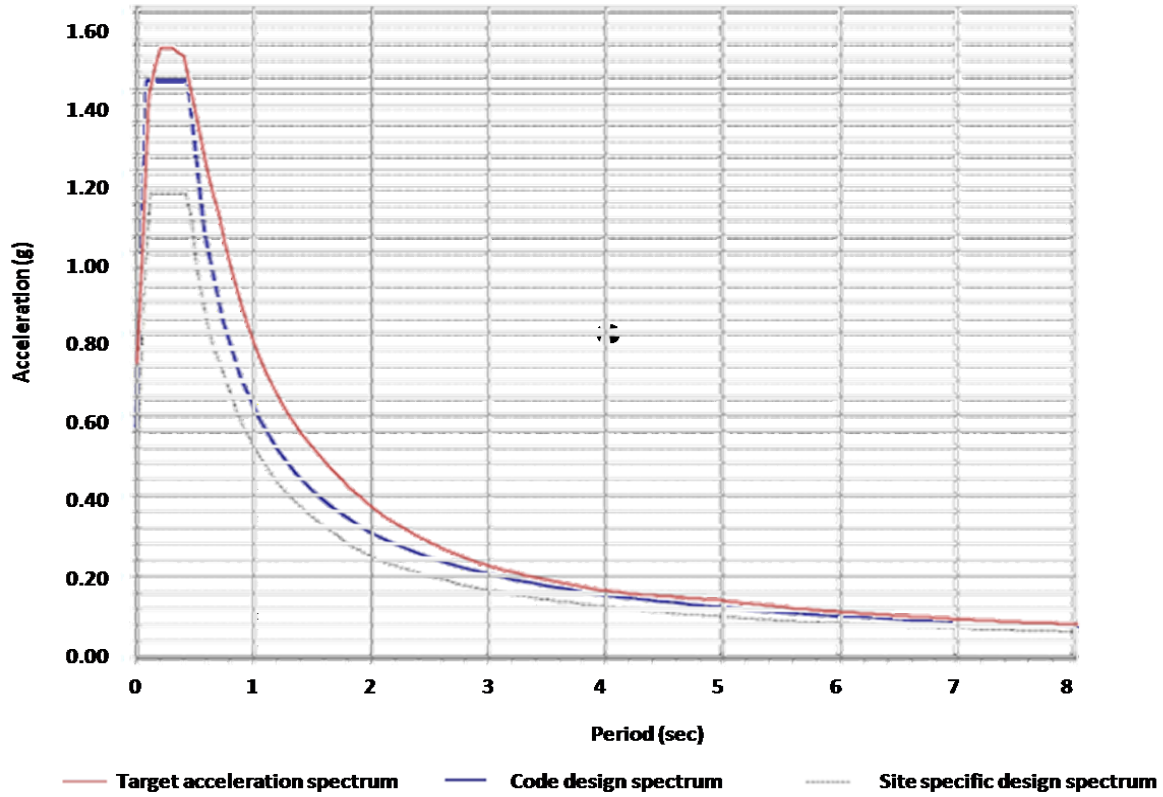


Figure 2-7. Target acceleration response spectra at MCE level

Table 2-6. Period and mass participation summary

| Vibration Mode | Period (sec) | Mass Participation | | Dominant Direction |
|----------------|--------------|--------------------|------------------|----------------------------------|
| | | H1 (East-West) | H2 (North-South) | |
| 1 | 4.276 | 70.75% | 0.02% | Translation mode on H1 direction |
| 2 | 3.881 | 0.01% | 70.94% | Translation mode on H2 direction |
| 3 | 2.39 | 2 e-7 % | 6 e-5 % | Torsion mode |

Core walls were modified for Building 2B to include specified concrete strength of $f'_c = 8000\text{psi}$ to 24" thick core walls (from foundation to 20th floor) and $f'_c = 6000\text{psi}$ to 18"

thick core walls (from 20th floor to 30th floor). Above the 30th floor, the wall thickness was decreased to 16" while keeping the same concrete strength. The configuration of the coupling beams for Buildings 2A and 2B were identical; however, capacities were increased in Building 2B by using a higher concrete strength. Frame members retained the same cross-section dimensions except for North and South corner columns (frames A and F), which were increased to 46"x46" (from foundation to 10th floor) and to 42"x42" (from 10th floor to 30th floor) due to limitations on axial load that are not contained in current prescriptive codes. The quantity of longitudinal reinforcement was decreased in frame beams and corner columns, but increased in East and West interior columns (Frames 2 and 5). Reinforcement details of members are available in Ghodsi et al., (2009).

2.2.4. Design of Building 2C (Enhanced Performance Based Design)

The primary difference in the design requirements of Building 2C relative to Building 2B was that return period for the service level earthquake was 25 years for Building 2B and 43 years for Building 2C. Figure 2-8 shows the comparison of the response spectra for return periods of 25 and 43 years. A linear analysis of Building 2C revealed that the building was close to satisfying design requirements for the high service level demands; therefore, a nonlinear dynamic procedure, which is allowed as an option for service level design, was employed to demonstrate adequate building performance. The design acceptance criteria are shown in Ghodsi et al. (2009). Use of the nonlinear response history approach demonstrated that the Building 2B satisfied the enhanced performance acceptance criteria; therefore, Building 2C was taken to be identical to Building 2B (no design changes). Therefore, in subsequent analytical studies presented in this chapter, results for only two designs are presented, for Building 2A and Building 2B (same as 2C).

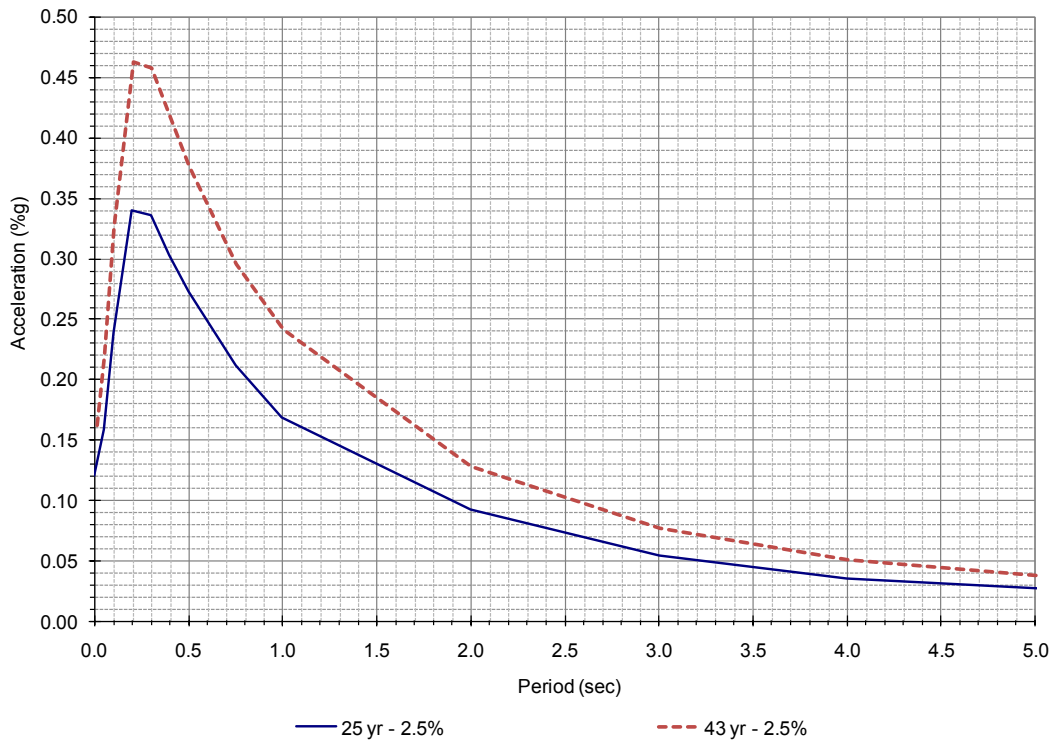


Figure 2-8. 25 and 43 years return period response spectrum with 2.5% of critical damping

2.2.5. Design Summary

Building 2A: Designed to satisfy current code (IBC 2006), linear design using linear dynamic procedure (LDP).

Building 2B: Designed to satisfy LATBSDC, two-level design: Serviceability level using LDP and Collapse Prevention level using Nonlinear Dynamic Procedure (NDP).

Building 2C: Based on results obtained for a nonlinear analysis for the SLE 43 earthquake, a new design was not necessary, i.e., Building 2C is the same as Building 2B.

Therefore, two different designs were used in the future studies: Building 2A and Building 2B. They had the same configuration and layout, but member capacities were higher in Building 2B; therefore, fundamental period was slightly lower in Building 2B.

2.2.6. Modeling

A uniform modeling procedure was established to allow EDPs for the models of the two building designs to be compared, as well as to allow comparison with Building 1 (core wall only). Stiffness modifiers given in Table 2-7 were used to determine force-displacement relationships. Expected material strengths of $1.3f'_c$ and $1.17f_y$ were used for concrete and reinforcing steel, respectively. Modeling details adopted are provided in the following sections.

Table 2-7. Stiffness assumptions

| Element | Building 2A | Building 2B and 2C | |
|------------------------------------|--|---|--|
| | Code-Level Analysis | Serviceability Design | MCE Level |
| Modulus of Elasticity ^A | Specified concrete strength | Expected concrete strength ^B | Expected concrete strength |
| Core Walls | Flexural – $0.6 EI_g$ Shear – $1.0 GA_g$ | Flexural – $0.9 EI_g$ Shear – $1.0 GA_g$ | Flexural – <i>See note C</i> Shear – $1.0 GA_g$ |
| Basement Walls | Flexural – $0.8 EI_g$ Shear – $0.8 GA_g$ | Flexural – $1.0 EI_g$ Shear – $1.0 GA_g$ | Flexural – $0.8 EI_g$ Shear – $0.8 GA_g$ |
| Coupling Beams | Flexural – $0.2 EI_g$ Shear – $1.0 GA_g$ | Flexural – $0.5 EI_g$ Shear – $1.0 GA_g$ | Flexural – $0.2 EI_g$ Shear – $1.0 GA_g$ |
| Ground Level and Basement slabs | Flexural – $0.25 EI_g$ Shear – $0.5 GA_g$ | Flexural – $0.5 EI_g$ Shear – $0.8 GA_g$ | Flexural – $0.25 EI_g$ Shear – $0.25 GA_g$ |
| Moment Frame Beams | Flexural – $0.35 EI_g$ Shear – $1.0 GA_g$ | Flexural – $0.7 EI_g$ Shear – $1.0 GA_g$ | Flexural – $0.35 EI_g$ Shear – $1.0 GA_g$ |
| Moment Frame Columns | Flexural – $0.7 EI_g$ Shear – $1.0 GA_g$ | Flexural – $0.9 EI_g$ Shear – $1.0 GA_g$ | Flexural – $0.7 EI_g$ Shear – $1.0 GA_g$ |

2.2.7. Modeling of Building 2A

The 3-D nonlinear model was built in Perform 3D to represent the lateral force resisting system of the building, i.e., the gravity system was excluded. The seismic mass was assigned as described in Section 0 and a rigid diaphragm was incorporated by slaving the horizontal translation degrees of freedom for each floor above the ground level (podium level). For the floors below the ground, the diaphragm system was modeled with a finite element mesh. The core wall and the moment frames extended down to the foundation level. The foundation of the building was modeled as rigid using lateral and vertical supports at the top of the foundation.

Soil-structure interaction was neglected; therefore, the building model was approximate, but adequate for the purpose of this (comparative) study. P-Delta effects were taken into account in the model by creating a dummy column with no lateral stiffness subjected to axial load of $P = D + 0.25L$, and by slaving the nodes at column ends to the floor levels at each column end.

2.2.7.1. Core Wall Modeling

Nonlinear vertical fiber elements representing the expected behavior of concrete and steel were used to model the core wall. For the fiber concrete elements, only confined concrete was used with the expected strength, i.e., the unconfined concrete cover was neglected. The concrete stress-strain relationship was based on the modified Mander model for confined concrete (Mander et al., 1988), in which the tension strength of concrete was neglected (Figure 2-9).

Since the computer program used, Perform 3D, requires that the concrete stress-strain relation be defined by four linear segments, four control points were selected to approximate the relation produced using the Mander model as shown in Figure 2-9.

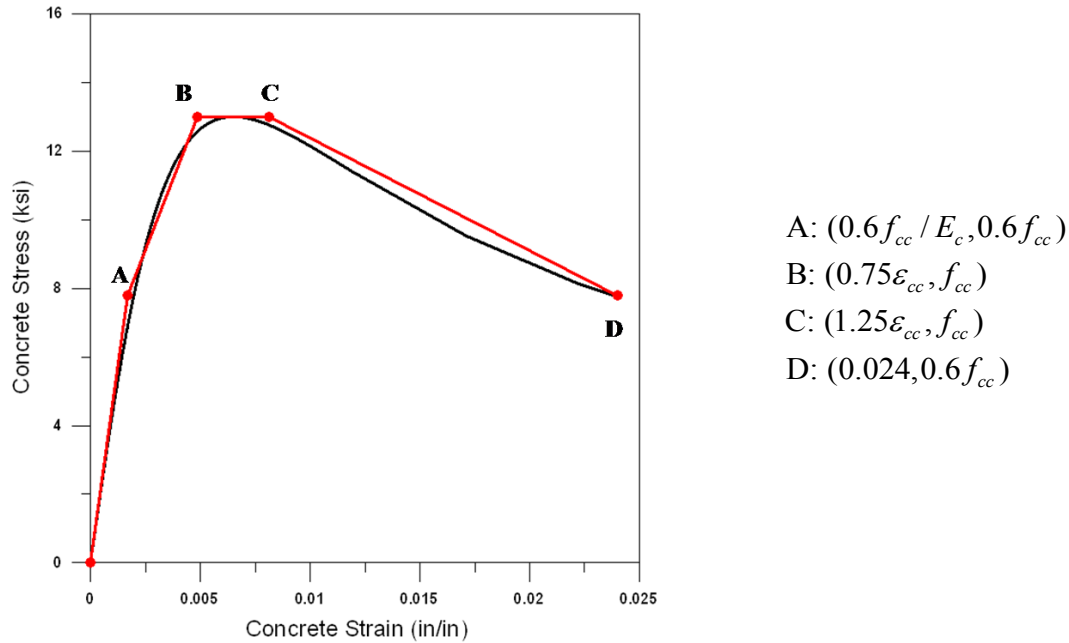


Figure 2-9. Concrete stress-strain relationship

Since the core walls were modeled using fiber elements, the effective stiffness EI_{eff} was not assigned explicitly because it is a product of the assumed material stress-strain relations; therefore, the effective bending stiffness EI_{eff} decreases with increasing fiber strains.

Shear behavior was modeled with an effective elastic stiffness $G = 0.2E_c$, where E_c was the expected elastic modulus and was determined based on the following equations using the expected concrete strength:

$$E_c = 57000\sqrt{f'_c} \quad \text{for } f'_c \leq 6000 \text{ psi}$$

$$E_c = 40000\sqrt{f'_c} + 1 \times 10^6 \quad \text{for } f'_c > 6000 \text{ psi} \quad (\text{ACI 363R-92})$$

Inelastic shear material was defined with an elastic-perfectly plastic stress-strain curve in which strength loss was neglected, (Figure 2-10). The ultimate shear strength, V_{ult} , was defined as $1.5V_n$ where V_n is nominal shear capacity of the shear wall based on ACI 318-08 as follows:

$$V_n = (\alpha_c \sqrt{f'_c} + \rho_t f_y) \text{ psi (ACI 318-08 §21.9.4.1) (Equation 2-1)}$$

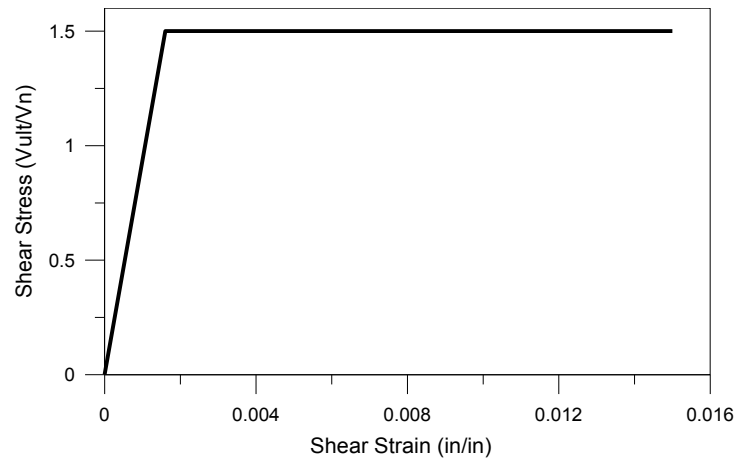


Figure 2-10. Inelastic shear stress-strain relationship

The steel stress-strain relationship was based on the material specifications for A706 steel. The steel material was modeled with expected yield strength of $f_y = 70ksi$ and an ultimate strength of $f_u = 105ksi$ as shown in Figure 2-11. The post-yield stiffness and cyclic degradation of reinforcing steel was modeled as described by Orakcal et al. (2006) and adjusted to match the lateral load vs. top displacement curve. The cyclic degradation parameters are shown in Ghodsi et al., (2009).

The cross section used to define the shear walls was reduced in order to account for spalling, e.g., the equivalent reinforcement ratio of a 24" thick wall for a minimum required reinforcement amount was calculated as $\rho = \frac{0.0025 * 24"}{22"}$.

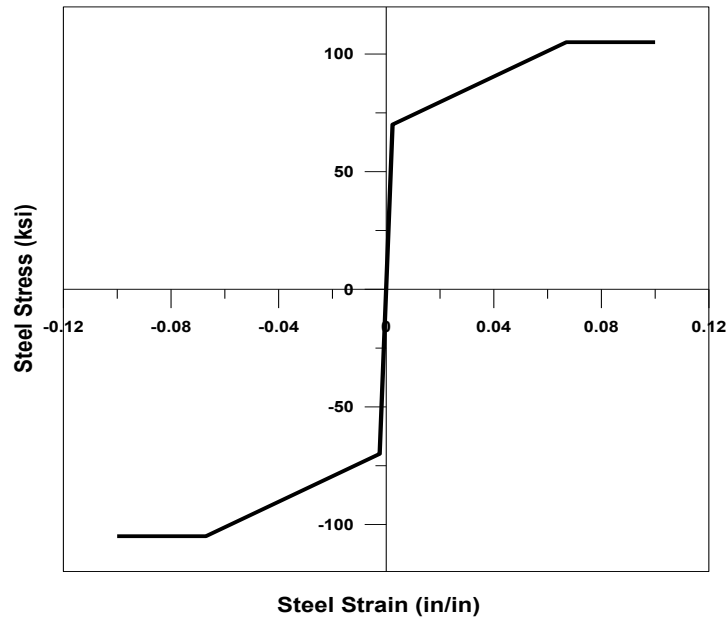


Figure 2-11. Inelastic steel stress-strain relationship

2.2.7.2. Coupling Beam Modeling

The coupling beams were defined as elastic beam elements with nonlinear displacement shear hinge at beam mid-span (Figure 2-12).

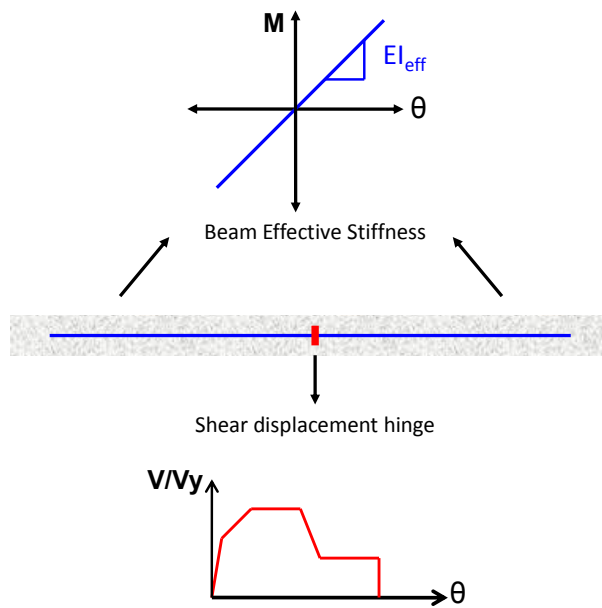


Figure 2-12. Typical coupling beam modeling

The shear displacement hinge behavior was based on test results by Naish et al. (2009) and represents a tri-linear force-rotation relationship with flexural stiffness of $EI_{eff} = 0.2EI_g$, expected yield shear strength of $V_{y,exp} = 2A_s(1.17)f_y \sin(\alpha)$, expected ultimate shear strength of $V_{u,exp} = 1.33V_{y,exp}$ and expected residual strength, $V_{r,exp} = 0.25V_{u,exp}$ (Figure 2-13).

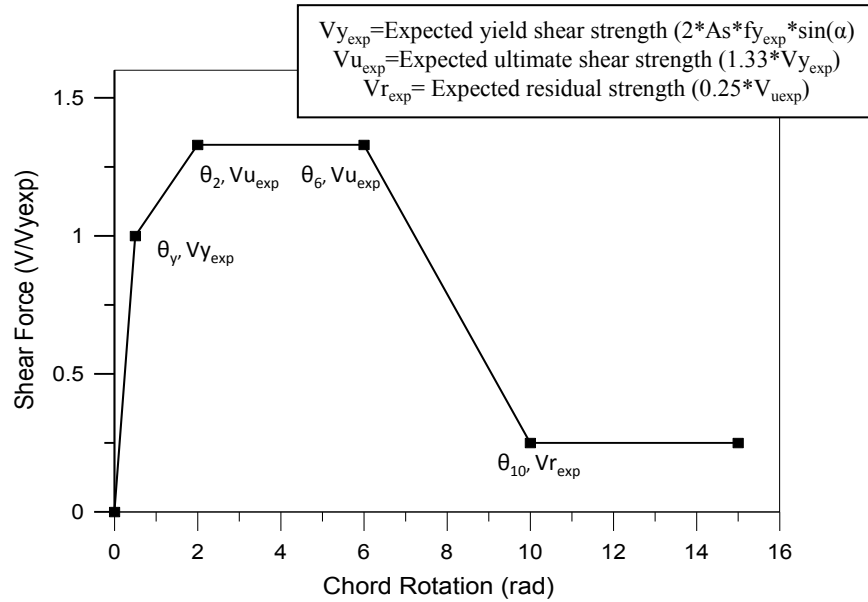
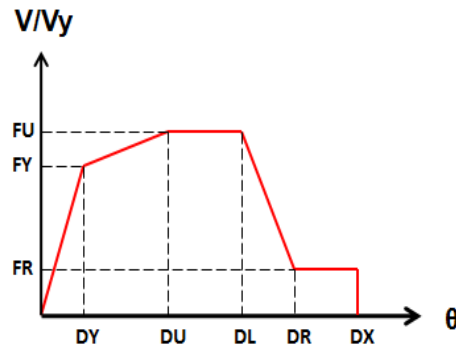


Figure 2-13. Shear displacement hinge backbone curve

Cyclic energy dissipation factors are shown in Table 2-8. Detailed information on coupling beam design is available in Ghodsi et al., (2009).

Table 2-8. Cyclic degradation parameters

| | |
|-----------|------|
| DY | 0.5 |
| DU | 0.45 |
| DL | 0.4 |
| DR | 0.35 |
| DX | 0.35 |



2.2.7.3. Moment Frame Beam Modeling

The moment frame beams were defined as elastic beam elements with nonlinear rotation hinges and rigid end zones at each end. Figure 2-14 illustrates the approach used in beam modeling.

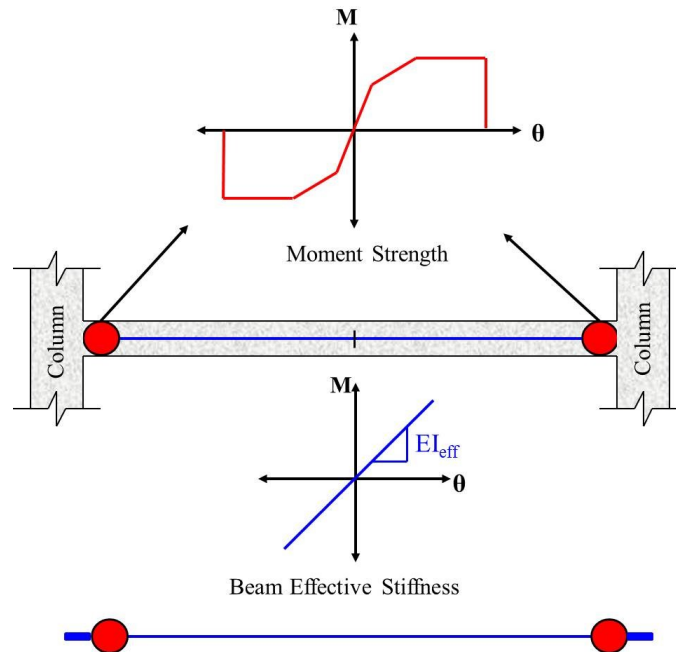


Figure 2-14. Typical beam modeling

The elastic portion of the beam was modeled with the cross-section properties and the stiffness modification factors such that $EI_{eff} = 0.35EI_g$ (flexural), $GA_{eff} = 1.0GA_g$ (shear). The non-linear moment-rotation hinges, which were defined based on the tests performed by Popov et al. (1972) to represent post-yield stiffness, were modeled as tri-linear backbone curves including cyclic degradation but neglecting strength loss.

Figure 2-15 shows a typical backbone curve used for beam moment-rotation hinges. Rigid end zones, with a stiffness of ten times the elastic stiffness of the beam, were used at each beam end. Further details on moment frame beam modeling can be seen in Ghodsi et al., (2009).

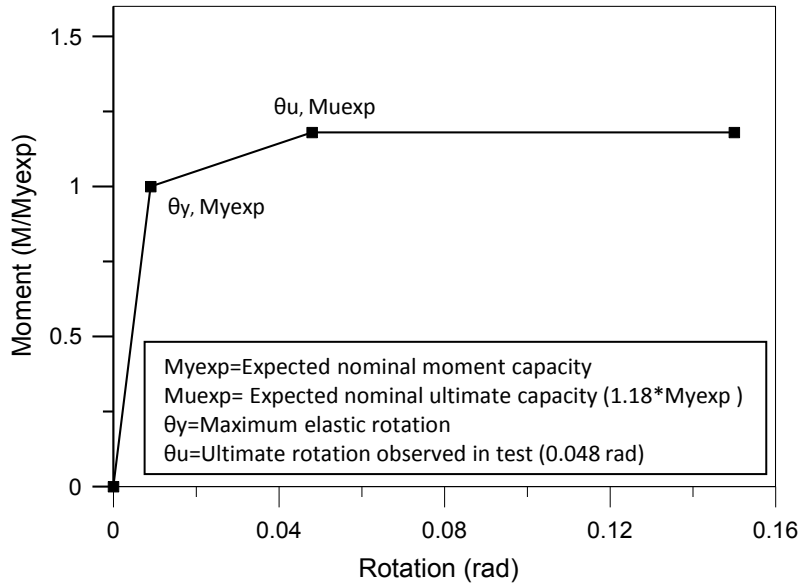


Figure 2-15. Moment-rotation hinge backbone curve

2.2.7.4. Moment Frame Column Modeling

The moment frame columns were defined as elastic column elements with plastic hinges and rigid end zones at each end, as summarized in Figure 2-16. The elastic portion of the column was modeled with the cross-section dimensions and the stiffness modification factors of $EI_{eff} = 0.7EI_g$ (flexural), $GA_{eff} = 1.0GA_g$ (shear). The yield moment for the column plastic hinges were determined from a moment-axial capacity interaction curve for expected material properties. The backbone curve was elastic-perfectly plastic, neglecting strength loss and cyclic degradation. Additional details on column modeling are available in Ghodsi et al. (2009).

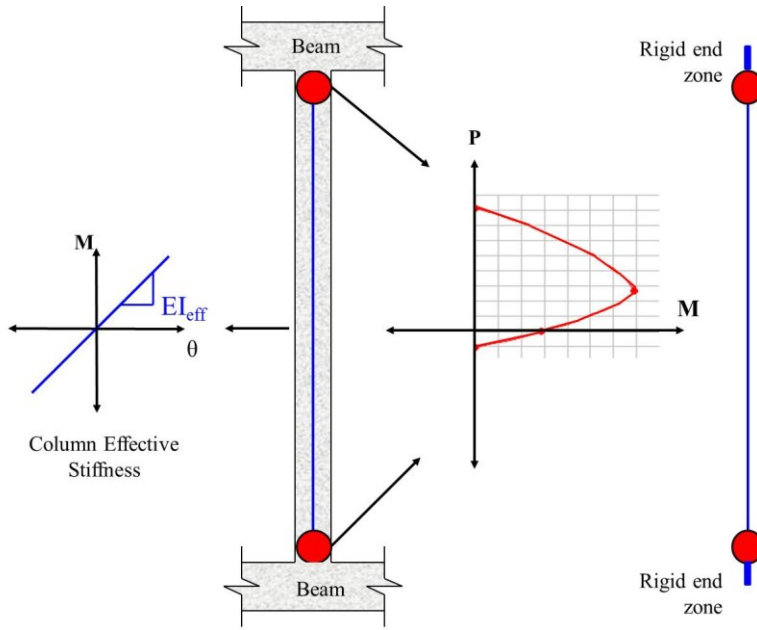


Figure 2-16. Typical column modeling

2.2.7.5. Slab Modeling

Slabs at ground level and below were modeled as elastic shell elements with stiffness values of $EI_{eff} = 0.25EI_g$ (flexural) and $GA_{eff} = 0.5GA_g$ (shear). All slabs had a specified concrete strength of $f'_c = 5000\text{ psi}$ and were modeled using the expected concrete strength of $f'_c = 6500\text{ psi}$ along with the associated modulus of elasticity. Shear modulus G was calculated using a Poisson's ratio, $\nu = 0.2$.

2.2.7.6. Basement Wall Modeling

Basement walls were modeled as elastic finite elements with stiffness values of $EI_{eff} = 0.8EI_g$ (flexural) and $GA_{eff} = 0.8GA_g$ (shear). Therefore, in the basement wall modeling, the elastic modulus and the shear modulus were taken as $E = 0.8E_{exp}$ and $G = 0.8G_{exp}$ ($G = 0.16E_{exp}$) respectively.

2.2.7.7. Damping

Rayleigh damping was used for the non-linear response-history analyses. The damping curve shown in Figure 2-17 was defined based on the damping of 2.5% of critical damping at a period of 1 second and at a period of 5 seconds. T_1 , the fundamental period was 4.456 seconds and the constants α and β were calculated by Perform 3D automatically. Table 2-9 shows the damping parameters as introduced into Perform 3D.

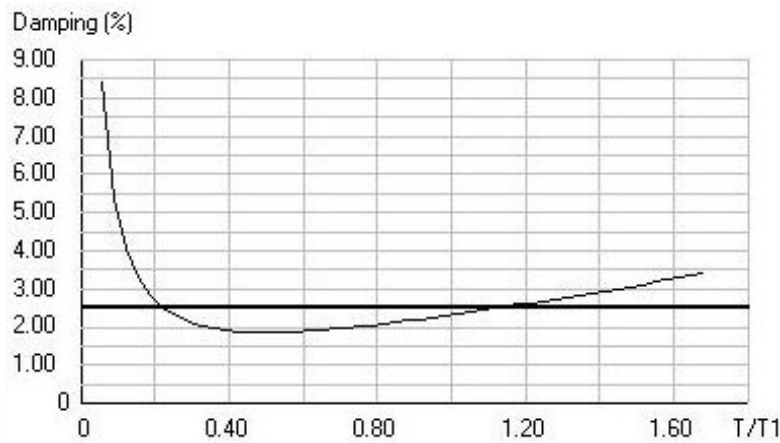


Figure 2-17. Rayleigh damping as defined in Perform 3D

Table 2-9. Damping parameters for Building 2A

| T/T_1 | Damping (%) |
|---------|-------------|
| 0.224 | 2.5 |
| 1.122 | 2.5 |

2.2.7.8. Masses

The seismic mass was lumped at the center of mass of each floor above the ground level in terms of dead load and the associated rotational moment of inertia. The mass at the ground level was assigned as distributed mass, and kept the same for all the levels below the ground. Although the

masses were assigned to the levels below the ground as well, they were ignored in the dynamic earthquake analysis, i.e., scaled by 0.0 in the dynamic earthquake analyses. Mass modeling is summarized in Figure 2-18.

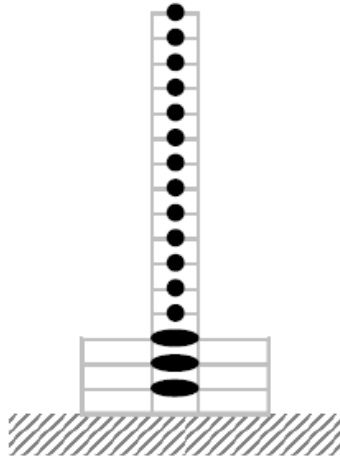


Figure 2-18. Mass modeling

2.2.8. Modeling of Building 2B

Considering a uniform modeling procedure, the previously mentioned modeling assumptions were followed in the model of Building 2B. Members were updated based on the performance-based design dimensions and the stiffness factors were modified as necessary.

2.2.8.1. Core wall modeling

Core walls of the building were updated according to the design. In this model, confined concrete with strength of $f'_c = 8000\text{ psi}$ was introduced to the model for the core walls from foundation to the 20th floor.

2.2.8.2. Coupling Beam Modeling

Based on the building design, stiffness of the coupling beams were increased by using higher values of concrete strength. The assumptions for stiffness and capacity were same as that of Building 2A model and the cyclic degradation parameters were identical as well.

2.2.8.3. Moment Frame, Slab and Basement Wall Modeling

Having the new member sizes, beams and columns were modeled in the previously discussed way with the same stiffness factors. Slabs and basement walls were unchanged except for the shear stiffness of slabs, which was $GA_{eff} = 0.25GA_g$ in this model (Table 2-7).

2.2.8.4. Damping

The fundamental period, T_1 , of Building 2B was 4.276 seconds. Rayleigh damping parameters depending on the new fundamental period are shown in Table 2-10. The damping curve of Building 2A is valid for Building 2B as well.

Table 2-10. Damping parameters for Building 2B

| T/T₁ | Damping (%) |
|------------------------|--------------------|
| 0.234 | 2.5 |
| 1.17 | 2.5 |

2.3. Non-linear Dynamic Earthquake Analyses Results

A nonlinear response history analysis was performed for the two models for five hazard levels, each consisting of 15 pairs of ground motions. The hazard levels, named SLE25, SLE43, DBE, MCE and OVE are briefly explained below. The methodology used for selection and preparation of the ground motions is summarized in Appendix A.

1. SLE 25: Serviceability with a probability of 70% in 30 years (25 year return period)
2. SLE 43: Serviceability with a probability of 50%/30 years (43 years return period)
3. DBE: Life-Safety with a probability of 10%/ 50 years (475 return period)
4. MCE: Maximum Considered Earthquake or Collapse Prevention with a probability of 2%/50 years (2475 return period).
5. OVE: Higher intensity than MCE with a probability of 1%/50 years (4975 return period).

Response history analysis was applied after a gravity load of $P=1.0D+0.25L$. Results are discussed in the following subsection.

2.3.1. Overall Behavior

2.3.1.1. Building 2A

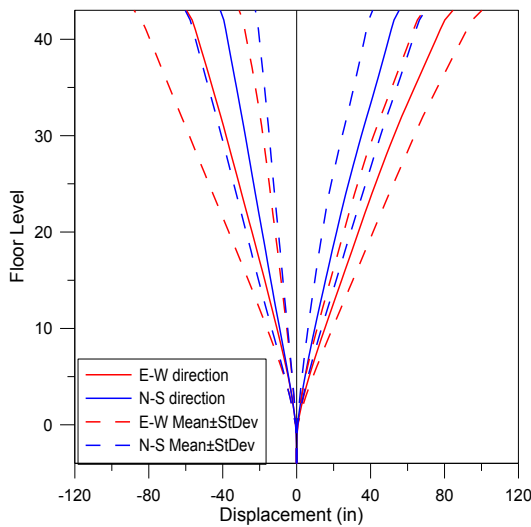
Mean values of fifteen floor displacements are shown with standard deviation for five hazard levels in Figure 2-19. Displacement was practically zero below grade, due to the stiffness of the perimeter basement walls, and increased approximately linearly from the grade to the roof level where the maximum displacement occurs. OVE level showed the most dispersion in displacements and a larger difference between two principle building directions compared with the other hazard levels. Maximum roof displacement was observed to be about 80 inches (1.5% drift) with a standard deviation of 20 inches (0.4% drift).

Inter-story drift profiles (Figure 2-20) showed that the maximum average inter-story drift for the OVE level was slightly higher than 2% in East-West direction and close to 1.5% in North-South direction, whereas the peak drift approaches 0.3% for serviceability levels in both directions. In all cases, the peak drift values occurred around the 30th floor and never exceed the acceptable limit which was 0.03 for MCE, 0.02 for DBE and 0.005 for SLE levels. For

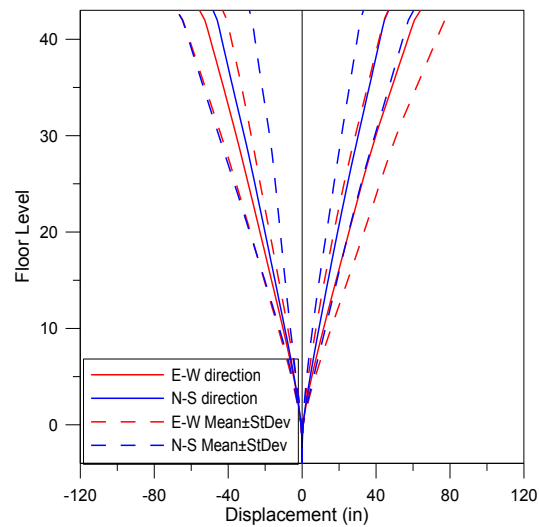
comparison purposes, acceptable limit of 0.03 was used for OVE. It can be concluded that the serviceability level drift was the most critical case since the peak drift values are the closest to the service-level limit.

Floor accelerations (Figure 2-21) indicated that fundamental modes were not excited under SLE (very low response associated with the tower, Figure 2-21(d)), although significant response of the stiff podium was observed. For the OVE and MCE events (Figures 2-21(a), (b)), accelerations were limited by yielding, with maximum values of approximately 0.5g over a majority of the tower.

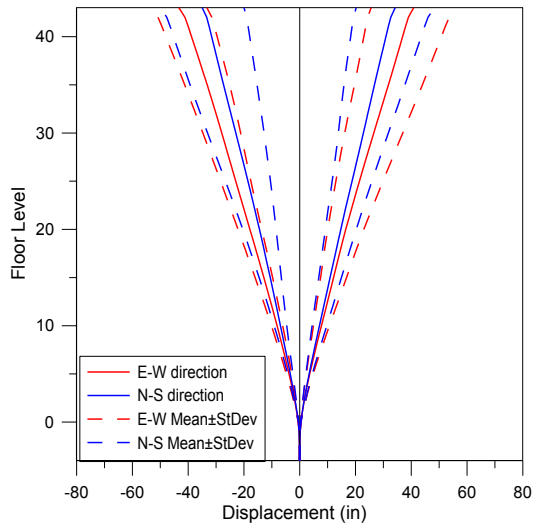
Floor displacements



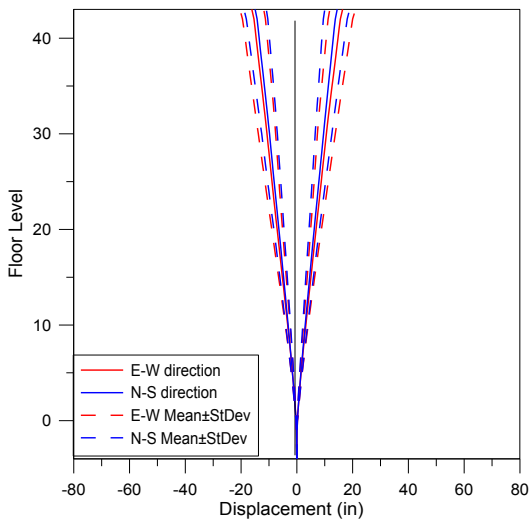
(a) Displacements under OVE level



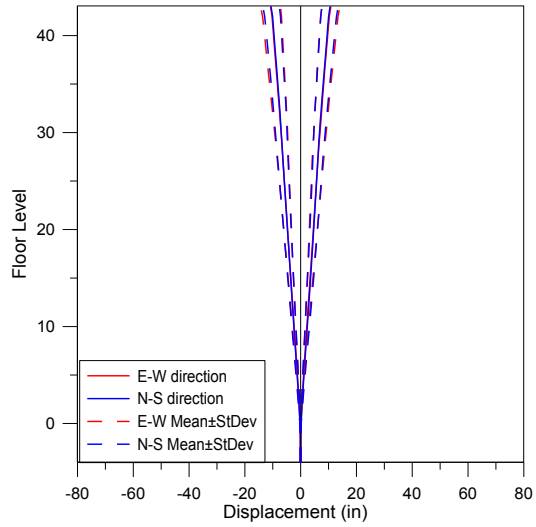
(b) Displacements under MCE level



(c) Displacements under DBE level



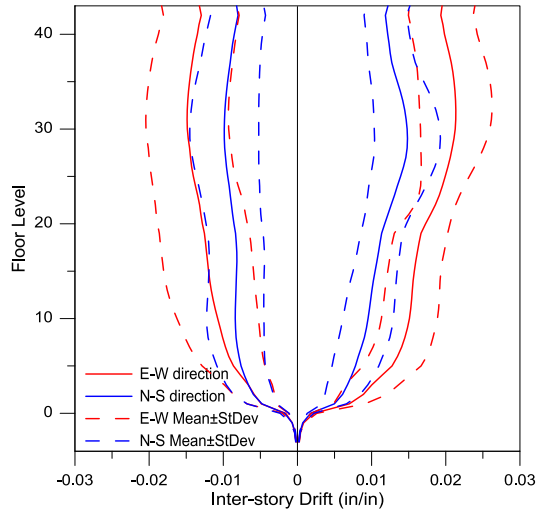
(d) Displacements under SLE43 level



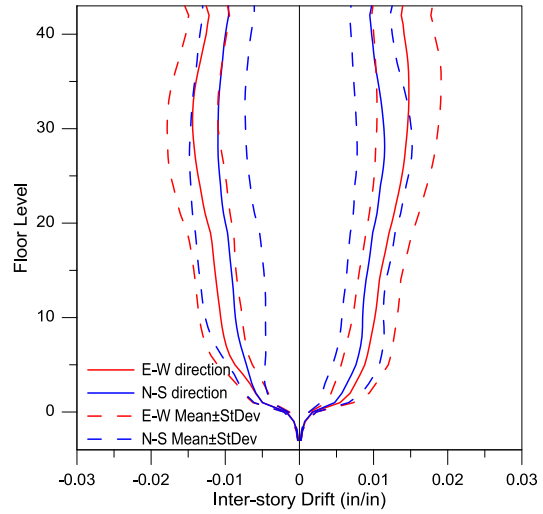
(e) Displacements under SLE25 level

Figure 2-19. Story displacements under various hazard levels

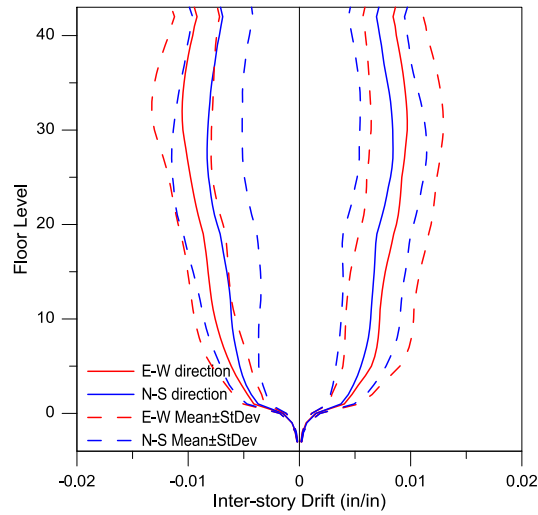
Inter-story Drifts



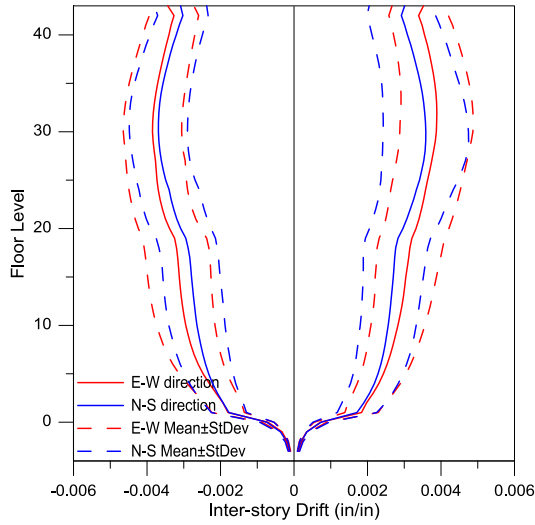
(a) Inter-story drifts under OVE level



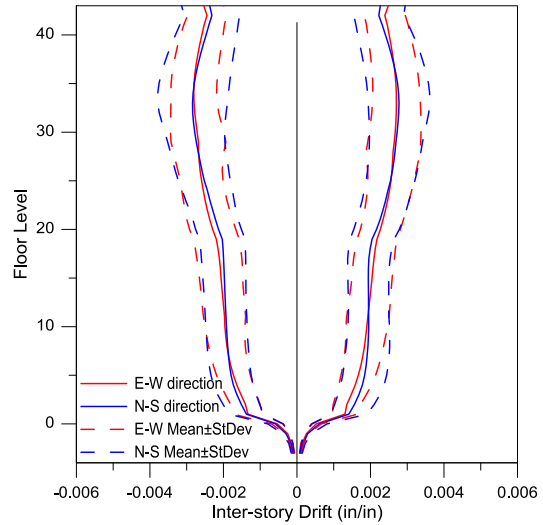
(b) Inter-story drifts under MCE level



(c) Inter-story drifts under DBE level



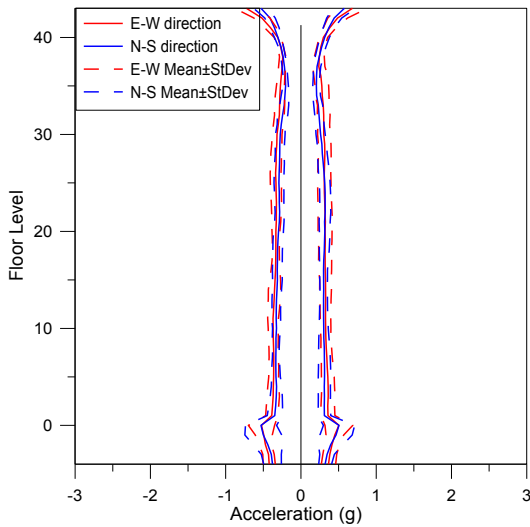
(d) Inter-story drifts under SLE43 level



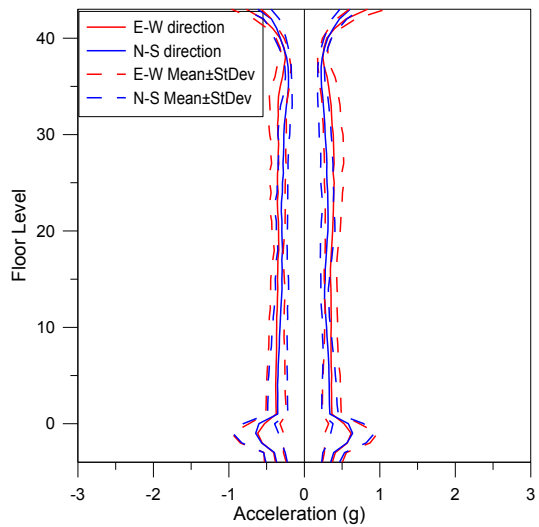
(e) Inter-story drifts under SLE25 level

Figure 2-20. Inter-story drift ratios under various hazard levels

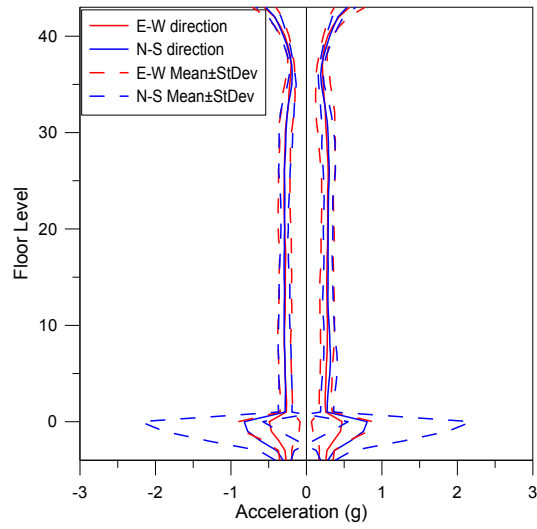
Floor accelerations



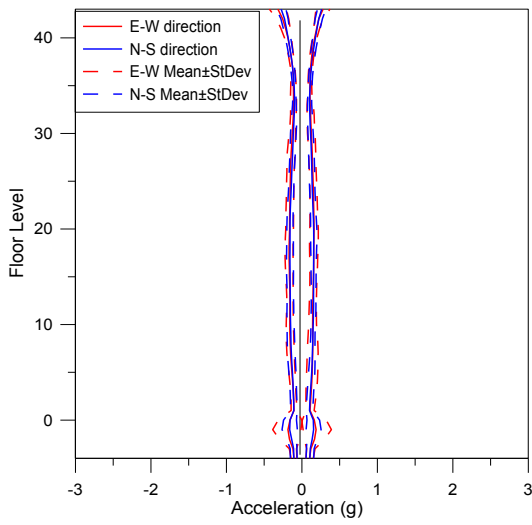
(a) Floor accelerations under OVE



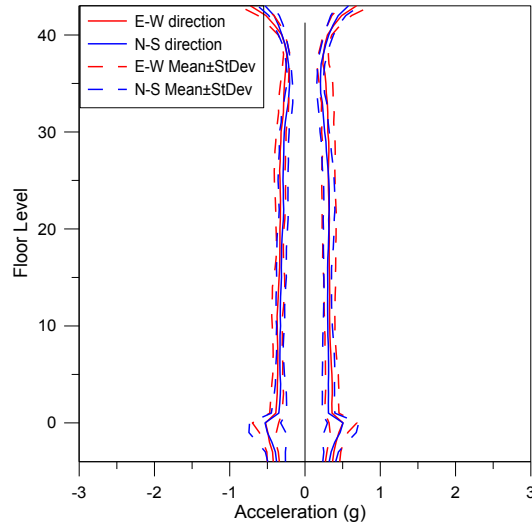
(b) Floor accelerations under MCE



(c) Floor accelerations under DBE level



(d) Floor accelerations under SLE43



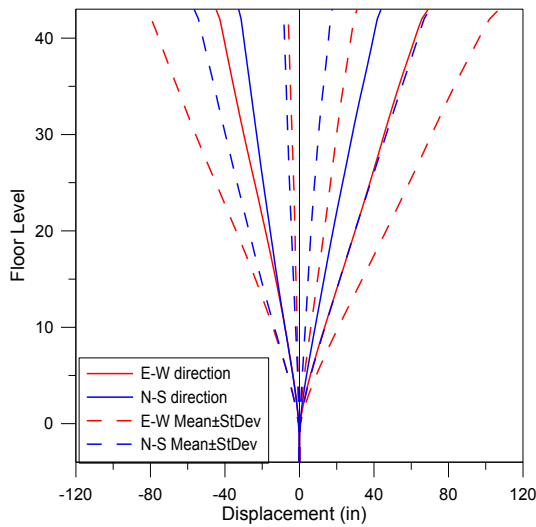
(e) Floor accelerations under SLE25

Figure 2-21. Floor accelerations under various hazard levels

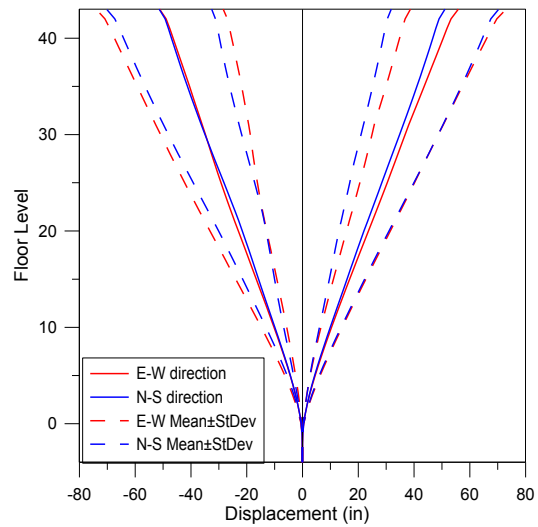
2.3.1.2. Building 2B

The same behaviors were observed for Building 2B with modestly lower drift values (approximately 15% less) due to the lower period (higher material strengths were used). The results were illustrated in Figures 2-22, 2-23 and 2-24.

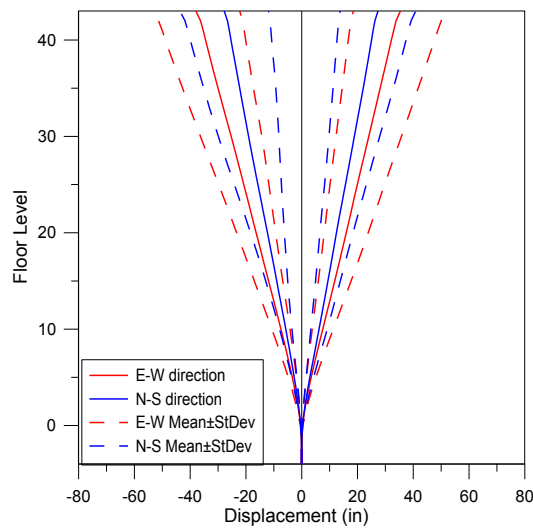
Floor displacements



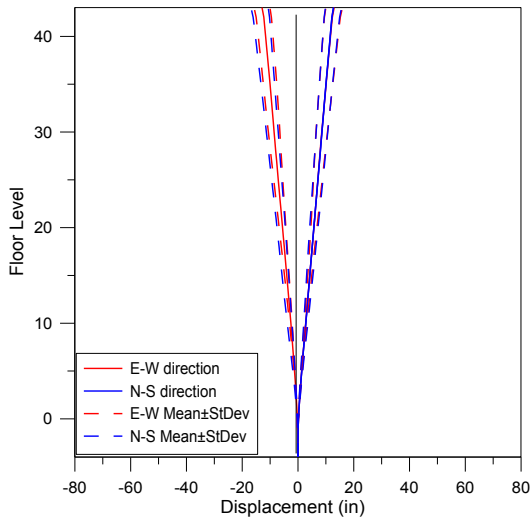
(a) Displacements under OVE level



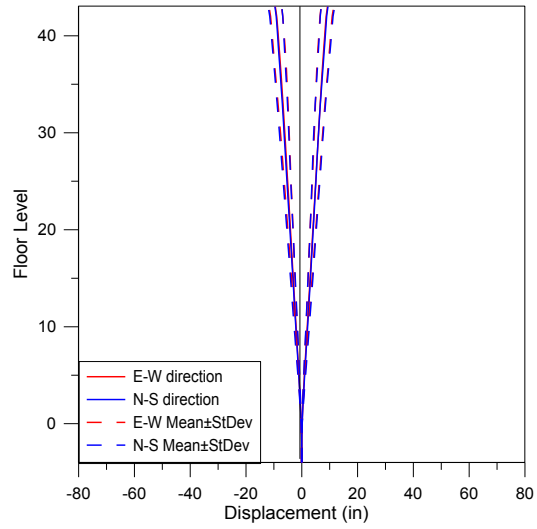
(b) Displacements under MCE level



(c) Displacements under DBE level



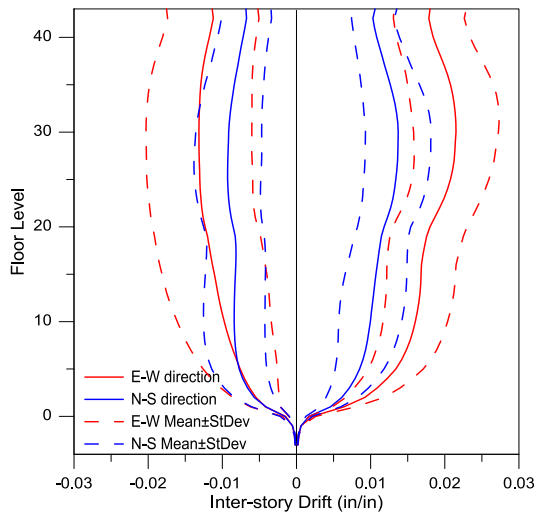
(d) Displacements under SLE43 level



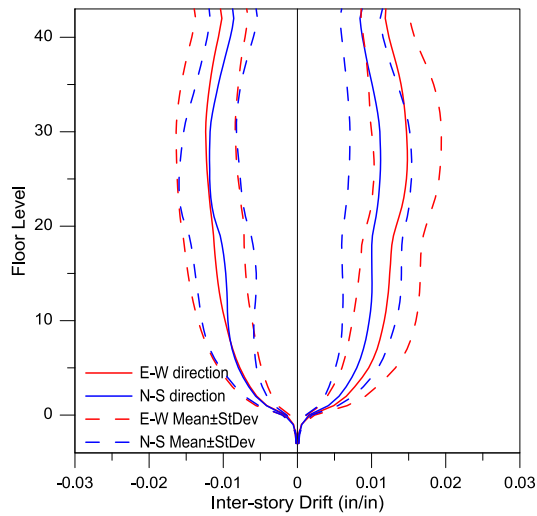
(e) Displacements under SLE25 level

Figure 2-22. Story displacements under various hazard levels

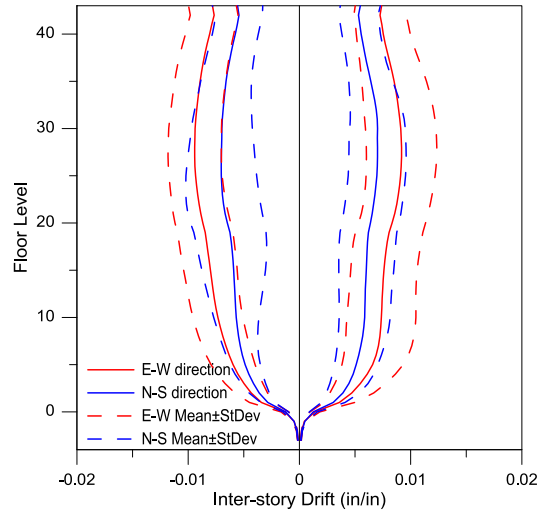
Inter-story Drifts



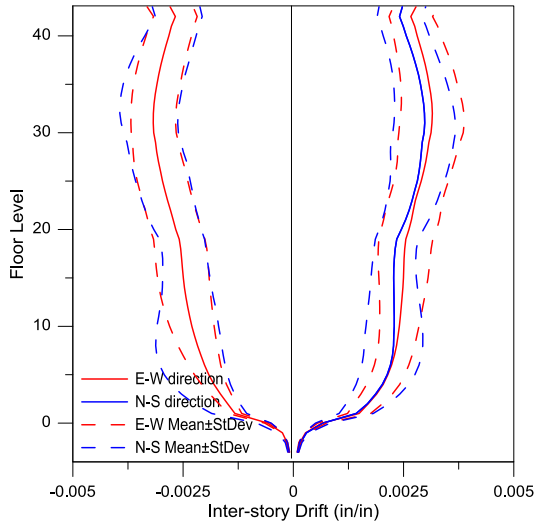
(a) Inter-story drifts under OVE level



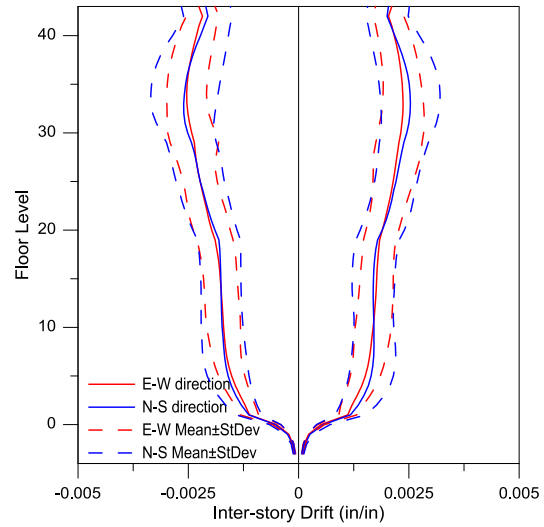
(b) Inter-story drifts under MCE level



(c) Inter-story drifts under DBE level



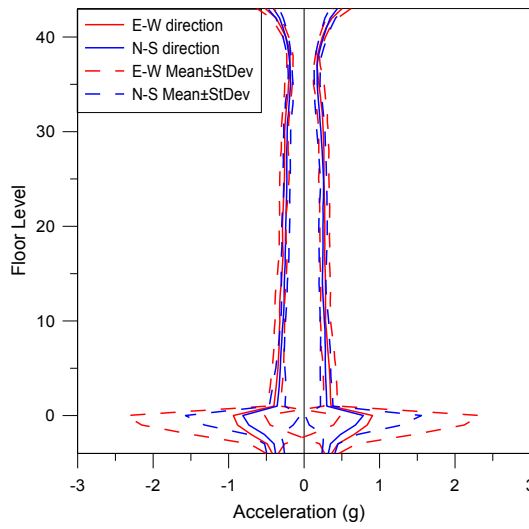
(d) Inter-story drifts under SLE43 level



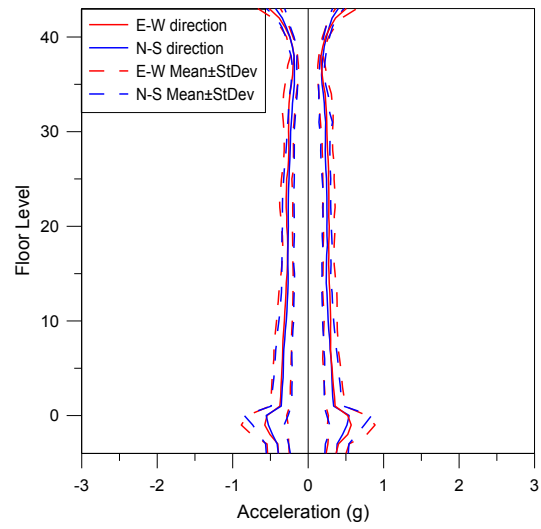
(e) Inter-story drifts under SLE25 level

Figure 2-23. Inter-story drifts under various hazard levels

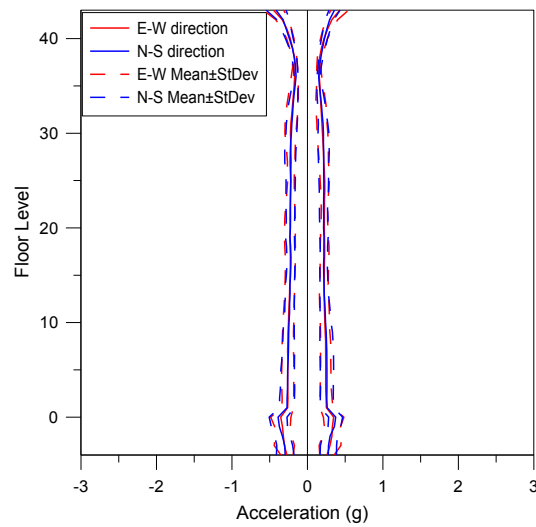
Floor accelerations



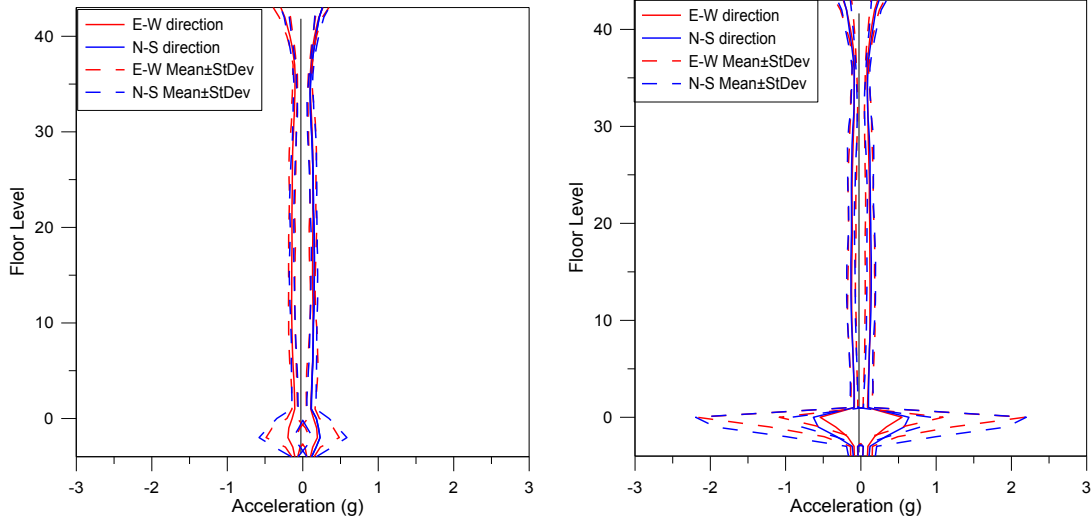
(a) Floor accelerations under OVE level



(b) Floor accelerations under MCE level



(c) Floor accelerations under DBE level



(d) Floor accelerations under SLE43 level

(e) Floor accelerations under SLE25 level

Figure 2-24. Floor accelerations under various hazard levels

2.3.2. Core Shear Wall Behavior

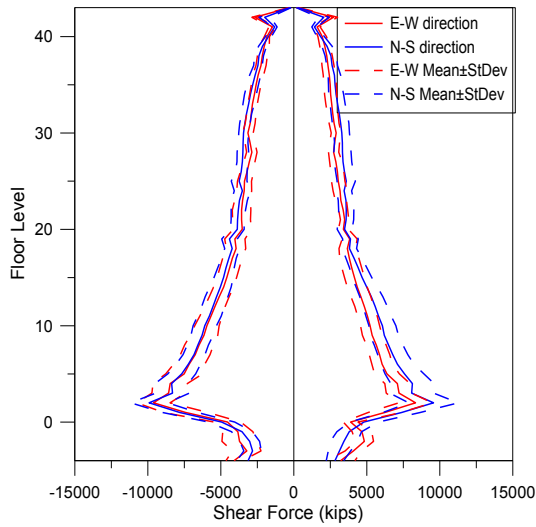
2.3.2.1. Building 2A

To assess building responses, peak values of shear and moment were analyzed over the core wall height; results are shown in Figure 2-25 and Figure 2-27. A large increase in core wall shear force was noted at the ground level due to the influence of the below-grade podium, which was much stiffer than the tower. From ground to roof level, a near-linear profile was observed for each hazard level, which indicates first mode dominant response. Studies by Salas (2009) showed that use of a linear model at upper levels results in significant higher mode contributions to wall moment and shear); therefore, nonlinear modeling was incorporated over the full wall height. Modest flexural yielding in upper levels of the wall reduced the impact of higher modes. For all hazard levels, peak wall shear stresses were much less than the ACI 318-08 limit of

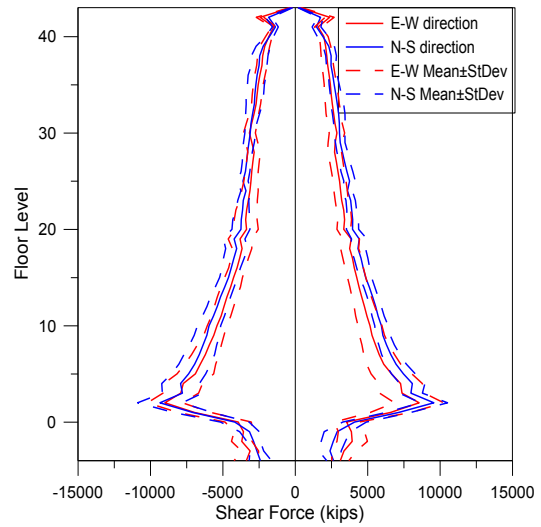
$(8\sqrt{f'_c})$, except for the OVE level where the shear stress reaches the limit around ground level

(Figure 2-26).

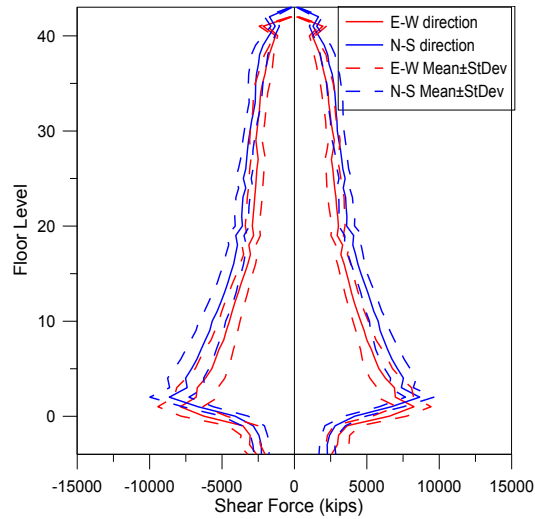
Core wall shears



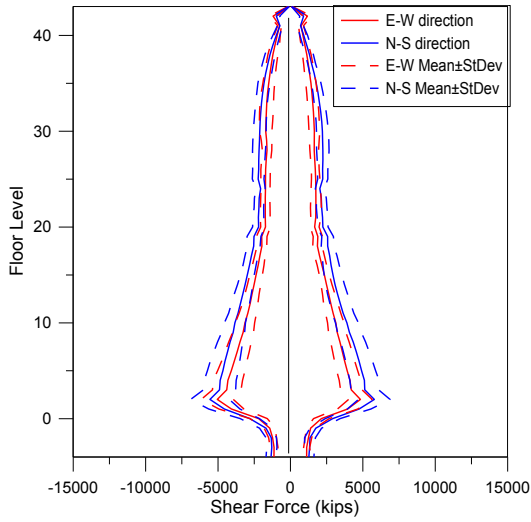
(a) Shear forces under OVE level



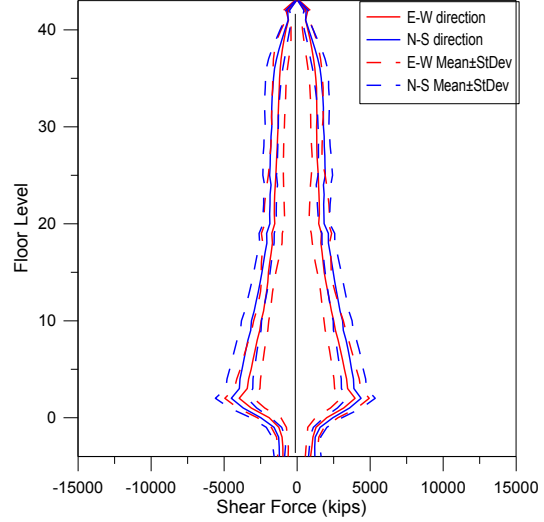
(b) Shear forces under MCE level



(c) Shear forces under DBE level



(d) Shear forces under SLE43 level



(e) Shear forces under SLE25 level

Figure 2-25. Core wall shear forces under various hazard levels

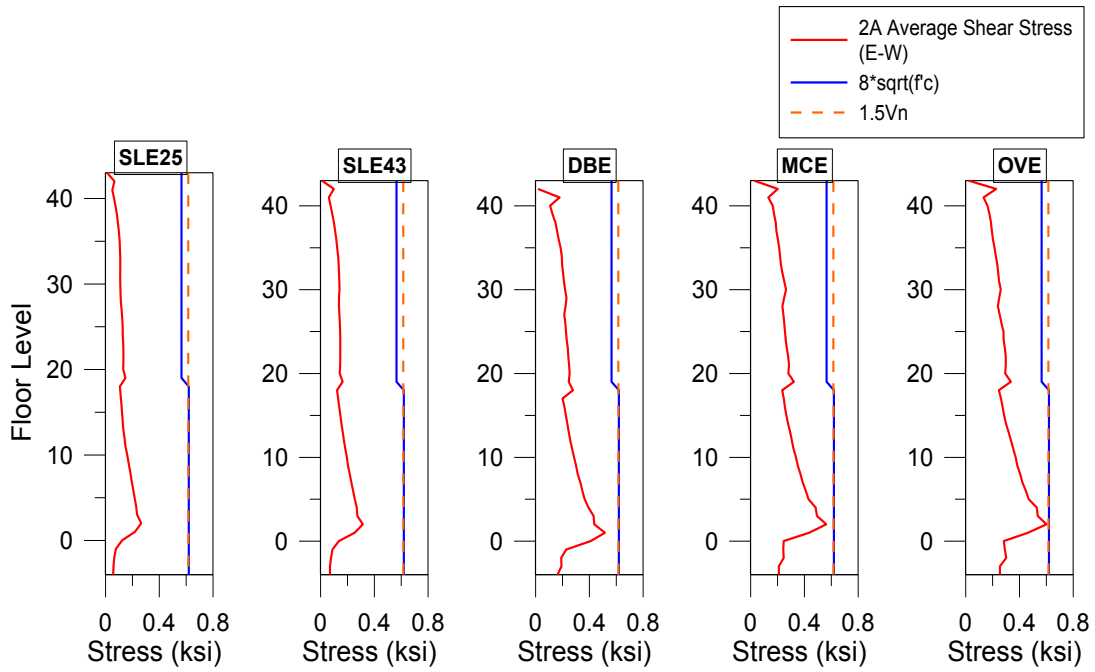
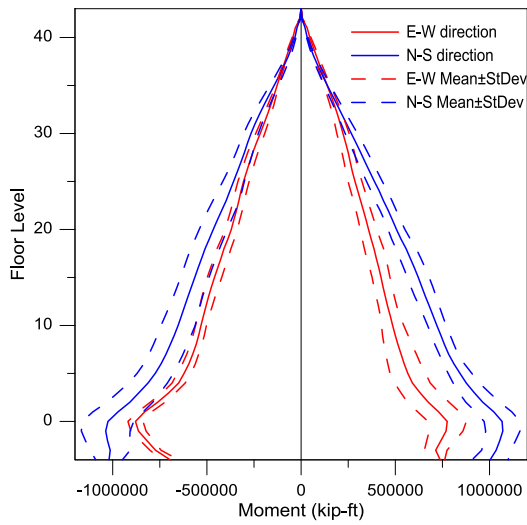
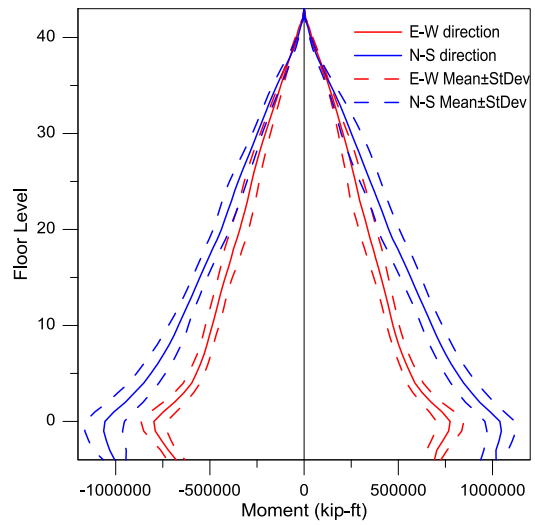


Figure 2-26. Average shear stress profiles of the core wall

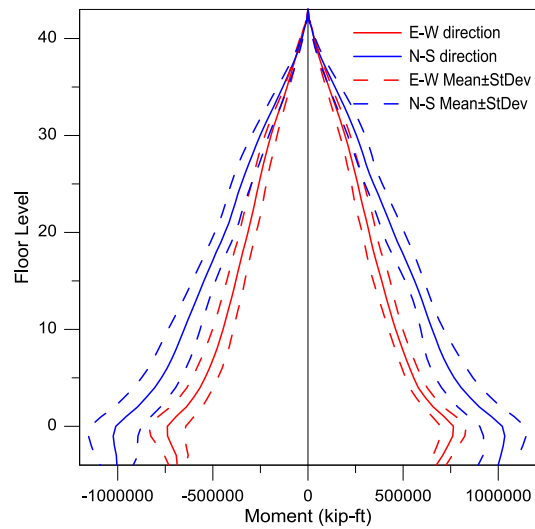
Core wall moments



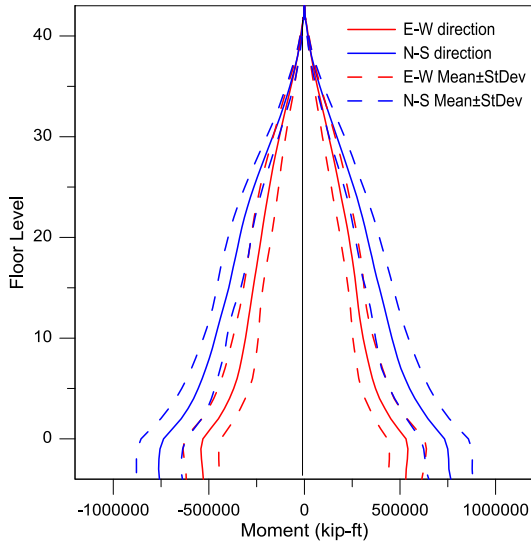
(a) Core wall moments under OVE level



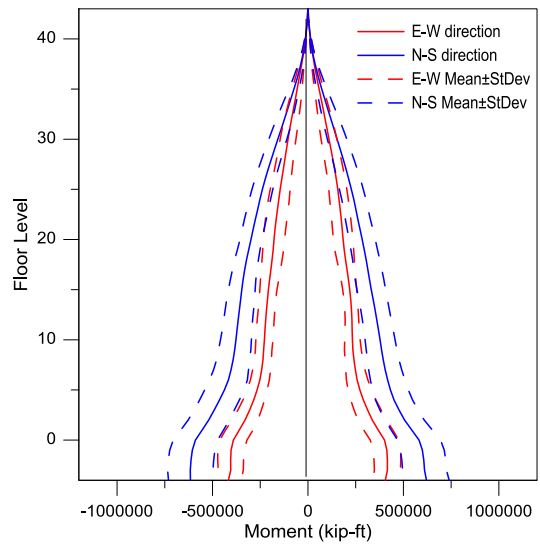
(b) Core wall moments under MCE level



(c) Core wall moments under DBE level



(d) Core wall moments under SLE43 level



(e) Core wall moments under SLE25 level

Figure 2-27. Core wall moments under various hazard levels

Core wall strains

Core wall strains were calculated at each node of each wall pier (Figure 2-28) and plotted over the wall height. Calculations were based on the mesh geometry and vertical nodal displacements.

Considering the wall pier deformed shape, as shown in Figure 2-29, axial strain values at the left

and right side of the wall can be obtained as $\varepsilon_{(1-3)} = \frac{(\Delta_{z1} - \Delta_{z3})}{H_w}$ and $\varepsilon_{(2-4)} = \frac{(\Delta_{z2} - \Delta_{z4})}{H_w}$,

respectively. Figure 2-30 and Figure 2-31 show the compression and tension strain profiles for loading in each direction. Since the maximum responses occurred in OVE level ground motions, compression and tension strains were presented only for this hazard level.

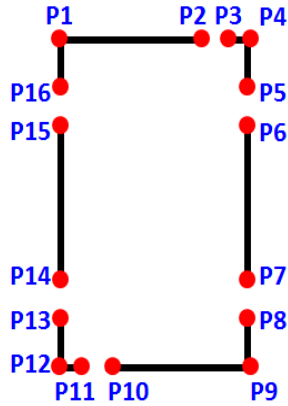


Figure 2-28. Locations of nodes used in strain calculations

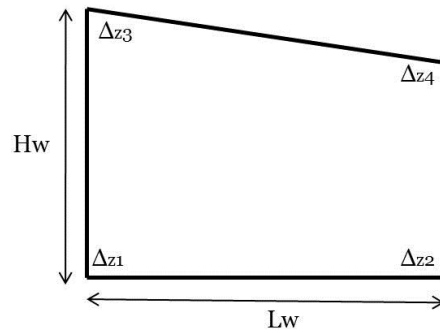


Figure 2-29. Elevation view of deformed wall segment

Tension strains showed that all core wall piers experience yielding around the ground floor and 5th floor, whereas only West and South wall piers yielded in upper stories. For the highest intensity level (OVE), wall tension strains did not exceed 0.01 and concrete compression strains were less than 0.002.

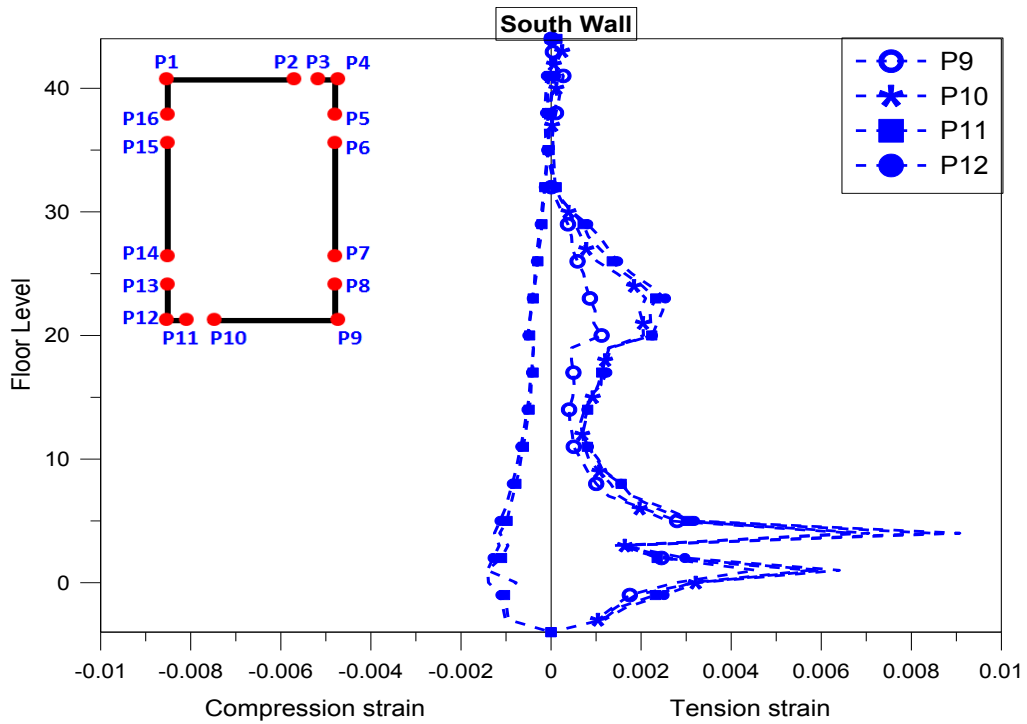
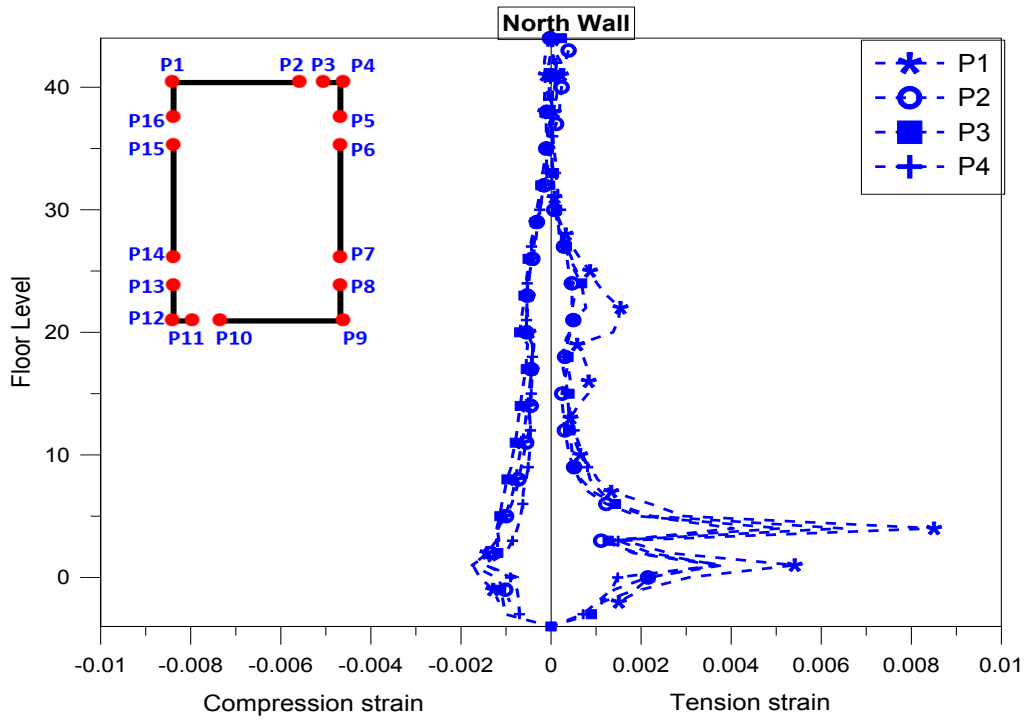


Figure 2-30. North and South wall strains under OVE level

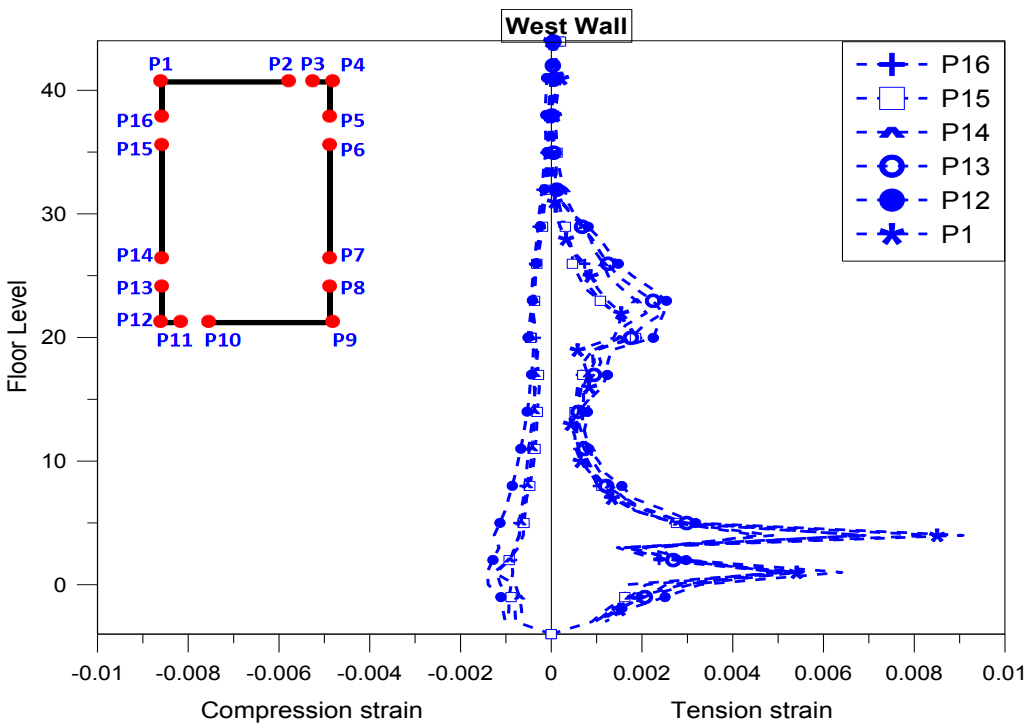
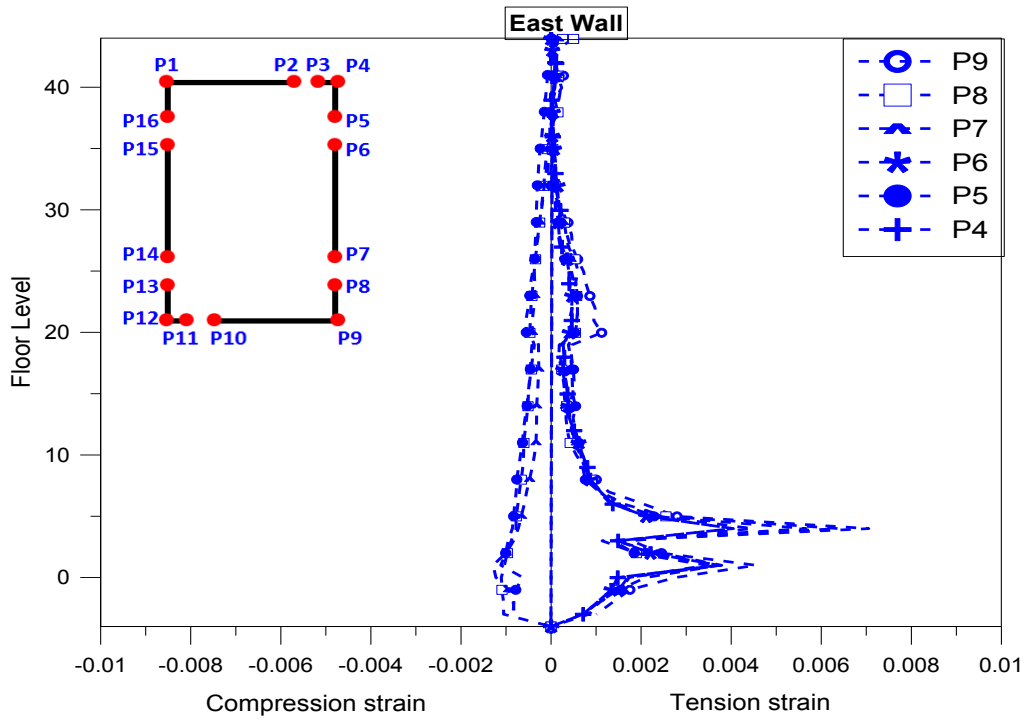


Figure 2-31. East and West wall strains under OVE level

Coupling beam rotations

Figure 2-32 sketches the coupling beam locations in the core walls. Coupling beam rotations (Figure 2-33) were examined for OVE to assess possible damage. Peak rotations of 0.015 and 0.02 were observed in the N-S and E-W directions, respectively (Figure 2-32); whereas serviceability level rotations were much smaller (<0.002 radians). Given the small rotations, according to the fragility curves developed by Naish (2010), no repair was likely to be needed (Figure 2-34).

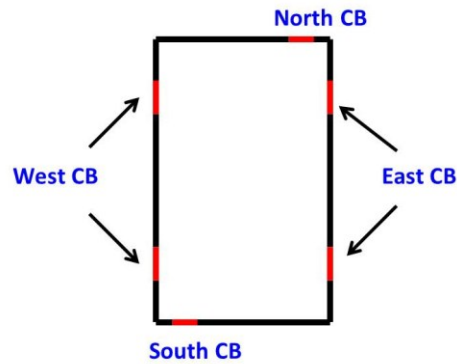
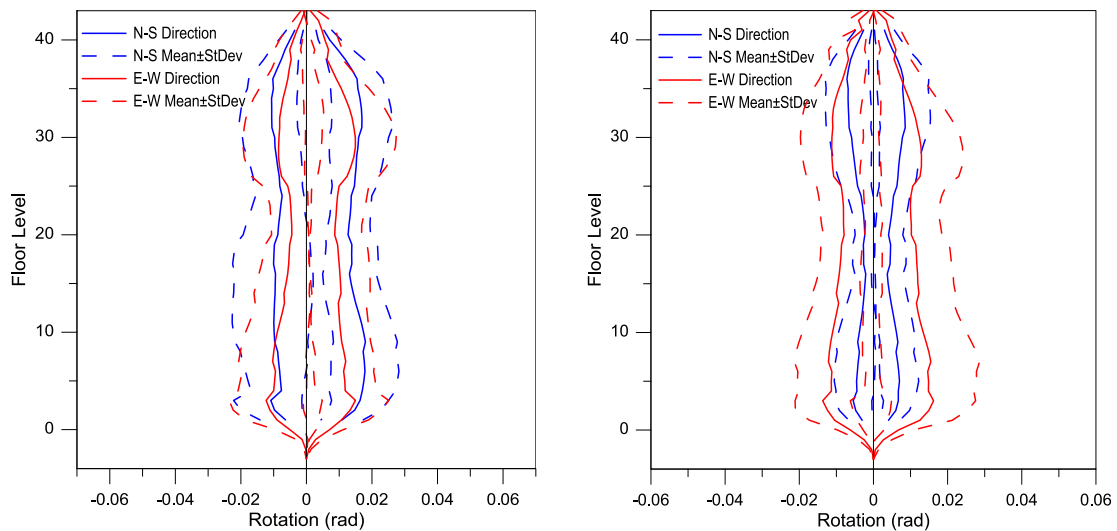
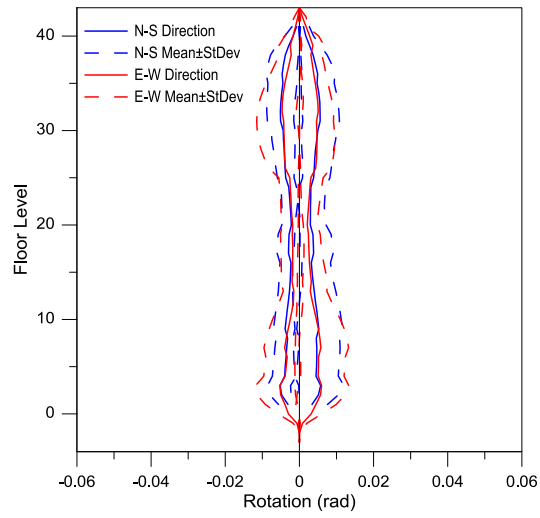


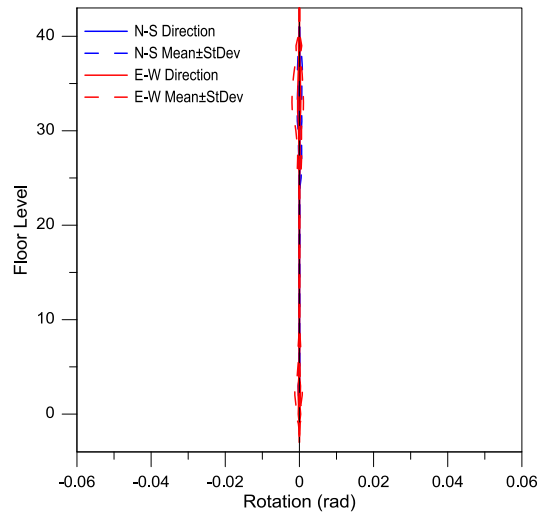
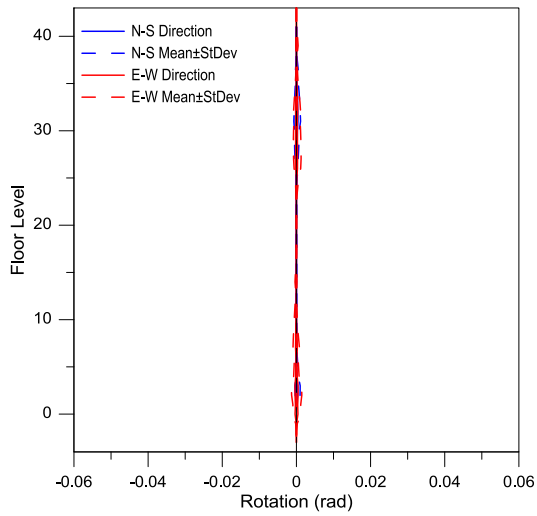
Figure 2-32. Coupling beam locations



(a) Coupling beam rotations under OVE level (b) Coupling beam rotations under MCE level



(c) Coupling beam rotations under DBE level



(d) Coupling beam rotations under SLE43 level (e) Coupling beam rotations under SLE25 level

Figure 2-33. Coupling beam rotations under various hazard levels

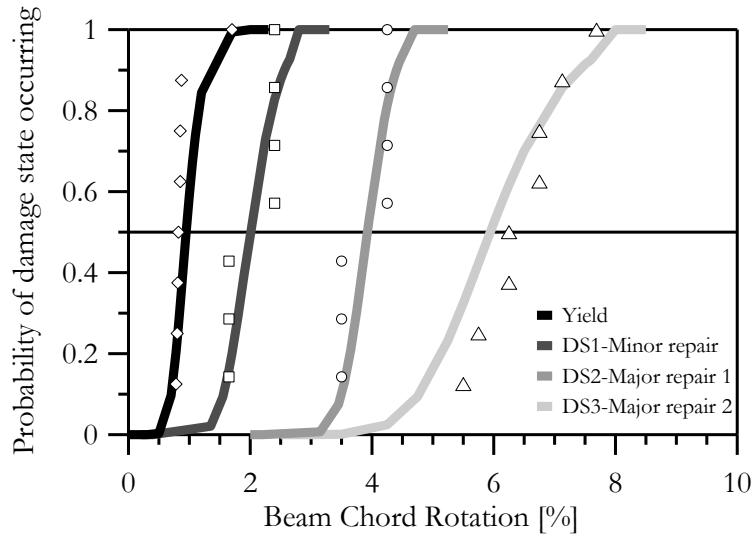
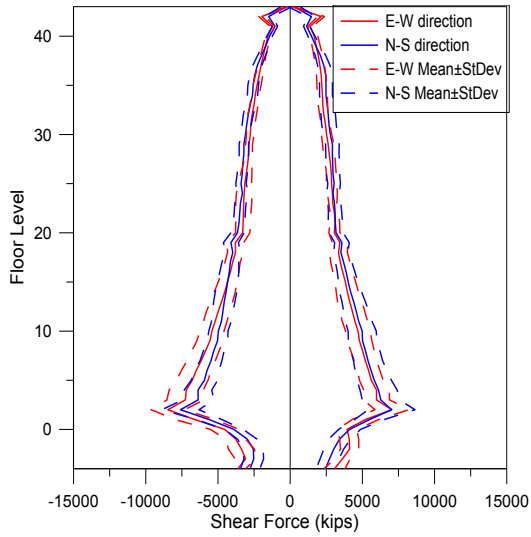


Figure 2-34. Fragility curves for diagonally reinforced concrete coupling beams at high aspect ratio
[Naish, 2010]

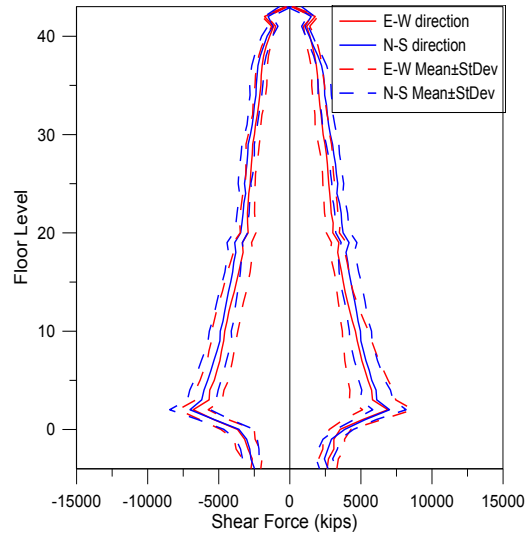
2.3.2.2. Building 2B

Aforementioned response quantities were analyzed for Building 2B for the same ground motions, (Figure 2-35 to Figure 2-40). Shear and moment profiles and core wall strains were similar to those reported for Building 2A; however, because thicker walls were used for Building 2B, modestly lower shear forces/stresses and core wall strains, and modestly higher coupling beam rotations, were computed (for all hazard levels). The peak values over the building height of the median and median plus one standard deviation for coupling beam rotations of 0.03 and 0.05, were still well below the limiting value of 0.06. Based on the fragility relations developed by Naish (2010), damage was expected to be limited and some epoxy injection repair (Damage State 2 – Major repair 1) might be needed for the North and South coupling beams at MCE and OVE levels (Figure 2-34).

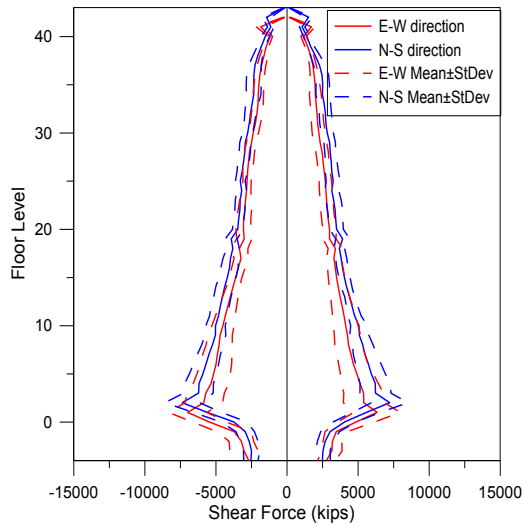
Core wall shears



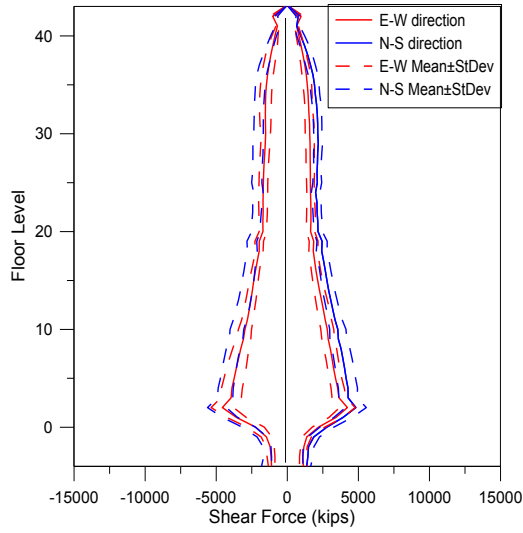
(a) Shear forces under OVE level



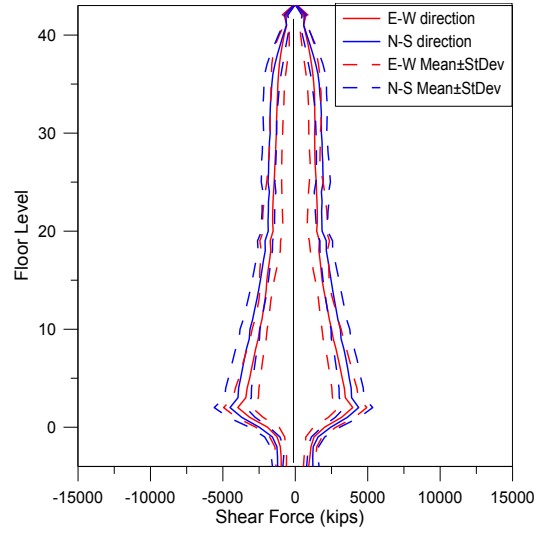
(b) Shear forces under MCE level



(c) Shear forces under DBE level



(d) Core wall shears under SLE43 level



(e) Core wall shears under SLE25 level

Figure 2-35. Core wall shear forces under various hazard levels

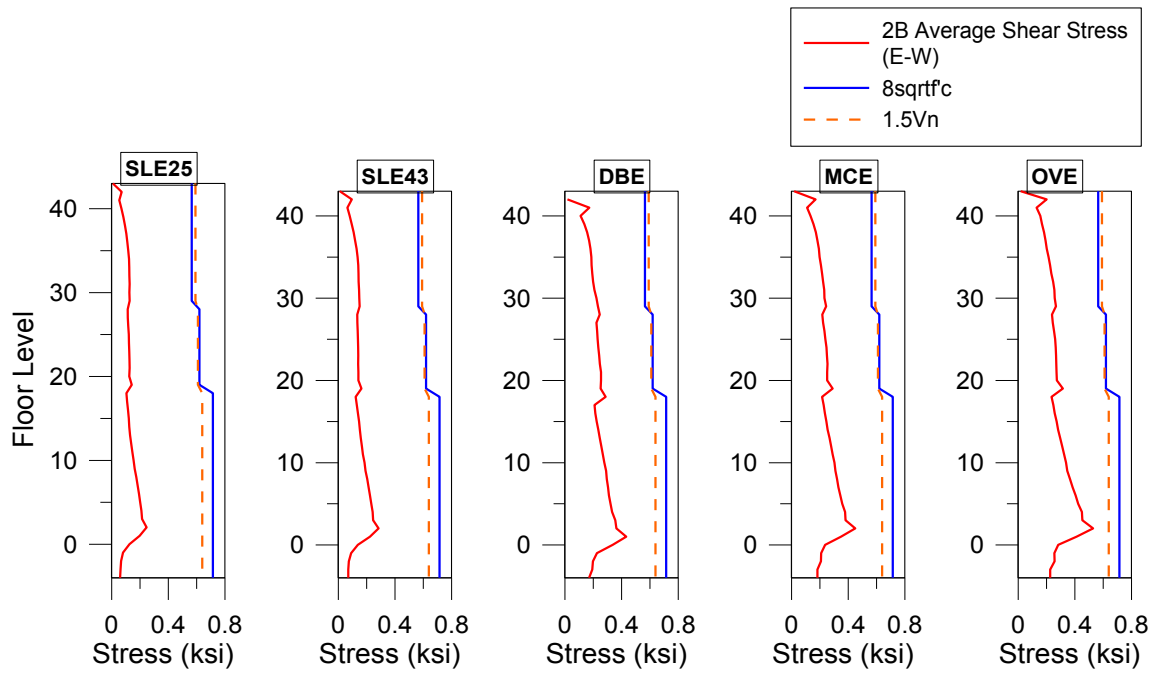
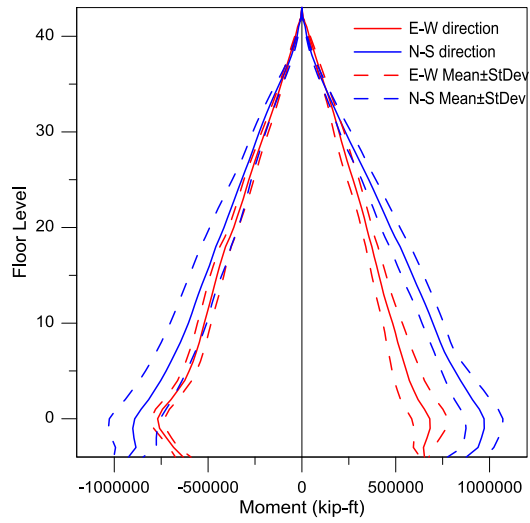
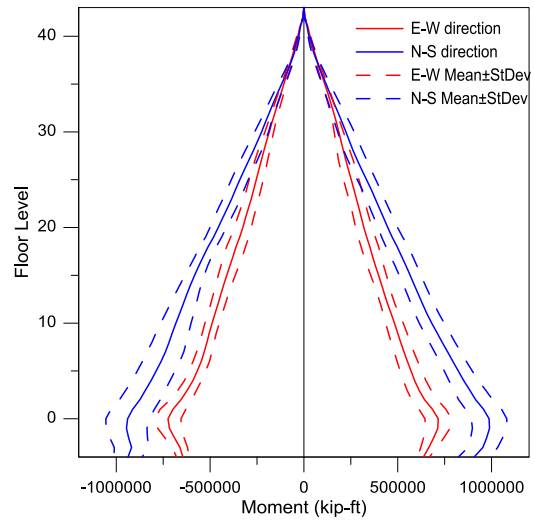


Figure 2-36. Average shear stress profiles of the core wall

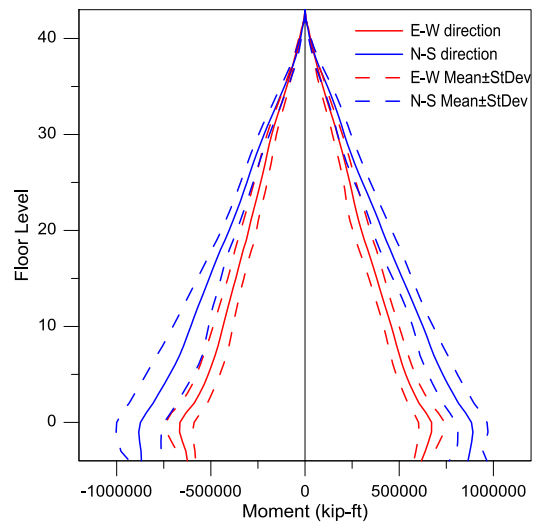
Core wall moments



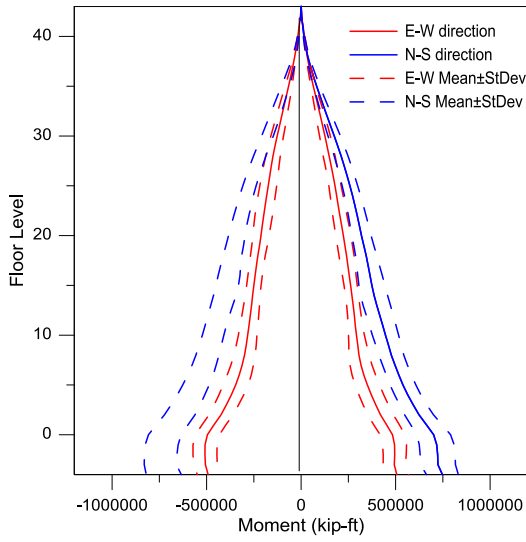
(a) Core wall moments under OVE level



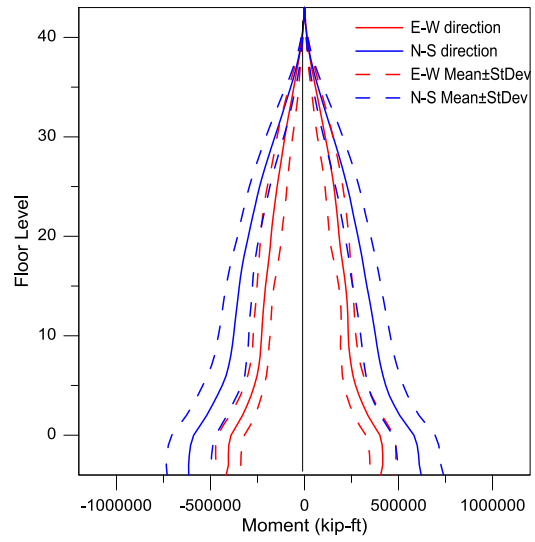
(b) Core wall moments under MCE level



(c) Core wall moments under DBE level



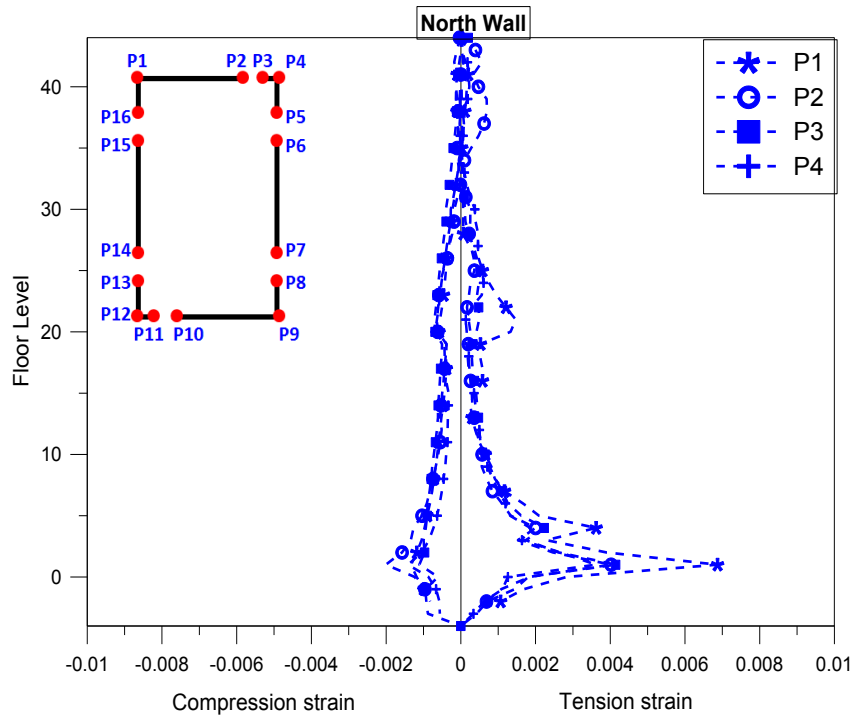
(d) Core wall moments under SLE43 level



(e) Core wall moments under SLE25 level

Figure 2-37. Core wall moments under various hazard levels

Core wall strains



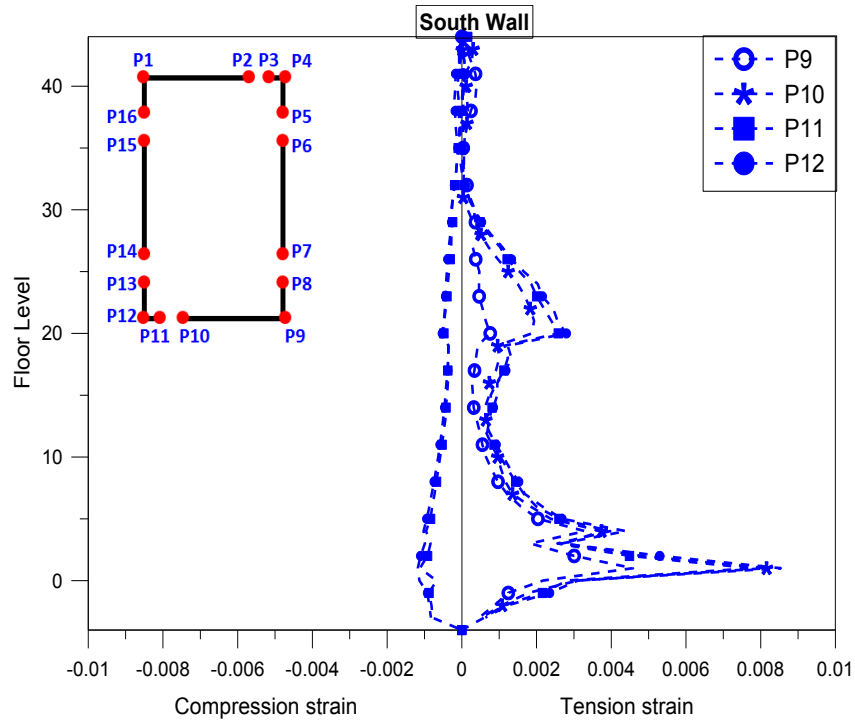
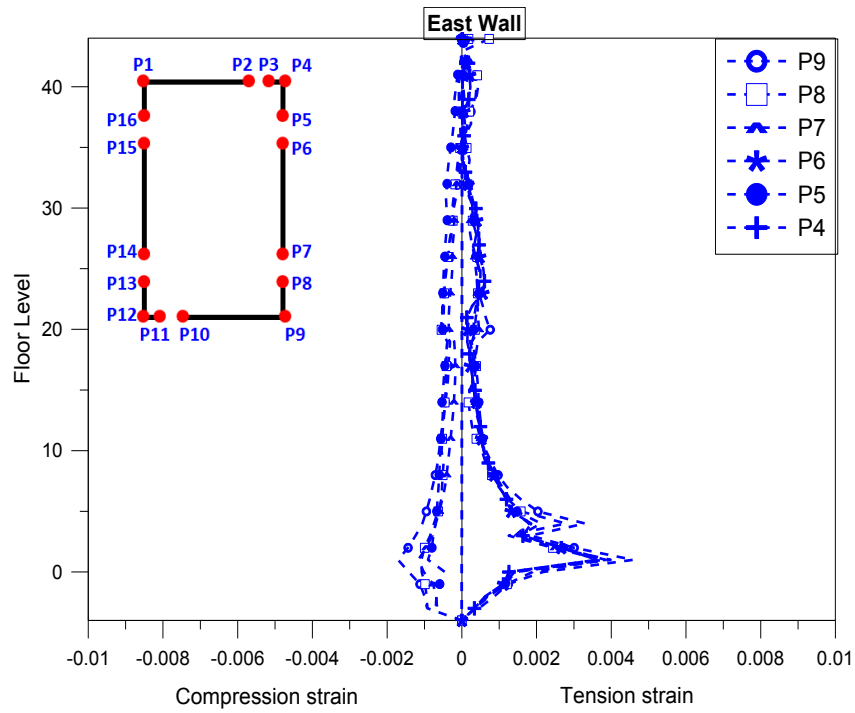


Figure 2-38. North and South wall strains under OVE level



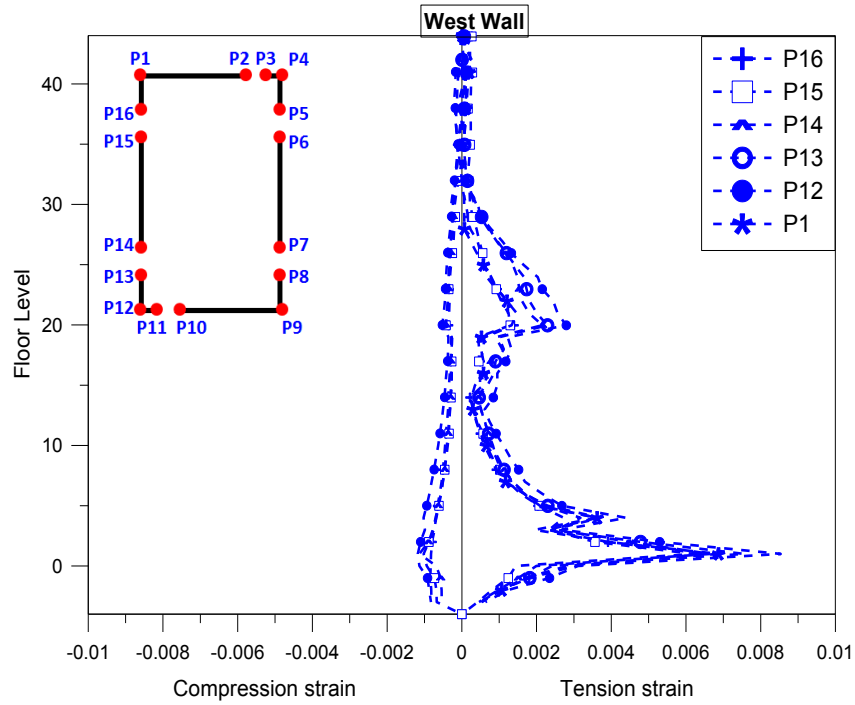
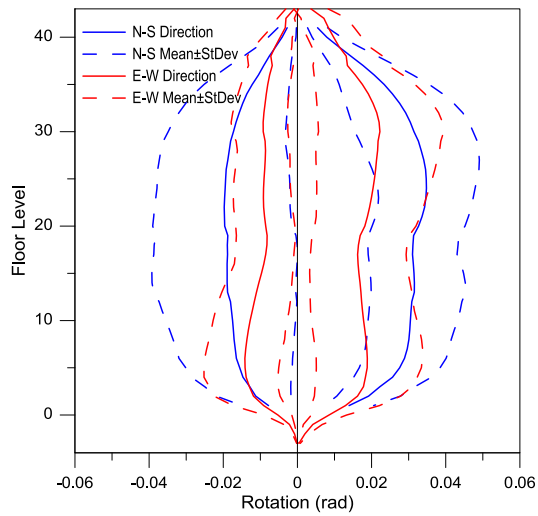
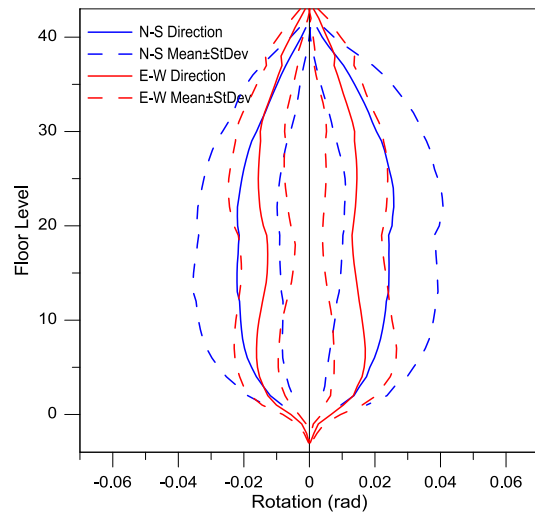


Figure 2-39. East and West wall strains under OVE level

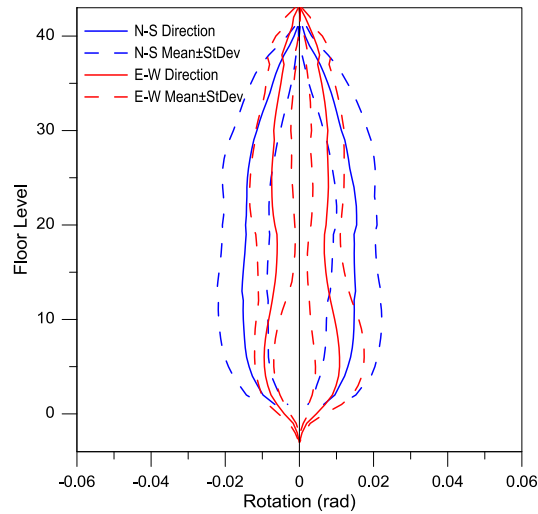
Coupling beam rotations



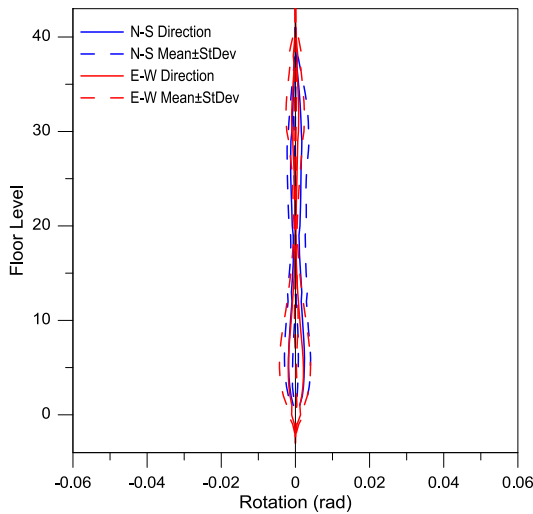
(a) Coupling beam rotations under OVE level



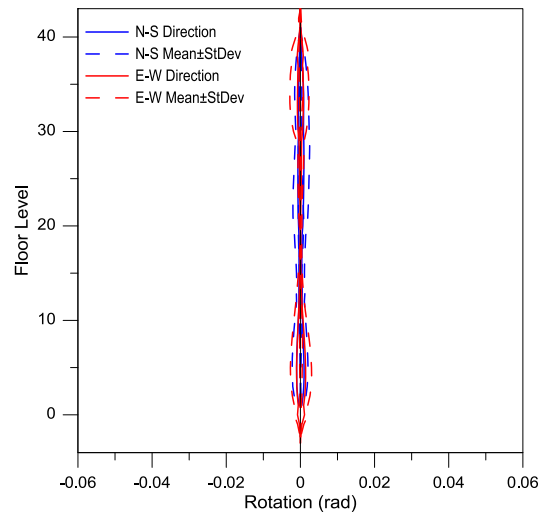
(b) Coupling beam rotations under MCE level



(c) Coupling beam rotations under DBE level



(d) Coupling beam rotations under SLE43 level



(e) Coupling beam rotations under SLE25 level

Figure 2-40. Coupling beam rotations under various hazard levels

2.3.2.3. Safety evaluation of core walls

Previous test results (Wallace, 1996; Orakcal et al, 2009) have indicated that the walls that fail in shear have median shear strength of approximately $V_{\text{expected}} = 1.5V_{n,ACI}$. However, in this study, the shear strength of walls that yield in flexure degrades depending on the level of the nonlinear

flexural deformation, similar to the relations defined for columns in ASCE 41-06 Supplement #1 (Elwood, et al, 2007). This issue is assessed by plotting test results, along with a tri-linear trend line, in Figure 2-41. The trend line, which represents the median strength, is anchored at a shear strength of $1.5V_n$ for curvature ductility less than 2.0, reduces linearly to $0.75V_n$ at curvature ductility of 8.0, and remains constant for larger ductility values. This strength envelope is used to assess failure in shear (when the demand reaches the strength envelope and also have a curvature ductility greater than 2.0) and for cases with flexural yielding followed by shear failure (when the demand reaches the strength envelope with a curvature ductility greater than 2.0, but less than 8.0), by post-processing analysis results. The failure criterion used here defines when significant lateral strength degradation was observed, not when loss of wall vertical load-carrying capacity was observed (the walls were not tested to large enough deformations to assess when axial failure occurred). New tests on moderate-aspect ratio walls (Tran, 2012) appear to indicate that axial failure follows closely after strength loss due to shear failure.

To observe potential failures based on aforementioned assumptions, pairs of normalized shear stress and curvature ductility are plotted for each time step together with predefined envelope. For this purpose, the following procedure (Figure 2-41; Equations 2-2 to 2-6) is used for curvature ductility calculations. This procedure is repeated for each core wall portion. Representative shear and flexural-shear failure plots can be seen in Figure 2-43 and Figure 2-44 respectively.

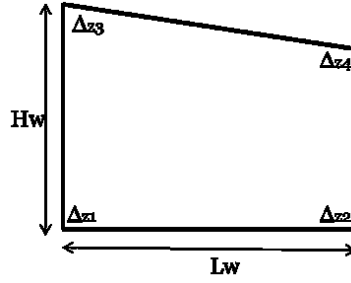


Figure 2-41. Elevation view of a core wall portion

$$\varepsilon_{(1-3)} = \frac{(\Delta_{z1} - \Delta_{z3})}{H_w} \quad \text{Equation 2-2}$$

$$\varepsilon_{(2-4)} = \frac{(\Delta_{z2} - \Delta_{z4})}{H_w} \quad \text{Equation 2-3}$$

$$\text{curvature } \phi = \frac{\varepsilon_{(1-3)} - \varepsilon_{(2-4)}}{L_w} \quad \text{Equation 2-4}$$

$$\text{yield curvature } \phi_y \approx \frac{0.0025}{L_w} \quad \text{Equation 2-5}$$

$$\text{curvature ductility} = \frac{\phi}{\phi_y} \quad \text{Equation 2-6}$$

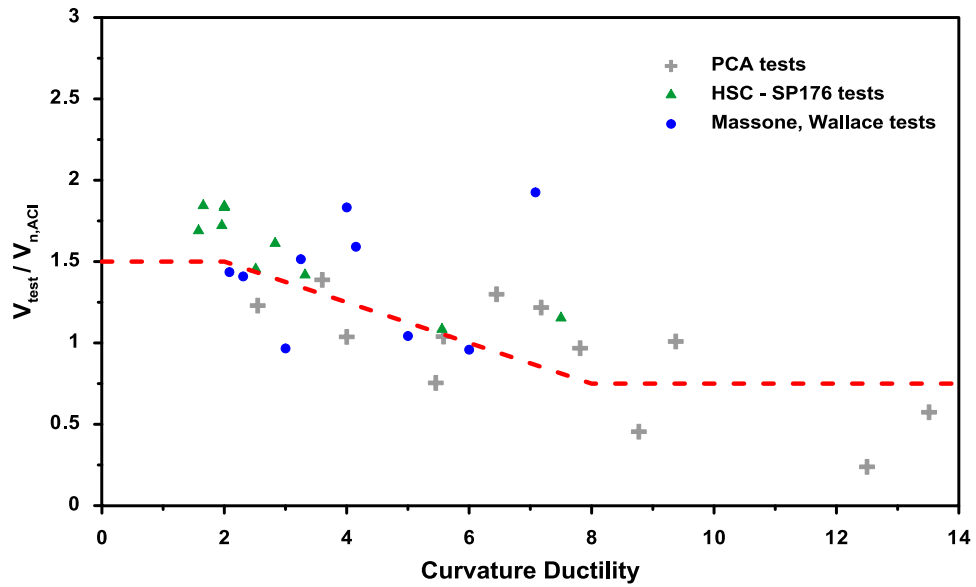


Figure 2-42. Shear failure criterion for structural walls

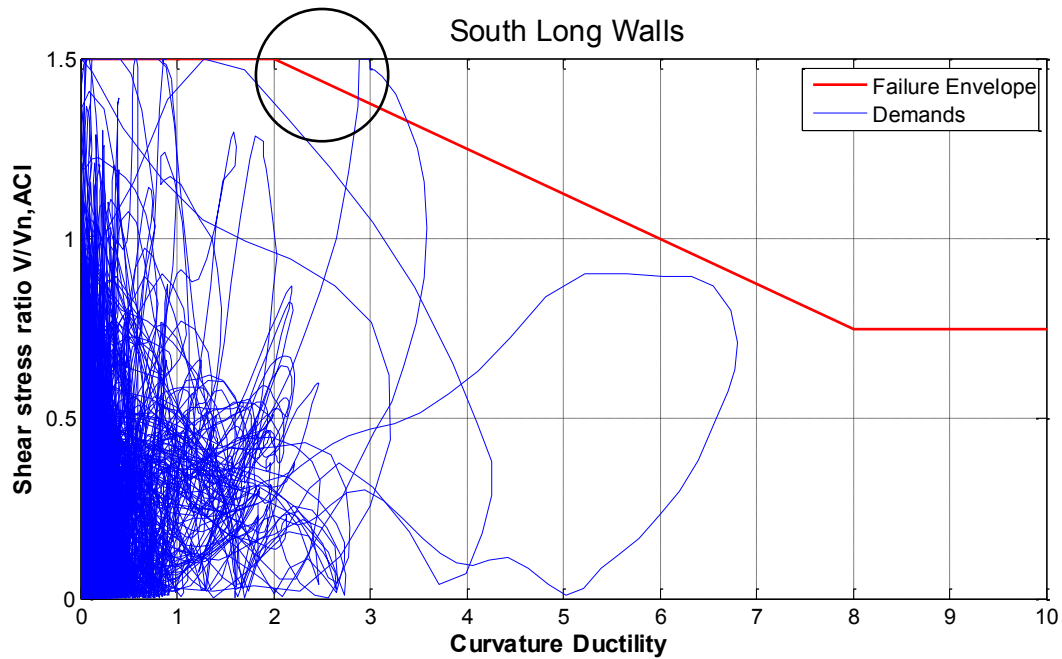


Figure 2-43. Representative shear failure (at the circle)

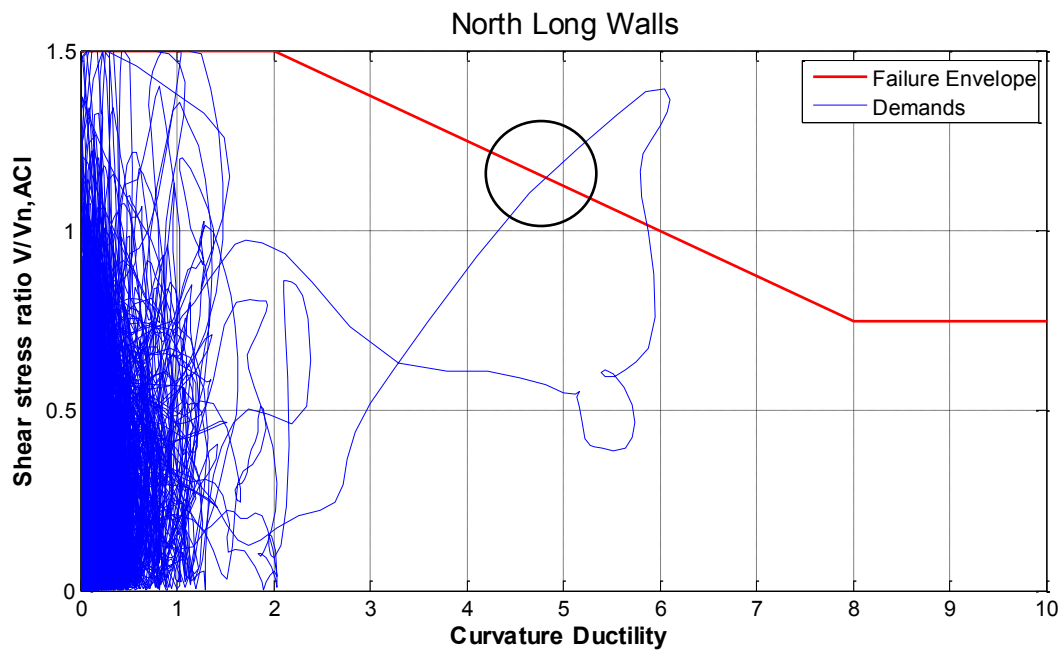


Figure 2-44. Representative shear-flexure failure (at the circle)

Based on the failure criteria and obtained results, 6 OVE ground motions caused failure in Building 2A whereas only 1 OVE ground motion caused failure in Building 2B. However, it is

noted that this method is based on a very limited data and needs to be investigated and verified with extensive research. This issue is discussed in Chapter 3.

2.3.3. Frame Behavior

2.3.3.1. Building 2A

To evaluate the Special Moment Frame response, peak values of beam and column rotations were obtained over the building height for OVE level ground motions (Figure 2-45 and Figure 2-48). Peak beam rotations were about 0.025 radians with a standard deviation of 0.005 radians, considerably less than the rotation limits established based on ASCE 41-06, and also supporting the decision not to model strength degradation.

To assess potential for column axial failures, axial forces were normalized by $A_g f'_c$, where A_g is the column cross sectional area and f'_c is the expected concrete strength, and column nonlinear rotation demands were evaluated (Figure 2-46 and Figure 2-48, respectively). Results for interior columns (represented with dashed lines in Figure 2-46) indicate that these columns experienced much smaller axial demands (0.25 and 0.45 $A_g f'_c$) than corner columns (as high as 0.6 and 0.8 $A_g f'_c$), which are shown as solid lines. Given that the axial stresses were significantly higher in South-West and North-East columns, these columns were examined in more detail to determine whether column axial failure was possible. For that purpose, axial load-moment interaction diagrams were created for the most critical regions (ground level and 15th level) and plotted along with the axial force - moment demand responses for various OVE level ground motions (Figure 2-47). Column yielding occurs when the demand reaches the surface of the P-M interaction diagram, either by yielding of tensile reinforcement below the balanced

point, or concrete in compression above the balanced point. The magnitude of the column nonlinear rotation was examined to assess the potential for axial failure. Results plotted in Figure 2-48 indicate that nonlinear rotations were much less than the limits of 0.01 and 0.035 (depending on the column properties) given in ASCE 41-06; therefore, if one accepts the ASCE-41 limits, axial failure was not expected. However, for tall buildings with such large columns, the idea of allowing nonlinear behavior in concrete compression (strains exceeding 0.003) is questionable.

Frame beams

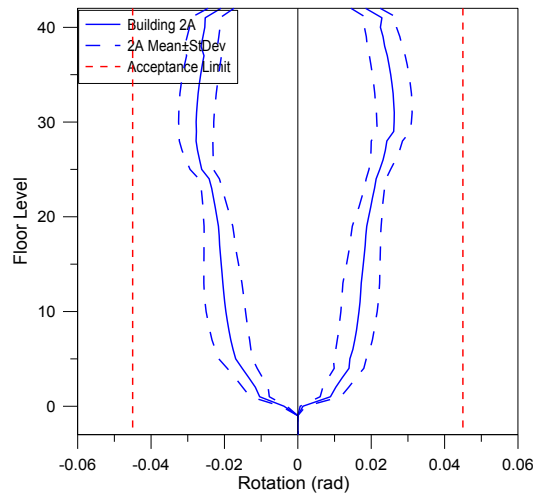


Figure 2-45. Frame beam rotations under OVE level

Frame columns

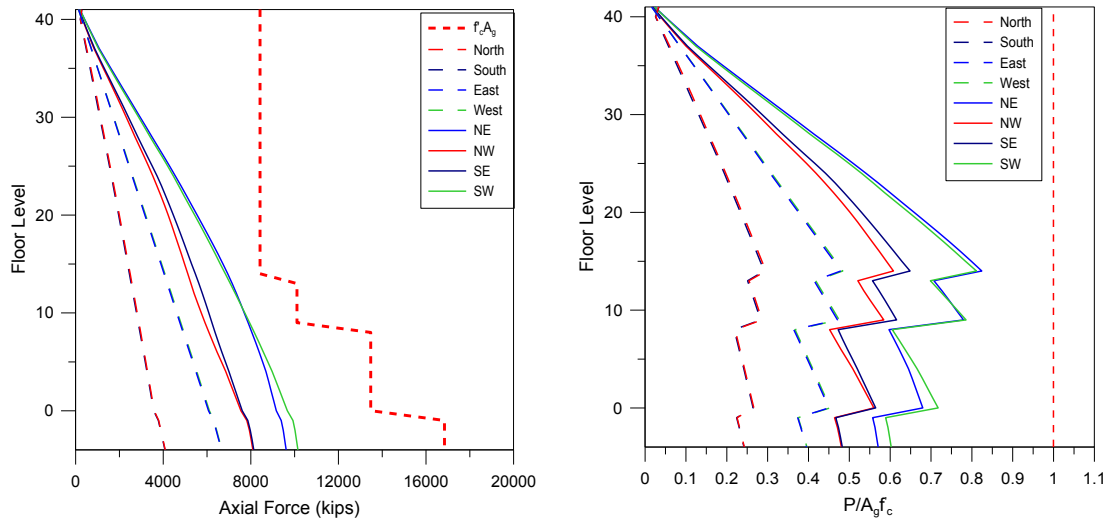


Figure 2-46. Absolute and normalized column axial forces under OVE level

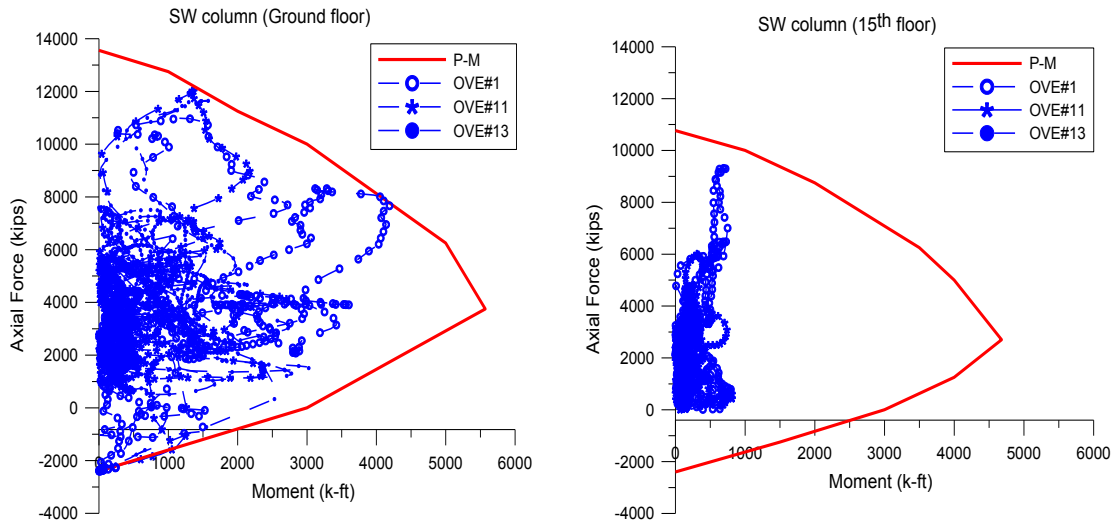


Figure 2-47. P-M interaction diagram for South-West column at (a) ground floor, (b) 15th floor

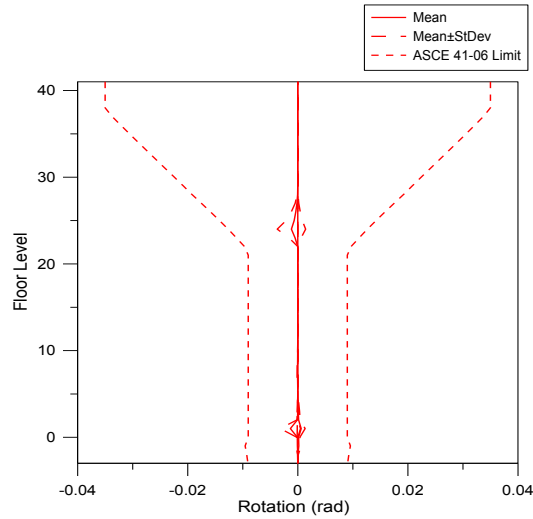


Figure 2-48. Frame column rotations under OVE level

2.3.3.2. Building 2B

Demands on Special Moment Frame beams and columns also were examined for Building 2B (Figure 2-49 to Figure 2-51). In general, similar results were obtained, except beam rotations were slightly larger (about 10%) and column axial forces were only about one-half the respective values noted for Building 2A. The one significant observation, that the performance-based design approach, which limits column axial loads to $0.35A_gf'_c$, does a better job of explicitly accounting for biaxial loading on corner columns. The precise impact on collapse potential is unknown, given our lack of understanding related to the behavior of well-detailed, large columns subjected to high axial loads.

Frame beams

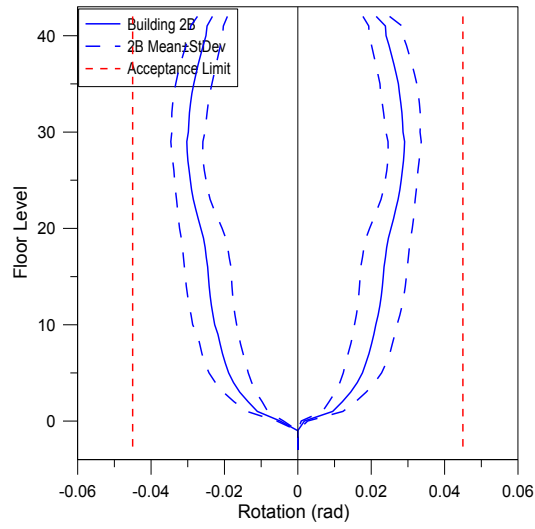


Figure 2-49. Frame beam rotations under OVE level

Frame columns

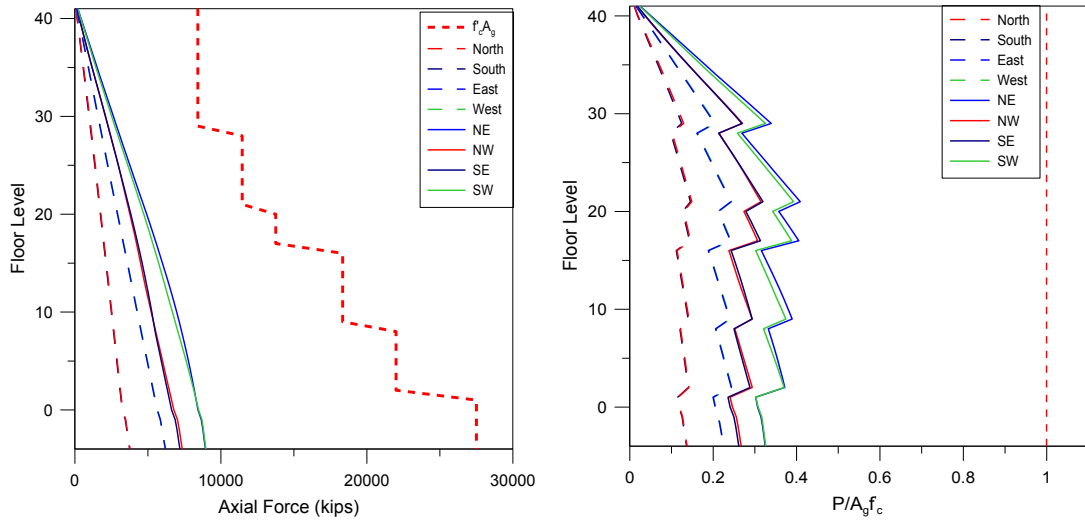


Figure 2-50. Absolute and normalized axial forces under OVE level

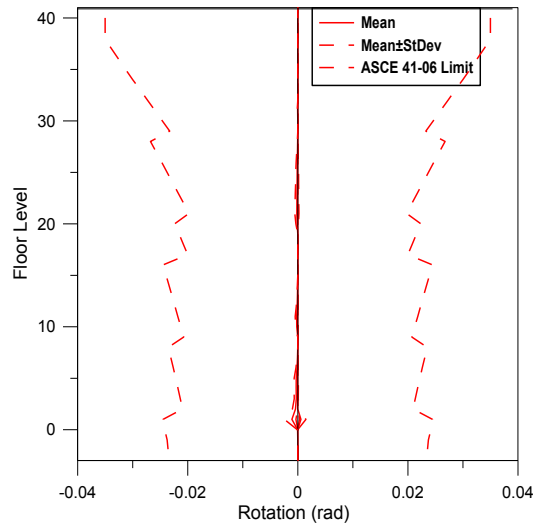


Figure 2-51. Frame column rotations under OVE level

2.3.3.3. *Frame contribution in the dual system*

The behavior of the Special Moment Frame within the dual system was examined by investigating various response quantities. The relative contributions of the core wall and the SMF to story shear are compared over the building height in Figure 2-52. The shear force resisted by the core wall and the SMF were essentially linear and constant over the building height, respectively. For both buildings, the SMF resists a significant portion of the story shear, about one-third at the ground level and one-half in upper stories. The thicker core wall in Building 2B resists slightly more story shear than the wall in Building 2A.

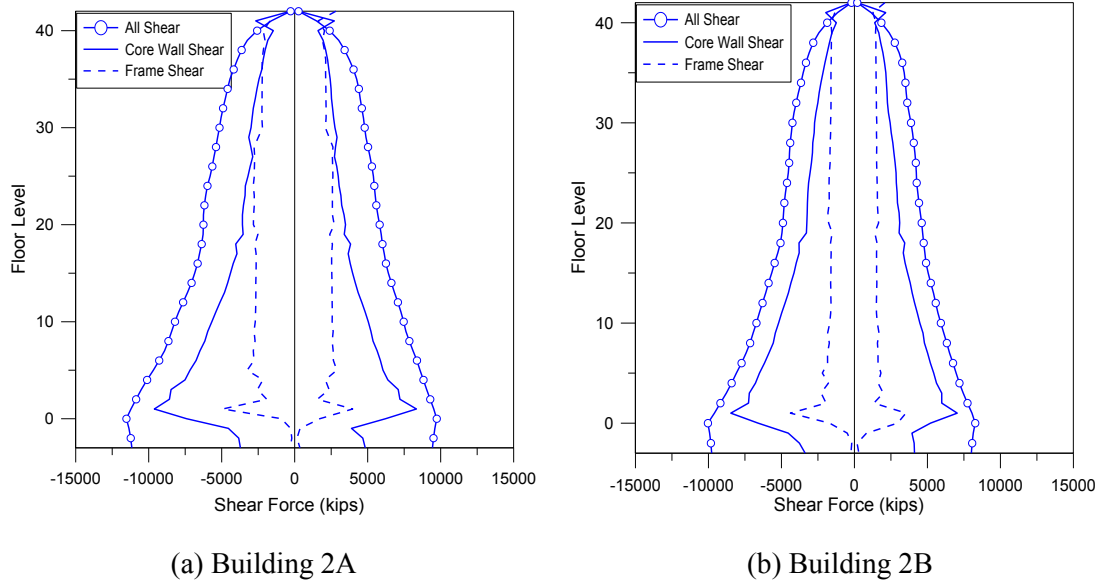


Figure 2-52. Distribution of shear forces in the system under OVE level

2.3.4. Comparison of two buildings

To enable direct comparisons between the two buildings, critical EDPs (inter-story drifts, core wall shear stresses, core wall strain values, coupling beam rotations, frame beam rotations and normalized column axial forces) are compared for two hazard levels (SLE, OVE) in Figure 2-53 to Figure 2-58. Since the dispersion in the response quantities was about the same for Building 2A and 2B, only mean values are presented.

The comparison indicates that inter-story drifts (Figure 2-53), core wall shear stresses (Figure 2-54) and axial compressive strains at the ground level (Figure 2-55) are slightly higher for Building 2A than for Building 2B, for both hazard levels presented. As previously noted, coupling beam rotations (Figure 2-56) and frame beam rotations (Figure 2-57) were slightly greater for Building 2B, indicating more energy dissipation. However, in both buildings, response quantities were typically well below limiting values (acceptance criteria), with the

exceptions noted previously, e.g., that normalized column axial demands in Building 2A were about twice the values in Building 2B (Figure 2-58).

2.3.4.1. Inter-story drifts

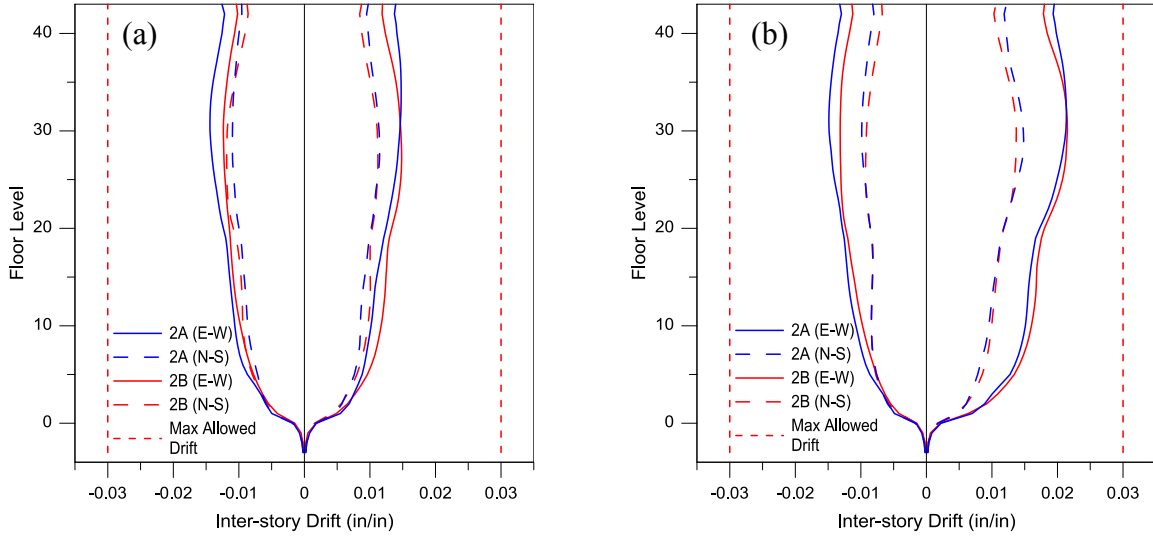


Figure 2-53. Comparison of inter-story drifts (a) under OVE level, (b) under SLE25 level

2.3.4.2. Core wall shear stresses

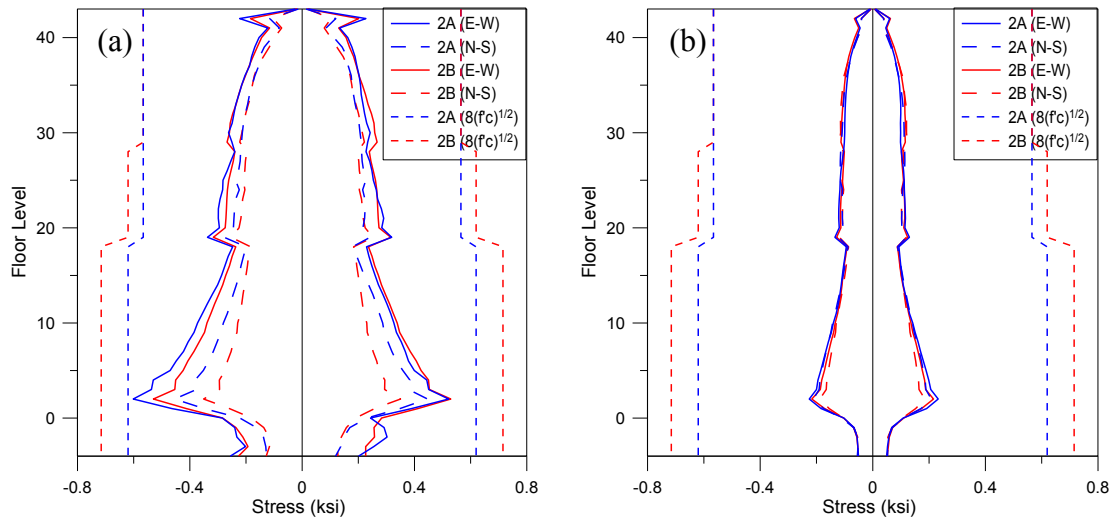
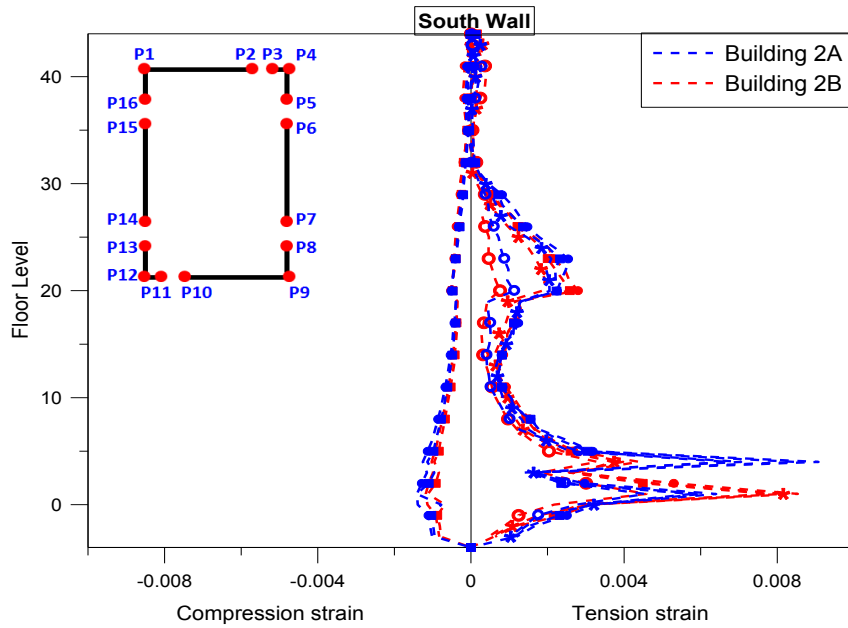
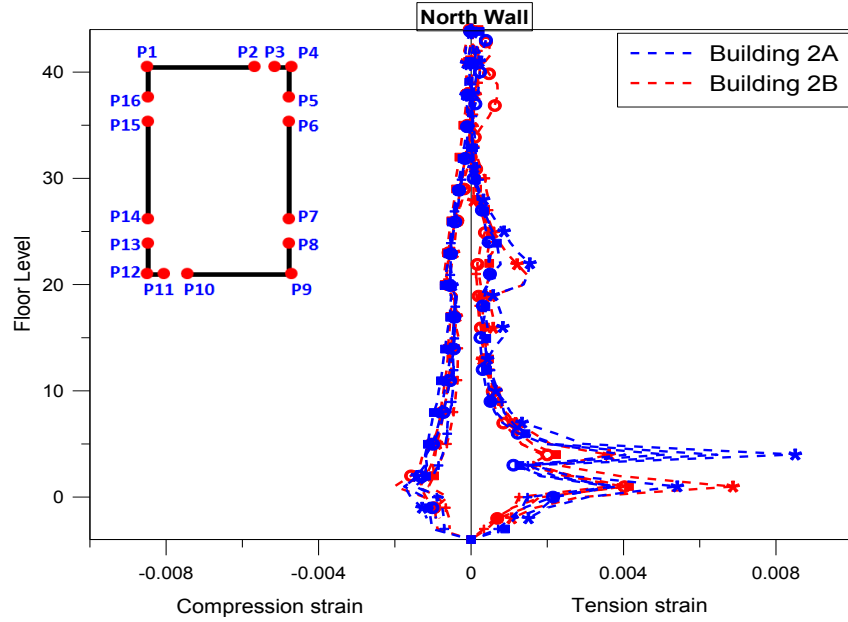


Figure 2-54. Comparison of core shear stresses (a) under OVE level, (b) under SLE25 level

2.3.4.3. Core wall strains



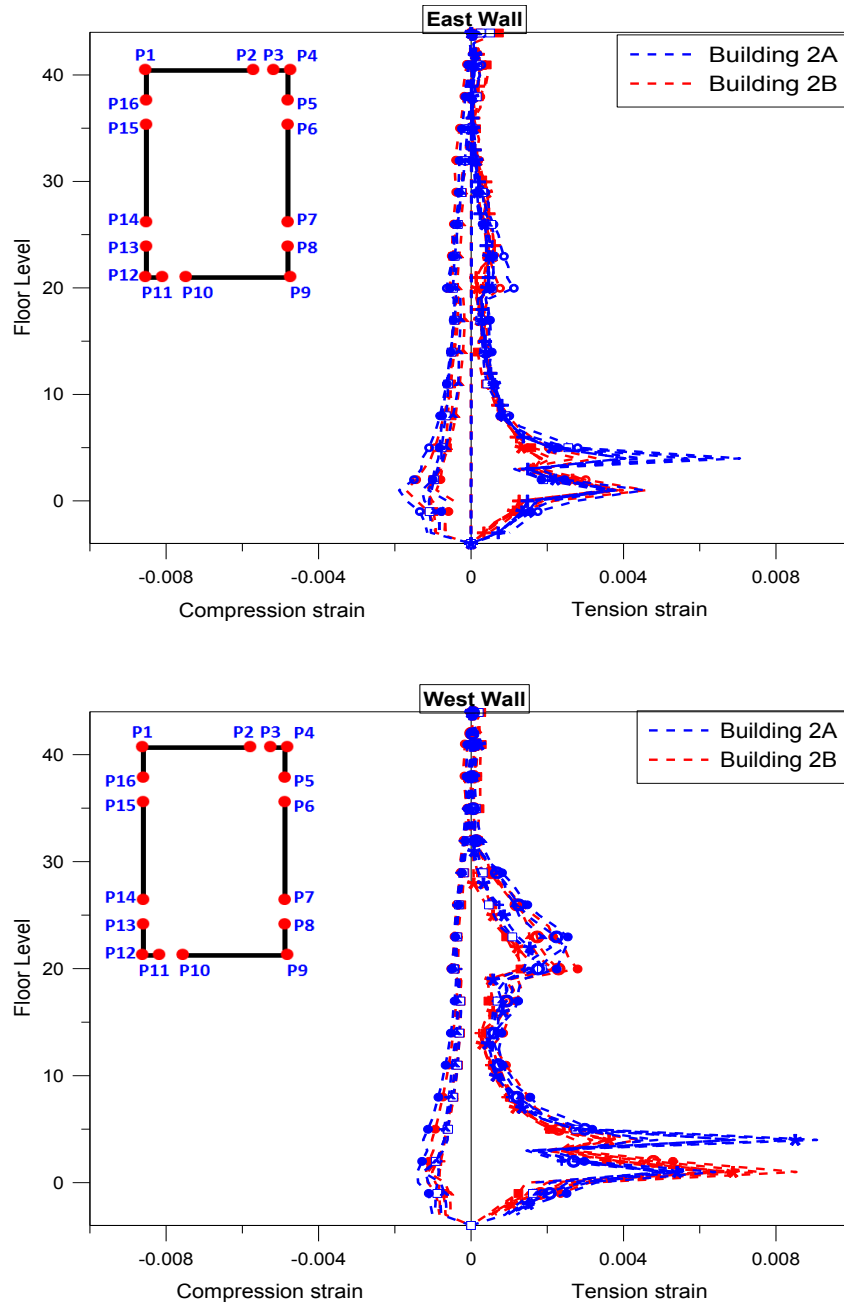


Figure 2-55. Comparison of core wall strains under OVE level

2.3.4.4. Coupling beam rotations

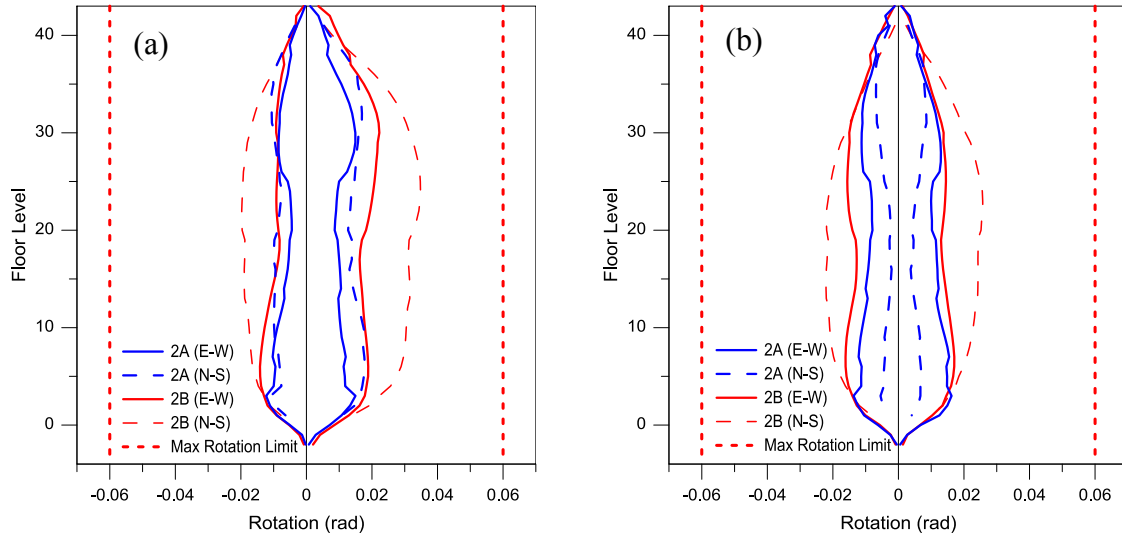


Figure 2-56. Comparison of coupling beam rotations (a) OVE level, (b) MCE level

2.3.4.5. Beam rotations

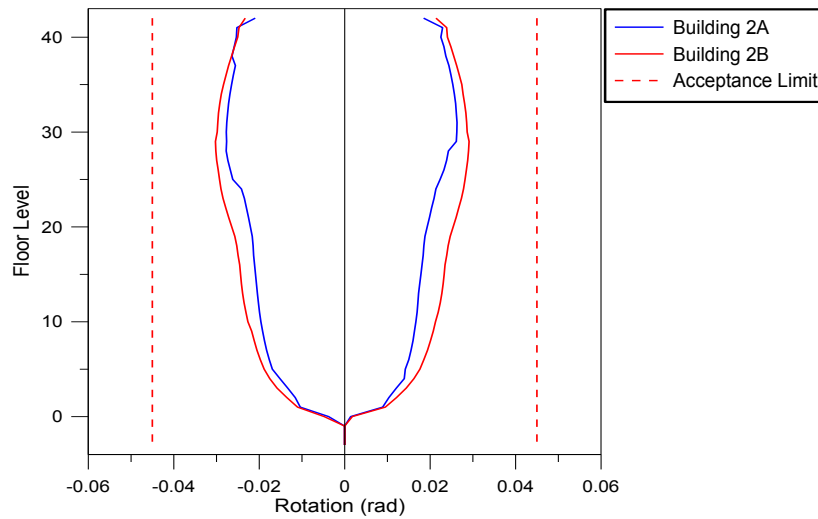


Figure 2-57. Comparison of frame beam rotations under OVE level

2.3.4.6. Normalized column axial forces

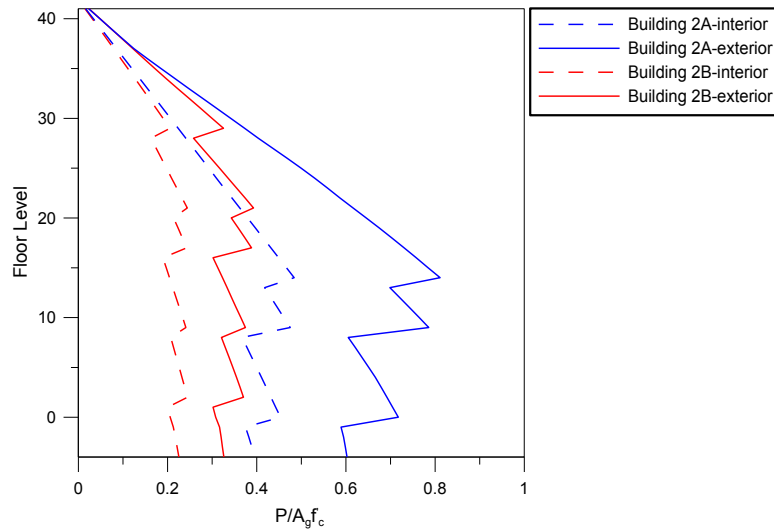


Figure 2-58. Comparison of normalized column axial forces under OVE level

2.4. Cost Analysis Results

As mentioned earlier, extensive nonlinear response analyses were carried out for each design (a total of 75 nonlinear dynamic analyses, 15 for each hazard level). The results of these nonlinear analyses were subsequently used for loss estimation, whereas the initial costs were obtained from the results of the design study. Cost analyses were conducted by a professional cost estimator (Langdon, 2010). Financial impacts associated with the results presented, including initial costs and projected damage repair costs associated with future earthquakes, are discussed in this section.

2.4.1. Initial construction cost

The initial building construction costs were estimated by professional cost estimator (Langdon 2010) based on the material usage and additional design fees.

The enclosed area considered for loss estimation was 683,748 square feet and 476,724 square feet for the entire building and above grade construction, respectively. Table 2-11 shows a summary of the initial structural costs and the total costs – which include structural and non-structural components, and contents, for both above ground and for the entire building. The results indicate that as, the design approach shifts from Design A to B, the initial construction cost increases about 20%. Detailed information is available in Langdon, 2010.

Table 2-11. Initial structural and content costs, in million U.S. dollars

| | | Above ground | Entire building |
|------------------------------|------------|--------------|-------------------|
| Code-based (Design A) | Structural | 134M | 237M (\$346/sqft) |
| | Total | 149M | |
| Performance-based (Design B) | Structural | 159M | 281M (\$411/sqft) |
| | Total | 174M | |

2.4.2. Annual repair cost

Two approaches were carried out to estimate financial earthquake losses. The first approach was consistent with the state-of-practice loss estimation, by which Risk Management Solutions, Inc. (RMS) estimated financial losses using the response history results. The second approach included using open-source financial analysis methodology according to the Applied Technology Council ATC-58 project [ATC-58 2009; Yang et al. 2009]. The two approaches had similar assumptions and limitations, while containing certain differences. Detailed information on the two methodologies is available in Moehle et al., 2011.

Financial losses estimated according to the state-of-practice by RMS are summarized in Table 2-12 in terms of mean annualized repair costs and total costs (total cost was defined as the initial construction cost plus the net present value of insurance premiums) for the two different

designs. The numbers represent the average repair cost per year, considering all hazard levels. The mean annualized repair cost decreased about 20% as the design shifted from Design A to Design B.

Loss estimation analysis according to ATC-58 methodology revealed that the annual repair cost for Building 2A was attributed to the damage to the shear wall webs and to interior partitions at all hazard levels including SLE25. At the DBE level, all interior partitions and contents, and more shear wall webs began to contribute to the total repair costs. As shaking intensity increased to the OVE level, additional damage occurred to the moment resisting frames. Similar damage trends were observed for Building 2B for all hazard levels considered.

Table 2-12. Annual repair costs

| | Mean annualized repair cost | Total cost |
|------------------------------|-----------------------------|---------------|
| Code-based (Design A) | \$323,000 | \$157,000,000 |
| Performance-based (Design B) | \$269,000 | \$180,000,000 |

2.5. Summary and Conclusions

Extensive use of performance-based design in recent years has led to the development of consensus documents to help guide the design and peer-review process. However, comparison of code-designed and performance-based designed buildings has not been studied and the potential differences in performance between the different design approaches have not been quantified. To compare performance for three design cases, a systematic study was undertaken to analyze different building designs using consistent modeling criteria at various levels of ground shaking intensity to determine engineering demand parameters (EDPs). Outside consultants used the

structural drawings (and other information) to assess construction costs and the EDPs to assess likely repair costs to enable direct comparisons.

Downtown Los Angeles was selected as the site for the hypothetical new buildings, and each building was designed using three procedures. Two of these designs were identical (performance-based and enhanced performance-based); therefore, the remaining two designs (code-based and performance-based) are summarized along with the modeling approach used. To investigate responses, five hazard levels were selected. Each building design was analyzed for 15 ground motions for each hazard level and the resulting response quantities are summarized to assess performance.

At the 25-year (SLE25) and 4975-year (OVE) hazard levels, median inter-story drift ratios were well-below established drift limits of 0.005 and 0.03, and maximum median core wall tensile and compressive strains at OVE level were about 0.008 and 0.0015; well-below limiting values of 0.05 and 0.015. It was noted that shear stresses and strains were slightly higher in Building 2A (code-based design). Median coupling beam rotations were about 0.01 and 0.02 radians at 2975-year (MCE) and 4975-year (OVE), respectively, also well-below the limiting value of 0.06 radians. Potential failures in the core walls were also investigated. Based on the failure criteria based on previous test results, wall shear failure was expected for Building 2A in 6 ground motions for OVE level, whereas wall shear failure was expected for Building 2B in only one OVE ground motion. Because the failure envelope was obtained using a limited database, there was a need for further investigation to reassess the failure criteria. A better assessment of wall failure would be possible with a more accurate estimation of median (expected) and dispersion of wall shear strength and deformation capacity (ductility). Chapter 3 provides detailed discussion of this issue.

Regarding the behavior of Special Moment Frame within the dual system, results show that for both buildings, the SMF resists about one-third of the base shear at ground level and one-half of the story shear in upper stories. The thicker core wall in Building 2B resists slightly more story shear than the wall in Building 2A. In terms of frame responses, median beam rotations were about 0.025 radians; smaller than the established limiting value of 0.045. Median normalized axial forces ($P/A_g f'_c$) in the most critical corner columns were about 0.6 to 0.8 for Building 2A and 0.25 to 0.45 for Building 2B. Despite the large compression forces in Building 2A columns, plastic rotation demands were low and concentrated at the base over levels 1-5, near level 10, and from levels 20 to 25. It is noted that gravity system behavior was not assessed.

Given these results, both buildings are expected to satisfy performance objectives and, in general, excellent performance is expected. Building 2B (performance-based design) achieves slightly better performance than the Building 2A (code-designed), because of lower wall shear stresses and lower wall compressive strains observed for Building 2B, although these differences were modest. The performance-based design approach (Building 2B), which limits column axial loads to $0.35A_g f'_c$, does a better job of explicitly accounting for biaxial loading on corner columns. The precise impact on collapse potential is unknown, given our lack of understanding related to the behavior of well-detailed, large columns subjected to high axial loads.

Based on all the information collected, relative merits associated with performance-based design were reviewed by a professional cost estimating company according to the state-of-practice. A benefit-cost analysis was developed for each design by estimating construction and repair costs. The total initial cost including structural and non-structural components, and contents for the entire building was estimated as \$346 per square feet and \$411 per square feet for the code-based designed building (Building 2A) and performance-based designed building

(Building 2B), respectively. The results indicate that the initial construction cost increased about 20% when the design approach shifted from code-based design to performance-based design.

Financial losses for the performance-based designed building (Building 2B) were about 20% lower than those for the code-based designed building (Building 2A). The mean annualized repair cost was \$323,000 and \$269,000 for Building 2A and Building 2B, respectively. Loss estimation analysis according to ATC-58 methodology revealed that the annual repair cost for both buildings was attributed to the damage to the shear wall webs and to interior partitions at all hazard levels including the service levels. At higher intensities of shaking, all interior partitions and contents, and more shear wall webs began to contribute to the total repair costs, followed by additional damage occurred to the moment resisting frames at the highest shaking level (OVE).

Chapter 3 Shear Strength and Deformation Capacity of Reinforced Concrete Shear Walls

3.1. Introduction

Reinforced concrete shear walls are commonly used in buildings to provide lateral load resistance to earthquake ground shaking, as they provide significant lateral stiffness and strength. However, experimental results have shown that behavior of the shear walls are different depending on the wall characteristics, with squat (short) wall responses governed by shear and taller (slender) wall responses dominated by flexural behavior (Massone et al, 2004; Orakcal et al., 2009). Squat walls, typically defined as walls with aspect ratio (or shear span ratio) less than 1.0 to 1.5, typically reach their shear strength prior to yielding of boundary longitudinal reinforcement, followed by rapid strength loss with little-to-no nonlinear deformation capacity (or ductility), i.e., brittle behavior. On the other hand, slender walls are designed to yield in flexure and to sustain large inelastic flexural deformations prior to strength loss, i.e., ductile behavior. Walls with aspect ratio greater than approximately three are generally classified as slender. Walls with aspect ratios between roughly 1.5 and 3.0 are generally classified as moderate-aspect ratio walls, i.e., walls that typically yield in flexure prior to reaching the wall shear strength, but where the wall nonlinear deformation capacity may be reduced due to the presence of shear. The ratio of the shear force developed to the shear force associated with reaching the wall nominal flexural capacity is commonly used to classify behavior (see ASCE 41-06 Supplement #1, ACI 318-11 S.9.3). In this study, shear walls are categorized as summarized in Table 3-1. Failure modes for each category are also given in Table 3-1; failure modes for shear-controlled walls include diagonal tension, web crushing, and sliding, whereas

failure modes for flexure-controlled walls include concrete crushing and reinforcement buckling at the wall boundary.

Table 3-1. Expected behavior and failure modes of the walls

| | Shear-controlled walls | Transition walls | Flexure-controlled walls |
|-------------------------------|---|--|--|
| Expected behavior | Reach their shear strength before boundary longitudinal reinforcement yields in flexure | Yield in flexure followed by shear failure (shear-flexure interaction) | Yield in flexure without reaching the shear strength |
| Expected failure types | Diagonal tension failure, sliding shear, and web crushing. | Diagonal tension failure, concrete spalling and crushing at wall boundaries, rebar buckling and lateral instabilities at boundary elements | Concrete spalling and crushing, rebar buckling and lateral instabilities at boundary elements. |

Figure 3-1 shows a shear wall failure criterion established using limited data for the study presented in Chapter 2. A simple relation is used in Figure 3.1 to represent the three categories defined above and in Table 3.1, with shear-controlled walls defined as walls with curvature ductility less than 2.0; flexure-controlled walls for curvature ductility greater than 8.0; and transition walls for curvature ductility between 2.0 and 8.0. The data trend for transition walls indicate that the peak shear stress at failure in the walls decreases as the curvature ductility increases.

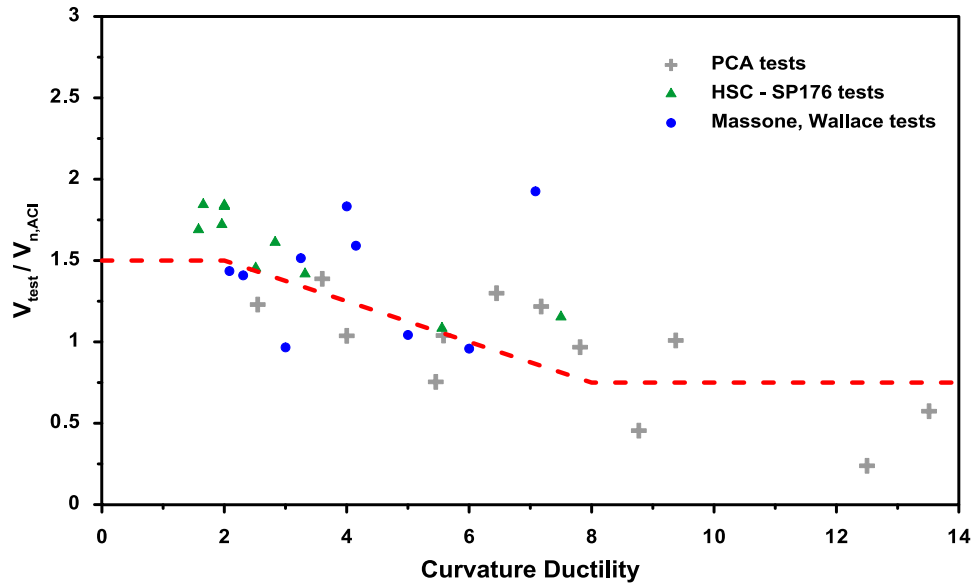
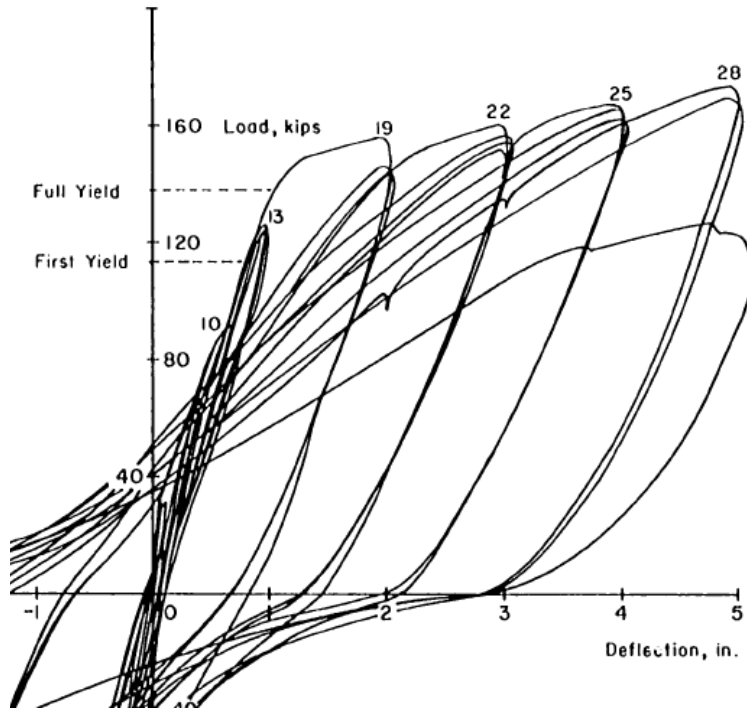
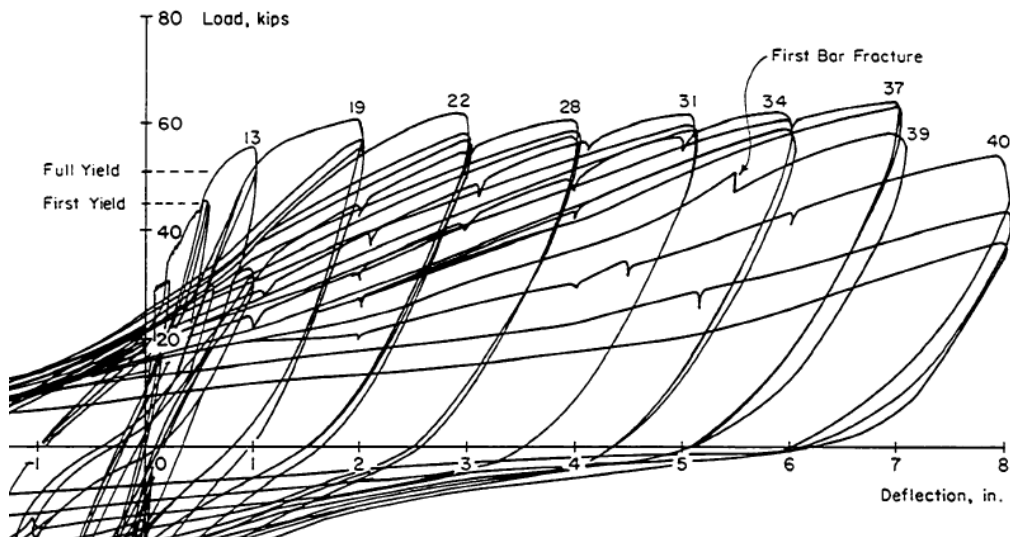


Figure 3-1. Failure criterion for shear walls

Results from two tests reported by Corley et al. (1981) clearly show that deformation capacity is impacted by the level of shear stress, as presented in Figure 3-2. Both tests (B3 and B5) were conducted on “barbell-shaped” wall cross-sections, with 300mm square boundary columns connected by 102mm thick wall webs 1300mm long (total wall length of 1910mm). Wall height was 4570mm from base to the top loading block. In wall B3, 8 - #4 vertical walls were used in the boundary columns, whereas in Wall B5, 12 - #6 vertical bars were used in the boundary columns. Vertical web reinforcement was identical for both walls; however, horizontal web reinforcement ratio was 0.55% for B5 and 0.27% for B3. No axial load (other than self-weight) was applied to either wall during testing. The data clearly show lower deformation capacity for the wall with higher shear demand; an alternative way to view this is to assume wall shear strength degrades with increasing ductility, leading to shear failure. The limited ductility of the walls with high shear stress is typically assumed to be associated with inelastic deformations leading to web crushing failures (Oesterle et al., 1984).



(a) Load – deflection relation: Specimen B5 ($v_{u,max} = 7\sqrt{f'_c}$)



(b) Load – deformation relation: Specimen B3 ($v_{u,max} = 4\sqrt{f'_c}$)

Figure 3-2. Wall shear strength versus ductility relation (Corley et al., 1981)

Shear strength versus ductility demand is discussed in PEER/ATC 72-1 (2010) both for columns and walls. The relation used for columns in ASCE/SEI 41-06 is presented in Figure 3-3, for three types of failure modes: shear, shear-flexure, and flexure. The report suggests including a reduction factor in the shear strength equation that reduces the shear strength with increasing ductility.

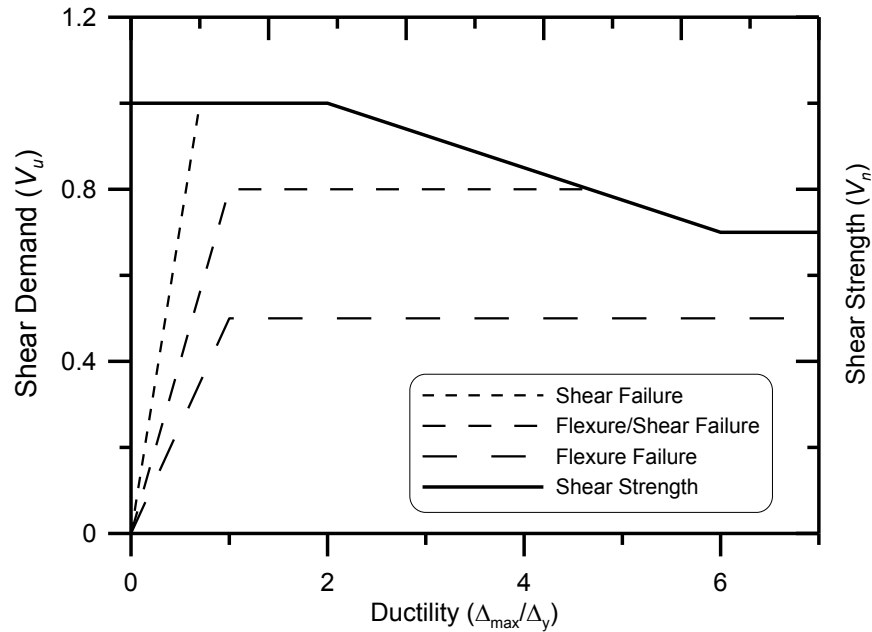


Figure 3-3. ASCE 41-06 (2007) Column Shear Strength – Demand Relation (PEER/ATC 72-1, 2010)

3.1.1. Shear strength

Shear walls are proportioned using ACI 318 to satisfy minimum strength requirements determined according to the general building code (ASCE 7-10) and then detailed according to prescriptive provisions per ACI 318-11. The wall flexural strength is typically calculated using fiber section analysis with the assumption that the plane section remain plane, while the wall shear strength is calculated using Equation 3-1 (ACI 318-11 S21.11.9),

$$V_n = A_{cv} \left(\alpha_c \lambda \sqrt{f'_c} + \rho_t f_{yt} \right) \quad \text{Equation 3-1}$$

where V_n is the wall nominal shear strength; A_{cv} is the wall web length multiplied by the web thickness in the direction of the applied shear force; α_c is a coefficient to define the relative contribution of concrete strength to the nominal wall shear strength, calculated using $2 \leq \left(\alpha_c = 6 - 2 \frac{h_w}{l_w} \right) \leq 3$, h_w and l_w are wall height and length, respectively; f_c' is the specified concrete strength; and ρ_t and f_{yt} are the reinforcement ratio and yield strength of the web horizontal reinforcement.

According to Equation 3-1, wall nominal shear strength is proportional to concrete compressive strength, quantity and yield strength of the web horizontal reinforcement, and wall aspect ratio; however, previous studies have shown that shear strength is influenced by other factors such as axial load (Massone et al, 2009), wall vertical reinforcement (Wood, 1990), and the quantity of boundary transverse reinforcement (Wallace, 1998).

The expression used in ACI 318 (Equation 3-1) for wall shear strength is a slightly modified form of the ACI 318 beam shear strength expression (Equation 3-2):

$$\begin{aligned}
 V_n &= V_c + V_s = 2\sqrt{f_c'} b_w d + A_v f_y d / s \\
 &= b_w d \left[2\sqrt{f_c'} + (A_v / s b_w) f_y \right] \\
 &= A_{cv} \left[2\sqrt{f_c'} + \rho_t f_y \right]
 \end{aligned}
 \tag{Equation 3-2}$$

where d is taken equal to the wall length (l_w), b_w equals to the wall thickness (t_w), concrete shear strength is increased as the wall aspect ratio reduces from 2.0 to 1.5, and web horizontal reinforcement is $\rho_t = A_v / s t_w$. Equation 3-1 has not changed since it was introduced in ACI 318 in 1983, although various studies have suggested alternative expressions (Wood, 1990; Wallace, 1998). As use of performance-based design approaches, which typically include the use of

nonlinear response history analysis, become more common, more comprehensive expressions for shear strength are needed. To address this need, a wall test database was developed and used to determine the influence of various parameters on wall shear strength and deformation capacity and to recommend alternative relations for wall shear strength depending on expected wall behavior. An important aspect of this study is to determine median values and dispersions of wall shear strength associated with different wall failure modes, as well as the impact of various parameters on wall deformation capacity for the three defined categories.

3.1.2. Deformation capacity

As discussed previously, a review of prior test results using a limited database, suggests that shear strength decreases as the magnitude of nonlinear flexural deformations increase (Figure 3-1). This trend is not considered in Equation 3-1, because common design approaches are based on linear analysis and because code design approaches are typically simple. In the following sections, results of statistical studies are presented to obtain expressions for wall shear strength and deformation capacity for the three different behavioral modes identified (flexure, transition, shear), by using a detailed database including a large number of reinforced concrete shear wall experiments conducted worldwide.

The database developed includes a wide range of information to enable comprehensive studies of wall shear strength and deformation capacity, including points needed to define backbone relations. Where possible, backbone relations were developed to include the deformation value at significant (20% drop for the peak strength) lateral strength degradation and residual strength. Developing relations for both shear strength and ductility provides several advantages: (i) the potential drop in shear strength associated with increasing nonlinear flexural deformation demands can be assessed, (ii) the nonlinear deformation capacity of shear-dominant

walls can be assessed, and (iii) statistics (median, dispersion) can be assessed, which is essential for the application of performance-based design approaches. Item (ii) is particularly important, because brittle failure criteria commonly assume that reaching the failure load results in rapid strength loss and loss of axial load capacity. More economical designs, especially for rehabilitation of existing buildings, would result if even modest nonlinear deformation capacities exist for so-called brittle failure modes.

To conduct this study, walls within the database were subdivided into three categories: 1) shear-controlled walls, 2) transition walls, and 3) flexure-controlled walls. Results obtained with detailed regression analyses are presented for walls in each category to identify parameters related to shear strength and deformation capacity. Regression analysis for shear strength was repeated for different parameter sets; one with parameters that are currently used by ACI 318-11 equation (Equation 3-1), and others with additional parameters in an attempt to achieve better correlation and/or to reduce dispersion. Two sets of regression analysis results are presented for deformation capacity, which is defined as either displacement or curvature ductility in this study. The first set of results present best-fit relations for normalized deformation capacity at failure, in which as many as 10 parameters were included. The second set of results present simplified equations using fewer parameters, which might be more appropriate for design, while maintaining a high degree of confidence.

The derived equations are valuable in that they can be used by engineers to provide more reliable designs by comparing demand distributions (e.g., demands obtained using nonlinear response history analysis) with the derived capacity distributions. The overlapping area of the two distributions defines the probability of failure. Design variables with the greatest impact can then be adjusted to improve safety.

3.2. Description of the database

A total of 124 test specimens from 19 different studies conducted worldwide were included in the test database. Primary database variables include wall aspect ratio, concrete and steel strengths, reinforcement ratios, axial load ratio, and wall thickness. Detailed information on specimen geometry, concrete and steel material properties, and boundary and web reinforcement ratios are provided in Appendix B in Tables B-1 to B-3.

The following criteria (Equation 3-3) were used to bin walls into three categories: 1) shear-controlled walls; 2) transition walls; 3) flexure-controlled walls:

$$\begin{aligned} \frac{V_n}{V@M_n} \leq 1 &\Rightarrow \text{Shear-controlled walls} \\ 1 < \frac{V_n}{V@M_n} < 1.67 &\Rightarrow \text{Transition} \\ \frac{V_n}{V@M_n} \geq 1.67 &\Rightarrow \text{Flexure-controlled walls} \end{aligned} \quad \text{Equation 3-3}$$

where V_n is the shear strength calculated using Equation 3-1, and $V@M_n$ is the shear force in the wall associated with reaching the wall nominal moment capacity M_n for the given distribution of lateral forces used in the test. Table 3-2 summarizes the specimens included in the study, Table 3-3 shows the range of the parameters included in the study for each bin (failure mode), and Figure 3-4 provides the distribution of $V_n/V@M_n$ for the database. Parameter ranges for each bin are summarized using bar charts in Figures B-2 to B-6 (Appendix B).

Table 3-2. Summary of the specimens included in the study

| Author, year | # of spec | Concrete strength (f'_c) | Yield strength, transverse web reinf. ratio, (f_{yt}, ρ_t) | Yield strength, longitudinal web reinf. ratio, (f_{yl}, ρ_l) | Yield strength, transverse boundary reinf. ratio, (f_{ysh}, ρ_{sh}) | Yield strength, longitudinal boundary reinf. ratio, (f_{ybl}, ρ_{bl}) |
|------------------|-----------|---------------------------------|--|--|--|--|
| | | (MPa) | (MPa,%) | (MPa,%) | (MPa,%) | (MPa,%) |
| Adebar, 2007 | 1 | 49 | (455, 0.27) | (455, 0.27) | (455, 1.7) | (455, 0.67) |
| Ali, 1991 | 2 | 34.5 | (562, 0.17) | (562, 0.17) | (540, 1.0) | (540, 3.1) |
| Carvajal, 1983 | 5 | (20.8-28.7) | (588, 0.25) | (588, 0.25) | (0.0, 0.0) | (412-451, 0.7-1.3) |
| Corley, 1982 | 9 | (21.9-53.6) | (461-532, 0.27-1.38) | (454-532, 0.24) | (454-502, 0.0-2.2) | (410-458, 1.1-3.7) |
| Dazio, 2009 | 4 | (39.2-45) | (535-601, 0.25) | (535-714, 0.3-0.54) | (583-662, 1.2-1.6) | (620-747, 0.0-1.6) |
| Hidalgo, 2002 | 12 | (15.7-23.9) | (314-471, 0.0-0.26) | (314-471, 0.13-0.26) | (0.0, 0.0) | (0.0, 0.0) |
| Ji, 2002 | 2 | 17.7 | (452, 0.42) | (452, 0.42) | (452, 2.1-3.1) | (365, 4.7-9.4) |
| Jiang, 1999 | 2 | (24.1-24.9) | (289, 1.11) | (289, 1.11) | (289, 1.5) | (289, 2.5) |
| Kabeyasawa, 1993 | 26 | (54.6-103.4) | (369-1079, 0.18-1.48) | (369-1079, 0.18-1.48) | (369-1395, 0.9-3.3) | (360-1009, 2.4-5.3) |
| Massone, 2006 | 11 | (25.5-33.6) | (352-424, 0.26-0.31) | (352-424, 0.26-0.38) | (0.0, 0.0) | (352-448, 1.4-3.1) |
| Paulay, 1982 | 3 | (27.2-30.2) | (380, 0.67-1.68) | (300-315, 0.39-0.81) | (300, 5.4-6.8) | (300, 1.36-2.26) |
| Pilakoutas, 1995 | 6 | (32-45.8) | (400-550, 0.35-0.6) | (550, 0.31-0.47) | (0.0, 0.0) | (500-530, 2.65-2.93) |
| Salonikios, 1999 | 11 | (21.6-27.5) | (610, 0.56) | (610, 0.28) | (610, 1.1-1.9) | (585, 1.3-1.7) |
| Sittipunt, 1995 | 2 | (35.8-36.6) | (450, 0.52-0.79) | (450, 0.39-0.52) | (0.0, 0.0) | (473, 2.29) |
| Thomsen, 1995 | 3 | (31.6-43.7) | (448, 0.33-0.45) | (448, 0.33-0.45) | (434, 1.3-2.4) | (434, 2.2-5.9) |
| Tran, 2011 | 3 | (47.1-48.7) | (448-517, 0.27-0.61) | (400-448, 0.27-0.61) | (472-477, 1.6) | (472-477, 3.17-7.14) |
| Wang, 2000 | 3 | (36.8-43.1) | (305, 1.0-1.35) | (305, 0.67) | (366, 1.5-2.3) | (375-432, 4.5-12.6) |
| Zhang, 2007 | 15 | (19.7-37.7) | (392, 0.36) | (392, 0.36) | (348-392, 0.5-1.5) | (325-379, 1.2-1.9) |
| Zhou, 2004 | 4 | 37.3 | (345, 0.84) | (345, 0.84) | (300, 1.8) | (527, 3.7) |

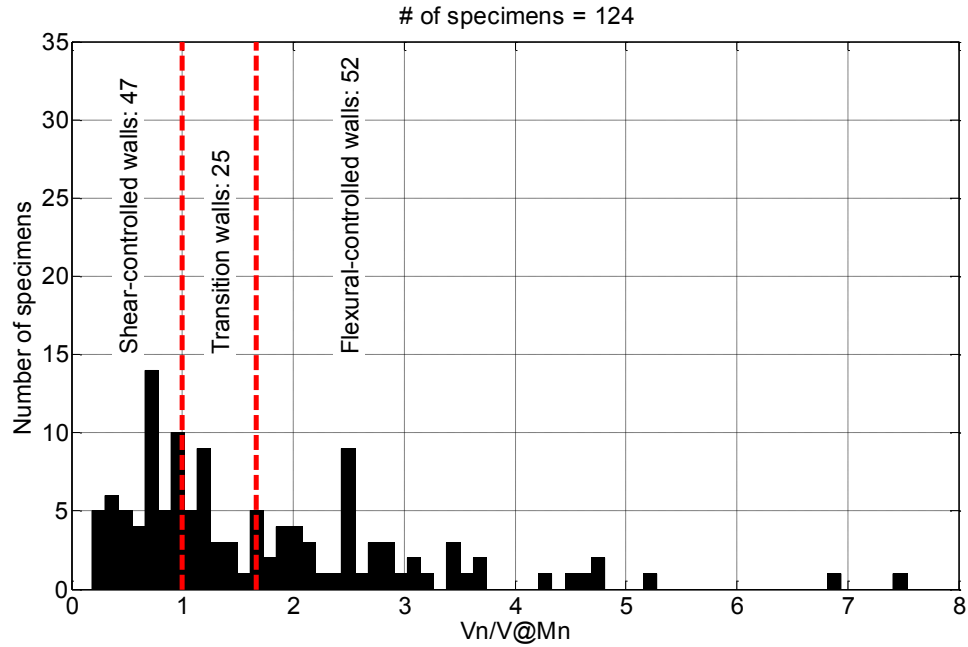


Figure 3-4. Summary of the experimental tests included in the study

Table 3-3. Range of the parameters in each of the category

| Parameter | Unit | Shear cont. | | Transition | | Flexure cont. | |
|---|------|-------------|-------|------------|-------|---------------|-------|
| | | Min | Max | Min | Max | Min | Max |
| Height, H_w | mm | 1000 | 4570 | 1200 | 4570 | 1200 | 11700 |
| Length, L_w | mm | 600 | 2700 | 700 | 1910 | 500 | 3000 |
| Thickness, t_w | mm | 60 | 152 | 60 | 152.4 | 75 | 152 |
| Shear span ratio, M/Vl_w | - | 0.44 | 2.5 | 0.35 | 3.0 | 0.44 | 7.2 |
| Axial load ratio, $P/A_g f'_c$ | - | 0 | 0.4 | 0 | 0.25 | 0 | 0.13 |
| Concrete strength, f'_c | MPa | 19.7 | 103.4 | 17.1 | 87.6 | 15.7 | 79.4 |
| Yield strength of transverse boundary reinf., f_{ysh} | MPa | 305 | 1079 | 305 | 1001 | 289 | 848 |
| Transverse boundary reinforcement ratio, ρ_{sh} | % | 0.18 | 1.29 | 0.00 | 1.72 | 0.13 | 1.68 |
| Yield strength of longitudinal boundary reinf., f_{ybl} | MPa | 305 | 1079 | 305 | 1001 | 289 | 848 |
| Longitudinal boundary reinforcement ratio, ρ_{bl} | % | 0.18 | 1.29 | 0.24 | 1.48 | 0.13 | 1.18 |

| Parameter | Unit | Shear cont. | | Transition | | Flexure cont. | |
|---|------|-------------|------|------------|-------|---------------|-------|
| | | Min | Max | Min | Max | Min | Max |
| Longitudinal web reinforcement ratio, ρ_l | % | 0 | 2.83 | 0.00 | 3.14 | 0 | 6.79 |
| Yield strength of transverse web reinf., f_{yt} | MPa | 325 | 1009 | 0 | 776 | 0 | 747.4 |
| Transverse web reinforcement ratio, ρ_t | % | 1.21 | 5.31 | 0.00 | 12.57 | 0 | 5.86 |
| Spacing/boundary bar diameter ratio, s/d_b | - | 0 | 10 | 0 | 8 | 0 | 14 |

3.3. Definition of failure

Figure 3-5 shows a typical cyclic force-deformation response of a concrete shear wall. Test results are shown with a broken line, with a moderate number of cycles in the inelastic range, followed by rapid strength loss, modest residual strength for a few more cycles, and then loss of axial load capacity. A tri-linear backbone curve is fit to the cyclic load - displacement relations, where yield displacement was defined based on “Equivalent Elasto-plastic Energy Absorption” method (Park, 1988), and deformation limit strength loss (Δ_1) was determined as the point where shear strength is reduced to 80% of the peak shear force (V_u). The slope of the descending branch is estimated to reasonably fit the test results. Details of backbone curves for each specimen are provided in Table B-4 (Appendix B).

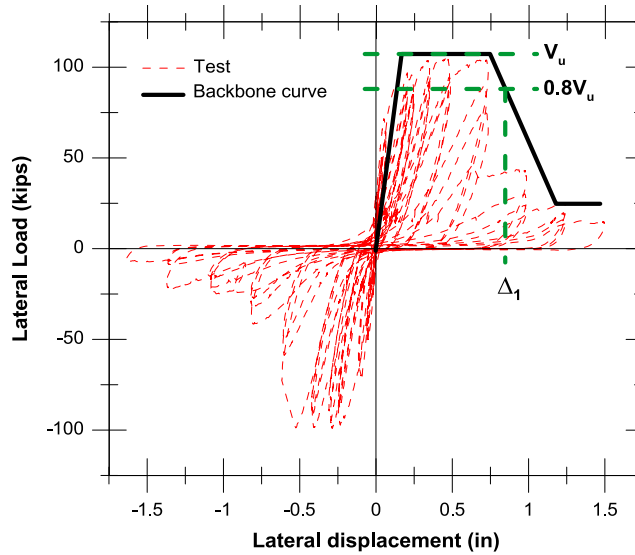


Figure 3-5. Force-deformation response of a reinforced concrete shear wall [Massone, 2006]

To represent the failure deformation limit (Δ_1) with a more convenient and generic term, “displacement ductility” was obtained for each backbone curve by normalizing the lateral displacements by the yield displacement. Figure 3-6, Figure 3-7, and Figure 3-8 show the normalized force-deformation backbone curves for the walls in the shear-controlled, transition and flexure-controlled bins, respectively. The vertical axis is the shear force normalized by the nominal shear strength calculated using Equation 3-1, whereas the horizontal axis represents normalized deformation, taken as displacement ductility in this case. Displacement ductility (μ_δ) is an indicator of member deformation capacity for test specimens that yield in flexure (i.e., walls in flexure-controlled and transition regions). However, displacement ductility is not a convenient indicator to use for computer modeling of structural walls within buildings, since the wall will likely span multiple levels (stories). To address this issue, the defined failure deformation limit (Δ_1) was related to local deformation capacity (“curvature ductility”, μ_ϕ) using Equation 3-4 and Equation 3-5 for single (cantilever) and double curvature (fixed-fixed) tests, respectively.

$$\phi_y = 3 \frac{\delta_y}{h_w^2}, \phi_u = 2 \frac{\delta_u}{h_w l_w} \text{ and } \mu_\phi = \frac{\phi_u}{\phi_y} \quad (\text{cantilever}) \quad \text{Equation 3-4}$$

$$\phi_y = 6 \frac{\delta_y}{h_w^2}, \phi_u = 2 \frac{\delta_u}{h_w l_w} \text{ and } \mu_\phi = \frac{\phi_u}{\phi_y} \quad (\text{fixed-fixed}) \quad \text{Equation 3-5}$$

where ϕ_y is yield curvature, ϕ_u is inelastic curvature, δ_y is yield displacement, δ_u is inelastic displacement, h_w is height of the wall, l_w is length of the wall. The yield curvature, ϕ_y , was derived using elastic beam theory (as shown in Equations 3-6 and 3-7 for cantilever and fixed-fixed walls, respectively), whereas the inelastic curvature (ϕ_u) was estimated assuming inelastic deformations occurred at member end(s) over a plastic hinge length of $0.5l_w$. Normalized force-deformation backbone relations are given in Figure 3-9, Figure 3-10, and Figure 3-11 for the walls in the shear-controlled, transition, and flexure-controlled bins, respectively.

$$\delta_y = \frac{Ph_w^3}{3EI} = \frac{M_y}{h_w} \frac{h_w^3}{3EI} = \frac{h_w^2}{3} \left[\frac{M_y}{EI} \right] = \frac{h_w^2}{3} \phi_y \quad (\text{cantilever}) \quad \text{Equation 3-6}$$

$$\delta_y = \frac{Ph_w^3}{12EI} = \frac{2M_y}{h_w} \frac{h_w^3}{12EI} = \frac{h_w^2}{6} \left[\frac{M_y}{EI} \right] = \frac{h_w^2}{6} \phi_y \quad (\text{fixed-fixed}) \quad \text{Equation 3-7}$$

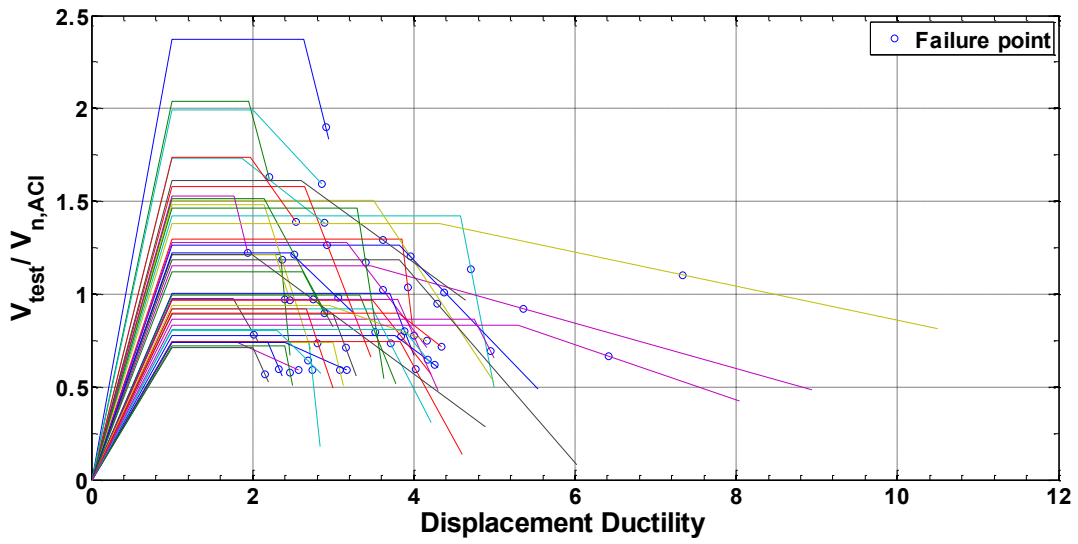


Figure 3-6. Normalized force-deformation response of the shear-controlled walls (47 specimens) – displacement ductility

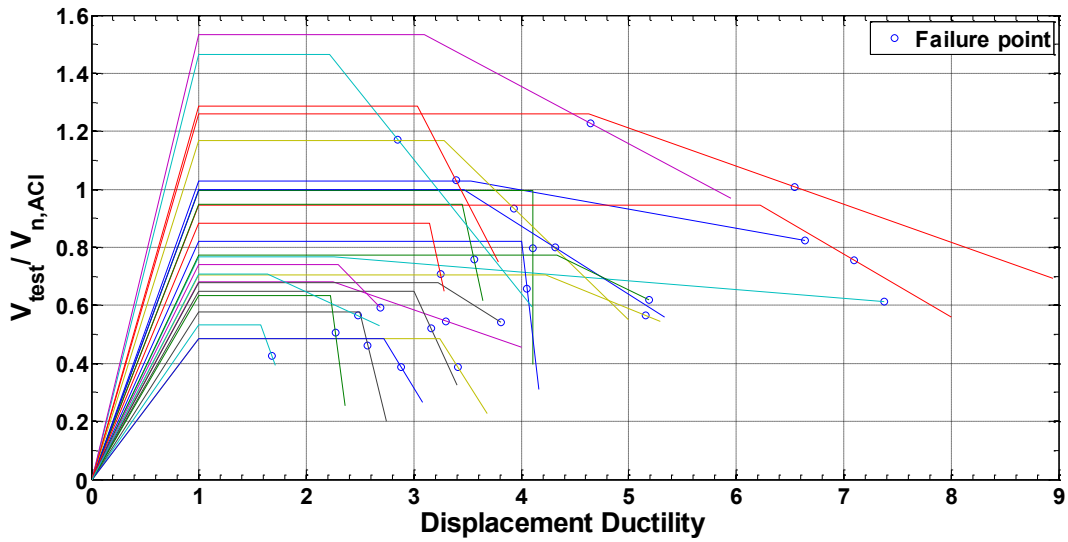


Figure 3-7. Normalized force-deformation response of the transition walls (25 specimens) – displacement ductility

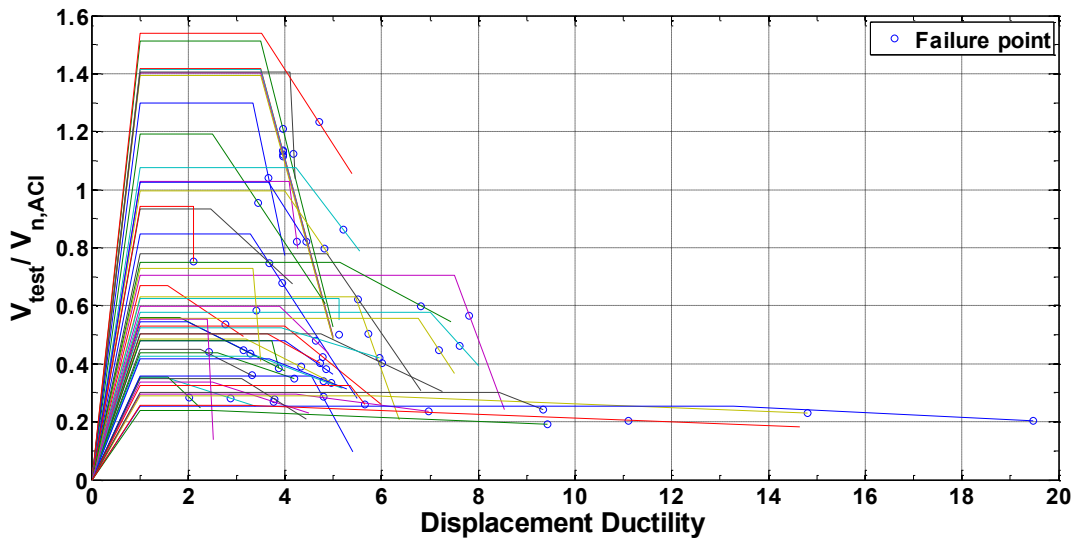


Figure 3-8. Normalized force-deformation response of the flexure-controlled walls (52 specimens) – displacement ductility

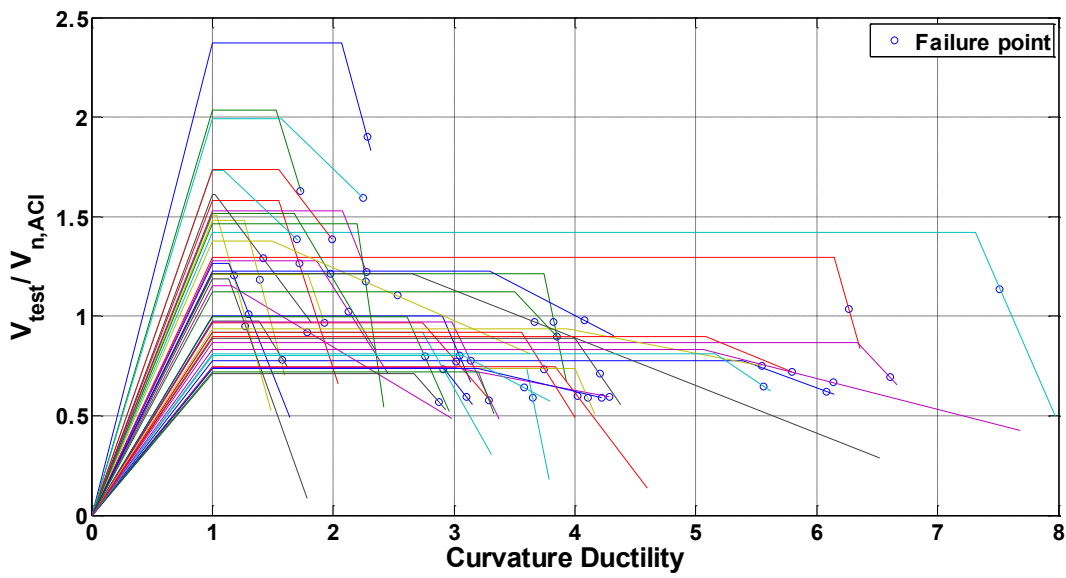


Figure 3-9. Normalized force-deformation response of the shear-controlled walls (47 specimens) – curvature ductility

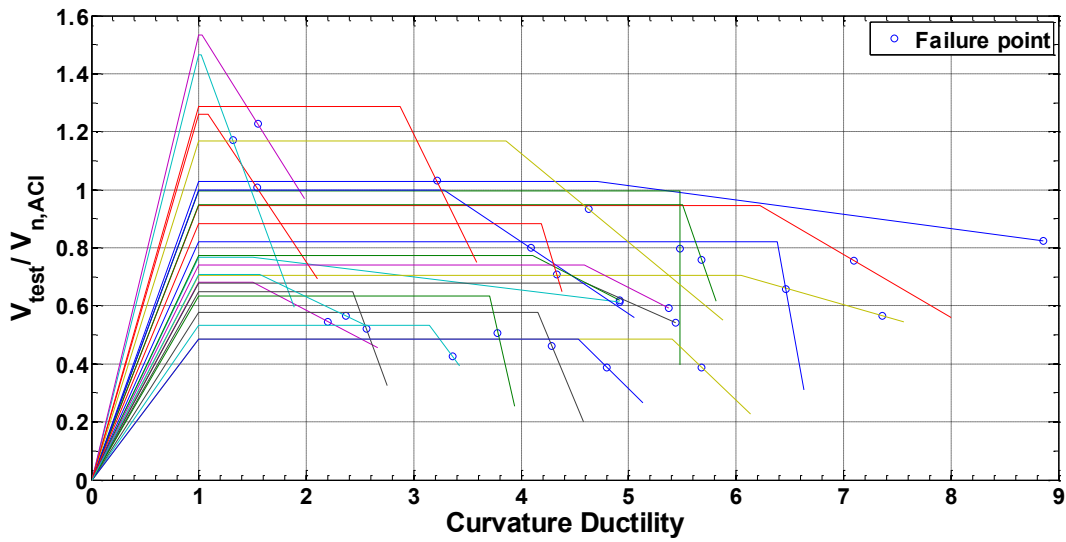


Figure 3-10. Normalized force-deformation response of the transition walls (25 specimens) – curvature ductility

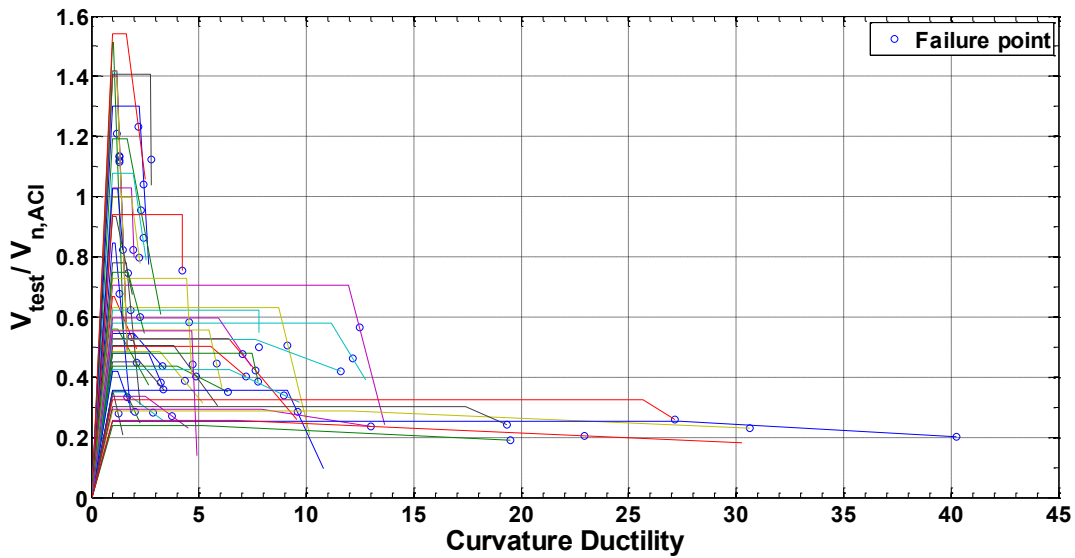


Figure 3-11. Normalized force-deformation response of the flexure-controlled walls (52 specimens) – curvature ductility

Statistical studies were conducted to formulate the normalized deformation capacity (i.e., curvature ductility at failure, $\mu_{\phi 1}$) in terms of key parameters (such as concrete strength,

longitudinal web reinforcement ratio, shear span ratio, axial load ratio) for wall specimens in each bin. It is noted that curvature ductility does not have a physical meaning for the shear-controlled walls because walls in this region are not expected to yield in flexural (i.e., nonlinear curvature is not expected); therefore, normalized deformation capacity equations are presented for both displacement ductility ($\mu_{\delta 1}$) and curvature ductility ($\mu_{\phi 1}$) for shear-controlled walls.

3.4. Statistical Analyses

Detailed regression analyses were carried out to derive equations for shear strength and normalized deformation capacity in terms of key parameters for specimens in each bin. Results are presented in terms of correlation coefficient ρ , representing the degree of which a linear relationship exists between two variables (ranges from 0 to 1). For example, in the regression analysis for shear strength, $\rho = 0$ indicates that a parameter is not correlated with shear strength, whereas $\rho = 1$ represents perfect correlation between the associated parameter and shear strength. The square of the correlation coefficient, R^2 , is also known as the coefficient of determination. For example, if ρ is 0.75 between shear span ratio and the shear strength, R^2 equals 0.56, indicating that 56% of the uncertainty in the shear strength is associated with shear span ratio while the remaining 44% of variability is associated with other parameters.

Details of the regression analyses and proposed equations for shear strength and normalized deformation capacity are discussed in the following subsections.

3.4.1. Regression analyses for shear strength

Table 3-4 shows the mean and standard deviation (shown in brackets) of the shear stress values calculated as $v_{n,ACI} = V_{n,ACI} / A_{cv}$, where $V_{n,ACI}$ is the shear strength defined by Equation 3-1, as well as the peak shear stress values extracted from test data (v_{test}). Both values were

normalized by concrete strength $\sqrt{f'_c}$ and presented separately for each bin. The average nominal shear stress ($v_{n,ACI}$) is about $7\sqrt{f'_c}$ for all three bins, while the measured peak shear stress (v_{test}) varies from $8.3\sqrt{f'_c}$ to $4.5\sqrt{f'_c}$ for shear-controlled and flexure-controlled walls, respectively. Results presented in Table 3-4 indicate that the ACI 318-11 (Equation 3-1) underestimates the shear strength by 20% for the shear-controlled walls, whereas the peak shear stress for flexure-controlled walls was only 70% of the ACI 318-11 nominal shear strength.

As indicated previously, the ACI 318-11 shear strength equation (Equation 3-1) does not account for the decrease in shear strength as the nonlinear flexural deformation increases (as presented in Figure 3-1 and Table 3-4). To address these deficiencies, alternative equations are proposed for each bin.

Table 3-4. Comparisons of nominal and measured normalized shear stress values

| | Shear-controlled (47 specimens) | Transition (25 specimens) | Flexure-controlled (52 specimens) |
|---------------------------|--|--------------------------------------|--|
| $v_{n,ACI} / \sqrt{f'_c}$ | 7.1 (2.7) | 7.7 (3.0) | 7.0 (3.5) |
| $v_{test} / \sqrt{f'_c}$ | 8.3 (3.8) | 6.3 (2.4) | 4.5 (2.3) |
| $v_{test} / v_{n,ACI}$ | 1.2 (0.4) | 0.9 (0.3) | 0.7 (0.4) |

Linear regression analyses were conducted to derive best-fit empirical equations for shear strength in each bin.

Table 3-5 summarizes the correlation coefficients of shear strength with respect to the parameters included, for example, it was noted that the shear strength is highly correlated to concrete strength ($\sqrt{f'_c}$), but not to the axial load ratio ($P/A_g f'_c$). Some parameters, such as boundary transverse reinforcement ratio (ρ_{sh}), are highly correlated to shear strength for shear-

controlled walls; however, they are not well-correlated with shear strength for transition and flexure-controlled walls.

Table 3-5. Correlation coefficients of key parameters with respect to the shear strength

| Parameter | Shear-cont. (47 specimens) | Transition (25 specimens) | Flexure-cont. (52 specimens) |
|---|-------------------------------|------------------------------|---------------------------------|
| Height, H_w | 0.18 | 0.22 | 0.23 |
| Length, L_w | 0.66 | 0.57 | 0.31 |
| Thickness, t_w | 0.51 | 0.07 | 0.03 |
| Shear span ratio, M/Vl_w | 0.27 | 0.05 | 0.40 |
| Axial load ratio, $P/A_g f'_c$ | 0.09 | 0.21 | 0.07 |
| Concrete strength, $\sqrt{f'_c}$ | 0.89 | 0.87 | 0.43 |
| Yield strength of transverse boundary reinf., f_{ysh} | 0.85 | 0.76 | 0.11 |
| Transverse boundary reinforcement ratio, ρ_{sh} | 0.75 | 0.18 | 0.21 |
| Yield strength of longitudinal boundary reinf., f_{ybl} | 0.88 | 0.23 | 0.16 |
| Longitudinal boundary reinforcement ratio, ρ_{bl} | 0.66 | 0.09 | 0.08 |
| Yield strength of longitudinal web reinf., f_{yl} | 0.88 | 0.52 | 0.03 |
| Longitudinal web reinforcement ratio, ρ_l | 0.53 | 0.59 | 0.46 |
| Yield strength of transverse web reinf., f_{yt} | 0.90 | 0.51 | 0.08 |
| Transverse web reinforcement ratio, ρ_t | 0.45 | 0.55 | 0.52 |
| Spacing/boundary bar diameter ratio, s/d_b | 0.17 | 0.36 | 0.15 |

Table 3-6 summarizes two equations derived for shear strength using linear regression analyses for each bin: The first equation (“With ACI 318-11 parameters”) represents an alternative to the equation provided in ACI 318-11 (Equation 3-1), using the same parameters

that are used in Equation 3-1. These parameters are concrete strength ($\sqrt{f'_c}$), and reinforcing ratio times yield strength of the transverse steel in the web ($\rho_t f_{yt}$). The second equation (“Best fitted equation”), on the other hand, shows an alternative equation which contains two more parameters to achieve a higher level of correlation. Figure 3-12 to Figure 3-17 show data dispersion relative to the best-fit relations and correlation between the fitted and measured peak shear stress values for each equation in each bin.

Table 3-6. Summary of the shear strength equations and the corresponding correlation coefficients and standard deviation with respect to the original data

| | | Shear Strength (MPa) | Number of parameters | Corr. coeff., ρ | Standard deviation, σ_Y |
|--|----------------------------|--|----------------------|----------------------|--------------------------------|
| Shear-controlled walls (47 specimens) | With ACI 318-11 parameters | $v_n = -7.1 + 1.5\sqrt{f'_c} + 0.0057\rho_t f_{yt}$ | 3 | 0.93 | 1.21 |
| | Best fitted equation | $v_n = -4.0 + 1.1\sqrt{f'_c} + 0.005\rho_t f_{yt} + 1.1\rho_{sh} - 0.26\frac{s}{d_b}$ | 5 | 0.96 | 0.95 |
| Transition walls (25 specimens) | With ACI 318-11 parameters | $v_n = -3.1 + 0.9\sqrt{f'_c} + 0.0034\rho_t f_{yt}$ | 3 | 0.90 | 0.89 |
| | Best fitted equation | $v_n = -4.4 + 0.78\sqrt{f'_c} + 0.0022\rho_t f_{yt} + 0.0021L_w + 10.1\frac{P}{A_g f'_c} - 0.78\frac{M}{VL_w}$ | 6 | 0.97 | 0.49 |
| Flexure-controlled walls (52 specimens) | With ACI 318-11 parameters | $v_n = 0.57 + 0.12\sqrt{f'_c} + 0.004\rho_t f_{yt}$ | 3 | 0.68 | 0.94 |
| | Best fitted equation | $v_n = -0.17 + 0.49\sqrt{f'_c} + 0.0033\rho_t f_{yt} - 0.52\frac{M}{VL_w} - 0.069\frac{s}{d_b}$ | 5 | 0.87 | 0.64 |

Note: f'_c and f_{yt} in MPa, ρ_t and ρ_{sh} in %, L_w in mm, other terms are dimensionless.

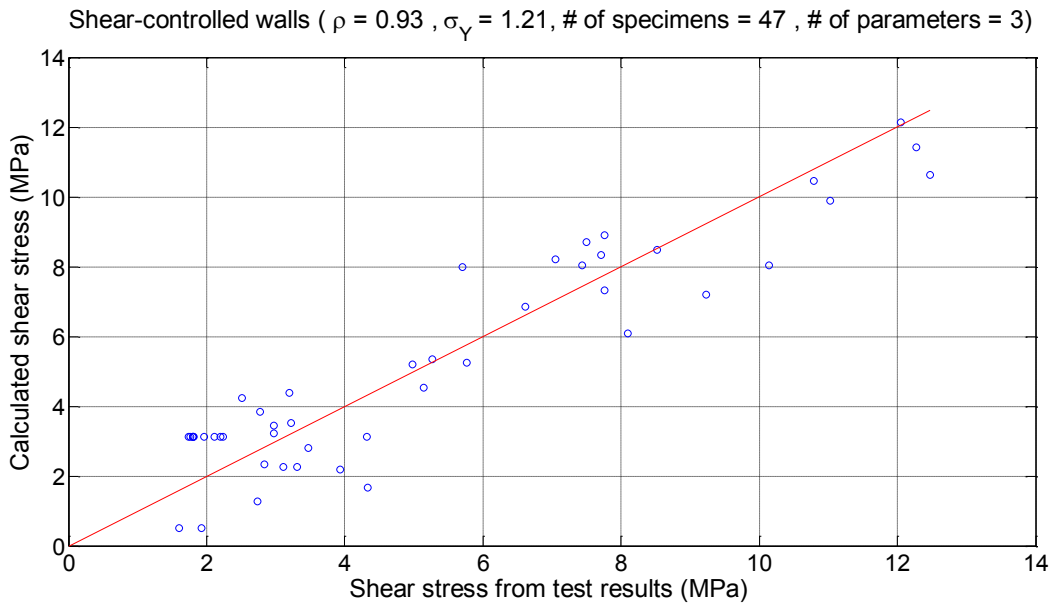


Figure 3-12. Correlation between the fitted (with ACI 318-11 parameters) and measured shear stress for the shear-controlled walls

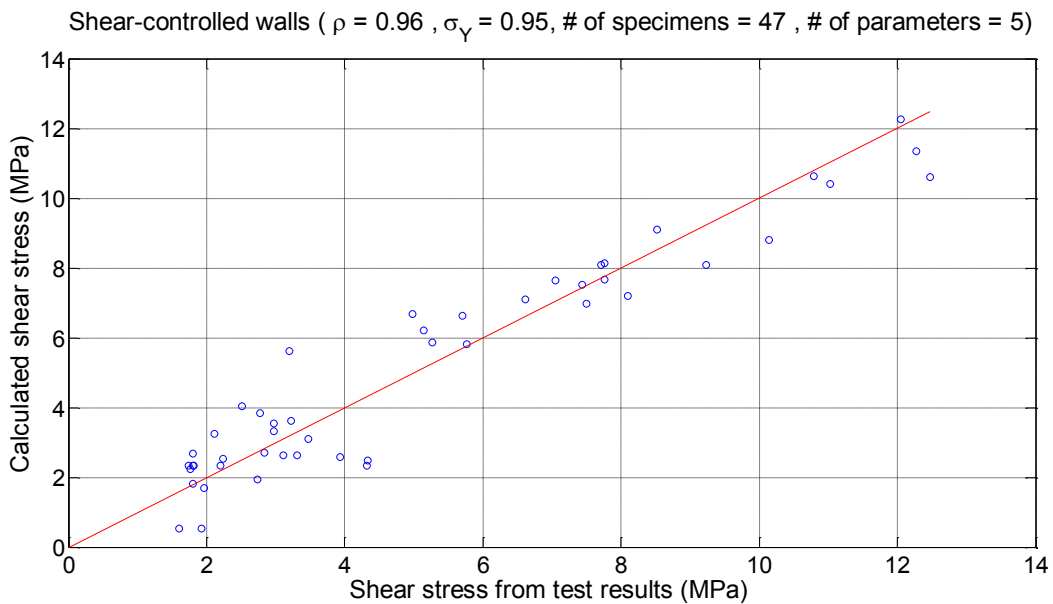


Figure 3-13. Correlation between the best fitted and measured shear stress for the shear-controlled walls

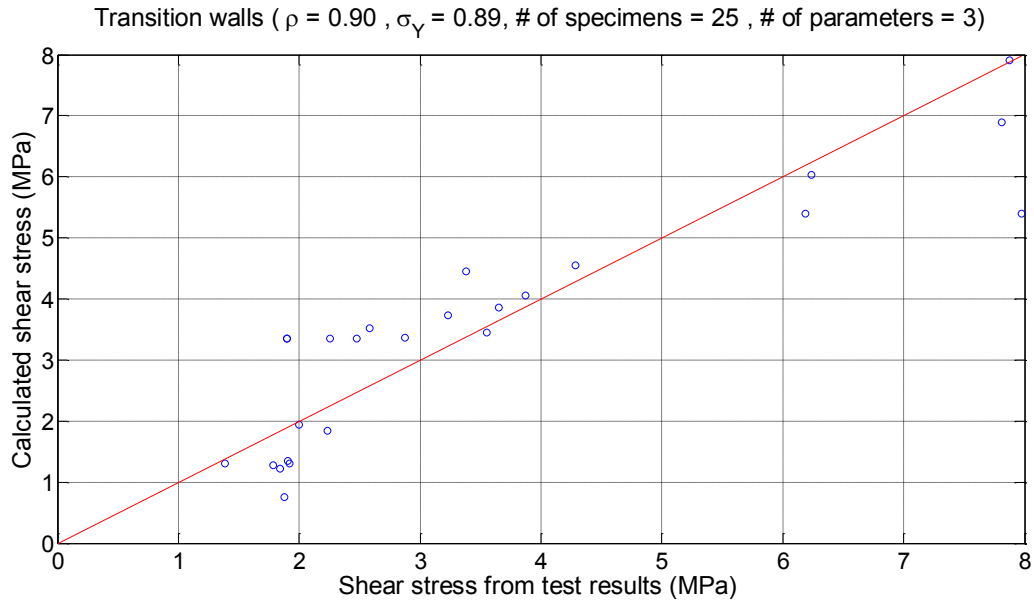


Figure 3-14. Correlation between the fitted (with ACI 318-11 parameters) and measured shear stress for the transition walls

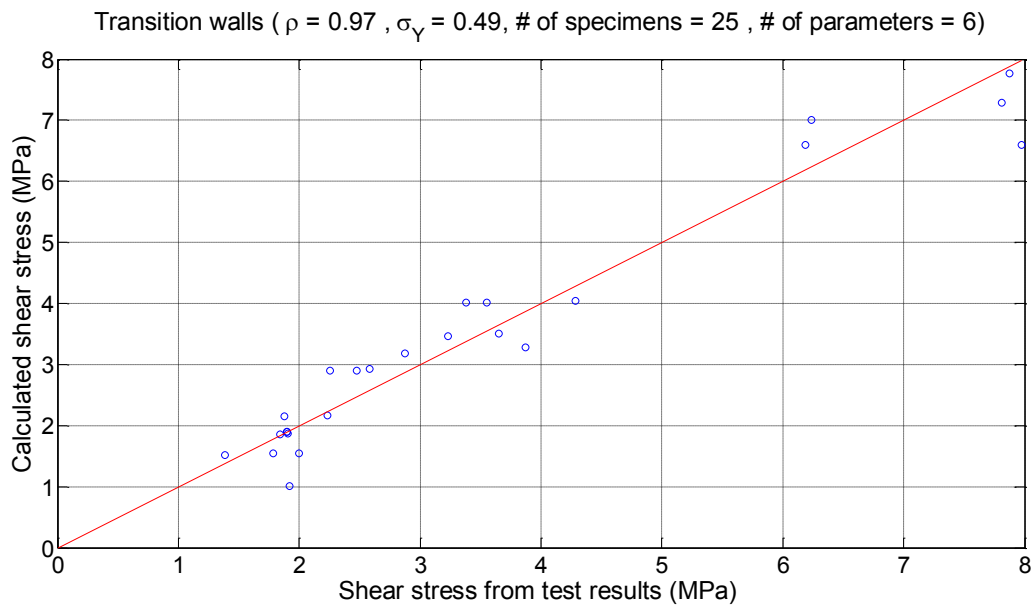


Figure 3-15. Correlation between the best fitted and measured shear stress for the transition walls

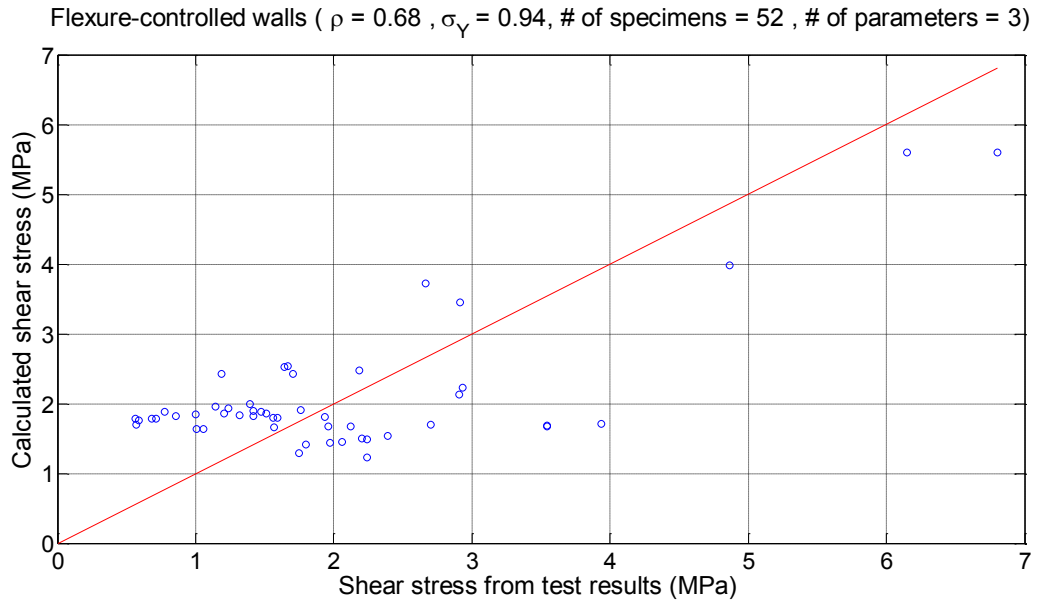


Figure 3-16. Correlation between the fitted (with ACI 318-11 parameters) and measured shear stress for the flexure-controlled walls

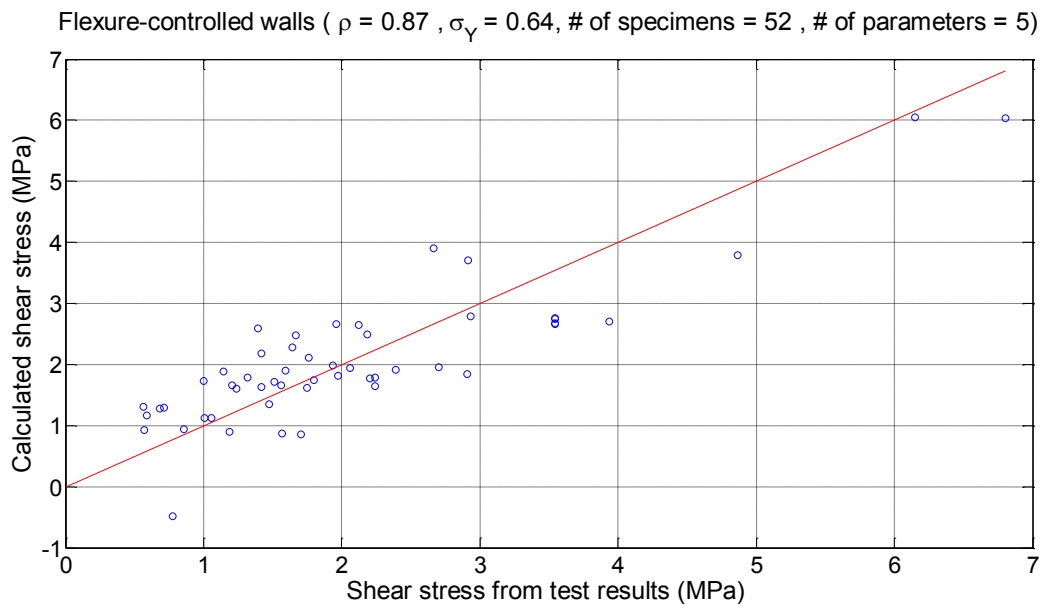


Figure 3-17. Correlation between the best fitted and measured shear stress for the flexure-controlled walls

Mean values and standard deviations (shown in brackets) for the ratio of measured to estimated peak shear stress values are summarized and compared in Table 3-7. The mean values for each bin provide a very good estimate of the measured shear stress (v_{test}), with correlation coefficients of 0.96, 0.97, and 0.87, for shear, transition, and flexure, respectively. Compared to Equation 3-1, the best fitted equation estimates the shear strength to be 18% lower in the shear-controlled region, 13% higher in the transition region, and 23% higher in the flexure-controlled region. Shear strength equations are presented here for the transition and flexure-controlled bins for completeness, it is noted that deformation capacity is of more interest for these bins since flexural yielding is supposed to occur prior to reaching the ACI 318-11 shear strength. Defining a relationship between shear strength and curvature ductility is not addressed here, but is considered as future work.

Table 3-7. Comparisons of alternative equations of shear strength

| | Shear-controlled (47 specimens) | Transition (25 specimens) | Flexure-controlled (52 specimens) |
|---|--|--------------------------------------|--|
| $v_{test} / v_{n,ACI}$ | 1.17 (0.4) | 0.87 (0.3) | 0.70 (0.4) |
| $v_{test} / v_{n,ACI \text{ parameters}}$ | 1.24 (0.9) | 1.07 (0.4) | 1.02 (0.5) |
| $v_{test} / v_{n,best \text{ fitted}}$ | 0.99 (0.4) | 1.00 (0.2) | 0.93 (0.5) |

Statistical results presented in Table 3-6 and Table 3-7 suggest that shear strength of the shear-controlled walls can be better estimated including two more parameters, namely, transverse boundary reinforcement ratio (ρ_{sh}) and spacing to boundary bar diameter ratio (s/d_b). Transverse boundary reinforcement ratio improves the wall shear strength (as discussed by Wallace, 1998), whereas spacing to boundary bar diameter ratio has a negative impact on shear strength, possible because dowel action is reduced for larger values of s/d_b .

3.4.2. Regression analysis for the normalized deformation capacity

Detailed regression analyses were carried out to obtain equations for the normalized deformation capacity (μ_{ϕ_1}) in terms of key specimen parameters. Table 3-8 summarizes correlation coefficients for normalized deformation capacity with respect to the parameters included. The normalized deformation capacity is highly correlated to shear span ratio (M/Vl_w), but not to hoop spacing divided by boundary bar diameter ratio (s/d_b). Some parameters, such as axial load ratio, are highly correlated to normalized deformation limit for flexure-controlled walls; however, the same parameter is not highly correlated to normalized deformation limit for shear-controlled walls. Potential reasons for these trends are discussed later.

Table 3-8. Correlation coefficients of key parameters to the normalized deformation capacity (μ_{ϕ_1})

| Parameter | Shear-cont. (47 specimens) | Transition (25 specimens) | Flexure-cont. (52 specimens) |
|---|-------------------------------|------------------------------|---------------------------------|
| Height, H_w | 0.19 | 0.34 | 0.34 |
| Length, L_w | 0.41 | 0.20 | 0.40 |
| Thickness, t_w | 0.06 | 0.44 | 0.21 |
| Shear span ratio, M/Vl_w | 0.59 | 0.52 | 0.75 |
| Axial load ratio, $P/A_g f'_c$ | 0.01 | 0.18 | 0.63 |
| Concrete strength, $\sqrt{f'_c}$ | 0.39 | 0.30 | 0.15 |
| Yield strength of transverse boundary reinf., f_{ysh} | 0.50 | 0.16 | 0.10 |
| Transverse boundary reinforcement ratio, ρ_{sh} | 0.25 | 0.42 | 0.16 |
| Yield strength of longitudinal boundary reinf., f_{ybl} | 0.49 | 0.48 | 0.20 |
| Longitudinal boundary reinforcement ratio, ρ_{bl} | 0.11 | 0.40 | 0.02 |
| Yield strength of longitudinal web reinf., f_{yl} | 0.47 | 0.18 | 0.24 |

| Parameter | Shear-cont. (47 specimens) | Transition (25 specimens) | Flexure-cont. (52 specimens) |
|---|---------------------------------------|--------------------------------------|---|
| Longitudinal web reinforcement ratio, ρ_l | 0.21 | 0.02 | 0.08 |
| Yield strength of transverse web reinf., f_{yt} | 0.51 | 0.06 | 0.23 |
| Transverse web reinforcement ratio, ρ_t | 0.10 | 0.20 | 0.11 |
| Spacing/boundary bar diameter ratio, s/d_b | 0.01 | 0.31 | 0.02 |

Linear regression analyses were conducted to derive best fitted empirical equations for normalized deformation capacity (μ_{ϕ_1}) for each bin; Figure 3-9 summarizes the two equations derived for each bin. The first equation (“Best fitted equation”) uses as many parameters as needed to achieve a correlation coefficient as high as possible, while the second equation (“Simplified equation”) uses as few parameters as possible to achieve nearly the same correlation. Figure 3-18 to Figure 3-23 show data dispersion relative to the best-fit relations and correlation between the fitted and derived deformation capacities for each equation in each bin.

Mean values and standard deviations (shown in brackets) for the normalized deformation capacities obtained using the best fitted and simplified equations are summarized in

Table 3-10. Results are very similar for the two equations; average curvature ductility at failure was obtained as about 3.2 for shear-controlled walls, 4.4 for transition walls, and 7.0 for flexure-controlled walls, respectively.

Table 3-9. Summary of the normalized deformation capacity equations and the corresponding correlation coefficients and standard deviation with respect to the original data

| | | (Curvature ductility) | Number of parameters | Corr. coef., ρ | Standard deviation, σ_Y |
|--|-------------|---|----------------------|---------------------|--------------------------------|
| Shear-controlled walls (47 specimens) | Best fitted | $\mu_{\phi 1} = 1.0 - 1.1 \frac{P}{A_g f'_c} + 0.2 \sqrt{f'_c} + 3.5 \rho_t - 4.1 \rho_l + 1.1 \rho_{sh}$ $+ 0.2 \rho_{bl} + 1.2 \frac{M}{VL_w} + 0.07 \frac{s}{d_b} - 0.006 t_w - 0.0041 f_{ysh}$ | 10 | 0.90 | 0.69 |
| | Simplified | $\mu_{\phi 1} = -0.54 + 1.6 \frac{M}{VL_w} + 0.35 f'_c - 0.0045 f_{ysh}$ $+ 1.3 \rho_{sh} - 0.79 \rho_l$ | 5 | 0.87 | 0.80 |
| Transition walls (25 specimens) | Best fitted | $\mu_{\phi 1} = -1.5 - 0.6 \frac{P}{A_g f'_c} + 0.62 \sqrt{f'_c} - 0.006 f_{yl} + 1.5 \rho_t - 3.2 \rho_l$ $+ 1.0 \rho_{sh} - 0.18 \rho_{bl} + 1.1 \frac{M}{VL_w} - 0.024 \frac{s}{d_b} + 0.031 t_w$ | 10 | 0.89 | 0.87 |
| | Simplified | $\mu_{\phi 1} = -3.0 + 0.27 \sqrt{f'_c} - 0.0032 f_{yl} + 0.72 \rho_{sh} + 1.1 \frac{M}{VL_w}$ $+ 0.043 t_w$ | 5 | 0.84 | 1.01 |
| Flexure-contr. walls (52 specimens) | Best fitted | $\mu_{\phi 1} = 3.0 + 71 \frac{P}{A_g f'_c} - 0.17 f'_c + 0.0082 f_{ybl} + 9.0 \rho_t$ $+ 4.4 \rho_l + 0.26 \rho_{sh} - 1.1 \rho_{bl} + 4.8 \frac{M}{VL_w} - 1.1 \frac{s}{d_b} + 0.015 t_w$ | 10 | 0.87 | 4.01 |
| | Simplified | $\mu_{\phi 1} = 2.9 + 69 \frac{P}{A_g f'_c} - 0.12 f'_c + 4.6 \frac{M}{VL_w} - 0.84 \frac{s}{d_b}$ | 4 | 0.84 | 4.37 |

Note: $f'_c, f_{ysh}, f_{ybl}, f_{yl}, f_{yt}$ in MPa, $\rho_t, \rho_l, \rho_{bl}, \rho_{sh}$ in %, L_w, H_w, t_w in mm, other terms are dimensionless.

Table 3-10. Average normalized deformation capacities ($\mu_{\phi 1}$)

| | Shear-controlled (47 specimens) | Transition (25 specimens) | Flexure-controlled (52 specimens) |
|----------------------|------------------------------------|------------------------------|--------------------------------------|
| Best fitted equation | 3.22 (1.45) | 4.39 (1.69) | 7.00 (7.16) |
| Simplified equation | 3.25 (1.41) | 4.45 (1.62) | 6.91 (6.92) |

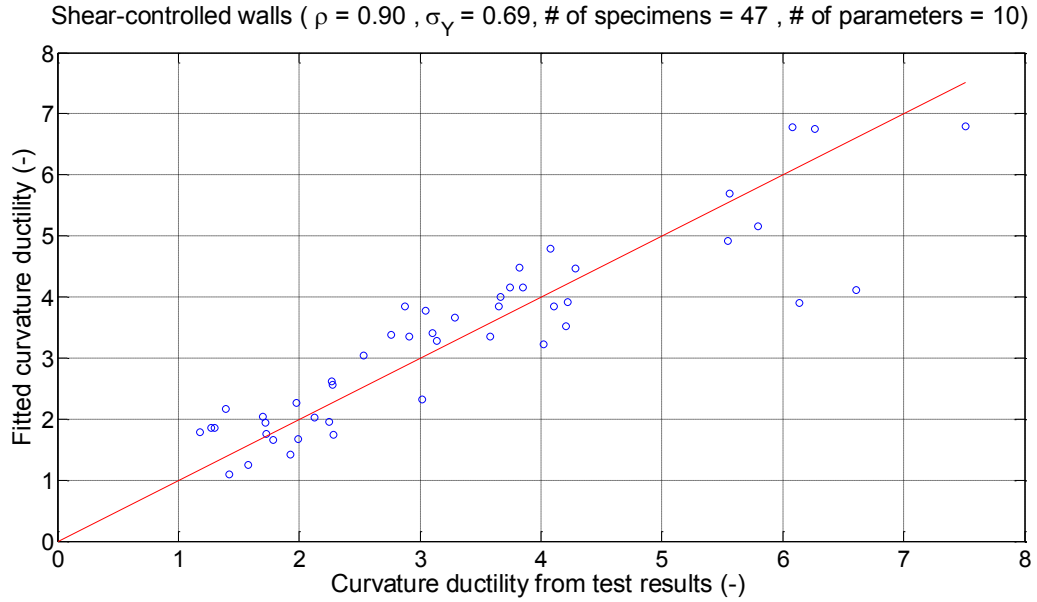


Figure 3-18. Correlation between the best fitted and calculated $\mu_{\phi 1}$ for the shear-controlled walls

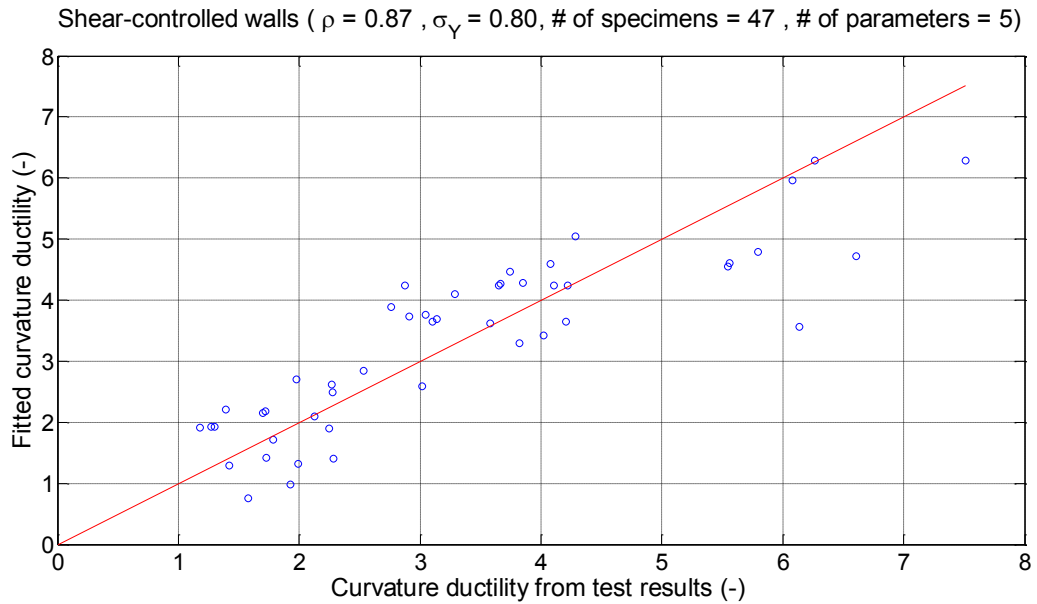


Figure 3-19. Correlation between the simplified and calculated $\mu_{\phi 1}$ for the shear-controlled walls

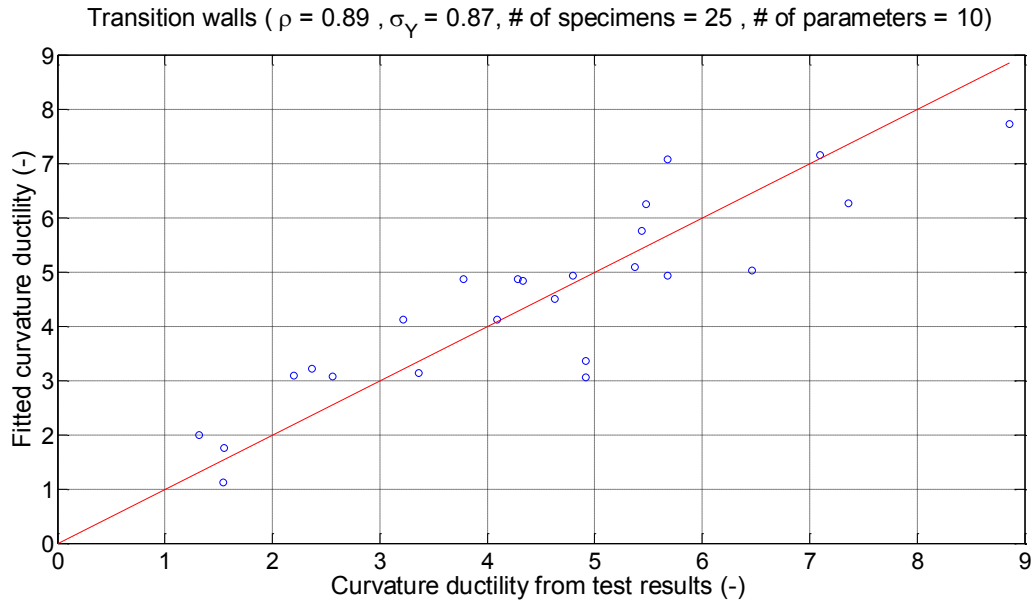


Figure 3-20. Correlation between the best fitted and calculated $\mu_{\phi 1}$ for the transition walls

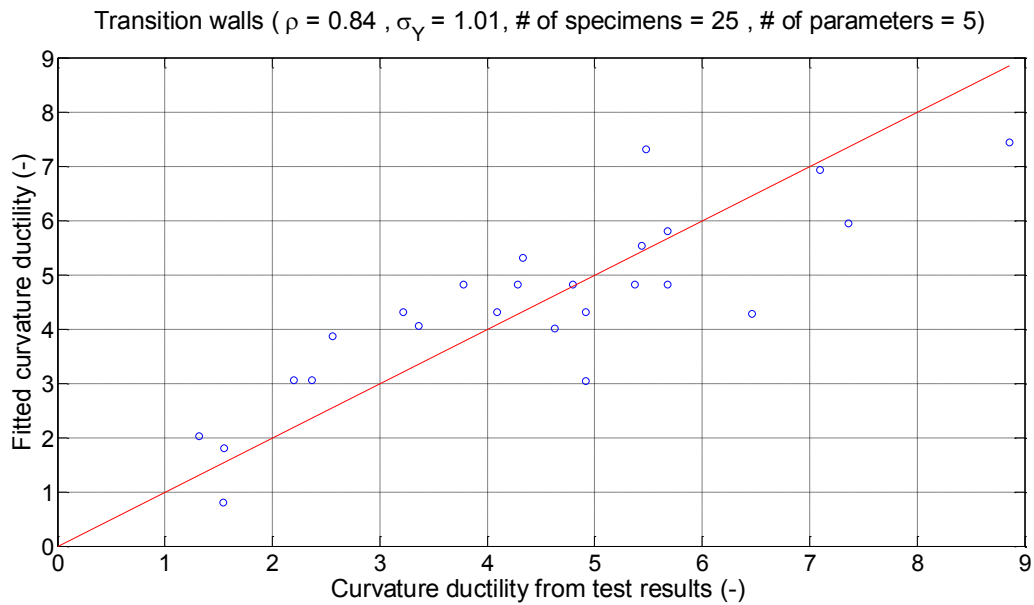


Figure 3-21. Correlation between the simplified and calculated $\mu_{\phi 1}$ for the transition walls

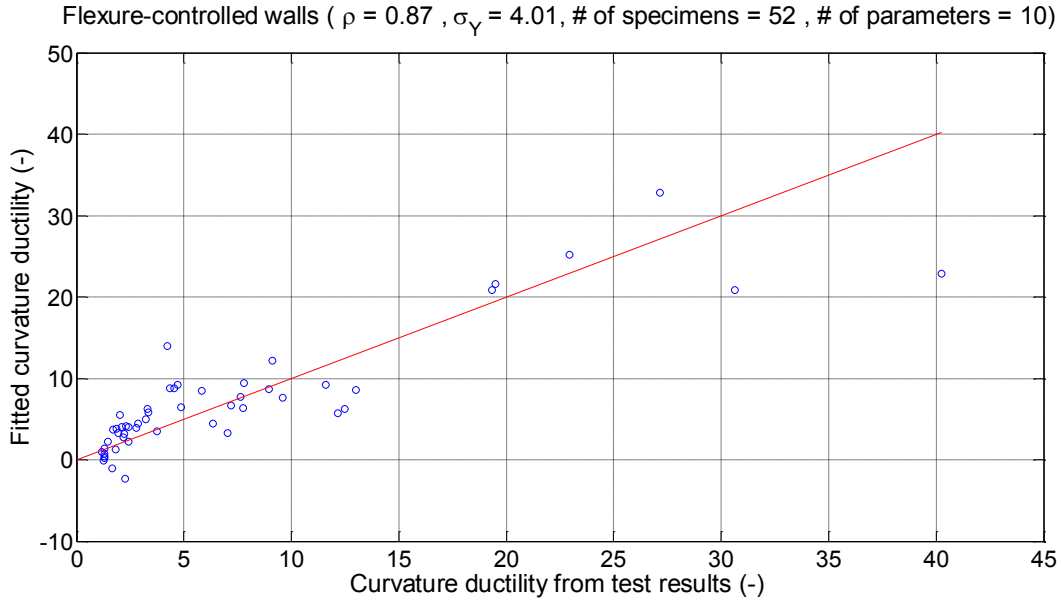


Figure 3-22. Correlation between the best fitted and calculated μ_{ϕ_1} for the flexure-controlled walls

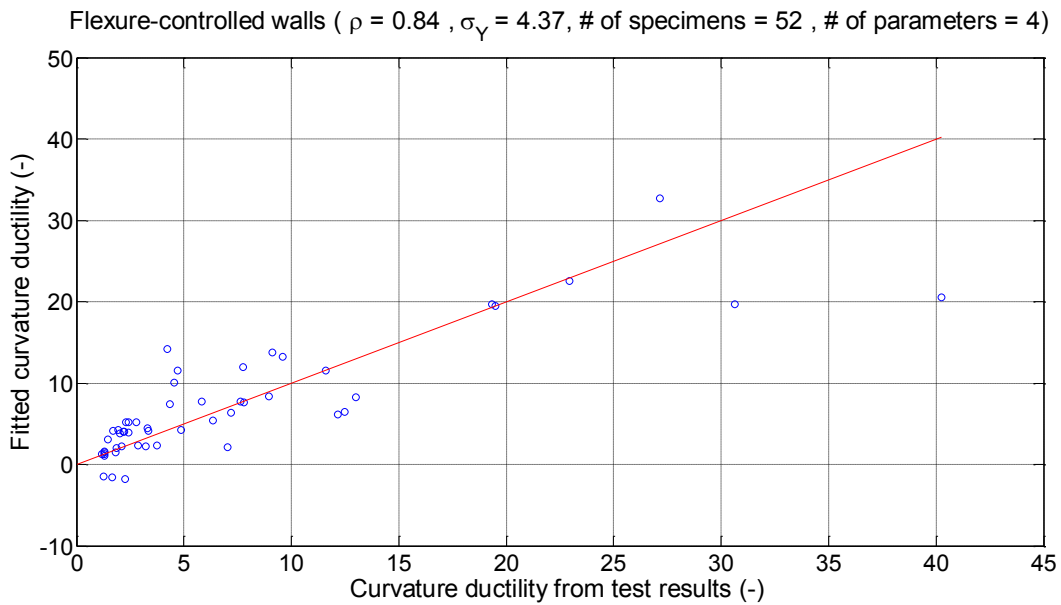


Figure 3-23. Correlation between the simplified and calculated μ_{ϕ_1} for the flexure-controlled walls

Equations obtained for curvature ductility (Table 3-9) show that shear span ratio (M/Vl_w), which is a measure of slenderness, has a positive impact on deformation capacity for all three bins. The more slender the wall is, the more deformation it typically can sustain prior to strength

loss; therefore, this parameter was expected to appear in the equation. Deformation capacity also greatly improves with confinement, which is imposed in the equations with transverse boundary reinforcement ratio (ρ_{sh}) or spacing to boundary bar diameter bar ratio (s/d_b), for shear-controlled and transition walls, and for flexure-controlled walls, respectively. Because shear-controlled walls are not expected to be affected by the confinement of boundary region, the improved correlation with transverse boundary reinforcement ratio (ρ_{sh}) and yield strength (f_{ysh}) suggests that some of the walls in the shear-controlled bin might actually be transition walls. A new criterion for classification of the walls might be needed to clarify this issue.

As reflected in the equation for deformation capacity of flexure-controlled walls, concrete compression strength (f'_c) is inversely proportional to deformation capacity, as high-strength concrete is more brittle than normal-strength concrete. On the other hand, the positive relationship between f'_c and deformation capacity for shear-controlled walls can be explained by the governing failure modes of such walls. As discussed before, shear-controlled walls are expected to have brittle failures such as web crushing and diagonal tension failure. Larger f'_c values (higher concrete strength) lead to higher web capacity, both in tension and compression, possibly delaying web crushing/failure and producing higher deformation at strength loss.

Other factors that affect deformation capacity include web vertical reinforcement and axial load ratio (for flexure-controlled walls). As noted in Table 3-9, vertical web reinforcement ratio (ρ_l) has a negative correlation for shear-controlled walls, possibly because the higher web reinforcing ratio increases shear (and moment) demands which increases the likelihood of web compression failure (reducing deformation capacity) and also increasing the yield deformation, and thus decreasing the ductility ratio. For flexure-controlled walls, axial load ratio has a positive

impact on the deformation capacity, which is counter to common expectations that higher axial load reduces curvature capacity. However, for the walls in the database, the axial load ratios tend to be low (maximum was 0.13 in this bin). The modest levels of axial stress would reduce the yield displacement but might not impact the deformation at failure, resulting in higher displacement (and curvature) ductility. It also is possible that buckling of boundary vertical reinforcement might be more likely for low axial load ratios, since tensile strains would be higher for a given drift ratio, and peak tensile strains have been shown to impact rebar buckling (Rodriguez et al, 1999).

As discussed earlier, normalized deformation capacity was also defined as displacement ductility for the shear-controlled walls. Table 3-11 shows the proposed equations for displacement ductility at failure ($\mu_{\delta 1}$), as well as values for correlation coefficients and standard deviations. Figure 3-24 and Figure 3-25 show data dispersion relative to the best-fit relations and correlation between the fitted and derived deformation capacities for each equation for shear-controlled walls. Mean values and standard deviations (shown in brackets) for displacement ductility at failure were obtained as 3.4 (0.94) and 3.5 (0.91) for the best fitted and simplified equations, respectively. It is noted that slightly higher correlation coefficients were achieved using curvature ductility versus displacement ductility for normalized deformation for the shear-controlled walls; however, significantly lower dispersion is achieved using displacement ductility. The reason for obtaining higher correlation using curvature ductility (versus displacement ductility) might be that cracks forming at the base of the walls influence the wall behavior similar to inelastic curvature.

Table 3-11. Summary of the normalized deformation capacity equations and the corresponding correlation coefficients and standard deviation with respect to the original data

| | | (Displacement ductility) | Number of parameters | Correlation coefficient, ρ | Standard deviation, σ_Y |
|--|-------------|---|----------------------|---------------------------------|--------------------------------|
| Shear-controlled walls (47 specimens) | | $\mu_\delta = 1.6 - 0.001H_w + 0.002L_w + 0.76 \frac{P}{A_g f'_c}$ | | | |
| | Best fitted | $+0.28 \frac{M}{VL_w} - 0.0028f_{ysh} + 1.6\rho_t - 2.3\rho_l$ $+0.43\rho_{sh} - 0.056 \frac{s}{d_b} + 0.2\sqrt{f'_c}$ | 10 | 0.84 | 0.59 |
| | Simplified | $\mu_\delta = 1.1 - 0.0003H_w + 0.002L_w + 0.28\sqrt{f'_c}$ $-0.0031f_{ysh} + 0.41\rho_{sh}$ | 6 | 0.82 | 0.62 |

Note: $f'_c, f_{ysh}, f_{ybl}, f_{yl}, f_{yt}$ in MPa, $\rho_t, \rho_l, \rho_{bl}, \rho_{sh}$ in %, L_w, H_w, t_w in mm, other terms are dimensionless.

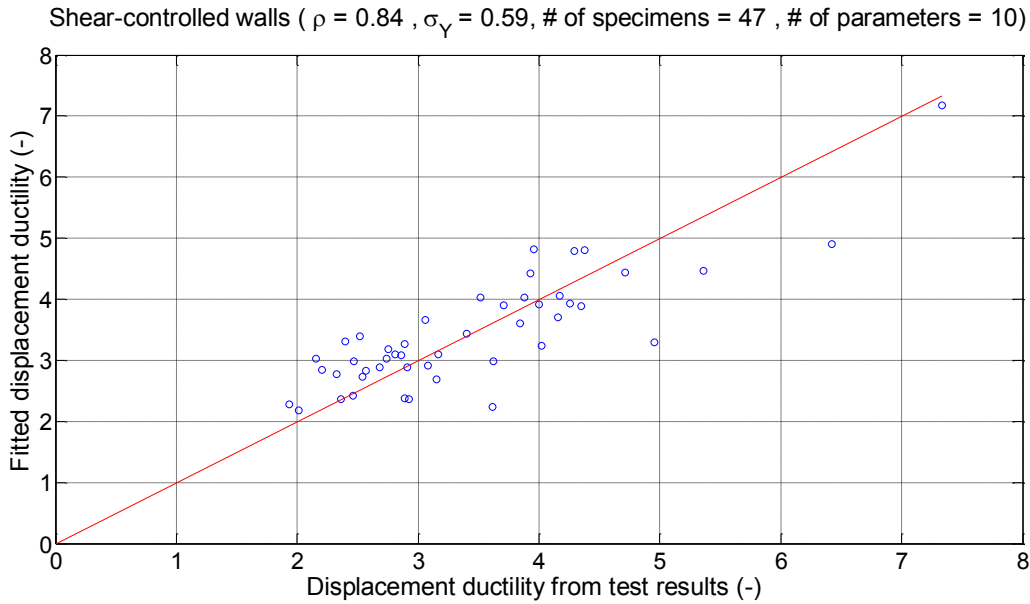


Figure 3-24. Correlation between the best fitted and calculated $\mu_{\delta 1}$ for the shear-controlled walls

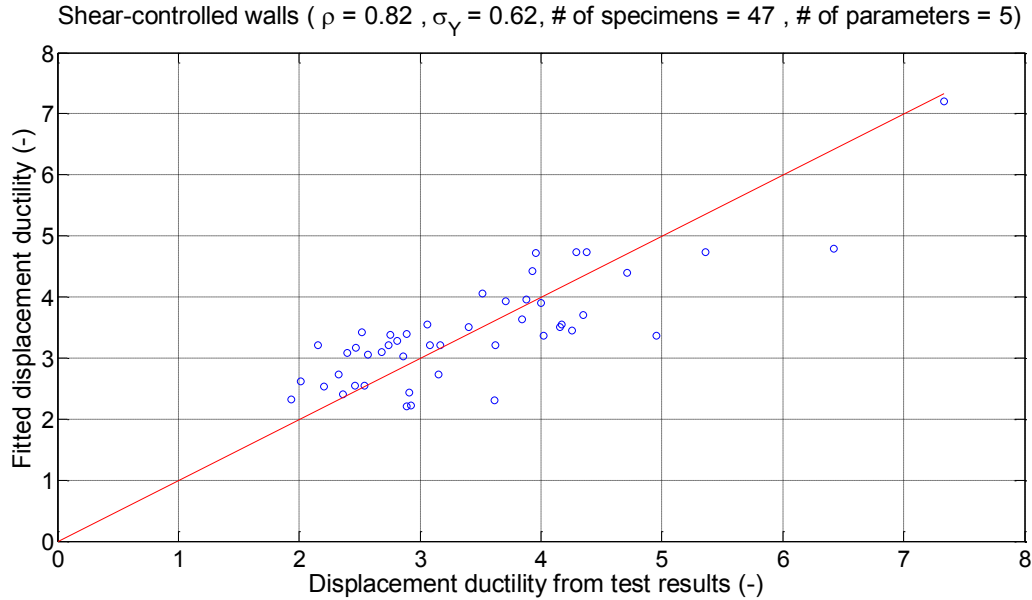


Figure 3-25. Correlation between the simplified and calculated $\mu_{\delta 1}$ for the shear-controlled walls

3.5. ACI 318-11 compliant walls

The results presented in the previous sections were obtained using the entire database regardless whether the test parameters, such as web reinforcement ratios or strength of concrete, were within ranges that satisfied ACI 318 requirements. A review of the database indicates that there were a number of test walls which do not satisfy the minimum quantity of web reinforcement or concrete strength required by ACI 318-11. Therefore, a new set of equations (strength and deformation) were derived for a reduced database of tests that comply with minimum ACI 318-11 requirements for minimum web reinforcement ($\geq 0.25\%$) and concrete strength (≥ 20.7 MPa (3 ksi)). After filtering, the number of specimens in each bin was reduced to 39 (47), 17 (25), and 36 (52) for shear-controlled, transition, and flexure-controlled regions, respectively (total number of specimens). Results for shear strength and deformation capacities of the ACI 318-11 compliant walls for each bin are presented in this section.

3.5.1. Shear strength for the ACI 318-11 compliant walls

Figure 3-12 summarizes two equations derived using the filtered database for each bin, as well as the corresponding values of correlation coefficients and standard deviations. The revised equations are only modestly different than those developed using the entire database and reported in Table 3-6; correlation coefficients slightly increased whereas standard deviation values remained about the same. Figure 3-26 to Figure 3-31 show data dispersion relative to the best-fitted relations and correlation between the fitted and measured peak shear stress values for each equation in each bin.

Mean values and standard deviations (shown in brackets) for the ratio of the measured shear stress to the calculated shear strength are summarized and compared in Table 3-13 for the ACI 318-11 compliant walls. The mean values for each bin provide a very good estimate of the measured shear stress (v_{test}). When compared to Equation 3-1, the best fitted equation estimates the peak shear stress 10% lower in the shear-controlled region, 10% higher in the transition region, and 30% higher in the flexure-controlled region. Shear strength equations are presented here for the transition and flexure-controlled bins for completeness and as noted previously, deformation capacity is of more interest for these bins since flexural yielding is supposed to occur prior to reaching the ACI 318-11 shear strength.

Table 3-12. Summary of the shear strength equations and the corresponding correlation coefficients and standard deviation with respect to the original data

| | | Shear Strength (MPa) | Number of parameters | Corr. coef., ρ | Standard deviation, σ_v |
|---------------------------------------|----------------------------|---|----------------------|---------------------|--------------------------------|
| Shear-cont. walls (39 specimens) | With ACI 318-11 parameters | $v_n = -7.6 + 1.7\sqrt{f'_c} + 0.0053\rho_t f_{yt}$ | 3 | 0.94 | 1.14 |
| | Best fitted equation | $v_n = -5.2 + 1.3\sqrt{f'_c} + 0.0042\rho_t f_{yt} + 1.1\rho_{sh} - 0.29\frac{s}{d_b}$ | 5 | 0.97 | 0.86 |
| Transition walls (17 specimens) | With ACI 318-11 parameters | $v_n = -5.9 + 1.3\sqrt{f'_c} + 0.0031\rho_t f_{yt}$ | 3 | 0.92 | 0.85 |
| | Best fitted equation | $v_n = -3.4 + 1.4\sqrt{f'_c} + 0.001\rho_t f_{yt} + 6.6\frac{P}{A_g f'_c} - 1.6\frac{H_w}{L_w}$ | 5 | 0.97 | 0.55 |
| Flexure-cont. walls (36 specimens) | With ACI 318-11 parameters | $v_n = -1.6 + 0.51\sqrt{f'_c} + 0.0031\rho_t f_{yt}$ | 3 | 0.73 | 0.98 |
| | Best fitted equation | $v_n = -2.1 + 0.85\sqrt{f'_c} + 0.0019\rho_t f_{yt} - 0.6\frac{M}{VL_w}$ | 4 | 0.90 | 0.63 |

Note: f'_c and f_{yt} in MPa, ρ_t and ρ_{sh} in %, L_w in mm, other terms are dimensionless.

Table 3-13. Comparisons of alternative equations of shear strength

| | Shear-controlled (39 specimens) | Transition (17 specimens) | Flexure-controlled (36 specimens) |
|---|------------------------------------|------------------------------|--------------------------------------|
| $v_{test} / v_{n,ACI}$ | 1.12 (0.4) | 0.80 (0.2) | 0.61 (0.4) |
| $v_{test} / v_{n,ACI \text{ parameters}}$ | 1.17 (0.7) | 1.07 (0.4) | 1.03 (0.6) |
| $v_{test} / v_{n,best \text{ fitted}}$ | 0.98 (0.3) | 0.91 (0.1) | 0.91 (0.8) |

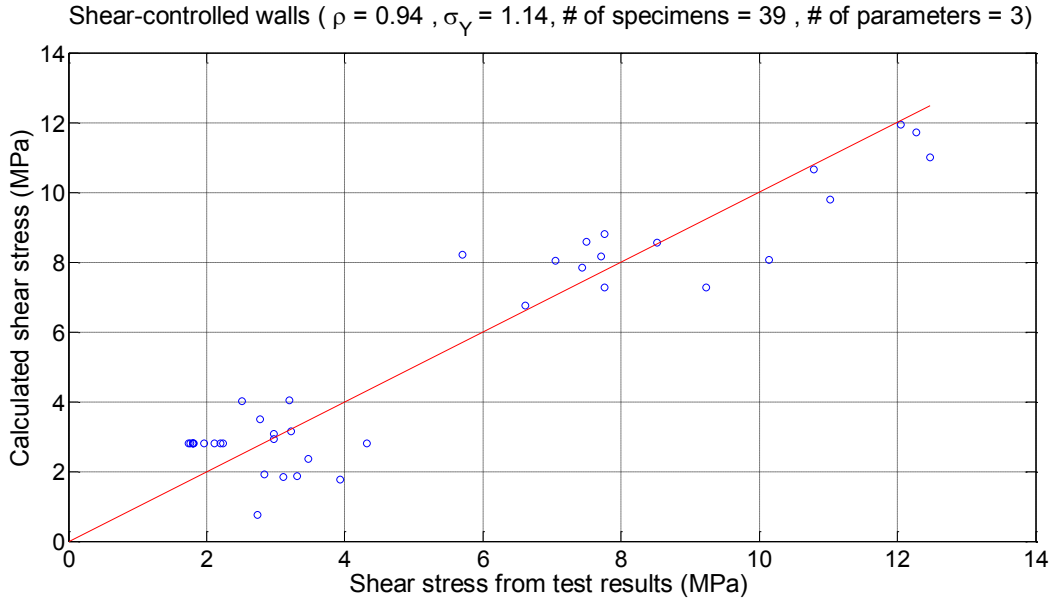


Figure 3-26. Correlation between the fitted (with ACI 318-11 parameters) and measured shear strength for the shear-controlled walls

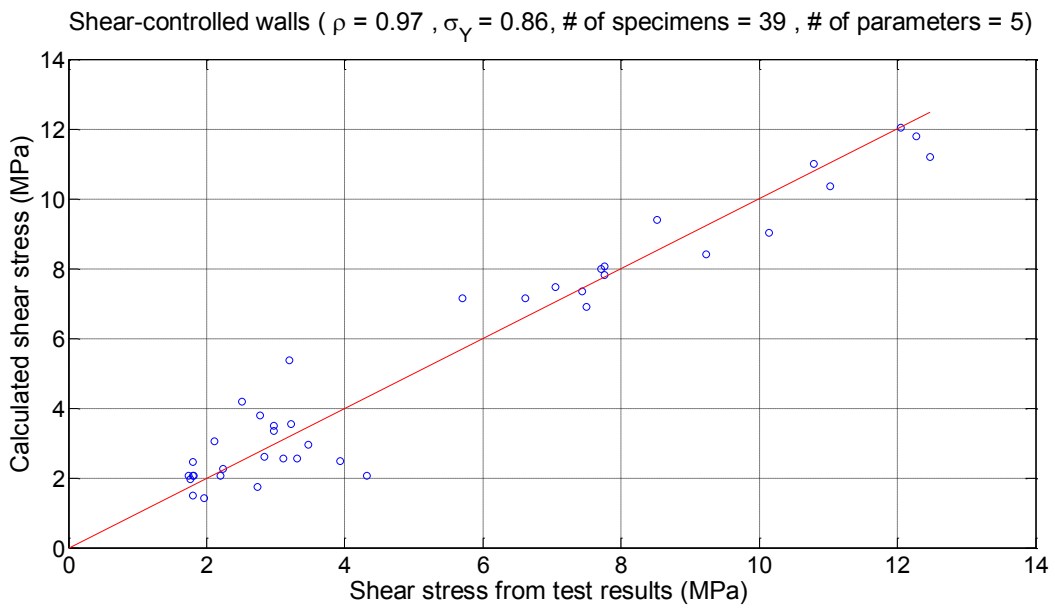


Figure 3-27. Correlation between the best fitted and measured shear strength for the shear-controlled walls

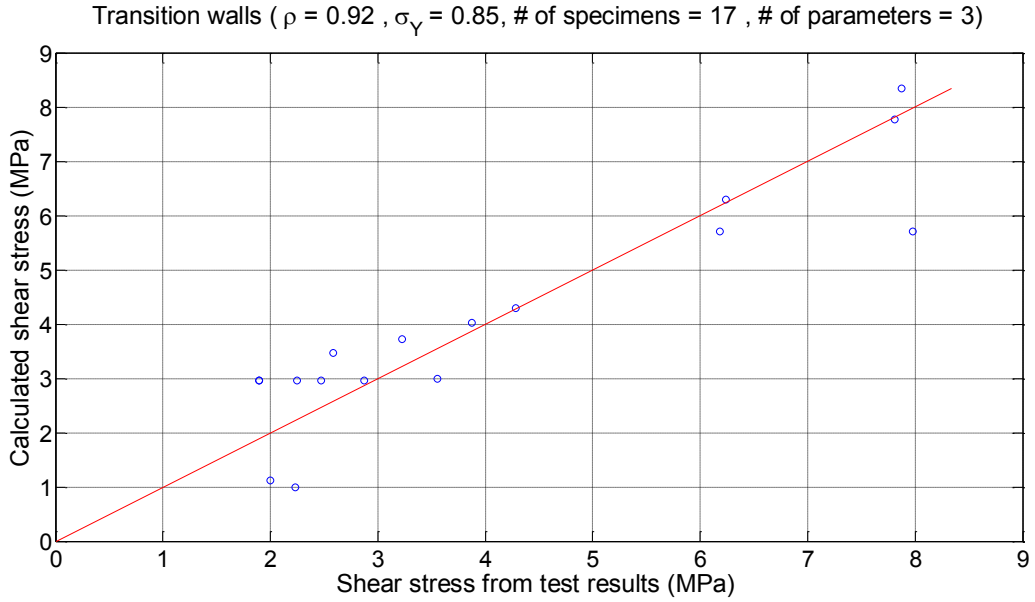


Figure 3-28. Correlation between the fitted (with ACI 318-11 parameters) and measured shear strength for the transition walls

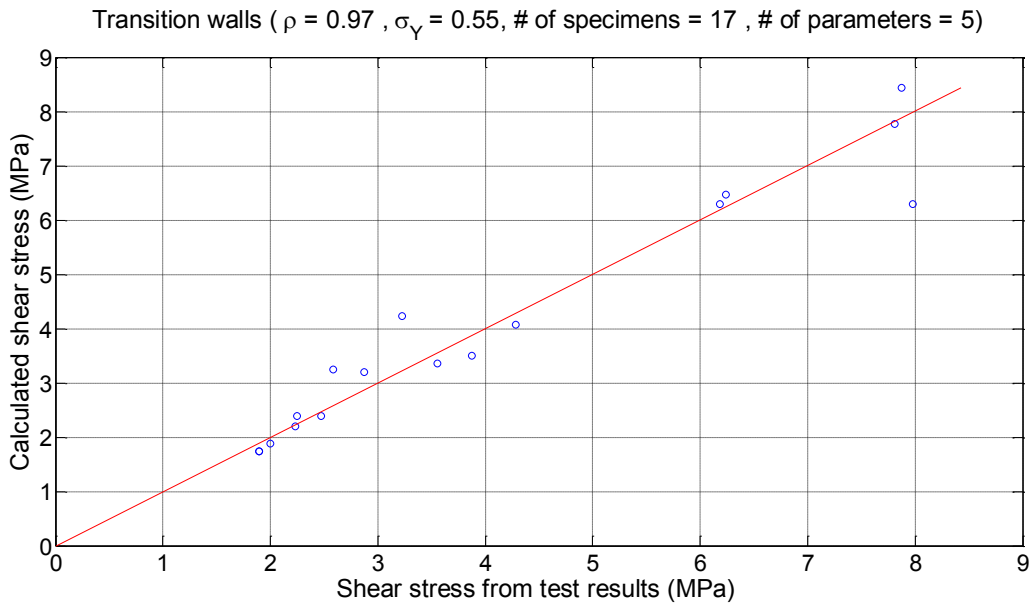


Figure 3-29. Correlation between the best fitted and measured shear strength for the transition walls

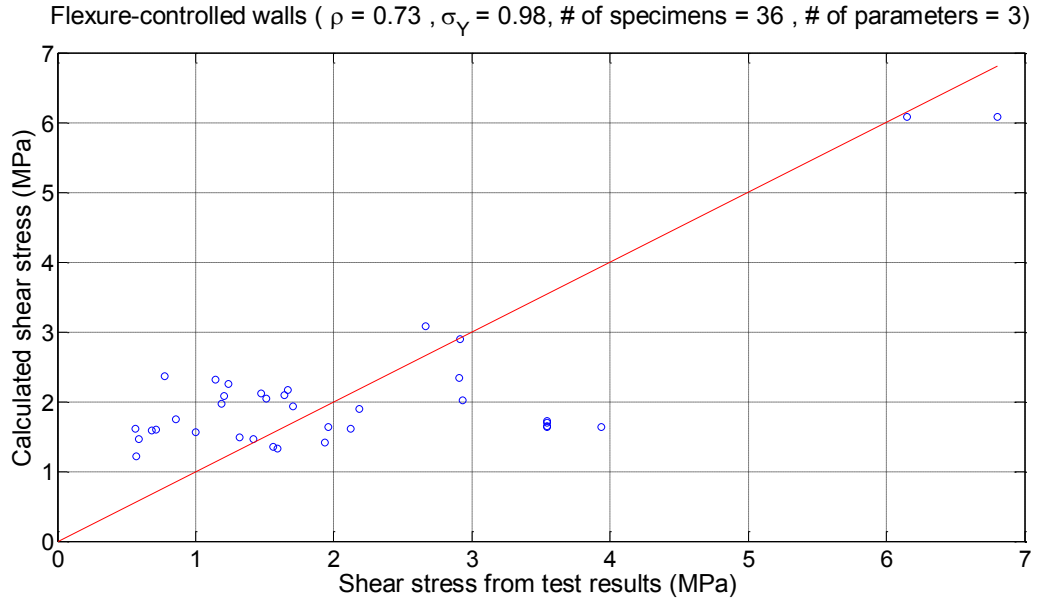


Figure 3-30. Correlation between the fitted (with ACI 318-11 parameters) and measured shear strength for the flexure-controlled walls

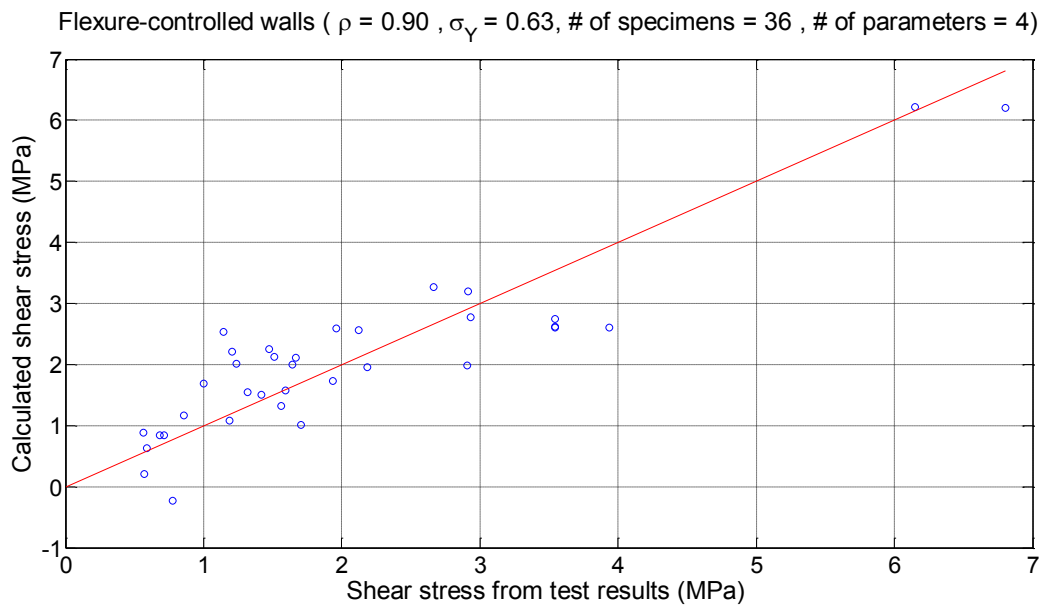


Figure 3-31. Correlation between the best fitted and measured shear strength for the flexure-controlled walls

Figure 3-32 allows direct comparison of the existing ACI 318-11 wall shear strength equation, i.e. Equation 3-1, (Figure 3-32 (a)) and the derived equation using the ACI 318-11 parameters (Figure 3-32 (b)) in terms of normalized wall parameters. Similar trends are observed in both cases, while the mean shear strength is slightly higher in Figure 3-32(a). The results suggest that the ACI equation does a reasonable job of capturing shear strength given the parameters used. It is noted that slightly higher correlation was achieved using two more parameters for the shear-controlled walls; however, dispersion was reduced significantly.

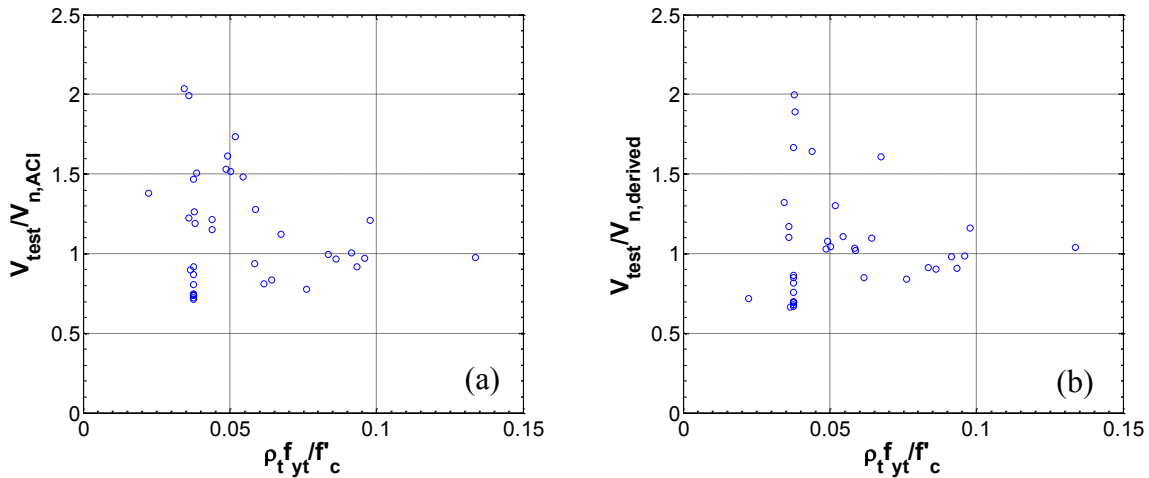


Figure 3-32. Dispersion of shear strength using: (a) ACI 318-11 equation, (b) derived equation with ACI 318-11 parameters

3.5.2. Normalized deformation capacity for the ACI 318-11 compliant walls

A new set of equations for normalized deformation capacity using the filtered database are tabulated in

Table 3-14. Compared to the prior presentation with the entire database, correlation coefficients and dispersion are slightly lower for shear-controlled walls, but slightly higher for flexure-controlled walls. For the walls in the transition region, correlation coefficient remained same, while the standard deviation decreased modestly. Figure 3-33 to Figure 3-38 show data

dispersion relative to the best-fitted relations and correlation between the fitted and derived deformation capacities for each equation in each bin.

Mean values and standard deviations (shown in brackets) for the normalized deformation capacities capacities obtained using the best fitted and simplified equations are summarized in Table 3-15. Results were close to the previously reported results (less than 10% difference) using the entire database (

Table 3-10). It is noted that dispersion decreased by 10% for the shear-controlled walls, whereas it increased by the 20% for the flexure-controlled walls. The dispersion remained about the same for the transition walls.

Table 3-14. Summary of the normalized deformation capacity equations for the ACI 318 compliant walls

| | | (Curvature ductility) | Number of parameters | Corr. coef., ρ | Standard deviation, σ_y |
|-------------------------------------|-------------|---|----------------------|---------------------|--------------------------------|
| Shear-cont. walls (39 specimens) | Best fitted | $\mu_{\phi 1} = 2.5 + 0.0013H_w - 0.0011L_w - 0.019t_w + 2.8 \frac{P}{A_g f'_c} + 0.33\sqrt{f'_c} - 0.0046f_{ysh} + 3.4\rho_t + 3.6\rho_l + 0.85\rho_{sh} + 0.18\rho_{bl}$ | 10 | 0.89 | 0.69 |
| | Simplified | $\mu_{\phi 1} = 1.5 + 1.4 \frac{M}{VL_w} - 0.0022f_{ysh} + 0.55\rho_{sh} - 5.8\rho_l + 5.7\rho_t$ | 5 | 0.87 | 0.74 |
| Transition walls (17 specimens) | Best fitted | $\mu_{\phi 1} = -2.6 + 6.6 \frac{P}{A_g f'_c} + 0.85\sqrt{f'_c} - 0.011f_{yl} + 6.0\rho_t - 5.5\rho_l + 2.9\rho_{sh} - 0.67\rho_{bl} + 0.29 \frac{M}{VL_w} - 0.18 \frac{s}{d_b} + 0.048t_w$ | 10 | 0.91 | 0.72 |
| | Simplified | $\mu_{\phi 1} = -1.3 + 0.28\sqrt{f'_c} - 0.006f_{yl} + 1.8\rho_{sh} - 0.045 \frac{M}{VL_w} + 0.04t_w$ | 5 | 0.85 | 0.92 |
| Flexure-cont. walls (36) | Best fitted | $\mu_{\phi 1} = 7.6 + 119 \frac{P}{A_g f'_c} - 0.21f'_c + 0.0015f_{ybl} + 7.1\rho_t - 4.9\rho_l - 0.64\rho_{sh} - 1.4\rho_{bl} + 3.5 \frac{M}{VL_w} - 0.83 \frac{s}{d_b} + 0.0023t_w$ | 10 | 0.90 | 3.98 |
| | Simplified | $\mu_{\phi 1} = 7.1 + 105 \frac{P}{A_g f'_c} - 0.25\sqrt{f'_c} + 3.4\rho_l + 3.9 \frac{M}{VL_w} - 1.1 \frac{s}{d_b}$ | 5 | 0.89 | 4.29 |

Note: $f'_c, f_{ysh}, f_{ybl}, f_{yl}, f_{yt}$ in MPa, $\rho_t, \rho_l, \rho_{bl}, \rho_{sh}$ in %, L_w, H_w, t_w in mm, other terms are dimensionless.

Table 3-15. Average normalized deformation capacities ($\mu_{\phi 1}$)

| | Shear-controlled (39 specimens) | Transition (17 specimens) | Flexure-controlled (36 specimens) |
|----------------------|------------------------------------|------------------------------|--------------------------------------|
| Best fitted equation | 3.33 (1.31) | 4.71 (1.67) | 7.76 (8.50) |
| Simplified equation | 3.19 (1.31) | 4.75 (1.54) | 7.63 (8.35) |

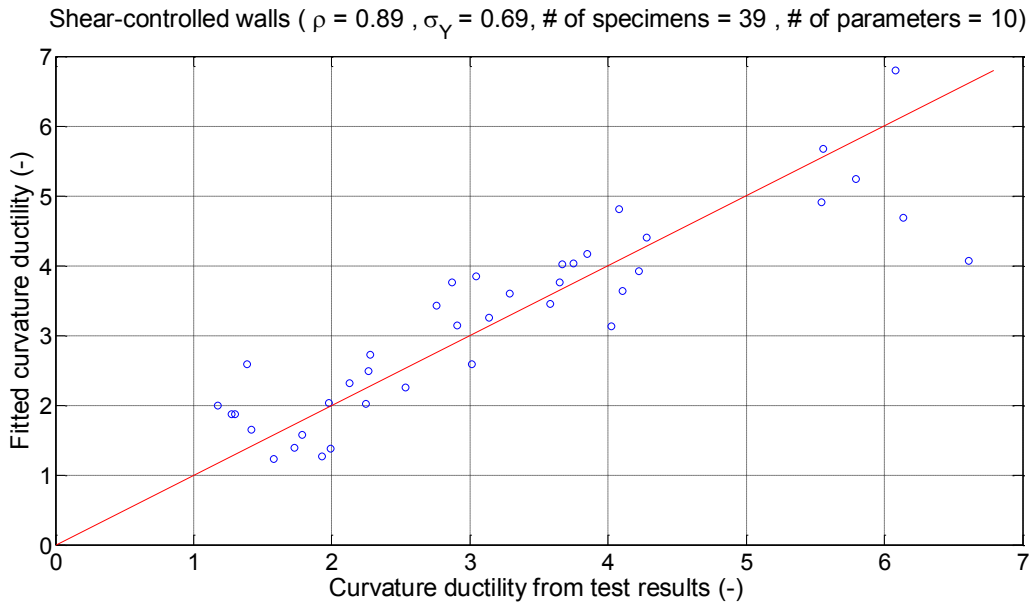


Figure 3-33. Correlation between the best fitted and calculated $\mu_{\phi 1}$ for the shear-controlled walls

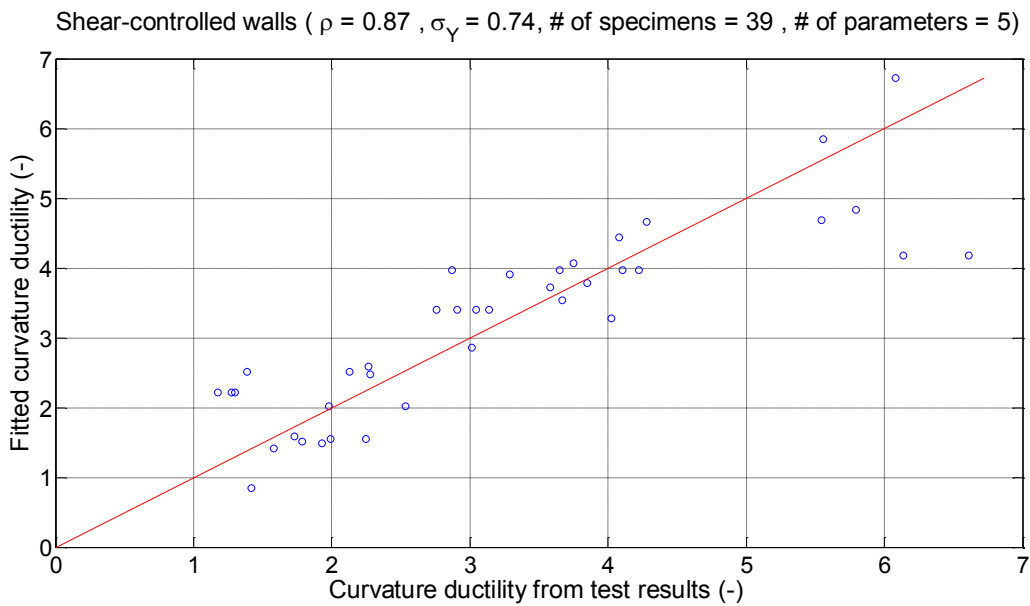


Figure 3-34. Correlation between the simplified and calculated $\mu_{\phi 1}$ for the shear-controlled walls

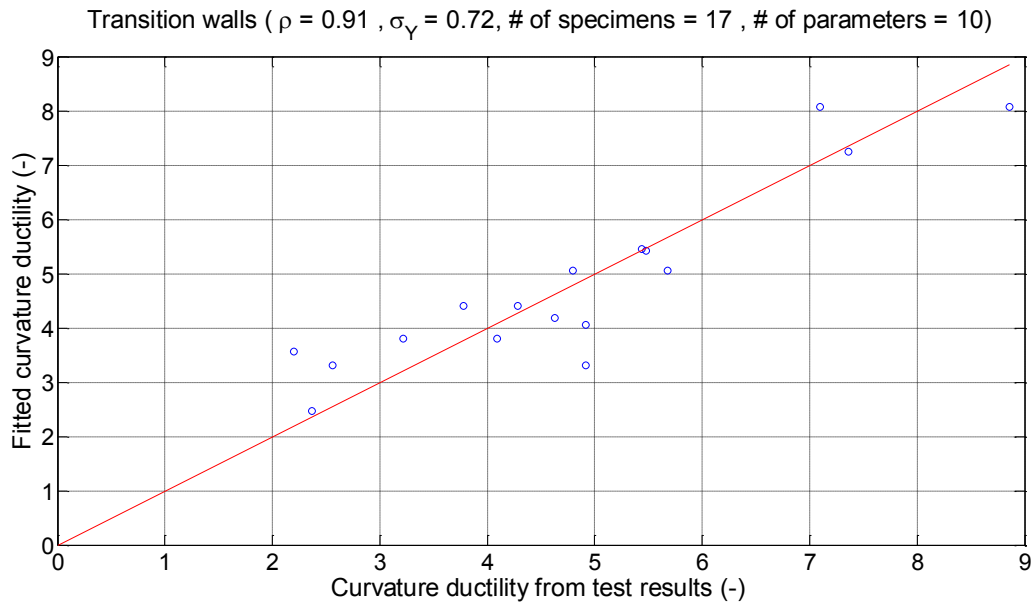


Figure 3-35. Correlation between the best fitted and calculated $\mu_{\phi 1}$ for the transition walls

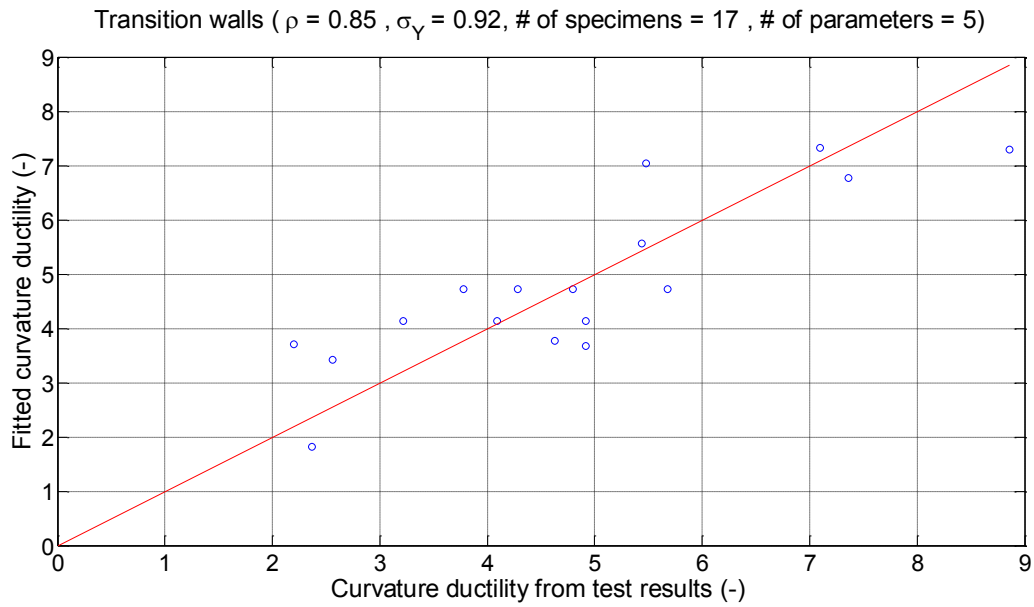


Figure 3-36. Correlation between the simplified and calculated $\mu_{\phi 1}$ for the transition walls

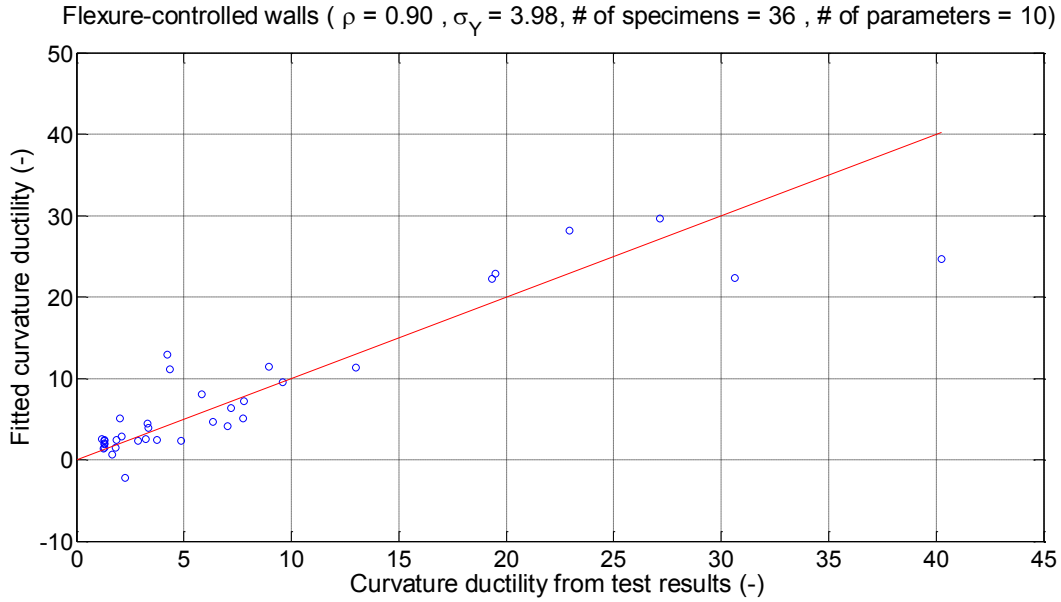


Figure 3-37. Correlation between the best fitted and calculated $\mu_{\phi 1}$ for the flexure-controlled walls

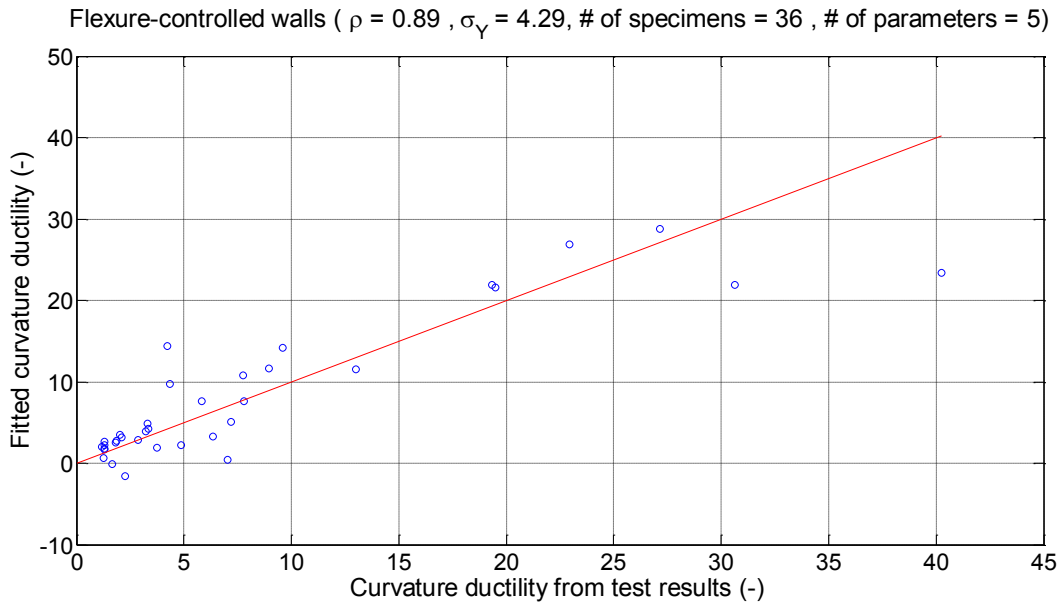


Figure 3-38. Correlation between the simplified and calculated $\mu_{\phi 1}$ for the flexure-controlled walls

3.6. Summary and conclusions

Experimental results have shown that behavior and response of shear walls are different depending on the wall properties, particularly aspect ratio or shear span ratio. In this study, squat

walls with lower aspect ratios, which are expected to reach their shear strength before boundary longitudinal reinforcement yields in flexure, are referred to as shear-controlled walls. Slender walls, which are expected to yield in flexure before reaching the shear strength, are referred to as flexure-controlled walls, whereas walls which are expected to yield in flexure followed by shear failure (includes shear-flexure interaction), are referred to here as transition walls.

A detailed database consisting of 124 reinforced concrete shear wall specimens tested worldwide was composed and utilized to understand how well the code estimates shear strength and to derive alternative equations for shear strength of shear-controlled walls. The database included 47 specimens for the shear-controlled walls, 25 specimens for the transition walls, and 52 specimens for the flexure-controlled walls.

Experimental results also have shown that the nonlinear deformation capacity of walls that yield in flexure prior to reaching their shear strength limit depends on the level of applied shear stress, and that walls that fail in shear prior to yield of boundary longitudinal reinforcement typically have some nonlinear deformation capacity. Therefore, the database also was used to obtain equations for normalized deformation capacity of walls for each bin. The normalized deformation capacity was defined as curvature ductility for the walls in all bins, while displacement ductility also was determined for the shear-controlled walls. Detailed regression analyses were conducted in each category to identify the critical parameters which can be used to estimate shear strength and the normalized deformation capacity, and a set of equations was determined for each bin.

The average shear stress at nominal capacity ($v_{n,ACI}$) was calculated to be approximately $7\sqrt{f'_c}$ for all bins using ACI 318-11 Equation (21-6), also Equation (3-1), whereas measured

shear stress from wall tests ranged between $8.3\sqrt{f'_c}$ to $4.5\sqrt{f'_c}$ (for shear-controlled walls and flexure-controlled walls, respectively). This indicates that the ACI 318-11 equation underestimates the shear strength by 20% for the shear-controlled walls, whereas the peak shear stress for flexure-controlled walls is only 70% of the ACI 318-11 nominal shear strength. It is noted that the 20% over-strength (ratio of $v_{test}/v_{n,ACI} = 1.2$) seems very low compared to the previous findings (Wallace, 1998; Orakcal, et al., 2009), as well as Figure 3-1 in which the ratio was 1.5), probably because there were some walls in the shear-controlled bin that actually did not fail in pure shear; therefore, wall classification criteria needs to be carefully reassessed. The current criterion used to classify the shear walls in the database was such that if the ratio of shear strength to shear force associated with reaching the moment capacity M_n is smaller than 1.0, i.e., $\frac{V_n}{V@M_n} \leq 1.0$, the wall would be shear-controlled. However, both previous studies and this study have shown that the shear strength is underestimated using the ACI 318 equation. Therefore, use of a higher value for the ratio of $\frac{V_n}{V@M_n}$ should be considered. Once the ratio of $v_{test}/v_{n,ACI}$ is obtained using the new criteria, interaction between shear stress and ductility will be assessed.

Based on the mean values of the v_{test}/v_n ratio, where v_n was obtained using the proposed (best-fitted) equations for each failure mode, the shear strength was estimated to be very close to the measured shear stress. It was noted that the ACI 318-11 equation estimates the shear strength of the shear-controlled walls 18% higher than the best fitted equation. Capacity of

the walls in the transition region is underestimated by 13% compared to the proposed equation. This number becomes 23% for the shear strength of flexure-controlled walls.

The average normalized deformation capacity, when defined as curvature ductility (μ_ϕ), was about 3.2 for the walls in shear-controlled region, whereas it was 4.4 and 7.0 for the transition and flexure-controlled regions, respectively. The displacement ductility (μ_δ) for the shear-controlled walls was 3.2.

The same procedure was followed for a filtered database in which only ACI-compliant shear walls were included; that is, specimens having longitudinal and transverse web reinforcement less than the minimum required amount (0.25%), and those with concrete strength less than 20.7 MPa ($f'_c = 3ksi$) were eliminated. The filtered database had 39, 17, and 36 specimens for shear-controlled, transition, and flexure-controlled walls, respectively. The resulting equations and statistical coefficients were slightly different while the average values remained about same for both shear strength and normalized deformation capacity.

The database provides a powerful tool to examine relationships between shear strength and ductility. Possible future studies might include:

1. Defining a new approach for categorizing bins (shear-controlled, transition, flexure-controlled),
2. Refining the procedure to obtain backbone curves, e.g. use of a tri-linear backbone curve that includes pre-crack and post-crack slopes as suggested by ASCE 41-06 (versus the bi-linear backbone curve),
3. Including deformation capacity term in the shear strength equation, which would provide a direct relation between shear strength and ductility,

4. Re-defining shear strength for the shear-controlled walls considering shear deformation capacity,
5. Improving the current methodology for modeling the shear behavior of reinforced concrete shear walls using the values obtained from this study, which would be particularly valuable for engineering practice,
6. Revising and improving the modeling parameters recommended in ASCE-41 using relationships between the parameters obtained from the database,
7. Considering slip of rebar from the foundation in displacement estimates,
8. Re-estimating equations for failure ductility using the “new” shear strength equations,
9. Applying the equations proposed for shear strength and ductility capacity to assess failure of shear walls in the reinforced concrete tall buildings (e.g. PEER/TBI Case Study).

Chapter 4 Collapse Assessment of the Alto Rio Building in the 2010 Chile Earthquake

4.1. Introduction

On Saturday, 27 February 2010, a $M_w = 8.8$ earthquake occurred in south central Chile impacting more than 8 million people (<http://earthquake.usgs.gov/earthquakes/pager>) in the most densely populated regions of Chile. The earthquake shaking resulted in damage to buildings, highways, railroads, and airports, including damage to taller reinforced concrete buildings (EERI, June 2010). Although a majority of the taller buildings performed well, with no more than light damage, systematic damage was reported for slender buildings with thin walls, especially in Concepción, where about 10% of approximately 100 tall reinforced concrete buildings were severely damaged (Massone et al, 2012). However, only one, modern, tall building completely collapsed, a 15-story residential Torre Alto Rio building in Concepción, referred to subsequently as “Alto Rio” in this paper. Photos of the building prior to and following the earthquake are shown in Figure 4-1.



Figure 4-1. Torre Alto Rio (a) before, (b) after the earthquake [(a) Bonelli, 2010; (b) Wallace, 2010]

Alto Rio, constructed in 2008, appears to be a fairly typical building for Chile, with a large number of reinforced concrete structural walls utilized to resist gravity and earthquake loads (Figure 4-2); however, as noted subsequently, the building has a number of features that make it more susceptible to damage than typical tall buildings in Chile. The building was designed using analysis procedures and computer programs similar to those used in the US. i.e., elastic code level analysis using ETABS (CSI, 2007) and the Chilean code for reinforced concrete design is based on ACI 318-95. However, it is important to note that the Chilean concrete code does not require tightly-spaced transverse reinforcement, or special boundary elements, at wall boundaries based on the generally good performance of buildings in Vina del Mar in the March 1985 earthquake (Wallace and Moehle, 1993). In addition, there are no provisions in the Chilean seismic code (NCh 433.of.96) that limit building or wall irregularities, either vertical or horizontal. Detailed study of this building provides an excellent opportunity to assess reasons for the collapse of a modern building designed using analysis approaches and code provisions similar to those used in the US.

The collapse appeared to initiate near the ground floor level, with the building overturning to the east, in the more slender building direction (Figure 4-2). Preliminary studies (Tuna and Wallace, 2011) noted significant vertical wall discontinuities existed along the east face of the building due to parking at and below ground level. Extensive concrete crushing and buckling of vertical reinforcement was observed in a number of buildings with wall discontinuities at parking levels following the 2010 earthquake (Wallace, 2011; Wallace et al., 2012); however, no other collapses of modern, tall buildings were observed. Spectra for ground motions recorded in Concepcion and elsewhere in the February 2010 earthquake (Figure 4-5) indicate that the ground shaking approximately 1.2 km from Alto Rio was similar to other

locations for periods less than 1.0 seconds, but stronger for longer periods. Detailed analytical studies are undertaken to identify most likely collapse scenarios and possible contributing factors.

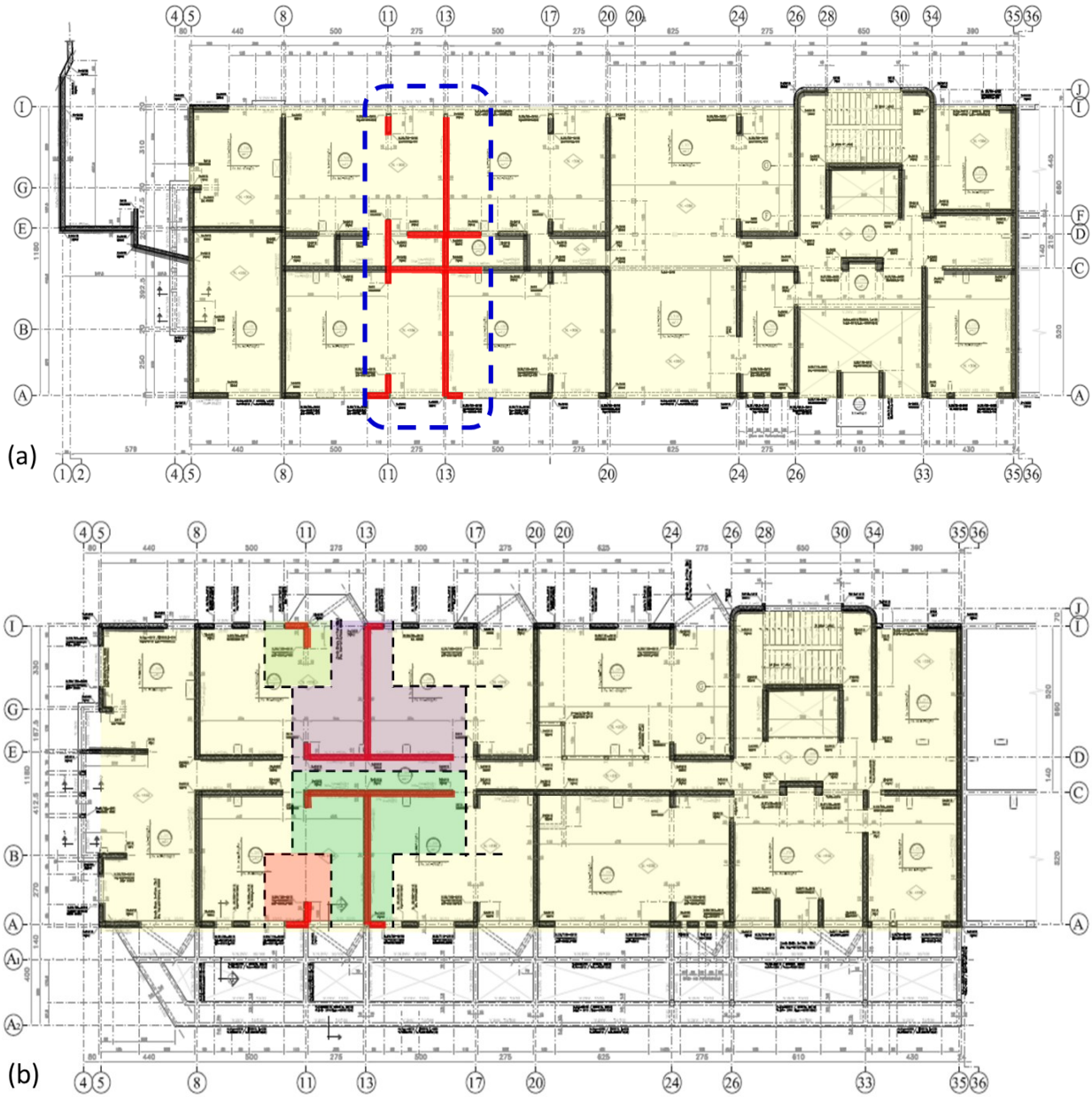


Figure 4-2. (a) Plan view (1st floor) and (b) Plan view (2nd floor). (Figures taken from <ftp://atc94:chile-concrete@ftp.atcouncil.org>.)

4.2. The February 27, 2010 Earthquake – A brief overview

The $M_w = 8.8$ earthquake occurred off the coast of the Maule Region of Chile on February 27, 2010, with strong shaking ($> 0.05g$) lasting two to three minutes. The earthquake epicenter was located at 335 km (210 miles) SW of Chile's capital city, Santiago, and 105 km (65 miles) NNE of Chile's second largest city, Concepción (Figure 4-3). Ground accelerations recorded at one location in Concepción (<https://nees.org/resources/3076>) are presented in Figure 4-4 for the east-west (collapse direction for Alto Rio) and north-south components, with peak ground accelerations of 0.40g and 0.37g, respectively.

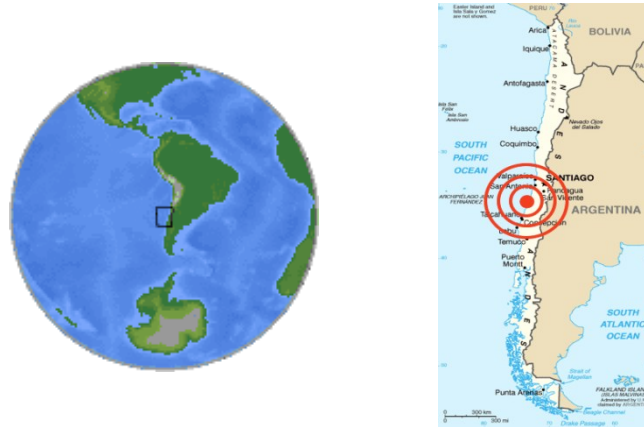


Figure 4-3. Location of the 2010 Chilean Earthquake [USGS, 2010]

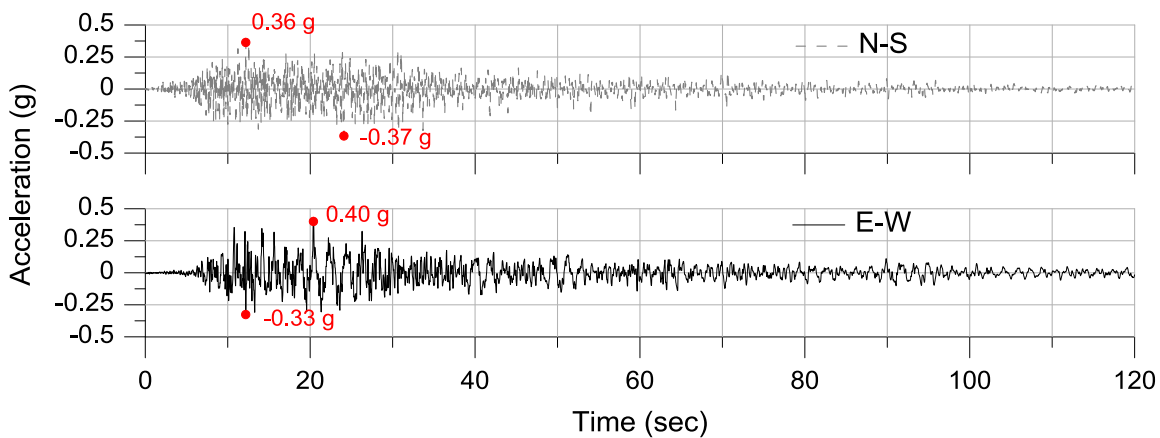


Figure 4-4. Ground acceleration histories recorded in Concepción

Figure 4-5 includes 5% damped elastic displacement response spectra computed using the records obtained during the earthquake at different locations, as well as design response spectra based on NCh 433.of.96 for soil types II, III, IV corresponding to stiff soil, medium stiff soil, and soft soil, respectively. Spectral displacements and accelerations for the Concepción (east-west) record are considerably larger than those for Soil II, the design spectrum used for Alto Rio (Uribe, 2010), particularly for periods between 1.5s and 2.5s. Inelastic spectra for Concepción, for displacement ductility of two, indicate modestly larger values for displacement and acceleration for periods less than 1.5s, but reduced elastic demands for periods greater than 1.5s. For the stiff structural wall buildings constructed in Chile, fundamental periods for low-amplitude vibrations (no concrete cracking likely) are typically close to $N/20$, where N is the number of stories (Massone et al, 2012). For the 15-story Alto Rio building, this translates into a fundamental period of 0.75s. Spectral demands between periods of 0.75s and 1.5 times this period (to account for concrete cracking), for either linear or nonlinear response (Figure 4-5), are similar to values for other locations. However, it is noted that period lengthening due to nonlinear responses (damage), could lead to significantly greater displacement demands (possibly 2 to 4 times) given the shape of the Concepcion EW spectrum.

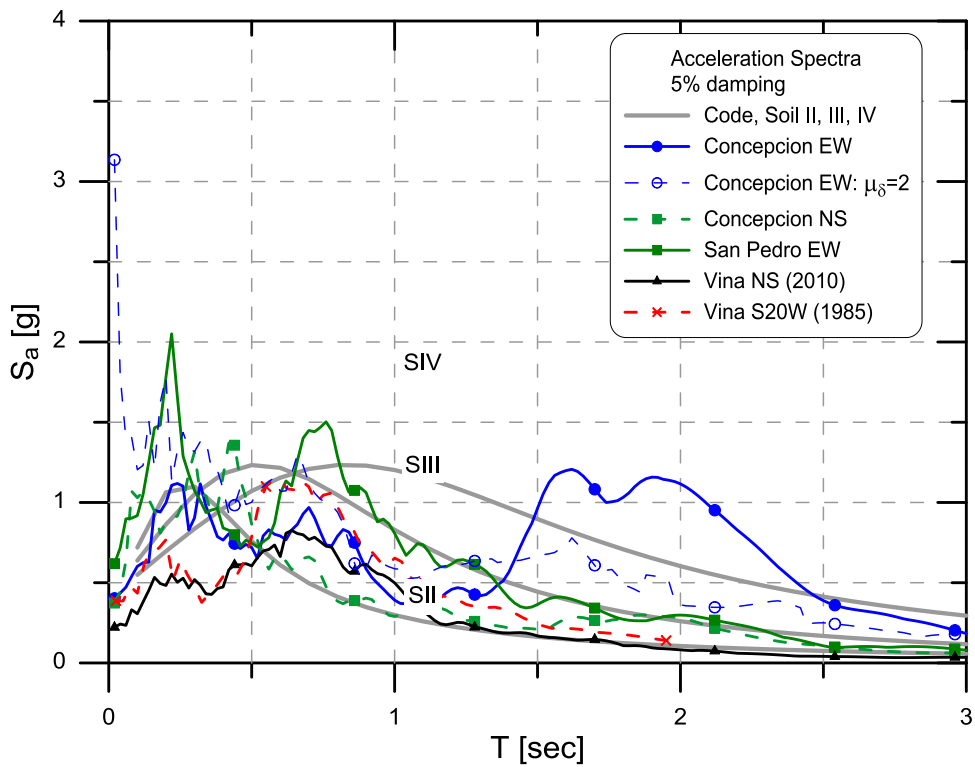
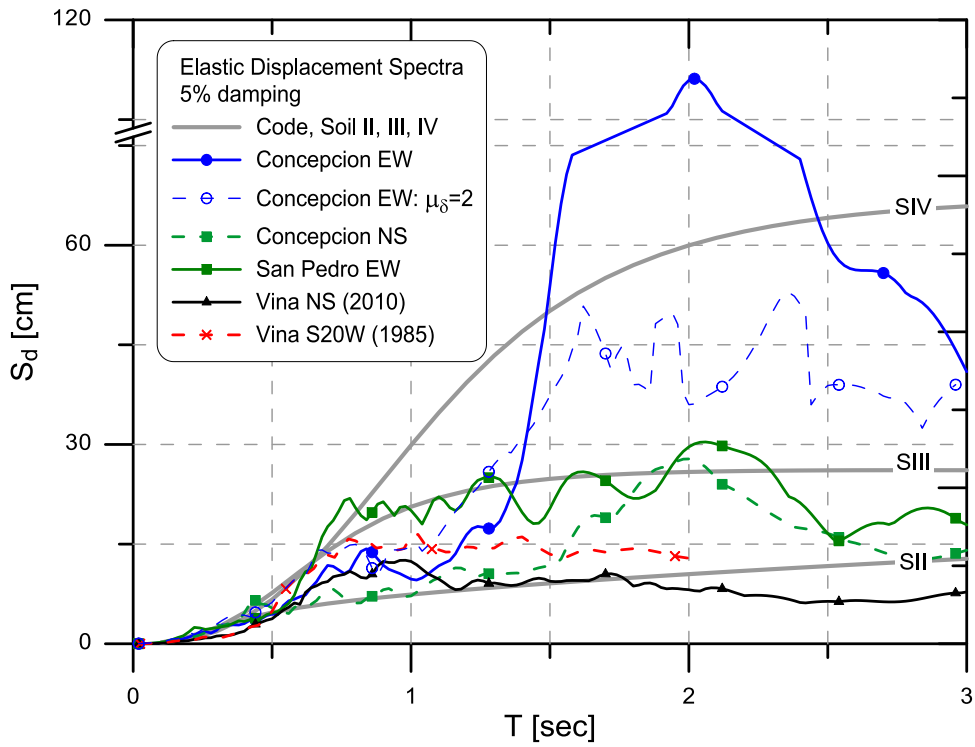


Figure 4-5. (a) Displacement spectra: Code ($A_0 = 0.4$), (b) Acceleration spectra, Elastic, and Inelastic

4.3. Building Code Provisions in Chile

Design of most RC buildings over 5 stories is typically accomplished using the modal spectral procedure of NCh 433.of.96. Similar to ASCE 7-05, the NCh 433.of.96 requires 90 percent mass participation and also includes a minimum design force. NCh 433.of.96 Section 5.9 limits relative displacements between two consecutive floors, measured at the center of the mass in each direction, to $0.002h_s$, where h_s is the story height. The relative displacements at other locations on the floor plan cannot exceed the value at the center of mass by more than $0.001h_s$. These limits are not for expected displacements, but displacements for reduced forces used to proportion members. The low drift limit tends to require use of stiff buildings, and along with minimum base shear strength requirements, produces buildings with an effective force reduction factors R_{eff}^* that vary from a maximum value of about 5.0 for a period of 0.5s to a value of about 3.0 for a period of 1.0s (Lagos and Kupfer, 2012), as shown in Figure 4-6.

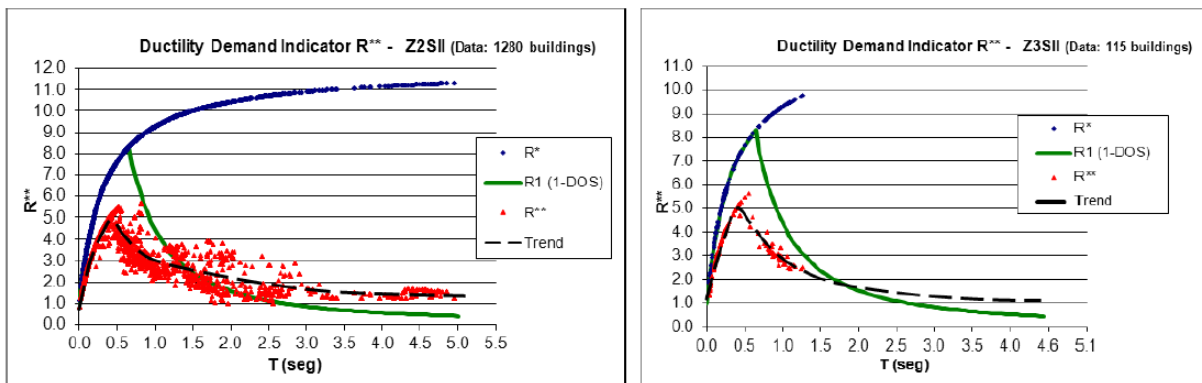


Figure 4-6. Effective force reduction factor R_{eff}^* (Lagos et al., 2012)

Modeling of buildings according to NCh 433.of.96 is commonly based on the use of gross concrete section stiffness and an elastic concrete modulus recommended by ACI 318, i.e., $E_c = 4700\sqrt{f'_c}$ (MPa). Although RC code provisions for shear walls are essentially the same as

those in ACI 318-95, based on the good performance of wall buildings in Viña del Mar in the 1985 earthquake, ACI 318-95 requirements for special transverse reinforcement at wall boundaries to confine the concrete and restrain rebar buckling were eliminated from the Chilean concrete code. Hoops with 90-degree hooks, typically spaced at 20cm vertically, are commonly provided around boundary longitudinal reinforcement (Figure 4-7, Massone et al, 2012). Typical web vertical and horizontal reinforcement in newer buildings consists of 8mm diameter bars spaced at 20cm ($\rho_v = 0.0025$). Horizontal web bars are typically placed outside of vertical bars and anchored at the wall edge with 90-degree hooks.

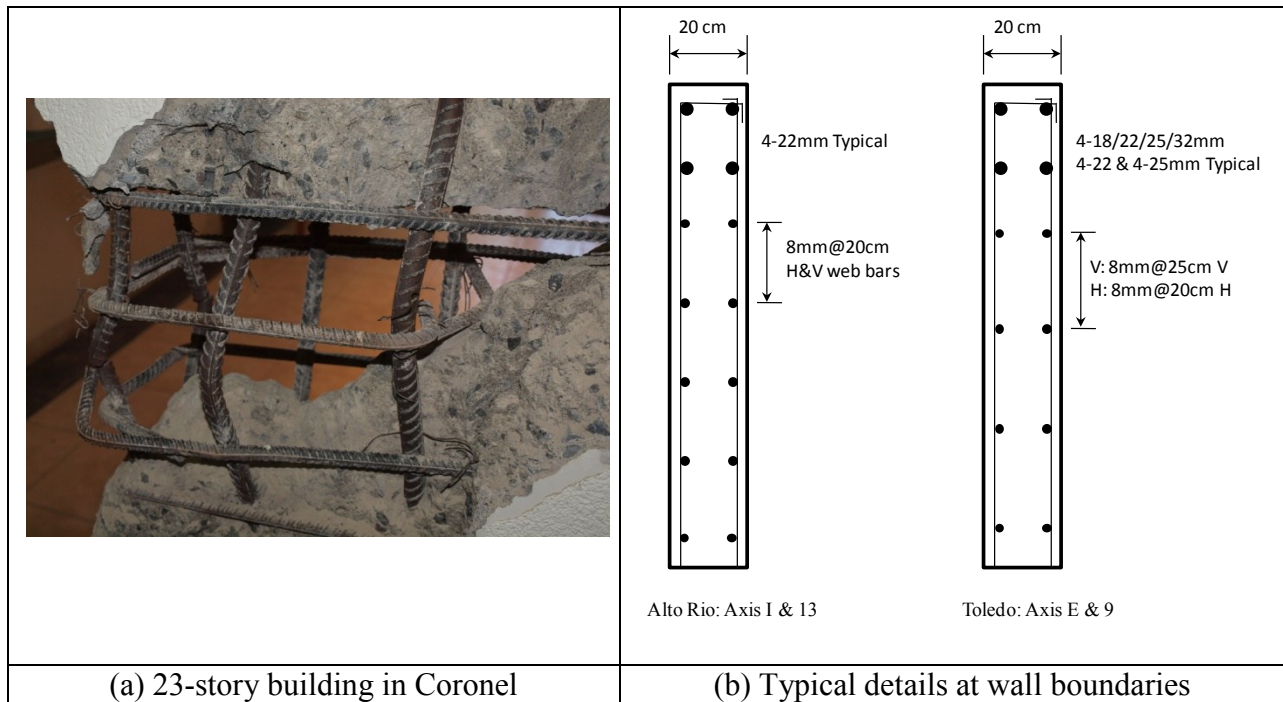


Figure 4-7. Typical detailing at wall boundaries in Chile (constructed in 2008)

4.4. Building Description

Construction of the 15-story residential building Torre Alto Rio was completed in 2008. Building plan dimensions were approximately 40m x 12m with a first story height of 3.06m and a typical story height of 2.52m (levels 2 to 15). Plan views of the first and second levels are shown in

Figure 4-2. Gravity and lateral loads are resisted by a large number of structural walls, which is common in Chile (Wood et al, 1987, Wallace and Moehle, 1993; Massone et al, 2012). In the transverse (east-west) direction, 20 cm thick walls were fairly uniformly spaced and served to separate condominium units. In the longitudinal (north-south) direction, the primary lateral resistance was provided by two lines of 20 cm thick walls forming a central corridor. The transverse and longitudinal walls connected to form T- and L-shaped walls, again, common for modern buildings in Chile. The wall web areas divided by the floor plan area aligned in the transverse and longitudinal directions were 3.2% and 2.7%, respectively for a typical story (e.g., level 2). These values are about average for buildings constructed in Chile (Massone et al, 2012). An elevation view of the east façade of the building is shown in Figure 4-8. At the first story and below, a number of irregularities existed. For example, at the east side of the building, east façade walls were discontinued (Figure 4-8) and the length of transverse walls along Axes 8, 13, and 20 were reduced from 5m to 4.6m to provide for parking, whereas at Axes 11, 17, and 24, 20cm thick L-shaped walls became 25cm thick rectangular walls below the second floor, and also included a horizontal offset of 40 cm. At the first story and below grade, walls were added across the corridor (at Axes 8, 11, and 13) and openings were added on some walls (e.g., Axis 13, west of corridor).

Design concrete compressive strengths of $f'_c = 20MPa$ (H25; $f_{cube} = 25MPa$) and $f'_c = 25MPa$ (H30; $f_{cube} = 30MPa$) were specified at and above the second floor and below the second floor, respectively. Specified yield strength of all reinforcement was 420 MPa (S420), including 8mm and 10mm bars used for wall web reinforcement, and 16, 18, and 22mm bars used for the wall boundary longitudinal reinforcement. Typical horizontal and vertical wall web reinforcement consisted of 8mm bars spaced at 150mm to 200mm (10mm bars were used in

some transverse walls), producing web horizontal and vertical reinforcement ratios of 0.0025 to 0.0034 and 0.0025, respectively. . Lap lengths of 125cm, or $57d_b$ for 22mm diameter bars, were specified for wall vertical boundary reinforcement just above ground line for the transverse walls on the west half of the building; this lap length is 96% of that required by ACI 318-08 outside of yielding (plastic hinge) region for a Special Structural Wall. A cross sectional view of several of the walls noted on Figure 4-2 is shown in Figure 4-9; wall vertical boundary reinforcement consisted of 4-18mm or 4-22mm bars at wall edges and wall intersections. The wall tributary (Figure 4-2b) gravity load at the base of first story was estimated to be approximately $0.1A_g f'_c$ for a floor unit weight of 1.0 t/m^2 (Wood et al, 1987; Massone et al, 2012).

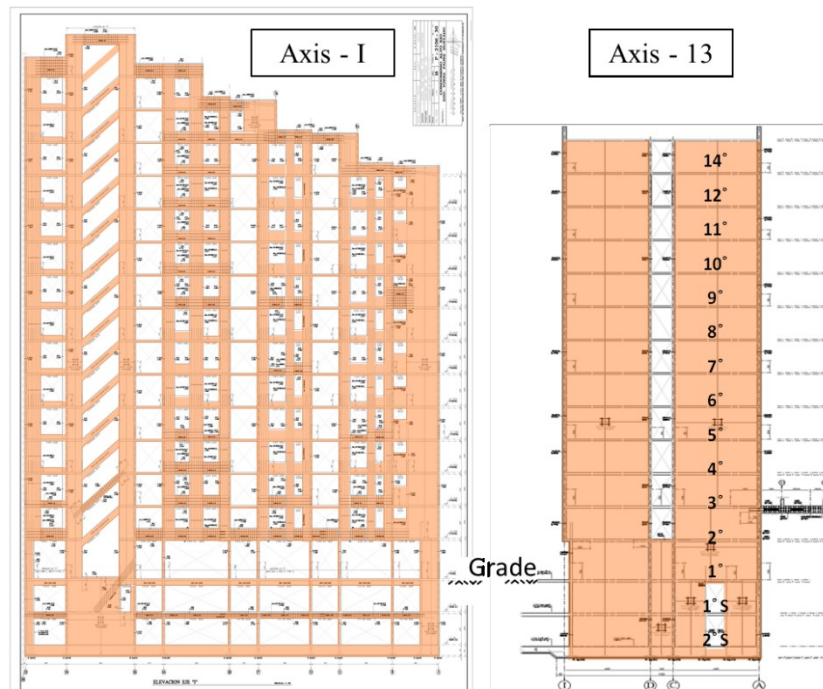
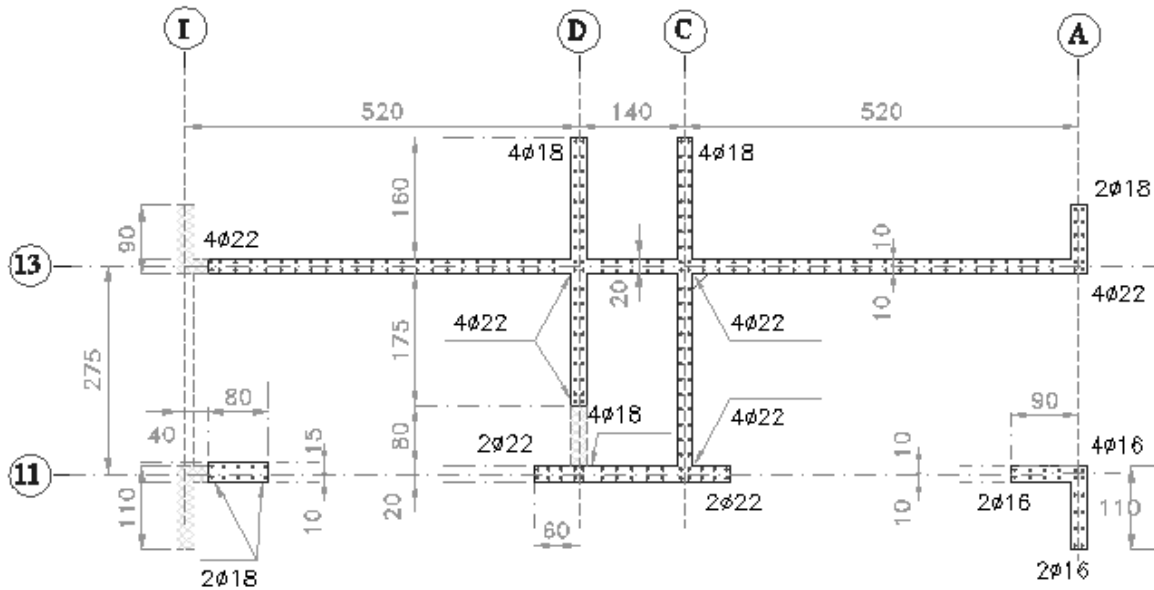


Figure 4-8. Elevation views of the walls (after Uribe, 2010)



Notes: Cross-sectional dimensions are in cm.
 φ22 means: 22mm diameter rebar.

Figure 4-9. Typical cross-sectional view of the walls in Axes 11 and 13 (@ 1st floor) (after Uribe, 2010)

4.5. Building Damage

Because the building collapsed and access was restricted, it was necessary to use multiple data sources to assess likely building damage. Primary data sources included the detailed report prepared by IDIEM (2010) that cataloged damage and identified potential factors that could have led to collapse, a site visit by J. Wallace (2010) on March 17, 2010, observed damage in similar buildings (Wallace et al, 2012), wall test results (e.g., Thomsen and Wallace, 1995, 2004), and discussions with other EERI reconnaissance team members and collaborators from Chile who visited or studied the building (see EERI Newsletter, 2010, for list of team members). From these sources, the following information was gleaned.

The building included features similar to those in other damaged buildings, such as irregularities/discontinuities near ground level, typically to accommodate parking. In general, crushing and spalling of concrete and buckling of vertical reinforcement were commonly

observed at wall boundaries of taller (>10 stories), fairly slender (height to length > 2.5) buildings with thin walls (15 to 20cm thick), where wall length was reduced significantly below grade (typically at the first subterranean level, referred to as the level (-1) in Chile). Damage at web boundaries of walls with T-shaped or L-shaped cross sections opposite the flange was common, and damage often extended along a significant portion of the wall length (EERI Newsletter, 2010; Wallace, 2011). Wall damage tended to concentrate over a short height equal to one to three times the wall thickness, apparently because buckling of vertical bars led to concentration of damage. Similar damage has been observed in tests of isolated cantilever walls (Figure 4-10) with relatively large spacing of boundary transverse reinforcement (Wall TW1, Thomsen and Wallace, 2004), where rapid strength loss occurred due to simultaneous, or nearly simultaneous, concrete crushing/spalling and buckling of wall vertical reinforcement (boundary and some web vertical reinforcement). Figure 4-11 shows the lateral load versus top displacement relation for Wall TW1. Alto Rio wall attributes are similar to those in other buildings where significant damage was observed as well as those of wall TW1 (T-shaped cross section, $8d_b$ vertical spacing of transverse reinforcement at wall boundaries, and axial load of $0.1A_g f'_c$), suggesting that similar damage may have occurred at wall web boundaries of the Alto Rio building. The discontinuities at the east side of the building suggest that damage was more likely to initiate at this location, which is consistent with the direction of the collapse (to the east).

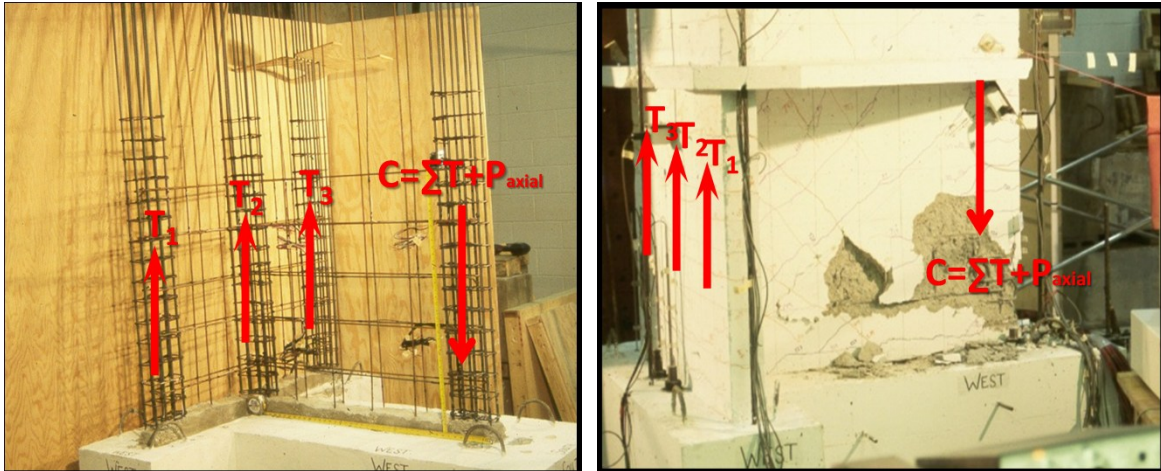


Figure 4-10. Specimen TW1 [Thomsen and Wallace, 2004]

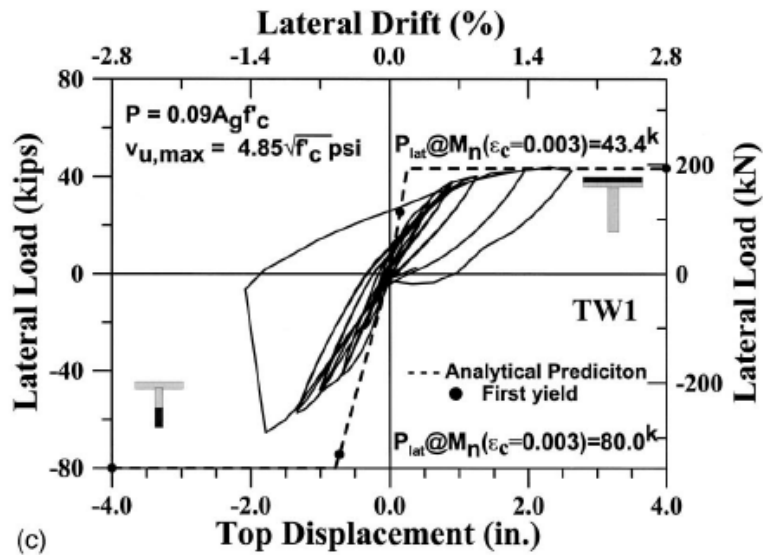
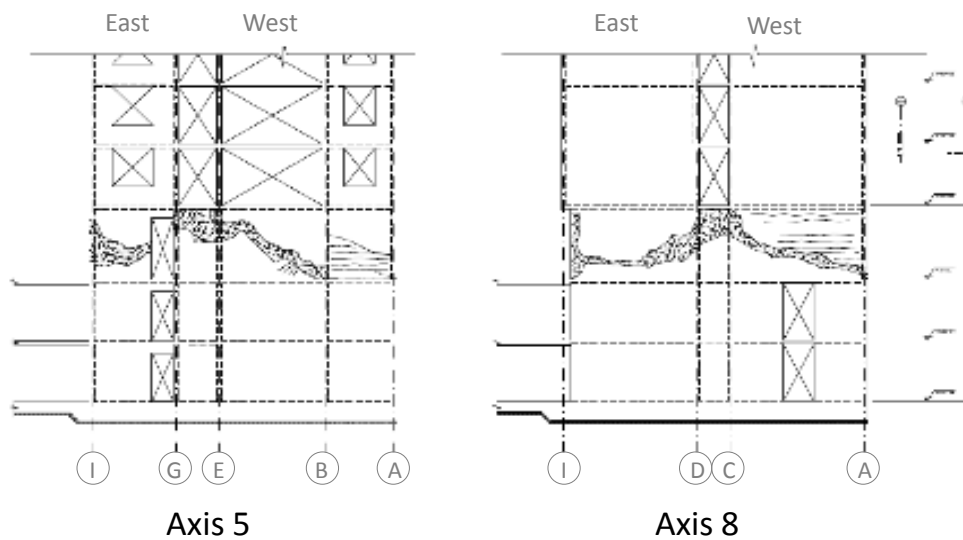


Figure 4-11. Lateral load vs. top displacement relation for specimen TW1 [Thomsen and Wallace, 2004]

Schematics of damage to transverse walls included in the IDIEM report (2010) at Axes 5, 8, 11, and 13 are reproduced in Figure 4-12. The damage along Axis 8 is consistent with concrete crushing/spalling and vertical reinforcement buckling just below the wall setback at the east edge of the building. Damage at Axis 11 is observed at the wall discontinuity (top of first story) at the east side of the building and at the ground level (bottom of first story) at the west side of the

building. Damage may have initiated at axes with T-walls (Axes 8, 13, and 20), or alternatively at the discontinuity in the L-shaped to rectangular transverse walls (Axes 11, 17, 24) at the top of the first story. In either case, once crushing/buckling initiated in either one of these walls, axial load would be redistributed, making the other wall more susceptible to failure.

The large flexural tension (horizontal) cracks along Axes 5 and 8 in the west wall indicate the development of significant tensile forces, possibly due to the compression damage at the east wall boundary leading to building rotation, placing large tensile demands on the west walls. Such large tensile demands, along with the large tensile strains that develop at the web boundary in flanged walls where the flange is in compression (as shown in Figure 4-13), could have led to lap splice failure of the boundary vertical reinforcement ($d_b = 22mm$) and web vertical reinforcement ($d_b = 10mm$), as well as the tensile fracture wall vertical reinforcement on west face perimeter walls ($d_b = 10mm$) that was observed during the site visit (Figure 4-14).



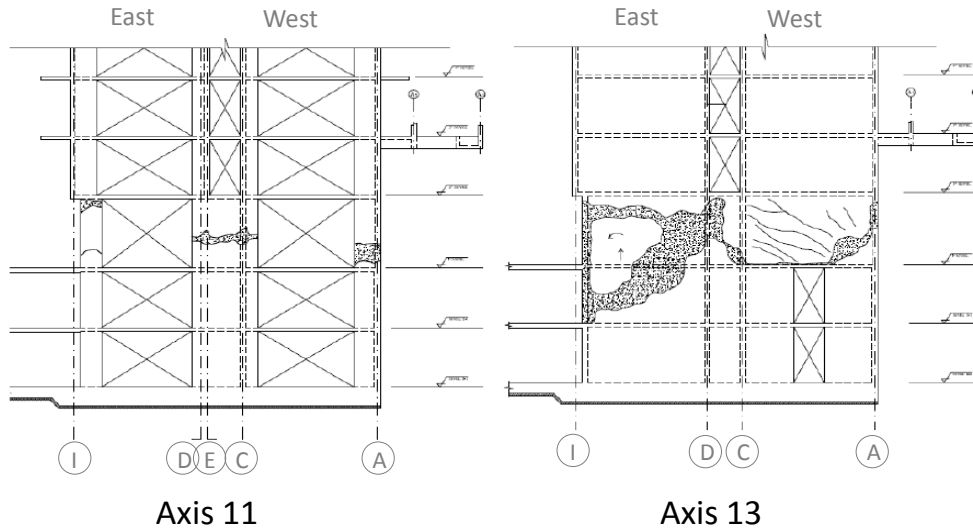


Figure 4-12. Damage at the transverse walls after the earthquake (Uribe, 2010)

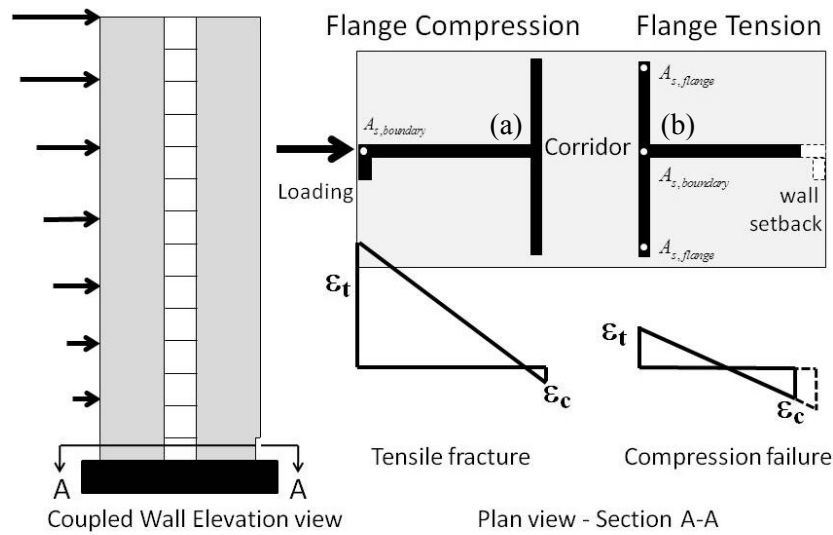


Figure 4-13. T-shaped wall strain gradients

The damage observed along Axes 5 and 8, as well as Axis 13, is consistent with the high shear demands that would be expected at these locations due to the discontinuity created by filling in the corridor openings at and below the first level and the large cyclic tension/compression demands from the walls above (Figure 4-15). Damage noted in Figure 4-12

at Axes 8 and 13 indicates that the damage could have initiated at these locations and then extended along a diagonal to connect to regions damaged due to concrete crushing/spalling and rebar buckling at the building edge and then propagated towards the central corridor. Observed damage for the east walls along Axis 8 is consistent with this hypothesis, with damage along a diagonal extending about one half the wall length, and then connecting with damage along a horizontal (due to flexural compression). The damage observed along Axis 13 is similar, except damage at the boundary extends over two levels and damage along a diagonal extends to the first below ground level (-1).

The observed damage indicates that a variety or series of factors may have influenced the building collapse, and that filling in the corridor walls may have played a pivotal role in forming a failure plane across the entire building (in the transverse direction). To gain insight into which of these factors might have played a more influential role in the collapse, analytical studies were undertaken. These studies are described in the following section.

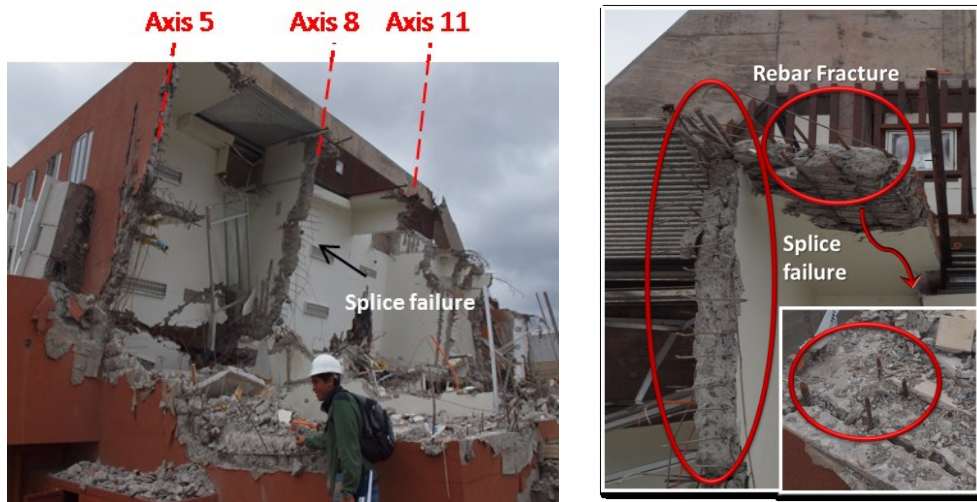


Figure 4-14. Collapsed building Torre Alto Rio

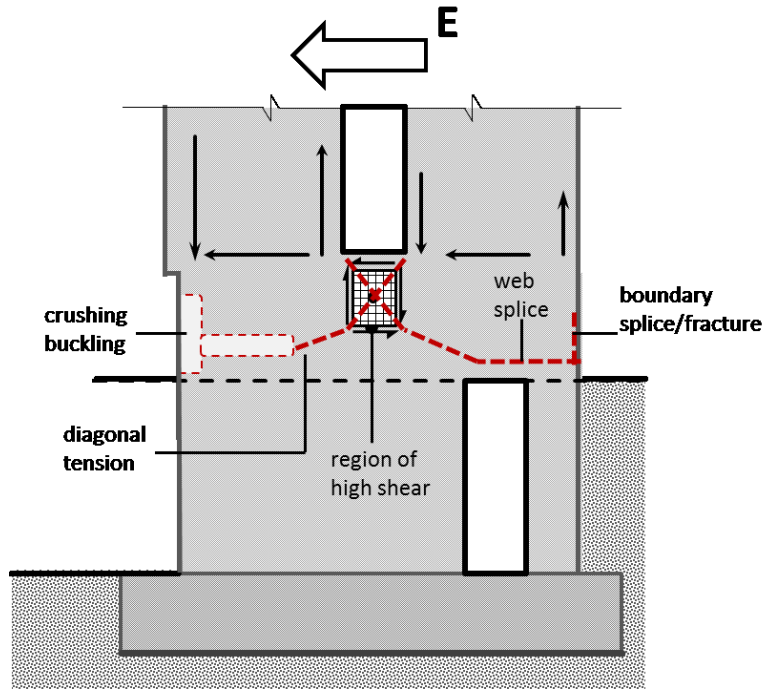


Figure 4-15. Damage illustration

4.6. Preliminary Studies

To understand the reasons for collapse, preliminary analysis was conducted using moment-curvature analysis. Curvature demand is compared with curvature capacity of one of the T-shaped walls (Axis 13; between Axes E and I). Curvature demand is calculated as 0.00012/cm using displacement-based design methodology, where spectral displacement is obtained from Figure 4-5 as 12 cm by estimating fundamental period of the building as 1 sec (Equation 4-1). In

Equation 4-2, the drift is calculated as $\frac{d_u}{h_w} = \frac{1.5S_d}{39m} = 0.0046$, whereas plastic hinge length is taken

as two times the wall thickness (i.e., $\alpha=2$) based on results presented by Wallace (2011).

Therefore, the curvature demand is estimated as $\phi_{demand} = (0.0046)(1/2 * 20cm) = 0.00012/cm$.

Curvature capacity is obtained using moment-curvature analysis and compared with curvature demand in Figure 4-16. The red solid line represents the behavior with axial load based on

tributary gravity load, whereas the blue dashed lines display the curvature demand; therefore, concrete crushing is expected (along with rebar buckling).

$$S_d(T = N/15 = 1\text{sec}) = 12\text{cm} \quad \text{Equation 4-1}$$

$$\phi_{demand} = \left(\frac{d_u}{h_w} \right) \left(\frac{1}{l_p = \alpha t_w} \right) \quad \text{Equation 4-2}$$

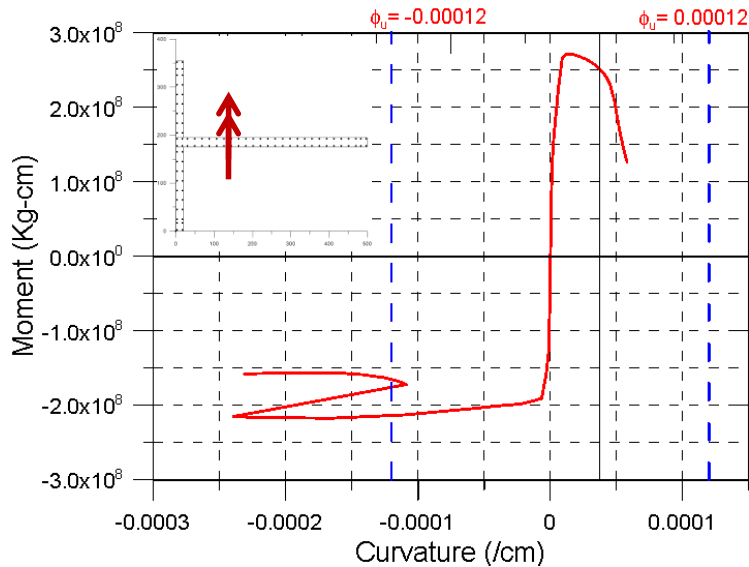


Figure 4-16. Moment-curvature relation of the T-shaped cross section

Primary lateral strength in the east-west direction was provided by walls with T-shaped cross sections (Figure 4-2), with flanges formed by the corridor walls (Figure 4-9). Therefore, when loaded, one of the T-shaped walls has flange in compression (Figure 4-13, Wall (a)), the other one (Figure 4-13(b)) has flange in tension. Once the wall web crushes/buckles, (Figure 4-13, Wall (b)), the wall shortens and causing the building to rotate/lean. Post-earthquake observations in Alto Rio (Figure 4-12), as well as other buildings (Figure 4-17), indicate that crushing/buckling of wall webs was very common for T-shaped walls, particularly when there is setback at the web boundary. Rotation of the building was likely to produce large tension on the

opposite wall (Figure 4-13, Wall (a)). Due to the large tensile force, longitudinal reinforcement fracture and splice failure are more likely. The large compression, along with the vertical wall discontinuities, were important factors leading to the observed building performance (collapse).



Figure 4-17. Examples for wall crushing: (a) Macul, Santiago [Wallace, 2010]; (b) Santiago [Moehle, 2010]

4.7. Nonlinear Analytical Studies

To better understand potential factors influencing the collapse of the Alto Rio building, a representative slice (see section of building enclosed by the broken lines in Figure 4-2(a)) of the Alto Rio building was modeled in CSI Perform 3D (CSI, 2011). Three-dimensional, elevation, and plan views of the model are presented in Figure 4-18. Structural walls were modeled using 4-node, uniaxial “Shear Wall elements” that include nonlinear axial-bending behavior (with fiber cross sections) and either a linear or nonlinear shear spring, which is uncoupled from the axial-bending behavior. Fiber cross sections were based on uniaxial stress versus strain relations for concrete and steel were for expected material strengths (expected strength of 1.3 and 1.17 times the design strength, respectively). It is noted that the difference between actual and expected material properties (Appendix B, IDIEM, 2010) were negligible; as tested concrete compression

strength was obtained as about $37MPa$ (versus $1.3f'_c = 32.5MPa$), whereas actual rebar yield strength was about $480MPa$ (versus $1.17f'_c = 491MPa$).

The stress-strain behavior of concrete prior to reaching the peak stress at a strain of 0.002 was modeled as “unconfined” using the Hognestad (1951) relation due to the lack of closely-spaced transverse reinforcement at wall boundaries with the post-peak branch was assumed to be a straight line with slope defined as suggested by Roy and Sozen (1965) (Figure 4-19a). The tensile strength of concrete was neglected.

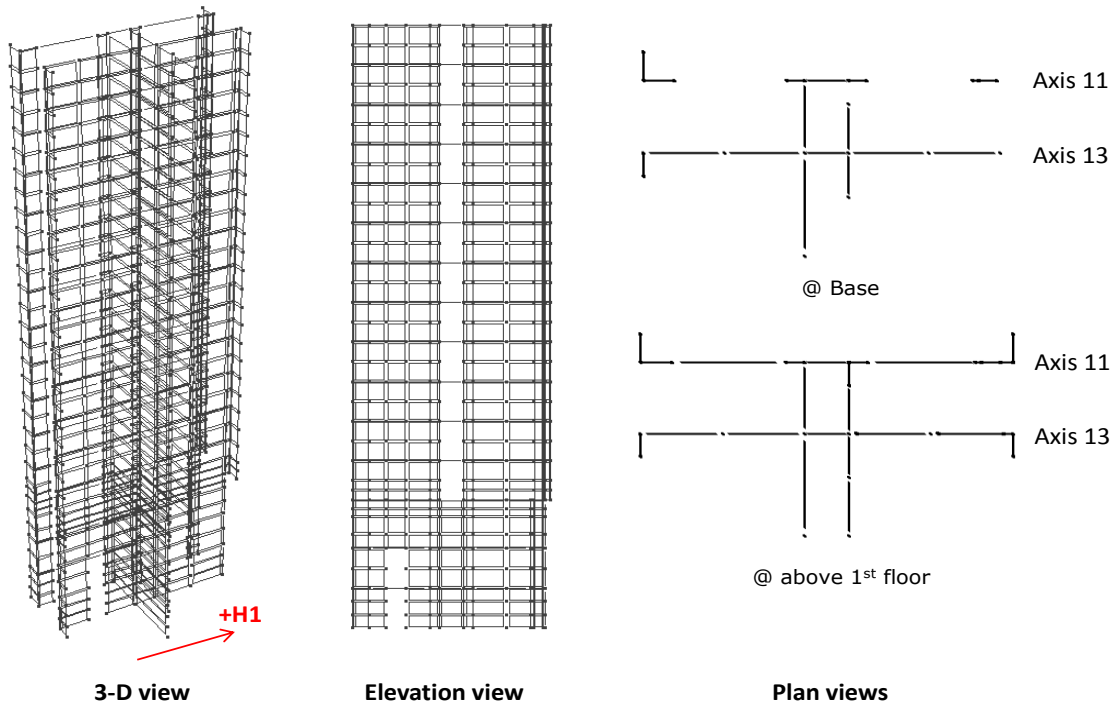
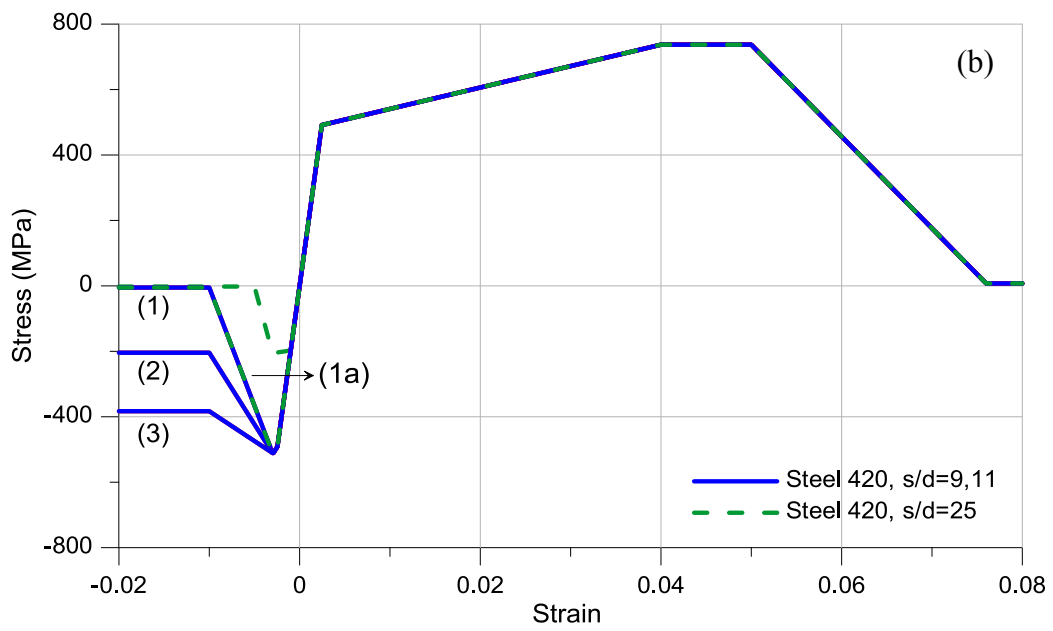
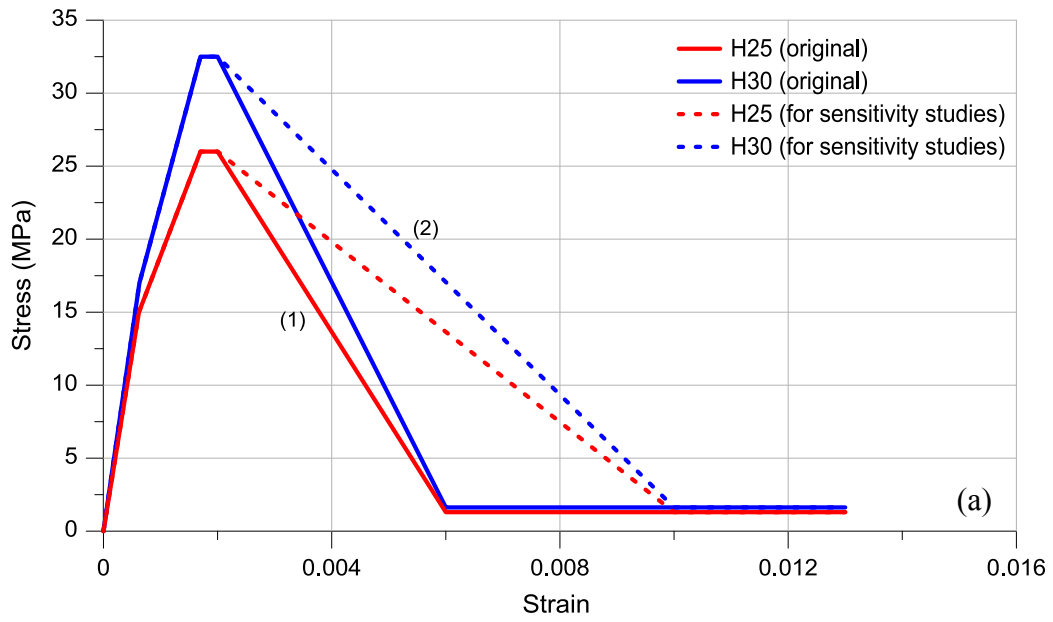


Figure 4-18. Views of the structural model in Perform 3D



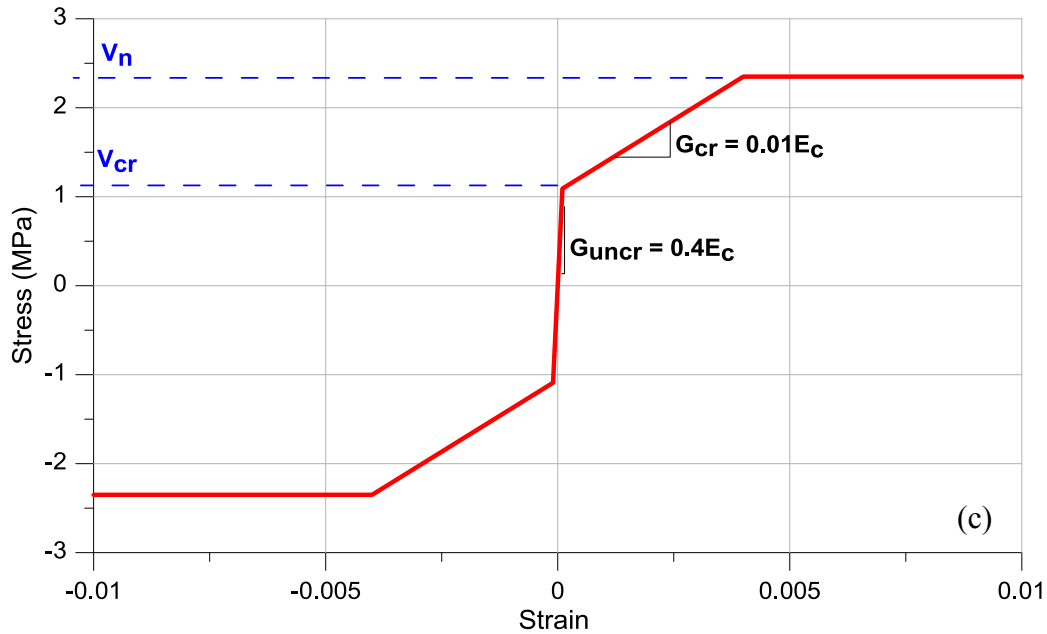


Figure 4-19. Material stress-strain relationships: (a) Concrete, b) Reinforcing Steel, (c) Shear material

Stress-strain relations of the reinforcing steel were defined using tri-linear relationships as shown in Figure 4-19b. Tensile behavior was modeled with expected yield strength of $f_y = 490\text{MPa}$, ultimate strength of 737MPa ($f_u = 1.5f_y$), with a stress drop to zero at a strain of 0.05 to represent rebar fracture (PEER/ATC-72, 2010). In compression, buckling of reinforcement was incorporated into the model based on a review of analytical models and experimental results (Cosenza et al., 2006; Bae et al., 2005; Rodriguez et al., 1999; Massone et al., 2010). A significant number of monotonic compression tests conducted on rebar specimens have revealed that the ratio of hoop/tie spacing to longitudinal bar diameter (s/d_b) has a significant effect on the stability of reinforcement subjected to cyclic tension and compressive forces; therefore, bar buckling was classified into two groups ($s/d_b = 9$ to 11; and $s/d_b = 25$) to determine the associated constitutive relationship. Given the s/d_b ratios, the limiting rebar compressive stress f_s at buckling was computed for each s/d_b ratio ($s/d_b = 9, 11, 25$) using

Tangent modulus theory:

$$f_s = \frac{E_t}{\left(\frac{s}{d_b} \frac{4k}{\pi}\right)^2} \quad \text{Equation 4-3}$$

where k is the effective length factor, and E_t is the initial modulus of elasticity. The effective length factor was assumed as 1.0 (pinned-pinned connection), because test results (Cosenza et al., 2006) show that end-restraint for large (s/d_b) ratios is not significant. For s/d_b ratios of 9 and 11, the compressive stress f_s computed with Equation 4-3 was approximately equal to the yield stress, which was also consistent with results reported by Cosenza et al. (2006) and Bae et al. (2005). Reinforcement with s/d_b of 25 (e.g., 8mm diameter web vertical bars supported by 8 or 10mm diameter web horizontal bars spaced at 200mm on center), develop less than half the yield stress at buckling using Equation (4-2); although it is possible that the restraint provided by cover concrete would allow larger compressive stress to develop prior to buckling. To address this issue, a small yield plateau was defined, with stress loss assumed to occur at a strain of 0.003, corresponding to concrete spalling, i.e., bars are assumed to buckle once the surrounding concrete reaches a compressive strain of 0.003. The stress capacity for smaller s/d_b ratios were assigned a value of near zero at a strain of about 0.01 based on the observed buckling behavior in reinforcing bars under cyclic loading reported by Massone et al. (2010) and Rodriguez et al. (1999); Cosenza et al. (2006) and Bae et al. (2005) report a modestly larger strain value for monotonic tests. A strain at zero stress of 0.005 was estimated for s/d_b of 25 by extrapolating results for the lower s/d_b ratios.

The stress-strain relations for reinforcement in compression were modified to reflect the influence of buckling as shown in (Figure 4-19b). The cyclic response of the reinforcement

model was adapted to ensure strength loss in tension also resulted in strength loss in compression, and vice versa. A limited study was conducted to assess the sensitivity of model results to the assumed steel stress-strain relations, with the primary parameters being the peak stress achieved for s/d_b of 25 and the slope of the descending branch after reaching a strain of 0.003; these results are reported later.

Shear behavior was modeled using a trilinear relation similar to that recommended by ASCE 41-06 Supplement #1 (Figure 4-19c). For short wall segments controlled by shear, such as wall segments below corridor openings, test results for lightly-reinforced walls reported by Massone (2006) were used to define the shear force - deformation relation. For slender walls, test results by Thomsen and Wallace (2004) along with calibration studies conducted by Gogus (2010) (see also PEER/ATC-72, 2010) were used to define the shear-force versus deformation relations. For both cases (shear-controlled wall segments and slender walls), the uncracked shear modulus was taken as $G_c = E_c / 2(1 + \nu) \approx 0.4E_c$ and shear (diagonal) cracking was assumed to occur at $0.25\sqrt{f'_c} \text{ MPa}$ ($3\sqrt{f'_c} \text{ psi}$), but not greater than $0.5V_n$, where V_n is the ACI 318-08 nominal wall shear strength. For slender walls, the post-cracking slope was taken as $0.01E_c$ based on the calibration studies reported by Gogus (2010) for wall test RW2 reported by Thomsen and Wallace (2004); the reduced post-cracking modulus accounts for nonlinear shear deformations due to shear-flexure interaction (Massone et al, 2006). The same post-cracking slope was used for shear-controlled wall segments based on results reported by Massone (2006) for lightly-reinforced wall segments with low axial load (see also ASCE 41-06 Supplement #1 and Elwood et al, 2007).

T-shaped walls along Axis 13 were modeled using two vertical panel-type elements per

floor, except adjacent to the discontinuity at the top of the first story (Figure 4-20). Use of two elements per story results in an element height of about one-half the wall length, a value commonly used to represent the plastic hinge length of slender walls. Two elements over one-half of the story height were used adjacent to the discontinuity (wall setback) at the top of the first story (Figure 4-18), producing an element height of 50cm or 2.5 times the wall thickness. In general, smaller element heights lead to strain concentration; however, post-earthquake observations indicated that wall damage was typically concentrated over a wall height of 2 to 3 times wall thickness (Wallace, 2011), because the lack of well-detailed boundary regions led to concentration of damage (crushing/spalling of concrete and buckling of vertical reinforcement). Along the wall webs for Axis 13, two, equal-length elements were used. Where openings existed, e.g., level (-1) on the west wall web at Axis 13, three horizontal elements were used to allow for the opening. A moderately refined mesh was used at the wall discontinuity created at the top of story one at the east side of the building at Axis 11, where the 20cm-thick L-shaped wall (stories 2-15) transitions to a 25cm-thick rectangular wall below, with a modest offset (Figure 4-20). As-built drawings (IDIEM, 2010) indicated that only three of the four vertical reinforcing bars at the discontinuity were properly lap spliced; therefore, vertical reinforcement within elements above and below the discontinuity were adjusted to reflect this (Figure 4-20). The discontinuities in the concrete section and the vertical reinforcement help explain the damage noted at the top of the first story at the east side of the building in Figure 4-12 for Axis 11. This discontinuity does not exist at the west side where damage is noted at ground level.

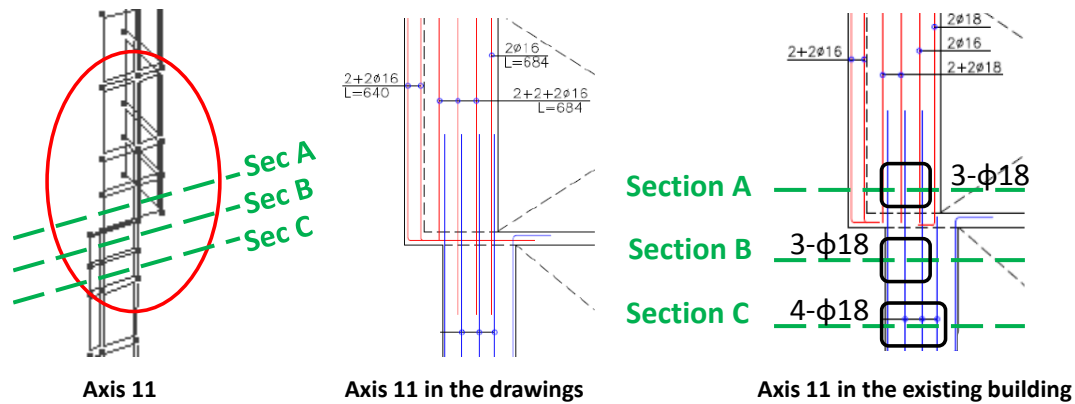


Figure 4-20. Analytical meshing of the model

Elastic beam elements with rigid-plastic moment hinges were used to model slab coupling across the central corridor and between the corridor walls and the walls at the perimeter of the building at Axis 11. The slab effective width across the corridor was taken as the full slab width along Axis 13, whereas the effective width along Axis 11 was taken equal to the wall width plus one slab thickness on either side of the wall web. According to structural drawings, the slab across the corridor was 15cm thick and reinforced with 10mm bars spaced at 15cm (top and bottom), whereas slabs between the corridor wall and the east and west faces of the building were typically reinforced with 8mm@15cm top and bottom bars, parallel to Axis 11 and 13. The elastic stiffness of the slab-beam was taken as $0.3E_cI_g$; sensitivity studies indicated that results were insensitive to the stiffness value selected. The nonlinear moment-rotation hinges were modeled as elastic, perfectly plastic with a yield moment determined from the reinforcement provided within the defined effective width. Strain hardening was neglected in the model. To ensure proper end fixity in the Perform 3D model, the slab-beams were embedded into the wall (connected to wall elements) with relatively large stiffness based on recommendations by Powell (2007).

A unit floor self-weight of $1000\text{kgf} / \text{m}^2$ was determined based on a detailed assessment of building component weights, which is the same value reported by Wood et al. (1987) for typical buildings in Chile. Gravity loads and seismic masses were calculated by multiplying the floor weight/mass by the tributary area of each wall, and assigned at the corners of L-shaped walls and mid-points of the rectangular wall segments. Lateral displacements in the transverse direction of the building (H1, Figure 4-18) were constrained to be equal at each floor level (i.e., a rigid floor diaphragm was assumed), whereas, the displacements in the orthogonal direction (H2) and out-of-plane rotations were restrained, since only a strip of the building was modeled to assess responses in the transverse (collapse direction).

A series of studies were conducted to address the sensitivity of results (e.g., periods, mode shapes, displacements, strains) to material, element, and mesh parameters. Results are presented in Section 4.9 for some response quantities.

4.8. Analysis Results

The analytical model was subjected to gravity loads and mode shapes and periods were determined; the first three periods and mode shapes of the model are presented in Table 4-1 and Table 4-2, respectively. The fundamental period of the structure ($T_1 = 0.7s$) corresponds to $N/20$, where N is the number of stories, which is consistent with results reported for typical pre-1985 buildings in Chile (Wood et al, 1987; Massone et al, 2012).

Table 4-1. Period and mass participation summary

| Vibration mode | Slabs (Yes/No) | Period | Mass participation |
|----------------|-------------------|-----------------------------------|--------------------|
| 1 | Yes | 0.70 seconds (N/20) | 68% |
| | No | 0.77 seconds (N/18) | 66% |
| 2 | Yes | 0.14 seconds (T ₁ /5) | 19% |
| | No | 0.15 seconds | 20% |
| 3 | Yes | 0.06 seconds (T ₁ /12) | 7% |
| | No | 0.06 seconds | 7% |

Table 4-2. Normalized displacements based on modal analysis results

| Level | Mode 1 | Mode 2 | Mode 3 |
|-------|--------|--------|--------|
| -2 | 0.00 | 0.00 | 0.00 |
| -1 | 0.00 | 0.00 | 0.00 |
| 1 | 0.02 | -0.14 | 0.38 |
| 2 | 0.05 | -0.32 | 0.78 |
| 3 | 0.10 | -0.50 | 0.99 |
| 4 | 0.16 | -0.68 | 1.00 |
| 5 | 0.23 | -0.81 | 0.78 |
| 6 | 0.31 | -0.88 | 0.37 |
| 7 | 0.39 | -0.86 | -0.12 |
| 8 | 0.48 | -0.76 | -0.56 |
| 9 | 0.56 | -0.57 | -0.83 |
| 10 | 0.65 | -0.32 | -0.85 |
| 11 | 0.74 | -0.01 | -0.61 |
| 12 | 0.83 | 0.32 | -0.17 |
| 13 | 0.91 | 0.67 | 0.39 |
| 14 | 1.00 | 1.00 | 0.95 |

4.8.1. Nonlinear Static (Pushover) Analyses

The analytical model was subjected to gravity analysis, followed by static pushover (nonlinear analyses in the +H1 (east, collapse) and -H1 (west) directions using a lateral force pattern associated with the first mode shape. Limit states were defined for concrete, steel, and shear materials as follows: compressive strength degradation in concrete (at $\varepsilon = 0.002$, referred as “Concrete comp. degrades”), maximum compressive strain reached in concrete (at $\varepsilon = 0.006$, referred as “Concrete crushing”), steel yielding (at $\varepsilon = 0.0025$, not plotted), compressive strength degradation in steel at about $\varepsilon = 0.003$, referred as “Steel comp. degrades”), maximum compressive strain reached in steel (at $\varepsilon = 0.005$ and $\varepsilon = 0.01$ for the bars with $s/d_b = 25$ and $s/d_b = 9,11$, respectively; referred as “Steel buckling”), maximum tensile strain reached in steel (at $\varepsilon = 0.08$, referred as “Steel fracture”), and maximum shear strain reached (at $\gamma = 0.01$, referred as “Shear failure”).

Results presented in Figure 4-21 indicate an abrupt stiffness change at approximately 0.1W due to shear cracking, followed by initial yield of wall boundary reinforcement, and then gradual softening as vertical web reinforcement yields. Significant lateral strength loss in the +H1 direction occurs at approximately 0.9% drift due to concrete crushing and rebar buckling at the east boundaries of T-shaped wall along Axis 13; defined limit states for the +H1 direction are fairly closely grouped. In contrast, significant lateral strength degradation for the -H1 direction occurs at a much larger drift, approximately 1.9%. Results of the pushover analyses indicate that the web boundaries of T-shaped walls are susceptible to concrete crushing and rebar buckling, which was commonly observed in newer, taller buildings following the February 2010 earthquake, and that the vertical discontinuities at the east façade of Alto Rio have a significant impact of expected behavior, with abrupt strength loss in the +H1 (collapse) direction at

approximately 45% of the drift level for abrupt strength loss for -H1 loading. The potential for collapse in the +H1 direction depends on the demands expected during the February 2010 earthquake. Nonlinear response history analyses are undertaken to investigate this issue.

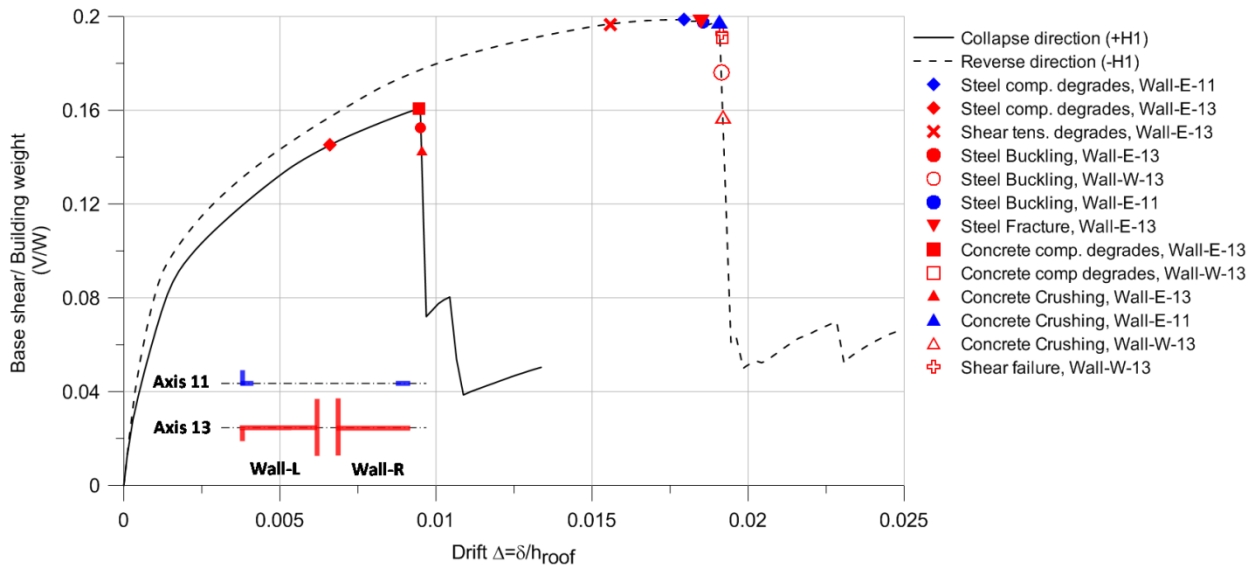


Figure 4-21. Pushover curves in positive and negative H1 directions

4.8.2. Nonlinear Response History Analyses

Following the application of gravity loading, the analytical model was subjected to the east-west component of the ground motion recorded in Concepción (see Figure 4-4). Rayleigh damping of 2.5% was used for the nonlinear response history analyses based on the recommendation of PEER/ATC Report 72. P-Delta effects were included in the analyses, whereas the stiffness reduction due to cyclic actions (cyclic degradation) was neglected.

Results of the response history analyses are given in Figure 4-22c for roof level lateral drift. A peak roof displacement of 44cm (1.4% drift) is reached before significant strength loss (at around $t=20$ sec, Figure 4-23) occurs due to concentration of damage in the East T-wall along Axis 13. To assess the potential for collapse, analysis results were post-processed to determine average vertical (axial) strains at various locations. Results shown in Figure 4-22(a) for

maximum, average vertical compression strains for elements over the building height indicate that, for both Axes 11 and 13, strains concentrate at the vertical discontinuity. Compressive strain histories over a single element and average values over the first story (gage) are shown in Figure 4-22(b), revealing that strain values rapidly increase to values in excess of 0.03 at the east ends of Axis 11 (at about $t = 22$ sec) and Axis 13 (at about $t = 20$ sec) over the first floor (Figure 4-22(b, c)). Results of the model became unreliable after this point.

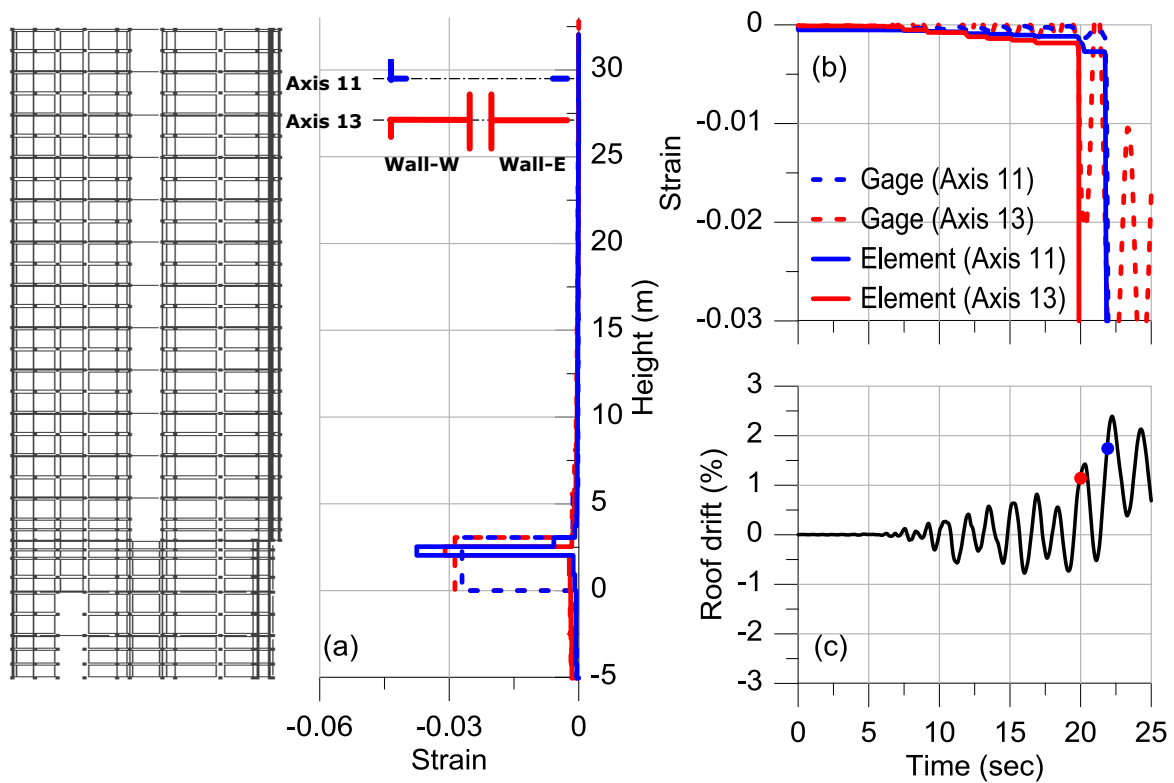


Figure 4-22. Compressive strain demands at the east-side walls and failure assessment

Maximum element compression and tension strains at the boundaries of walls on each side of the corridor are shown in Figure 4-24 at the base of the building (up to $t = 22$ sec). As noted for Figure 4-22, large compressive strains occur near the discontinuities at the east façade. At the west façade, fairly large tensile strains, on the order of 0.01 to 0.02, develop over the first

story (after the large compressive strains develop at the east façade), where the discontinuities do not exist. The splice failures (Figure 4-14) and flexural (horizontal) cracks shown in Figure 4-12 are consistent with the development of large tensile strains (up to 2%).

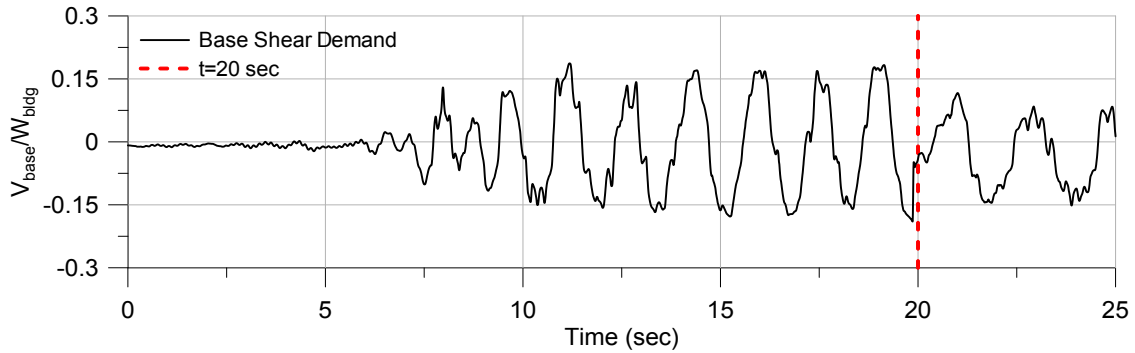


Figure 4-23. Base shear response history

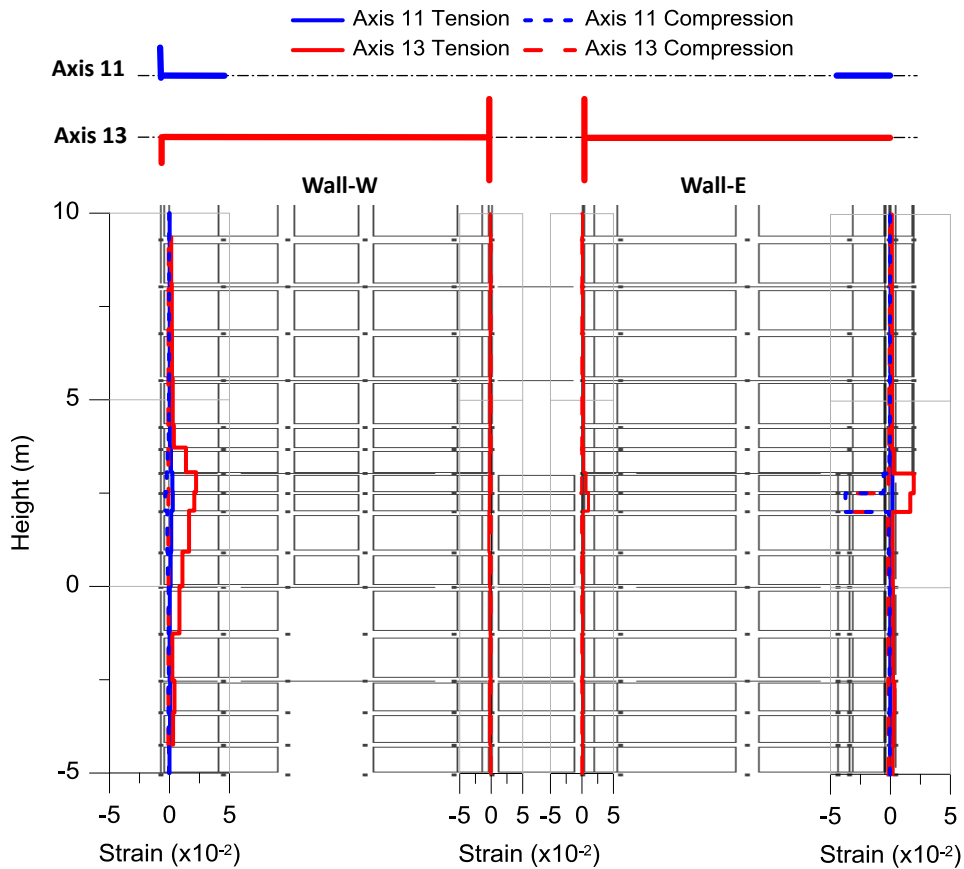


Figure 4-24. Maximum strain demands at the transverse walls

Models of the building with and without slabs were analyzed to assess the influence of floor slab coupling on system and wall responses. Moment versus rotation for the slab across the corridor at Axis 13 is presented in Figure 4-25, whereas the response with and without slabs is compared for roof drift and wall axial load in Figure 4-26. Figure 4-25 indicates that large slab rotations (about 0.03 rad) develop, which is not unexpected, as corridor slab damage was observed in a number of buildings (Wallace et al, 2012). Including slab coupling results in modest variation of wall axial load at the first floor, from $0.06A_g f'_c$ to $0.13A_g f'_c$ (versus approximately $0.09A_g f'_c$ for the no-slab case), and about a 10% reduction in roof drift (Figure 4-26a) over the no-slab model.

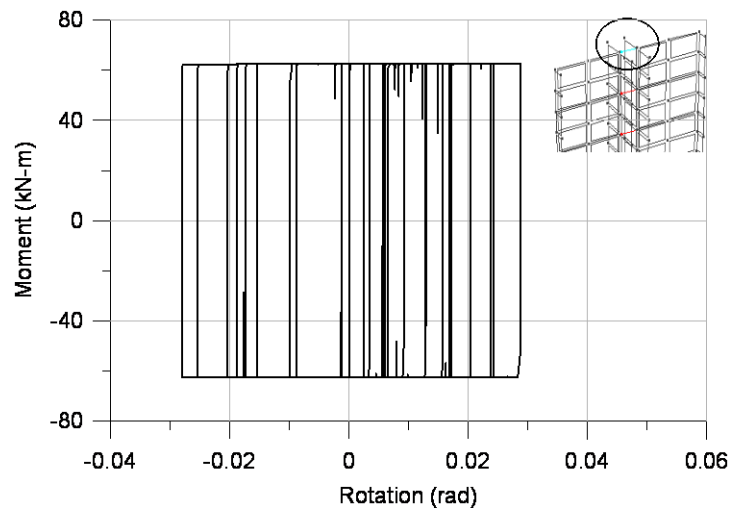


Figure 4-25. Moment-rotation relationship for the top floor slab in Axis 13

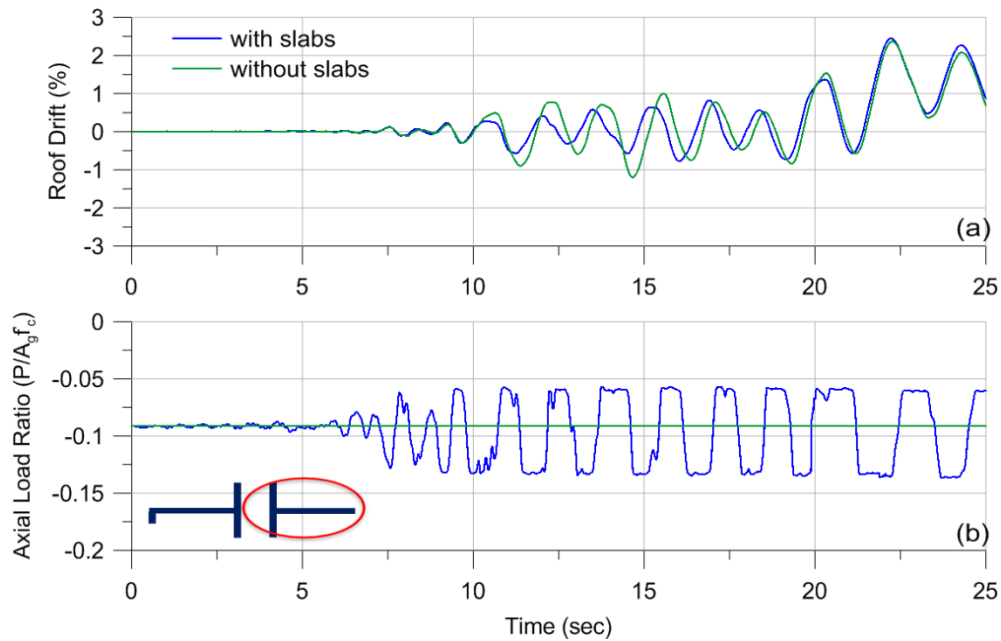


Figure 4-26. Comparison of the models with and without slabs

The analysis results clearly indicate that the Alto Rio building was susceptible to collapse towards the east, with the primary factors impacting the behavior being the wall configuration (T-shaped cross section), the lack of closely-spaced transverse reinforcement at wall boundaries, the vertical discontinuities that existed at the east façade, and also the variation of wall axial load due to corridor slab coupling and redistribution of axial load after damage concentrated in any given wall. Observed damage is reasonably consistent with the analysis results. However, a fairly large number of buildings, including about 10 in Concepcion, had somewhat similar features and did not collapse. Additional features of this building, such as the filled-in openings that created regions of high shear (Figure 4-27), splices of web vertical bars, and splices of vertical boundary bars that lacked sufficient transverse reinforcement, also may have contributed to the collapse (Figure 4-15). The potential impacts of these items are discussed in the following paragraphs.

The potential impact of discontinuities and openings near the base of the building, such as the shear demands in the filled-in corridor wall at Axis 13 were assessed using a truss (strut and

tie) model (Figure 4-27). Forces at the top of the free-body diagram were determined for a triangular-distribution of lateral forces over the building height, with magnitude determined to produce a moment equal to the wall nominal moment capacity of the east wall at the ground level. The lateral forces acting on the west wall were proportional to the stiffness of the wall, determined from a moment – curvature analysis including the impact of variation of axial load. The shear demand in the below the openings above for the filled-in corridor wall was represented by diagonal tension and diagonal compression members, with $T_u = 2670kN$ and $C_u = 3960kN$, respectively. The demands were compared to the strut/tie capacities based on strut/tie properties, e.g., strut properties (effective area per ACI 318-11, Appendix A, for a prismatic strut), and the quantity and yield strength of tie reinforcement. The nominal compressive strength of the struts were obtained based on ACI 318-08 (Equation A-2); however, a conservative (high) estimate of capacity was obtained by neglecting the concrete strength reduction (β_s), whereas the tensile strength of the ties were calculated by multiplying the steel yield strength by the effective area of reinforcement acting perpendicular to the cross-section. Demand to capacity ratios (DCR) are presented in Figure 4-27 (red colored, in parenthesis) for the diagonal elements at the first floor and indicate that the tie demands below the corridor opening are significantly greater than the estimated capacities (DCR ratios are 12.7 and 1.2 for the diagonal tension and compression, respectively). Given these values, wall web reinforcement below the opening would be expected to yield significantly in tension, and upon reversed loading, would buckle in compression, leading to “shear” damage below the opening as shown in Figure 4-12. Demand to capacity ratios also were calculated for diagonal struts (east wall) and tie (west wall, tie 2-3). For the east wall, the DCR is 0.1, indicating a low likelihood of damage; whereas for the west wall, DCR for the tension tie is 2.0, which implies that tension yielding could occur (this tension tie is still

needed after damage below the opening occurs).

The ability of the slab above the filled-in corridor wall to transfer the forces developed in the truss model also were assessed. Slab reinforcement consisted of $8\text{mm}@150\text{mm}$ and 2- 18mm bars within the wall web (Figure 4-27); therefore, the tie strength (T_n) across the top of the filled-in corridor wall is approximately 345 kN, if 2- 18mm bars along with an additional 12- 8mm bars (0.9m on each side of the wall web) are assumed to contribute, whereas the demand is 320 kN; therefore, sufficient slab reinforcement existed, suggesting that the failure of the filled-in wall would occur prior to slab (diaphragm) failure.

The damage at the filled-in walls would likely occur prior to flexural-compression damage at wall edges along the east side of the building, both at the web of T-shaped walls (Axis 13), and at the L-shaped walls (Axis 11). Spalling of concrete and lack of ties at the boundaries resulted in buckling of longitudinal bars very soon after concrete crushing, causing the building to rotate/lean towards east. Poor splice details, especially in some west transverse walls at ground line, may also have made the building susceptible to overturning, especially after the boundary zones at the west edge of the building were damaged (i.e., concrete crushing and buckling of boundary longitudinal reinforcement). Once the building leaned east, larger tension demands (Figure 4-24) were placed on the transverse walls west of the corridor, possibly leading to fracture and splice failures at wall web boundaries and splice failure of web vertical reinforcement. High shear stresses (Figure 4-27), along with flexural compression damage in the asymmetric (T-shaped) walls, the unconfined wall splices of vertical boundary and web reinforcement, and the long duration of strong shaking, created the potential for damage to propagate across the entire wall length, as shown in Figure 4-15).

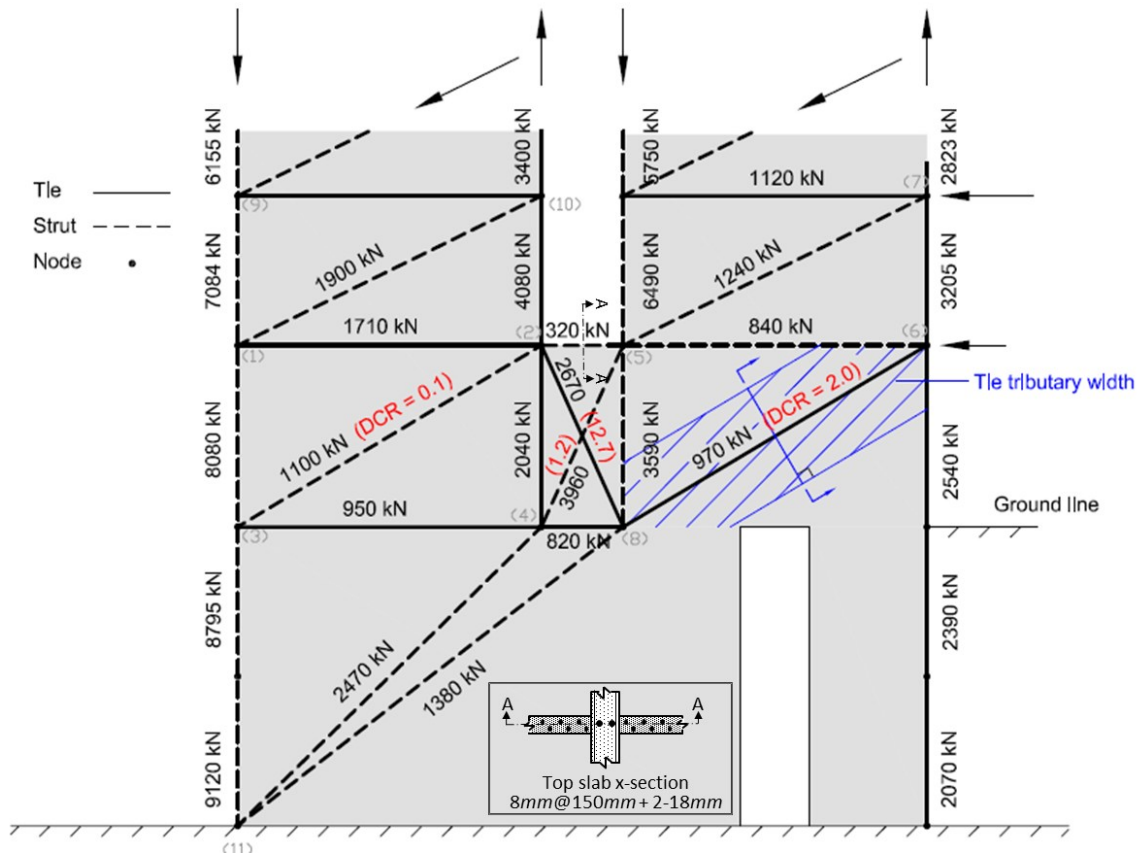


Figure 4-27. Strut and tie model and assessment of shear demands in the filled-in corridor walls (Axis 13)

4.9. Sensitivity Studies

Sensitivity of computed results, such as periods, roof drifts, and wall compressive strain to model mesh (Figure 4-29a) and material parameters (Figure 4-19) was investigated (Figure 4-29b). Roof drift and wall compressive strain (east wall) comparisons for six different cases indicate that computed results are not very sensitive within the range of variation considered; results for axial strains and roof drifts, respectively, are compared in Figure 4-29b and Figure 4-29. Results indicate that use of a coarser mesh and variation in the slope of the descending branch of the concrete compressive stress-strain relation produce only modest changes in the drift profile as damage concentrates; however, the overall results are not impacted (i.e., damage concentrates at

around time equal to 20 to 22s for all models). The variations become more significant after the failure along Axis 11, however, the results are considered to be unreliable after this point, based on a detailed review of analysis results. (See Figure 4-22 (b): strains reach unrealistically large values after $t=22$ sec).

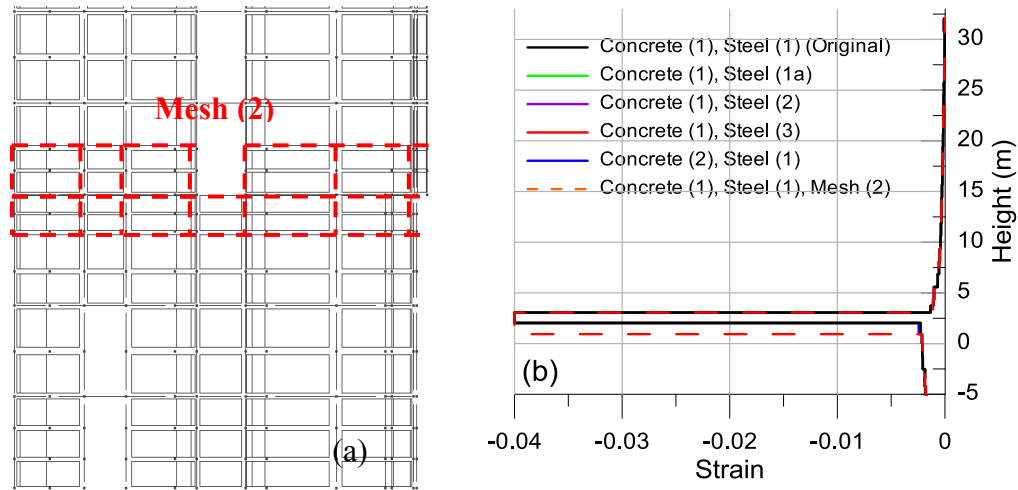


Figure 4-28. (a) Alternative meshing for sensitivity studies and (b) comparisons of strains for six different cases

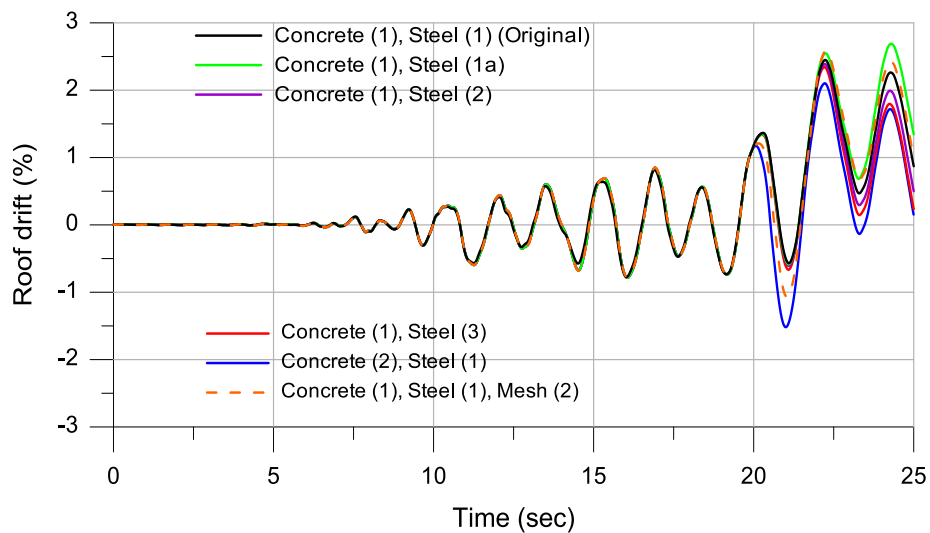


Figure 4-29. Roof drift comparisons for six different cases

4.10. Failure Assessment Using Ductility Approach

Failure assessment of the shear walls in the Alto Rio building was also considered using the ductility approach presented in Chapter 3. However, as noted in the prior sections, damage and collapse of the Alto Rio building was more likely due to flexural compression (concrete crushing, rebar buckling) and the influence of discontinuities (openings, filled-in wall sections); therefore, reassessing the role of wall shear in the continuous walls was not undertaken.

4.11. Summary and Conclusions

The $M_w = 8.8$ February 27, 2010 Chile Earthquake provides an excellent opportunity to study the performance of tall reinforced concrete buildings designed using a modern seismic code and reinforced concrete design provisions based on ACI 318-95. The 15 story residential building, Torre Alto Rio, was the only modern, tall reinforced concrete building to collapse during the earthquake. Ground accelerations recorded near the building indicate that the building was subjected to more than two minutes of strong shaking and that spectral displacement demands in the vicinity of the building were two to three times that used for design. Demands near the effective (cracked) fundamental period for Alto Rio were similar to other buildings; however, once damage initiated, period elongation would produce higher displacement demands (about 2 to 4 times) those for locations outside of downtown Concepcion.

Reasons for the collapse were studied using post-earthquake observed damage, structural drawings, nonlinear static and dynamic response analyses, and a strut-and-tie model. A detailed nonlinear finite element model of a representative slice of the building was developed that included wall setbacks and irregularities, as well as the actual reinforcement details. The fundamental period of the building model was computed to be $N/20$, which is consistent with reported periods for low-amplitude vibrations. Based on the pushover analysis results, significant

lateral strength degradation was expected at 0.9% and 1.9% drift for the +H1 and -H1 directions, respectively. Strength degradation in the pushover analysis was primarily attributed to concrete crushing/spalling and rebar buckling at the east side of the building (at wall web boundaries). Model results are consistent with damage observed at a fairly large number of buildings in the impacted region, as well as with the direction of the observed collapse.

Post-processing of the nonlinear response history analysis results indicated that compressive concrete and rebar strains rapidly reached very large values (exceeding 0.03) at the web boundary of the T-shaped wall cross section (at the east side of the building) relatively early in the response history ($t= 20$ seconds). Similar results would be expected for other T- and L-shaped walls in the building (although these walls were not modeled). Damage observations from other buildings as well as prior test results for a poorly detailed wall boundary of a T-shaped wall indicate that web boundaries at the east façade of the Alto Rio building were susceptible to flexural compression damage (concrete crushing and rebar buckling). Test data indicate that this type of failure tends to be abrupt, extend significantly into the wall web, and produces significant lateral strength loss (about 90% in the test). Discontinuities, both in cross section and in vertical reinforcement, likely led to a concentration of damage at the top of the first story in the walls at the east edge of the building at Axis 11 (and also Axes 5, 17, and 24). Slab coupling across the corridor reduces drift demands only modestly (about 10%), whereas slab coupling causes only a modest variation in wall axial stress ($-0.09A_gf'_c \pm 0.03A_gf'_c$). Analysis results were generally consistent with reported damage; however, significant wall damage was observed in other buildings that did not collapse.

Other features of the building also may have contributed to the collapse, such as walls placed across the corridor at the first story at Axes 8, 11, 13, wall openings within the first story

and the first subterranean level, and splices of wall vertical boundary and web reinforcement. A strut and tie model was used to assess potential impacts of discontinuities and openings near the base of the building and revealed that slabs were capable of carrying the lateral loads; whereas the wall web reinforcement below the opening would most likely yield in tension, and would buckle under reversed loading, resulting in shear damage below the opening. This damage would likely occur prior to flexural-compression damage at wall edges along the east side of the building. The poor splice details, especially in some west transverse walls at ground line, may have made the building susceptible to overturning once boundary regions of the east walls and corridor walls were damaged, leading to reduced overturning resistance of the building. Each of these factors created conditions that made extension of damage across the entire wall length in the transverse direction more likely.

The larger spectral displacement demands, along with the long duration of strong shaking also likely played a factor, as the analytical studies suggest collapse potential after about 20 seconds of strong shaking, whereas strong shaking continued for approximately another 30 seconds.

Lessons learnt from the collapse of Alto Rio building include:

1. As discussed before, one of the major reasons for collapse was stress concentrations at the discontinuities on the east side of the building. Therefore, severe vertical discontinuities and setbacks should be avoided or the impact on expected behavior carefully assessed.
2. It was noted that the Chilean concrete code does not require special boundary elements at wall boundaries. Use of tightly-spaced transverse reinforcement at wall

boundaries is essential, especially at the discontinuity regions (if any). Alternatively, thicker walls could be used in the sensitive regions.

3. Another major reason for collapse was found to be the high shear demands in the filled-in corridor walls at the first story. To avoid this failure, partition walls could be used instead of solid walls, or if possible, filled-in openings and cross-sectional discontinuities should be avoided.

Behavior of the Alto Rio building was examined using nonlinear response history analysis. Although the analysis results were consistent with observed damage, the reliability of the model was somewhat uncertain because the building did not have sensors to measure the actual response quantities. Therefore, nonlinear modeling and analysis of the four-story reinforced concrete building that was tested on E-Defense shaking table (in December 2010) is investigated in Chapter 5 as a means to validate the modeling techniques used in this Chapter. As well as Chapter 2, and to identify issues that still require additional study.

Potential reasons for collapse show that Alto Rio building has different failure issues than the failure modes discussed in Chapter 3, i.e., flexural compression and rebar buckling and shear failures at discontinuities. Thus, although important to understand possible reasons for the collapse of the Alto Rio building, it is not very representative of buildings constructed in the U.S., and the ground motions also tend to be different (large, subduction event). Study of the E-Defense building was undertaken to address this need for a building generally consistent with those constructed in the United States.

Chapter 5 2010 E-Defense Four-Story Reinforced Concrete Building - Comparative Study of Experimental and Analytical Results

5.1. Introduction

The 2010 NIED E-Defense tests included testing of two buildings, a conventional reinforced concrete (RC) building, and a high-performance post-tensioned (PT) building. The two buildings were similar in geometry and configuration, with shear walls in one principle direction, and moment frames in the other direction. The buildings were subjected to increasing intensity shaking using the Kobe and Takatori records until large deformations were reached. The conventional RC building was designed according to the Japanese Standard Law (2007) and Architectural Institute of Japan requirements (AIJ, 1999), and also satisfied a majority of ASCE/SEI 7-05 and ACI 318-08 requirements for Special RC Structural Walls and Special RC moment frames (with an exception of strong column-weak beam requirements). The PT building was designed using a performance-based seismic design methodology and included high performance, post-tensioned lateral force-resisting systems. Moment frames consisted of precast pre-stressed beam and column elements, whereas structural walls utilized unbonded post-tensioned and mild steel to provide re-centering and energy dissipation characteristics, respectively. In addition, the PT building incorporated high performance materials such as high-strength concrete with steel fibers and high-strength transverse reinforcement. To meet the various design objectives, the base shear design strength of the PT building was about twice that of the RC Building in both directions.

This study focuses on providing comparisons between measured and predicted (analytical) responses for the shear wall direction of the RC Building. Although use of relatively complex nonlinear modeling approaches have become common for design of shear wall buildings (e.g., PEER/ATC 72-1, 2010), field and laboratory data for full-scale buildings subjected to multi-axis shaking are lacking to assess the reliability of these models. Experimental data are mostly available for two-dimensional, moderate-scale structures tested under quasi-static loading (including tests on: isolated cantilever wall with rectangular cross sections with and without lap splices (Thomsen and Wallace, 2004; Birely et al., 2010), cantilever walls with both rectangular and T-shaped cross sections subjected to uniaxial and biaxial loading, low-to-moderate aspect ratio isolated walls with rectangular cross sections (Tran et al. 2011)), and relatively limited buildings systems tested under uniaxial motions on shaking tables (Panagiotou al., 2008). Therefore, the full-scale, three dimensional, dynamic tests on the NIED E-Defense shaking table provide information to fill an important knowledge gap as well as a wealth of data to assess the ability of both simple and complex nonlinear modeling approaches to reliably predict important global and local responses, including system interactions. This chapter presents results obtained from nonlinear response history analyses of the RC Building along with comparisons with experimentally measured data. The model was developed using Perform 3D (CSI, 2011) because this software is commonly used in engineering practice in the United States, and similar programs are used worldwide. Preliminary results for a range of responses are compared including roof drifts, inter-story drifts, base overturning moments, floor accelerations, base wall rotations, and wall shear deformations. The test program, analytical models, and the ability of the analytical models to capture the measured responses are discussed in the following sections. Detailed information about the test program, including information about

instrumentation and ground (table) motions is available in PEER Report 2011/104 (Nagae et al., 2011).

5.2. Description of the test

The E-Defense shake table, the largest in the world, has plan dimensions of 20 m × 15 m (Figure 5-1). The table can produce a velocity of 2.0 m/sec and a displacement of 1.0 m in two horizontal directions, simultaneously, and can accommodate specimens weighing up to 1200 metric tons. In this study, two four-story buildings were tested, one RC and one PT. The two buildings were almost identical in geometry and configuration, and were tested simultaneously, as shown in Figure 5-2. Each building weighed approximately 5900 kN; therefore the combined weight of the two buildings was 98% of E-Defense Table capacity. The test buildings utilized different structural systems to resist lateral forces in the longitudinal and transverse directions. In the longitudinal direction, a two-bay moment frame system was used, whereas in the transverse direction, structural (shear) walls coupled to corner columns by slab-beams were used at each edge of the buildings (Figure 5-3). Story heights at all levels for both buildings were 3 m, for an overall height of 12 m. The plan dimensions of the buildings were 14.4 m in the *x*- or frame direction and 7.2 m in the *y*- or wall direction.

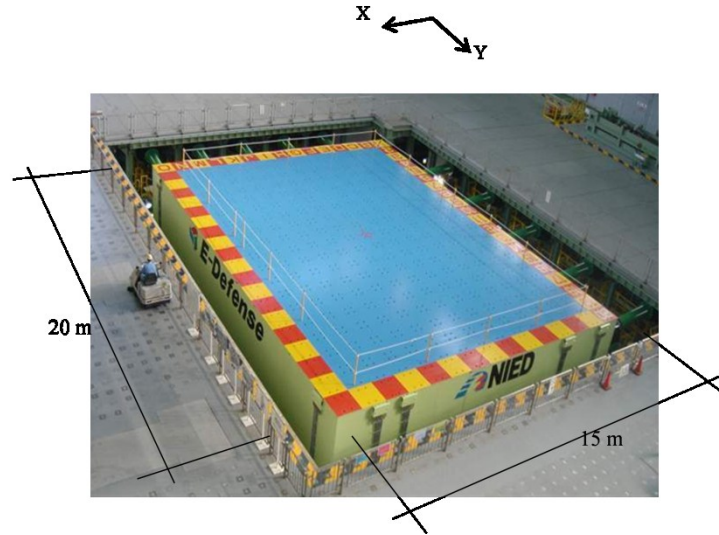


Figure 5-1. E-Defense shaking table



Figure 5-2. Overview of test set up on the shaking table

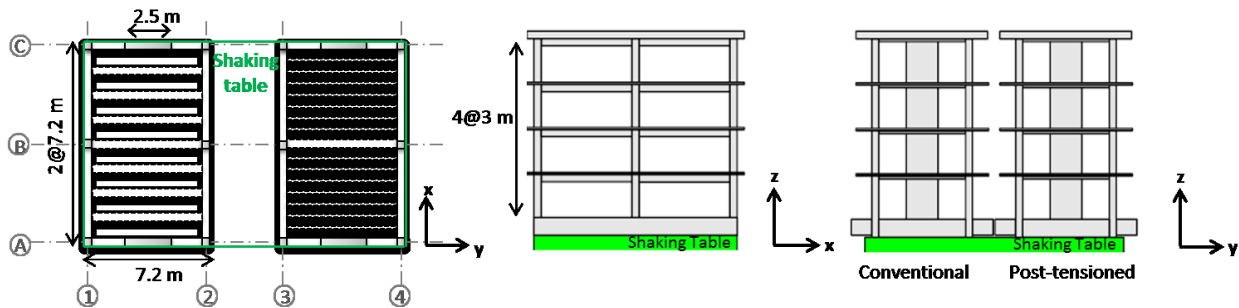


Figure 5-3. Plan and elevation views of the test specimens

5.3. Conventional reinforced concrete building (RC Building)

Plan and elevation views of the structure are shown in Figure 5-3. Cross-section dimensions of columns were 500 mm × 500 mm, and walls were 250 mm × 2500 mm; beam cross-sections were 300 mm × 600 mm (width × depth) in the x-direction and 300 mm × 400 mm for interior beams and 300 mm × 300 mm for exterior beams in the y-direction. Additional beams with cross sections of 300 × 400 mm supported the floor slab at intervals of 1.5 m in the y-direction. A 130 mm-thick floor slab was used at floor levels 2 through 4 and at the roof level. Reinforcement details of the members are presented in

and Table 5-2. It is noted that transverse reinforcement was different in the North (Axis A) and South (Axis C) walls. Further information on member geometry and reinforcement used is given in Nagae et al., 2011. Information on the building weight is contained in Table 5-3. Floors 2 through 4 weighed about 900 kN, whereas the weight of the roof was 1000 kN; the remaining weight was in the foundation.

Table 5-1. Reinforcement details of columns, walls, and slabs

| List of Column | | | |
|----------------|----------------|-------------|-------------|
| | | C1 | C2 |
| 4Fl. 3Fl. | Section | | |
| | B x D | 500 x 500 | 500 x 500 |
| | Rebar | 8-D22 | 10-D22 |
| | Hoop | 2,2-D10@100 | 2,2-D10@100 |
| | Joint | 2,2-D10@140 | 2,2-D10@140 |
| 2Fl. | Section | | |
| | B x D | 500 x 500 | 500 x 500 |
| | Rebar | 8-D22 | 10-D22 |
| | Hoop | 2,3-D10@100 | 2,4-D10@100 |
| | Joint | 2,2-D10@140 | 2,2-D10@140 |
| 1Fl. | Top Section | | |
| | B x D | 500 x 500 | |
| | Rebar | 8-D22 | |
| | Hoop | 2,3-D10@100 | |
| | Joint | 2,2-D10@140 | |
| | Bottom Section | | |
| | B x D | 500 x 500 | 500 x 500 |
| | Rebar | 10-D22 | 10-D22 |
| Hoop | 3,4-D10@100 | 3,4-D10@100 | |
| Joint | 2,2-D10@140 | 2,2-D10@140 | |

| List of Wall | | | | |
|----------------------|-------------|-----------------------------------|------------|-----------------|
| Wall | | | | |
| 4Fl. 3Fl. 2Fl. | Section | | | |
| | B x D | 2,500 x 250 | | |
| | Rebar | 2 x 6-D19 | Vertical | D13@300 (W) |
| | Hoop | 2,2-D10@100 | Horizontal | (A) D10@125 (W) |
| | | | | (C) D10@200 (W) |
| Joint | 2,2-D10@150 | | | |
| 1Fl. | Section | | | |
| | B x D | 2,500 x 250 | | |
| | Rebar | 2 x 6-D19 | Vertical | D13@300 (W) |
| | Hoop | (A) 2,3-D10@80 (C) 2,3-D10@100 | Horizontal | (A) D10@125 (W) |
| | | | | (C) D10@200 (W) |
| | Joint | 2,2-D10@150 | | |

| List of Slab | | | |
|--------------|--------|-------------------|------------------|
| Depth: 130mm | | | |
| | | Shorter direction | Longer direction |
| S1 | Top | D10@200 | D10@250 |
| | Bottom | D10@200 | D10@250 |
| CS1 | Top | D10,D13@200 | D10@250 |
| | Bottom | D10@200 | D10@250 |
| CS2 | Top | D10@200 | D10@250 |
| | Bottom | D10@200 | D10@250 |
| CS3 | Top | D10,D13@200 | D10,D13@200 |
| | Bottom | D10@200 | D10@200 |

Table 5-2. Reinforcement details of beams and girders

| List of Girder | | | | |
|----------------|----------|-----------|--------|-------|
| G1 | | | | |
| | Location | End | Center | End |
| RFI. 4Fl. | Section | | | |
| | B x D | 300 x 600 | | |
| | Top | 4-D22 | 3-D22 | 4-D22 |
| | Bottom | 3-D22 | 3-D22 | 3-D22 |
| | Web | 4-D10 | | |
| | Stirrup | 2-D10@200 | | |
| 3Fl. | Section | | | |
| | B x D | 300 x 600 | | |
| | Top | 5-D22 | 3-D22 | 5-D22 |
| | Bottom | 3-D22 | 3-D22 | 3-D22 |
| | Web | 4-D10 | | |
| | Stirrup | 2-D10@200 | | |
| 2Fl. | Section | | | |
| | B x D | 300 x 600 | | |
| | Top | 6-D22 | 3-D22 | 6-D22 |
| | Bottom | 3-D22 | 3-D22 | 3-D22 |
| | Web | 4-D10 | | |
| | Stirrup | 2-D10@200 | | |

| List of Girder | | | |
|----------------------|----------|-------------------|--------|
| G2 | | | |
| | Location | End | Center |
| RFI. | Section | | |
| | B x D | 300 x 300 | |
| | Top | 3-D19 | 3-D19 |
| | Bottom | 2-D19 | 3-D19 |
| | Web | - | |
| | Stirrup | 2-D10@100(KSS785) | |
| 4Fl. 3Fl. 2Fl. | Section | | |
| | B x D | 300 x 300 | |
| | Top | 3-D19 | 4-D19 |
| | Bottom | 3-D19 | 3-D19 |
| | Web | - | |
| | Stirrup | 2-D10@100(KSS785) | |

| List of Girder | | | |
|----------------------|----------|-----------|--------|
| G3 | | | |
| | Location | End | Center |
| 4Fl. 3Fl. 2Fl. | Section | | |
| | B x D | 300 x 400 | |
| | Top | 5-D19 | 3-D19 |
| | Bottom | 3-D19 | 4-D19 |
| | Web | 2-D10 | |
| | Stirrup | 2-D10@200 | |
| 1Fl. | Section | | |
| | B x D | 300 x 400 | |
| | Top | 4-D19 | 3-D19 |
| | Bottom | 3-D19 | 4-D19 |
| | Web | 2-D10 | |
| | Stirrup | 2-D10@200 | |

| List of beam | | | |
|--------------|----------|-----------|--------|
| B1 | | | |
| | Location | End | Center |
| All | Section | | |
| | B x D | 300 x 400 | |
| | Top | 3-D19 | 3-D19 |
| | Bottom | 4-D19 | 7-D19 |
| | Web | 2-D10 | |
| | Stirrup | 2-D10@200 | |

Table 5-3. Weight of the RC Building

| Structural | | RC | | | | 2.4 | t/m ³ |
|-----------------------|----------------|-------|------|------|------|-------|------------------|
| | | RFL | 4FL | 3FL | 2FL | Base | |
| RC | Column | 5.4 | 10.8 | 10.8 | 10.8 | 5.4 | |
| | Girder | 16.4 | 16.4 | 16.4 | 16.4 | 216.2 | |
| | Wall | 4.1 | 8.1 | 8.1 | 8.1 | 4.1 | |
| | Slab | 44.1 | 43.7 | 43.3 | 42.8 | 10.6 | |
| | Beam | 8.0 | 8.0 | 8.0 | 8.0 | 0.0 | |
| | Parapet | 5.3 | 0.0 | 0.0 | 0.0 | 0.0 | |
| Steel | Temp. Girder | 0.0 | 0.0 | 0.0 | 0.0 | 0.3 | |
| Sum | [t] | 83.3 | 87.0 | 86.6 | 86.2 | 236.5 | |
| Non-Structural | | | | | | | |
| Steel | Stair | 330 | 360 | 360 | 360 | 0 | |
| | Measurement | 0 | 3000 | 1750 | 1690 | 1690 | |
| | Handrail | 244 | 271 | 271 | 271 | 197 | |
| Machine | on the slab | 4633 | 180 | 0 | 0 | 0 | |
| | under the slab | 495 | 0 | 0 | 0 | 0 | |
| | RC Base | 6042 | 346 | 0 | 0 | 0 | |
| Ceiling | under the slab | 296 | 0 | 0 | 0 | 0 | |
| Sum | [kg] | 12040 | 4157 | 2381 | 2321 | 1887 | |
| Total | | RFL | 4FL | 3FL | 2FL | Base | |
| Sum | | 95.3 | 91.2 | 89.0 | 88.5 | 238.4 | |
| Whole Building [t] | | 602.4 | | | | | |

The design concrete compressive strength was 27 N/mm^2 , with SD345 D19 and D22 bars used for primary longitudinal reinforcement. Information on the design material properties for concrete, and longitudinal and transverse reinforcement used in all members is provided in Table 5-4, whereas Table 5-5 presents as-tested material properties.

Table 5-4. Design material properties

| (a) Concrete | | (b) Steel Bar | | | | |
|--------------|--------------------------------|---------------|--------|------------------------------------|------------------------------------|------------------------------------|
| | f'_c (N/mm ²) | | Grade | A_{normal} (mm ²) | σ_y (N/mm ²) | σ_t (N/mm ²) |
| Foundation | 33 | D22 | SD345 | 387 | 345 | 490 |
| Upper Part | 27 | D19 | SD345 | 287 | 345 | 490 |
| | | D13 | SD295 | 127 | 295 | 440 |
| | | D10 | SD295 | 71 | 295 | 440 |
| | | D10 | KSS785 | 71 | 785 | 930 |

Table 5-5. Actual material properties

| (a) Concrete | | (b) Steel Bar | | | | |
|----------------|--------------------------------|---------------|-------|------------------------------------|------------------------------------|------------------------------------|
| | f'_c (N/mm ²) | | Grade | A_{normal} (mm ²) | σ_y (N/mm ²) | σ_t (N/mm ²) |
| 1st-2nd floor | 39.6 | D22 | SD345 | 387 | 370 | 555 |
| 2nd-3rd floor | 39.2 | D19 | SD345 | 287 | 380 | 563 |
| 3rd-4th floor | 30.2 | D13 | SD295 | 127 | 372 | 522 |
| 4th-roof floor | 41.0 | D10 | SD295 | 71 | 388 | 513 |

5.4. Assessment of RC Building using ASCE 7-05 and ACI 318-08

A detailed assessment of the RC Building was conducted to assess whether the final design satisfied U.S. code provisions. This assessment is completed both for the shear wall direction and the moment frame direction, to provide the reader with information to help understand the measured responses and observed behavior once this information becomes available. The shear wall direction is covered in this section, whereas the moment frame direction is available in Nagae et al., 2011.

For the shear wall direction, the structural system was assumed to be a Building Frame System Special RC Shear Wall ($R = 6, C_d = 5$) as the framing provided by the shallow beam and

column at the building edge was insufficient for a Dual System designation. Based on this designation, all lateral forces are resisted by the shear wall. Given that the building system is relatively simple, the ASCE 7-05 S12.8 Equivalent (Static) Lateral Force Procedure was used, assuming that the building was located in a region where the mapped short period and 1-sec-period accelerations were 1.5 and 0.9, respectively; for Site Class B, design spectral acceleration parameters were 1.0 and 0.6 with $T_0 = 12$ and $T_s = 0.6$.

The seismic weight (ASCE 7-05, 12.7.2) of the building was taken as the combined dead and live loads as 3630 kN (see Table 5-3), i.e., the live load value includes permanent live load attached to the building. The fundamental period of the building was computed using a two-dimensional model of a single wall, i.e., a cantilever assuming an effective moment of inertia $I_{eff} = 0.51g$ over the full wall height and one-half the seismic weight at the floor levels. A fundamental period of $T = 0.58$ sec was computed from an eigenvalue analysis. According to ASCE 7-05 12.8.2, $T_a = 0.488(h_n = 12 \text{ m})^{0.75} = 0.315$ sec and $T_u = C_u T_a = 1.4 T_a = 0.0440$; therefore, $T = 0.44 = T_u$ was used to determine a base shear of $V = C_s = 0.167W = 302.5$ kN. Because only two shear walls were used, one at each end of the building, the redundancy factor (ASCE 7-05 12.3.4) was taken as 1.3. Therefore, $E_h = \rho Q_E = 1.3(302.5 \text{ kN}) = 393.3$ kN (ASCE 7-05 Equation 12.4-3). Vertical earthquake loading (E_V) was included in the load combinations (ASCE 7-05 12.4.2 and 12.4.2.3).

5.4.1. Strength Requirements for Walls

Dead and live loads for the wall were calculated by assuming the dead and live loads (see Table 5-3) were uniformly distributed based on a tributary area equal to the wall length (2.5 m) plus the beam clear length (2.5 m + 2.1 m) times one-half the joist spacing and the slab overhand (0.9 m

+ 0.8 m), or 7.82 m² (84.2 ft²). The resulting story forces shown in Figure 5-4 produced wall base moment $M_u = 3569$ kN-m with axial load $P_u = 285$ kN. Note that the axial load ratio was low $\left[\frac{P_u}{A_g f'_c} = 285 \text{ kN} / (0.25 \text{ m} \times 2.5 \text{ m})(27 \text{ MPa}) = 0.017 \right]$. Demands were calculated using different load combinations, and compared with a wall P-M interaction diagram (see Figure 5-5), demonstrating that the wall P-M strength does not satisfy ASCE 7-05 12.8 requirements. Considering the outmost P-M pair among five load combinations, $M_u / \phi M_n$ was 0.7 at the given axial load level. On the other hand, $P_u / \phi P_n$ was about 4.0 when the moment was equal to $M_u = 3569$ kN-m.

5.4.2. Capacity Design Checks

Wall shear strength was computed as $\phi V_n = 0.75 A_{cv} (\alpha_c \sqrt{f'_c} + \rho_t f_y) = 912$ kN, using the minimum horizontal web reinforcing ratio (2D10 @ 200 mm spacing for the wall at Axis C, $t_w = 250$ mm; $\rho_t = 0.0031$; $\alpha_c = 0.167$; $f'_c = 27$ MPa; $f_y = 345$ MPa). Calculated shear strength $\phi V_n = 912$ kN is much greater than shear demand $V_u = 393$ kN, as would be expected given the relatively high wall aspect ratio (12 m/2.5 m = 4.8). The wall shear strength at Axis A is much larger as a result of the 125 mm spacing of the horizontal web reinforcement.

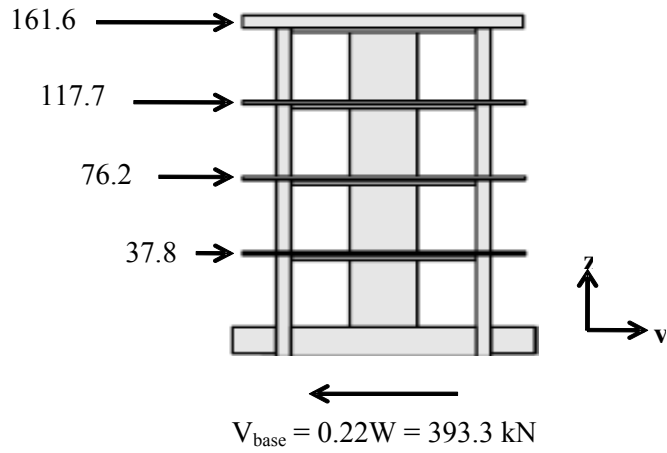


Figure 5-4. Equivalent lateral loads on the shear wall system

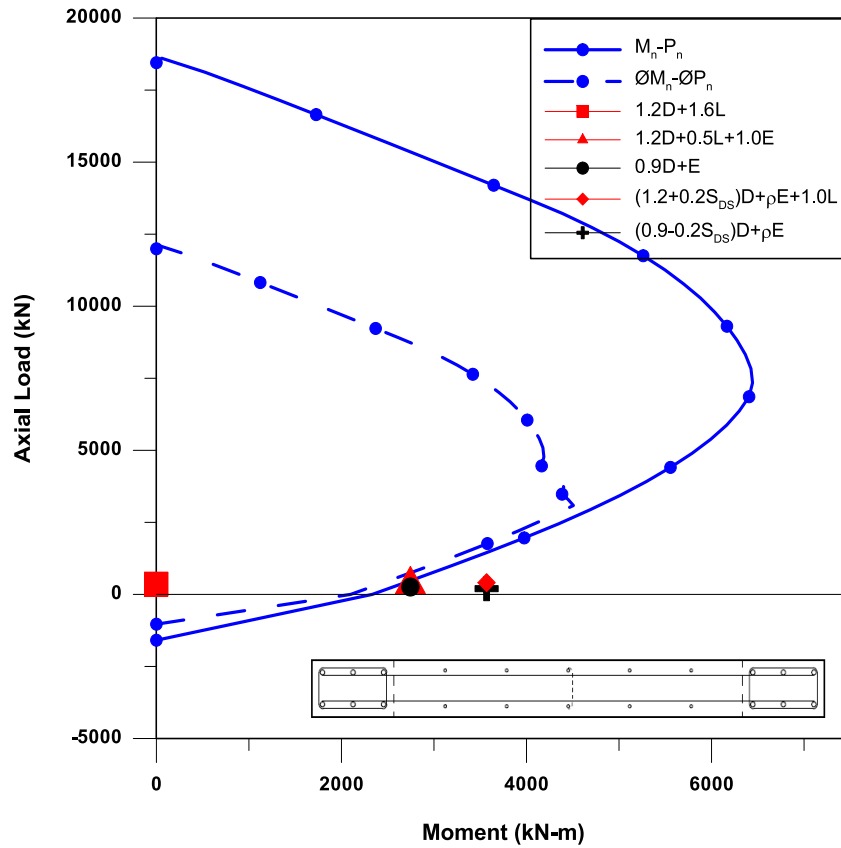


Figure 5-5. P-M interaction diagram for the wall

5.4.3. Drift Requirements in the Wall

Lateral displacements and story drifts were computed according to ASCE 7-05 12.8.6 and compared to allowable story drift per Table 12.12-1 where $0.02h_{sx}/\rho = 1.3 = 0.0154h_{sx}$. Story drift ratios of 0.0045, 0.0113, 0.0151, and 0.0167 were computed (Figure 5-6). The drift ratio for the fourth level exceeded the ASCE 7-05 limit by 8% ($0.0167/0.0154 = 1.08$).

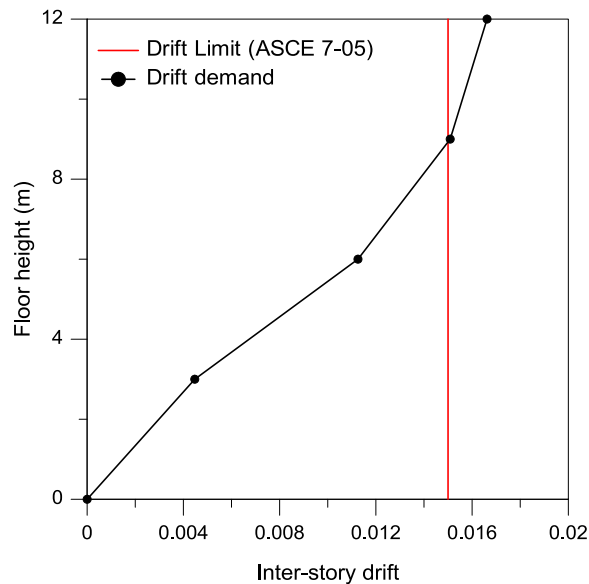


Figure 5-6. Inter-story drift demands for the wall

5.4.4. Detailing Requirements for the Wall

Detailing requirements at wall boundaries were checked using the displacement-based approach of ACI 318-08 21.9.6 (21.9.6.2); the roof drift ratio ($\delta_u/h_w = 0.142/12 \text{ m} = 0.012$) exceeded the minimum value of 0.007. Based on this value, the critical neutral axis depth using ACI 318-08 equation (21-8) is 352 mm. The neutral axis depth computed for the given wall cross section for an extreme fiber compression strain of 0.003 with $P_u = 285 \text{ kN}$ is 244 mm; therefore, special boundary elements are not required per 21.9.6.2. The vertical reinforcing ratio of the boundary

reinforcement $[\rho = 6A_b/h(2x+a) = 0.017$, with $A_b = 284 \text{ mm}^2$, $h = 250 \text{ mm}$, $(2x+a) = 400 \text{ mm}]$, exceeded $\rho = 2.3/f_y = 0.0067$, where $f_y = 345 \text{ MPa}$; therefore, ACI 318-08 21.9.6.5(a) must be satisfied as a hoop spacing cannot exceed 203 mm. The configuration and the spacing used at the wall boundary satisfies the requirements of 21.9.6.5(a), since the spacing of hoops and crossties is 80 mm (Axis A) and 100mm (Axis C), and a hoop and a crosstie are provided (all 6 bars are supported) over a depth of almost 400 mm, which significantly exceeds the minimum depth required from 21.9.6.4(a) of one-half the neutral axis depth (244 mm/2).

If the “stress-based” approach of 21.9.6.3 is used, however, the extreme fiber compression stress of $f_c = M_u/s + P_u/A = 11.56 \text{ MPa}$ ($M_u = 3569 \text{ kN-m}$; $P_u = 285 \text{ kN}$; $I_g/S = 0.26 \text{ m}^3$; and $A_g = 0.625 \text{ m}^2$) significantly exceeds the stress limit of $0.2f'_c = 5.4 \text{ MPa}$, with 21.9.6.4 left to be satisfied and requiring special boundary elements. Based on a wall boundary zone with $b_{cx} = 160 \text{ mm}$, $b_{cy} = 320 \text{ mm}$, $A_{shx} = 2A_b$, $A_{shy} = 3A_b$, $A_b = 78.5 \text{ mm}^2$, $s = 80 \text{ mm}$ (Axis A) or 100 mm (Axis C), $f'_c = 27 \text{ MPa}$, and $f_{yt} = 345 \text{ MPa}$, the provided A_{sh} values are 1.39 and 2.09 times that required by ACI 318-08 Equation (21-5) for 100 mm spacing, satisfying 21.9.6.4. Note that the provided A_{sh} values are only 0.45 and 0.34 times that required by ACI 318-08 Equation (21-4), which is no longer required for wall boundaries, but is being considered for reinstatement (Wallace, 2012).

In summary, the RC shear wall generally satisfies ASCE 7-05 and ACI 318-08 requirements for the assumed design spectrum, although the wall P-M strength does not meet the requirement (by 30%) and the interstory drift ratio in the top floor exceeds the limiting value by 8%.

5.5. Collapse Mechanism

A collapse mechanism analysis was conducted for both the shear wall and moment frame directions using the code prescribed distribution of lateral forces over the building height. Four different collapse mechanisms were assumed for each direction: column yielding at the first, the second, the third, and the fourth floors. Figure 5-7 shows base shear calculated for each collapse mechanism assumption. For the shear wall direction, the mechanism involves beam hinging accompanied by yielding at the base of first floor walls (Figure 5-8), assuming either triangular or uniform loading. The actual strength coefficient was approximately 0.50 for the wall directions, or 3.0 times the values given in ASCE 7-05. Note that the overstrength factor given in ASCE 7-05 Table 12.2-2 was taken as 2.5; therefore, the computed overstrength for the wall was higher than expected (3.0 versus 2.5).

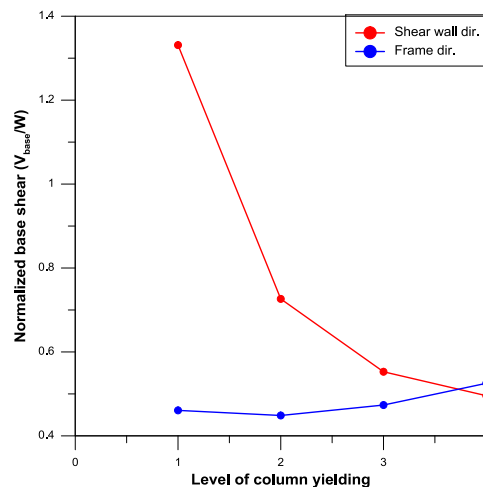


Figure 5-7. Collapse mechanism assessment-influence of wall yielding level

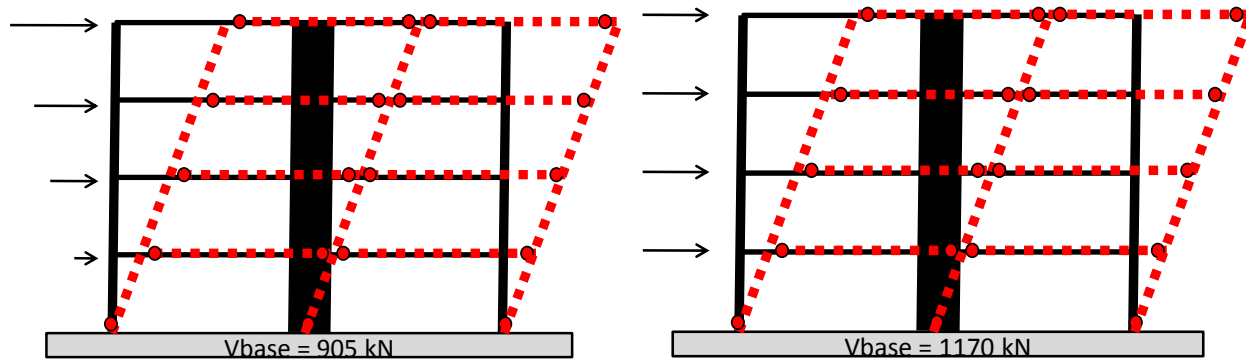


Figure 5-8. Controlling collapse mechanism in the wall direction a) triangular load, (b) uniform load

5.6. Test plan, Ground (Table) Motions, and Instrumentation

5.6.1. Test plan

The test buildings were subjected to the JMA-Kobe motions recorded in 1995, scaled by 25%, 50%, and 100%, to produce a range of shaking intensities. At the completion of these tests, two additional tests were conducted using the JR-Takatori record scaled by 40% and 60%. This chapter presents results only for the JMA-Kobe motions.

5.6.2. Instrumentation

The two test buildings were heavily instrumented to enable performance assessment and post-test analytical studies. A total of 609 channels of data were collected during the tests for RC and PT specimens, including 48 accelerometers, 202 displacement transducers, and 235 strain gauges. The accelerometers were placed on the foundation and on each floor slab to record accelerations in three directions. Displacement transducers were arranged to measure inter-story displacements, beam end rotations, column end rotations, and base wall rotations. Strain gauges were glued to longitudinal and transverse reinforcement of beams, columns, and walls. Strain gauges were largely used for the RC specimen, whereas displacement transducers were used for the PT specimen (to measure member end rotations). Video cameras were used to record the tests

and included overall views of the test specimens, as well as close up views of regions where yielding and damage were anticipated. Data acquisition was accomplished using 24 bit A/D converters using a sample rate of 0.001 sec (1000 Hz). Further details and locations of instrumentation are available in Nagae et al. (2011). Typical instrumentation of the shear walls in the RC Building are shown in Figure 5-9, whereas the sensor layout is sketched in Figure 5-10. Four linear variable differential transducers (LVDTs) were used over a gauge length of 550 mm at the base of the walls to enable the curvature along the wall length (depth) to be determined; additional displacement transducers were provided at each wall boundary over the entire height of the building. Two pairs of diagonally-oriented displacement transducers were used over the first story height to enable the determination of shear deformations.



Figure 5-9. Instrumentation of the RC shear walls

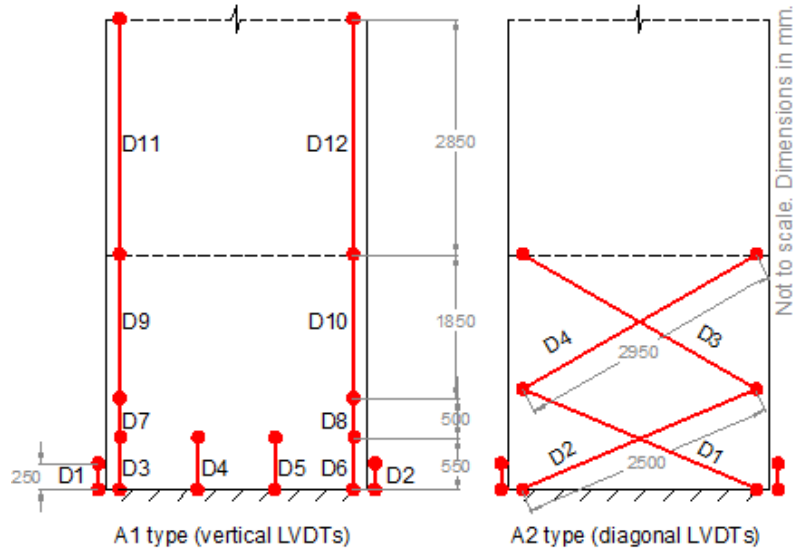


Figure 5-10. LVDT layout in the RC Building (South Wall)

5.6.3. Ground (Table) Motions

Pseudo acceleration and displacement spectra of the Kobe ground motions are presented in Figure 5-11 and Figure 5-12, respectively, along with spectra for a service level (SLE; 50% in 30 years), design level (DBE; 10% in 50 years), and maximum considered earthquake level (MCE; 2% in 50 years) based on ASCE 7-10 requirements (ASCE, 2010) assuming that the buildings were located in downtown Los Angeles for Site Class B. Peak spectral accelerations observed on the shaking table were 0.89g, 1.58g and 3.42g at 25%, 50% and 100% Kobe records, respectively. It is noted that spectral acceleration demands for the 25% Kobe record are close to the SLE spectrum. For the 50% Kobe record, the demands are bounded by the DBE and MCE spectra near building fundamental periods (approximately 0.3 sec for both buildings), whereas the demands for the 100% Kobe record were much higher than the MCE spectrum.

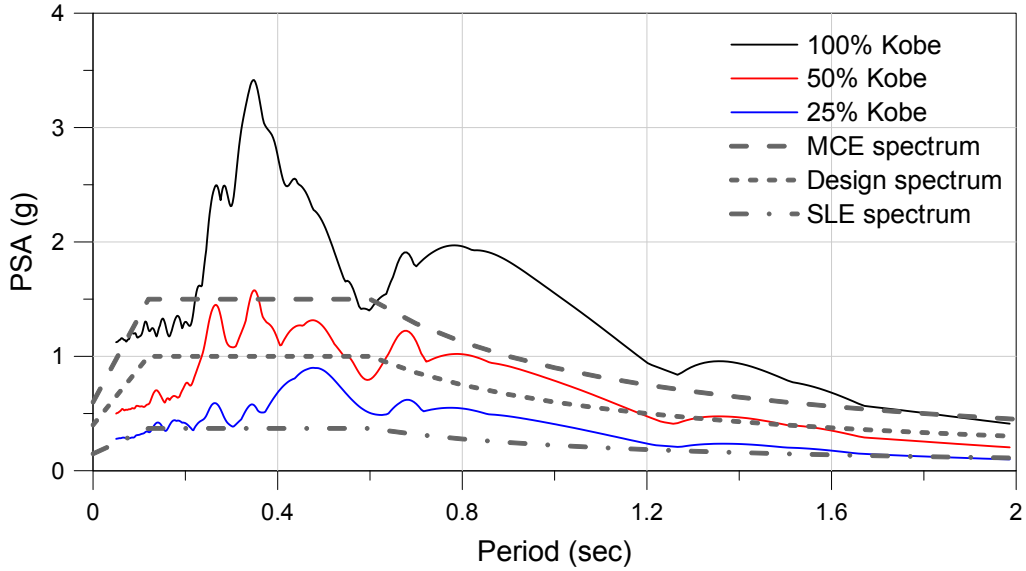


Figure 5-11. Acceleration spectra of the Kobe records

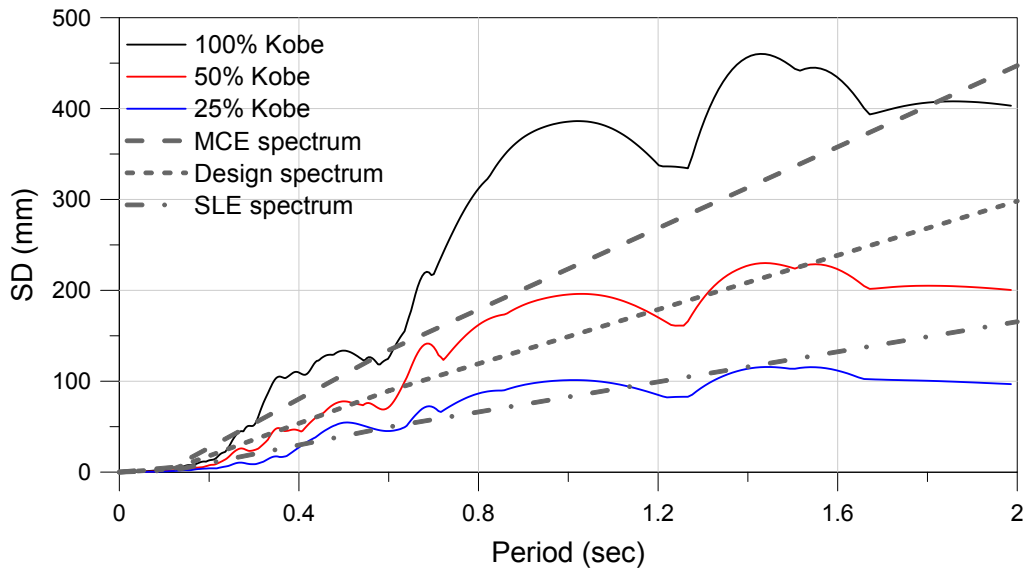


Figure 5-12. Displacement spectra of the Kobe records

5.7. Test Results

Figure 5-13(a) shows the roof drift histories of the RC Building. Peak roof drifts are 0.2% ($\delta=23.5$ mm), 0.84% ($\delta=100.7$ mm), and 2.54% ($\delta=304.2$ mm) for 25%, 50% and 100% Kobe records, respectively. Residual roof level displacement of 21 mm (0.2% drift) is noted for the

100% Kobe record. Figure 5-14a presents the building overturning moment versus roof drift relations, with base moment calculated as floor masses times absolute floor accelerations, multiplied by the associated floor heights from the base. Results presented in Figure 5-14(a) indicate essentially elastic response for the 25% Kobe record and some inelastic response (yielding, along with modest stiffness and strength degradation) for the 50% Kobe record. Significant yielding and stiffness degradation, along with modest strength degradation, are noted for the 100% Kobe record. Based on test observations, strength loss was likely due to concrete crushing and reinforcement buckling at wall boundaries (Figure 5-16(a)). Following crushing of concrete at the wall boundaries, substantial sliding was observed at the wall base for the 50% and 100% Kobe records.

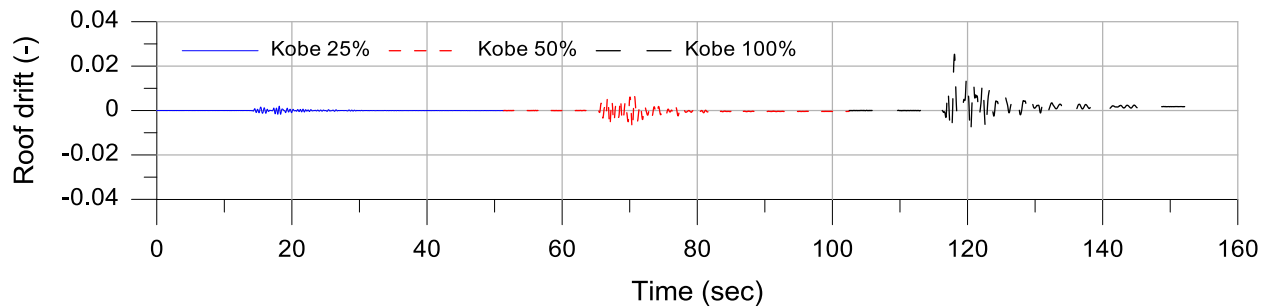


Figure 5-13. Roof drift history of the RC Building

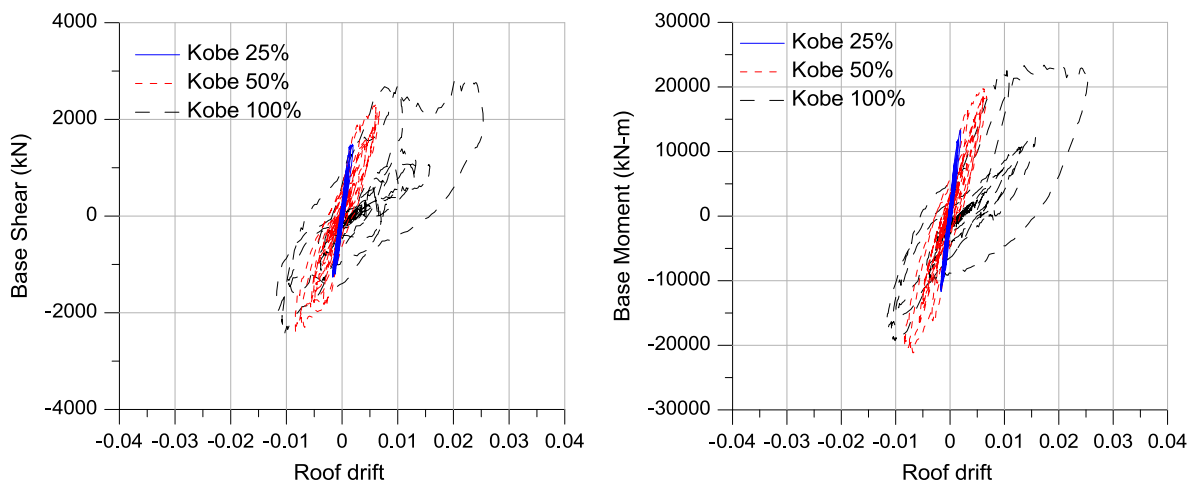


Figure 5-14. (a) Base shear vs. roof drift; (b) Base moment vs. roof drift

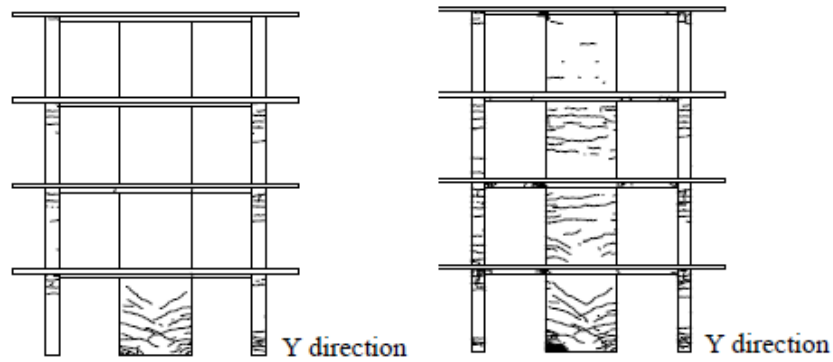


Figure 5-15. Overall damage of the RC Building (a) 50% Kobe, (b) 100% Kobe [Nagae et. al., 2012]



Figure 5-16. Damage on the RC shear walls (Axis A) at (a) 50%, (b) 100% Kobe record

5.8. Preliminary Modeling and Analysis Results

Preliminary analytical model for the shear wall direction of the RC Building (Axes A, B and C in Figure 5-3) was developed using Perform 3D. This model represents “blind” predictions without taking advantage of information gleaned from test data. The model was based on current modeling techniques (Tuna, 2009) and recommendations provided by PEER/ATC Report 72 (2010). Three-dimensional, elevation, and plan views of the model are presented in Figure 5-17. The model consists of shear walls with fiber cross sections and frame elements for beams and columns. Additional information on the modeling is described in the following subsections.

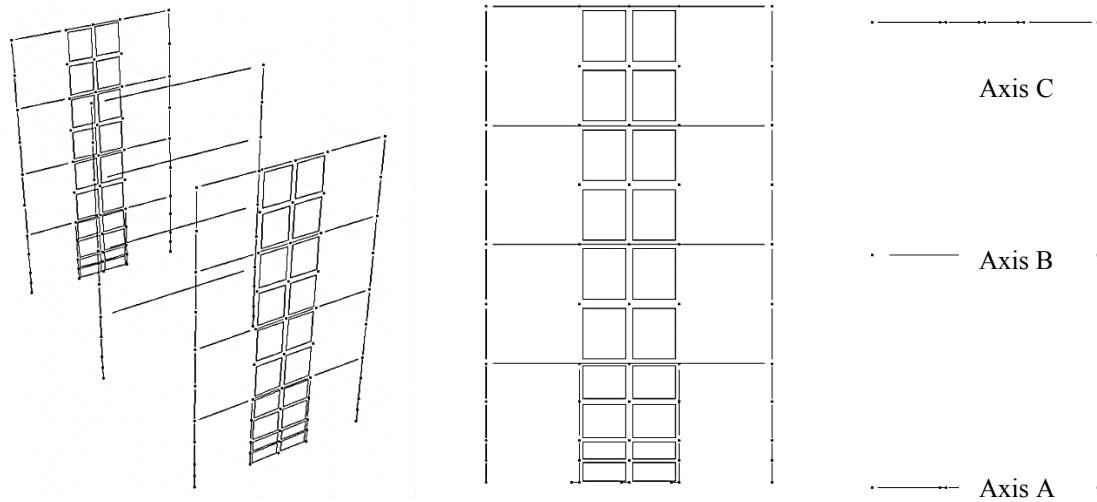


Figure 5-17. Views of the structural model in Perform 3D

5.8.1. Shear Wall Modeling

Shear walls were modeled using 4-noded, uniaxial, fiber “Shear Wall Elements”. Plane sections are assumed to remain plane after loading and uniaxial material models for concrete and reinforcement are used to determine section and element responses. Unconfined concrete was modeled using a stress-strain relation based on the results of material characterization tests that were performed prior to the shake table testing (Nagae et al., 2011).

Unconfined concrete behavior was defined by fitting a tri-linear relationship to the stress-strain relationships obtained from 12 compression test results (3 tests per floor). An example to the fitted-curve (for Floor 1) is presented in Figure 5-18(a). Peak unconfined concrete strength was about 40 MPa at all floors, except third floor concrete strength was 30 MPa. Strain at the peak strength was approximately 0.0018, and initial modulus of elasticity was approximately 33000 MPa and 30500 MPa in the first two floors and top two floors, respectively. Confined concrete parameters (Figure 5-18(b)) were defined based on the model developed by Saatcioglu et. al. (1999); which uses the unconfined concrete peak stress and strain values, as well as the

boundary details of the associated members (shear walls or columns), to determine the peak confined concrete stress and strain, and the post-peak behavior. Confined concrete parameters were different in the walls and columns; and varied over the wall/column height at locations where transverse reinforcement changed. The tensile strength of concrete was neglected in the preliminary model.

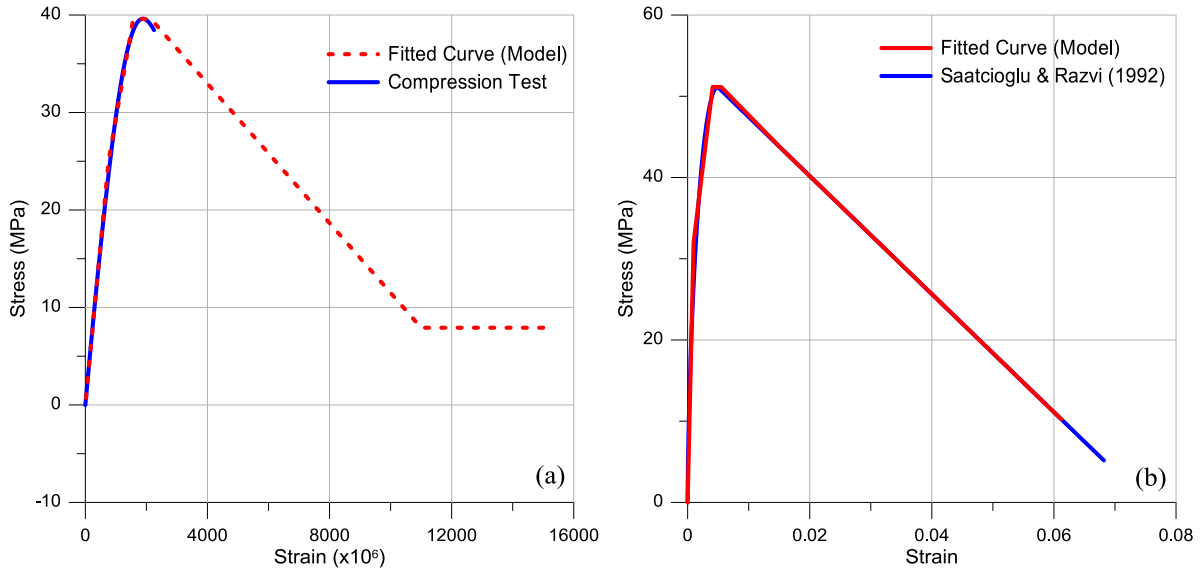


Figure 5-18. (a) Unconfined concrete stress-strain relationship (Floor 1), (b) Confined concrete stress-strain relationship (Floor 1)

Reinforcing steel stress-strain relations were defined using trilinear relationships based on the test results (Figure 5-19). Tension and compression behaviors were modeled symmetrically with the yield strength and ultimate strength values presented in Table 5-5, and a stress drop to zero at a strain of 0.05 to represent rebar fracture (PEER/ATC-72, 2010). Elastic modulus was approximately 200 GPa for all rebar. Slight differences in material properties of the rebar with different diameters were reflected in the model.

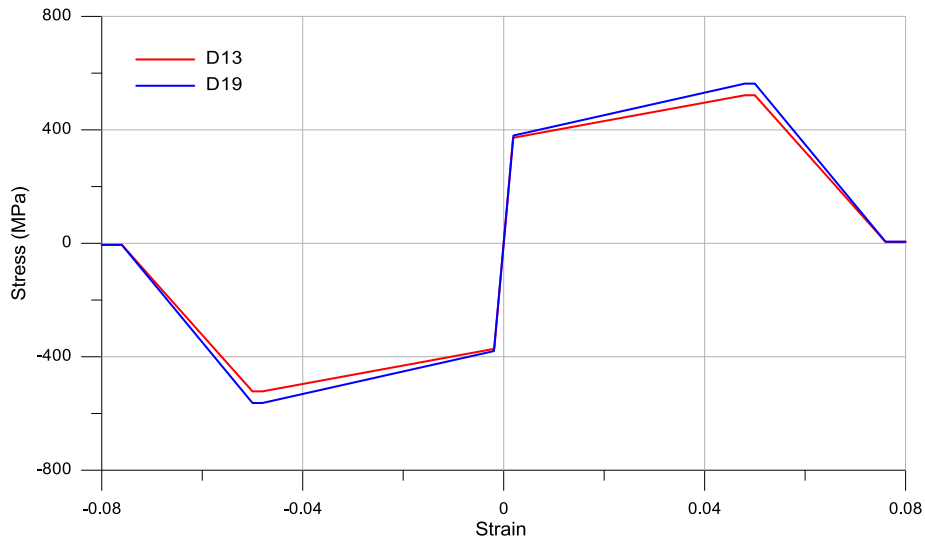


Figure 5-19. Reinforcement material stress-strain relationships

Shear behavior was modeled using the same procedure described in Chapter 4 (Figure 5-20), as a trilinear relation similar to that recommended by ASCE 41-06 Supplement #1. The uncracked shear modulus was taken as $G_c = E_c 2(1 + \nu) \approx 0.4E_c$ and shear cracking was assumed to occur at $0.25\sqrt{f'_c} \text{ MPa}$ ($3\sqrt{f'_c} \text{ psi}$), but not greater than $0.5V_n$, where V_n is the ACI 318-08 nominal wall shear strength. The post-cracking slope was taken as $0.01E_c$ to account for nonlinear shear deformations due to shear-flexure interaction (Massone et al, 2006; PEER/ATC 72-1, 2010).

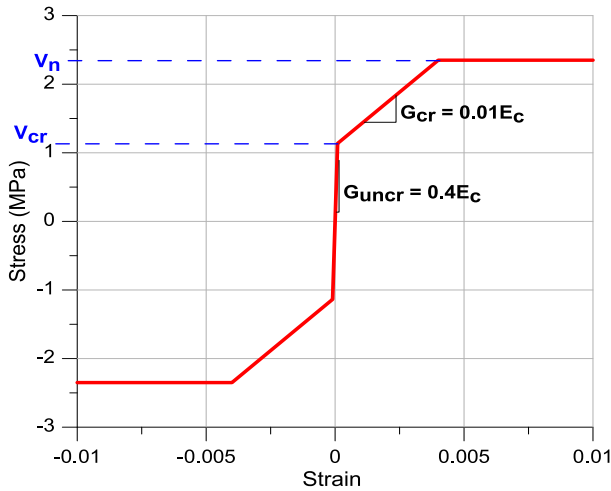


Figure 5-20. Shear material stress-strain relationship

5.8.2. Beam and column modeling

Beams and columns were defined as elastic beam-column elements with rigid end zones and plastic hinges at member ends. Elastic element effective stiffness of $0.3EI_g$ was used for both beams and columns as recommended in ASCE 41-06. Beam moment-rotation hinges were modeled using tri-linear backbone curves, whereas for the column plastic hinges, moment-axial capacity interaction curves were calculated using actual material properties. Cyclic degradation and strength loss were neglected in both beam and column hinges in the preliminary model.

5.8.3. Damping and masses

Rayleigh damping of 2.5% at $0.2T_1$ and $1.5T_1$, where T_1 is the calculated first mode period, were used for the nonlinear response history analyses based on the recommendation of PEER/ATC Report 72 (2010). The seismic masses, lumped at center of the wall at each floor level, were based on the weight of the structures reported by Nagae et al. (2011). Axial load ratio at the base of the walls were estimated to be about $0.02A_gf'_c$, whereas column axial loads were $0.12A_gf'_c$ and $0.06A_gf'_c$ for the interior (C2) and corner columns (C1), respectively.

5.8.4. Comparisons of the preliminary analytical results with test results

Figure 5-21, Figure 5-23, and Figure 5-25 display comparisons of the preliminary analytical results with test results in terms of (a) roof drift, and (b) base overturning moment for 25%, 50%, and 100% Kobe records, respectively. The model was capable of capturing the fundamental period of the structure; however, the displacements and forces were generally overestimated at 25% Kobe record, i.e., the model was too flexible. Figure 5-22, which compares the global response of the building at 25% Kobe record, also shows that overall stiffness of the building was underestimated with the preliminary model. Potential factors that could lead to model results overestimating roof displacements of the test building include neglecting tension behavior of concrete.

Figure 5-23 and Figure 5-24 indicate that roof displacement and moments were better captured at 50% Kobe record, although displacements were underestimated after yielding, particularly in the negative direction. Overall stiffness of the building was slightly higher in the model, which may be related to the following factors: (i) stiffness reduction due to slip/extension deformations at beam-joint and column-joint interfaces was underestimated (e.g., see Elwood et al, 2007; Naish, 2010), (ii) cyclic degradation was neglected in the initial model.

At 100% Kobe record, neither stiffness nor peak displacement was captured with the preliminary model, as presented in Figure 5-25 and Figure 5-26. Overall stiffness of the model was much higher than that of actual building, which might be improved by the previously mentioned factors. Additional factors that might impact model results include (i) strength degradation of the beam and column elements, (ii) deformations associated with sliding at the wall base are neglected (and test observations indicate modest sliding occurred for the 50% Kobe record, and significant sliding displacements were measured for the 100% Kobe record).

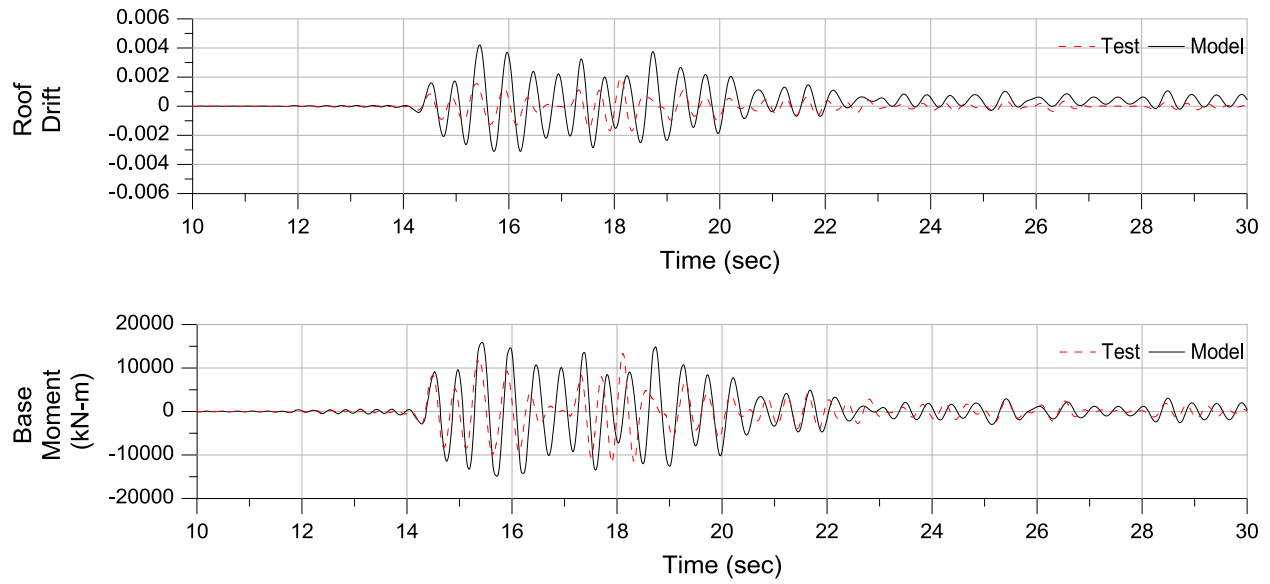


Figure 5-21. Comparisons at 25% Kobe: (a) roof drifts, (b) base overturning moments

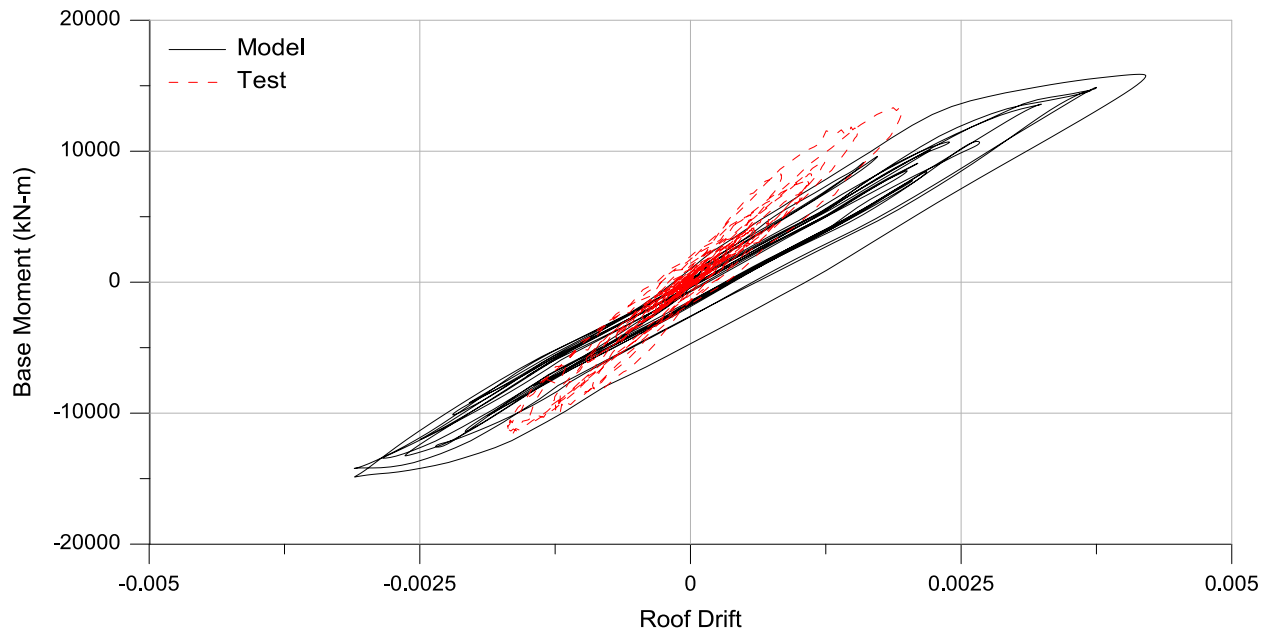


Figure 5-22. Comparison of global response at 25% Kobe

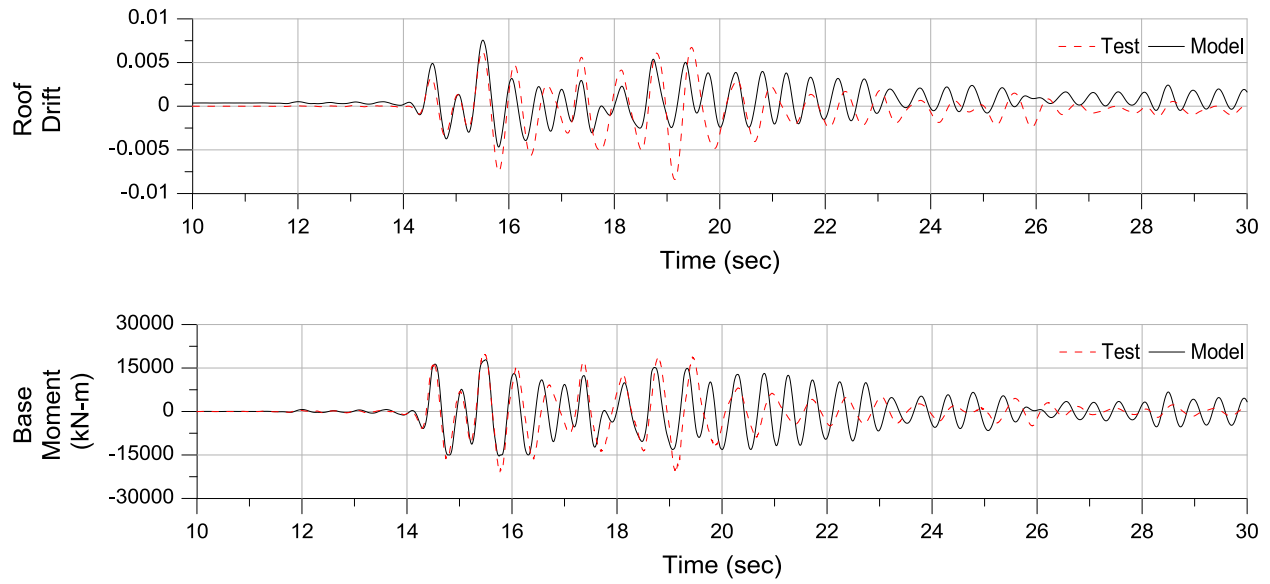


Figure 5-23. Comparisons at 50% Kobe record: (a) roof drifts, (b) base overturning moments

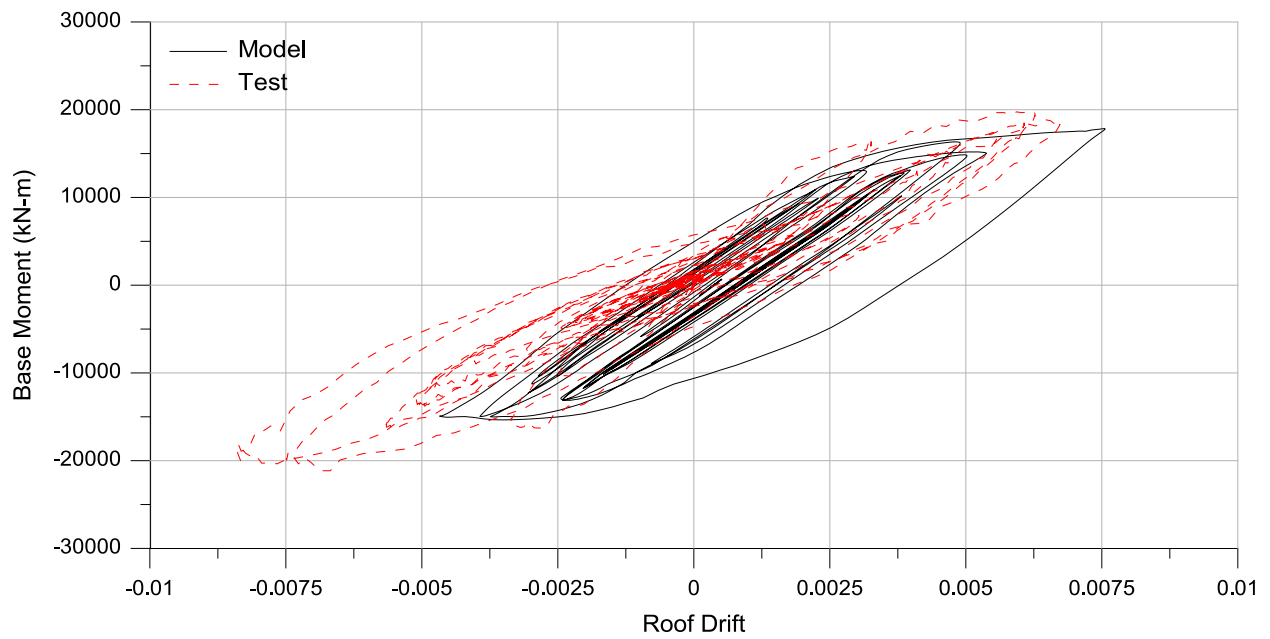


Figure 5-24. Comparison of global response at 50% Kobe record

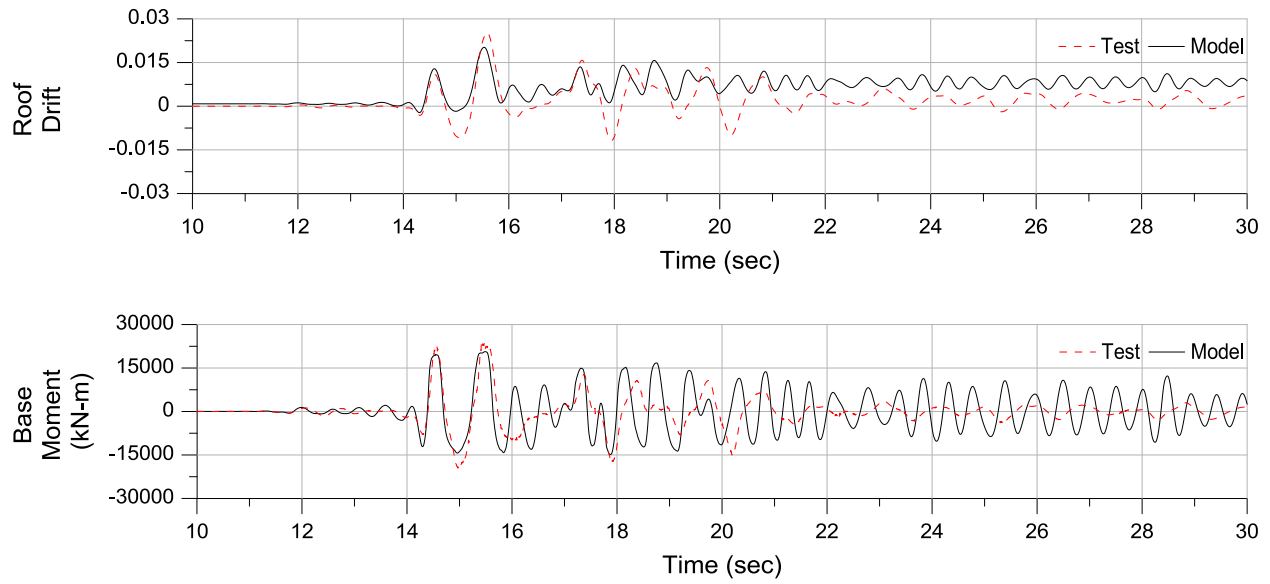


Figure 5-25. Comparisons at 100% Kobe record: (a) roof drifts, (b) base overturning moments

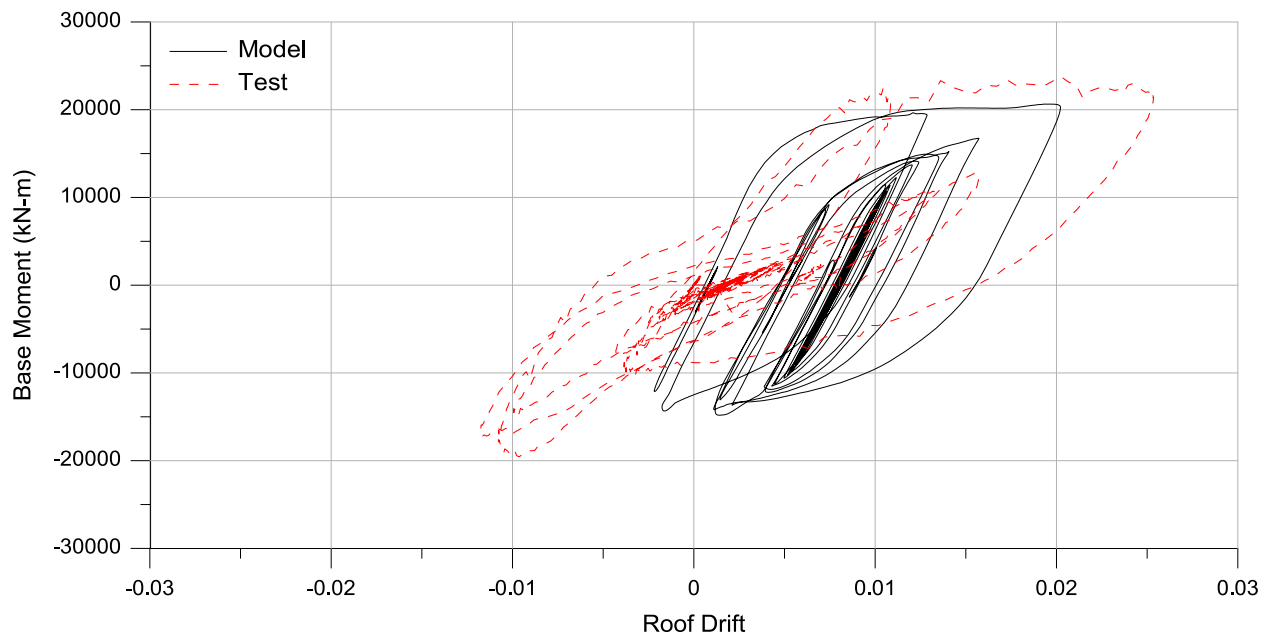


Figure 5-26. Comparison of global response at 100% Kobe record

5.9. Enhanced Modeling and Analysis Results

5.9.1. Additional properties

To better capture the results, additional modeling features were investigated and included. These features include tensile behavior of concrete, slip/extension behavior of longitudinal reinforcement, degradation of stiffness (here referred as cyclic degradation) and strength due to cyclic actions. It is noted that each feature that improved the results were maintained in the model and the new feature was included in addition to the previous one.

5.9.1.1. Tensile behavior of concrete

Tensile behavior of concrete was included in the model with peak tensile capacity of $f_t = 7.5\sqrt{f'_c}$ and post-peak stiffness of $E_t = 0.05E_c$ (Orakcal, 2004), where E_c is modulus of elasticity of concrete. As presented in Figure 5-27, this feature significantly improved overall stiffness of the model at 25% Kobe record, as well as peak displacement and forces.

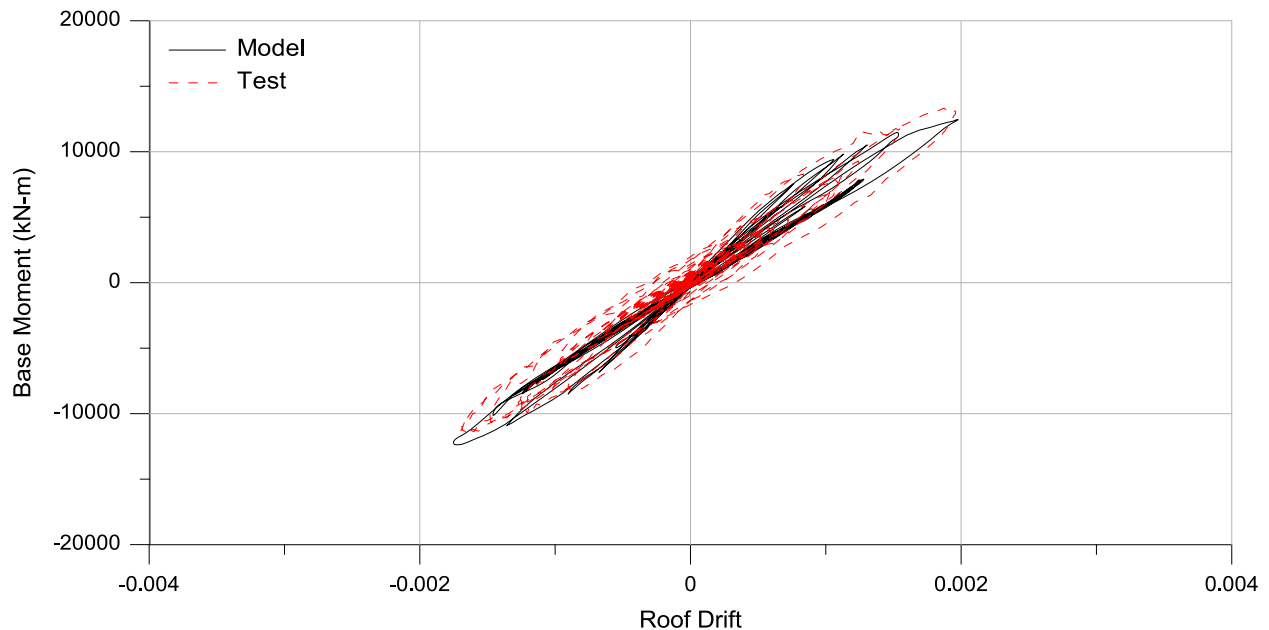
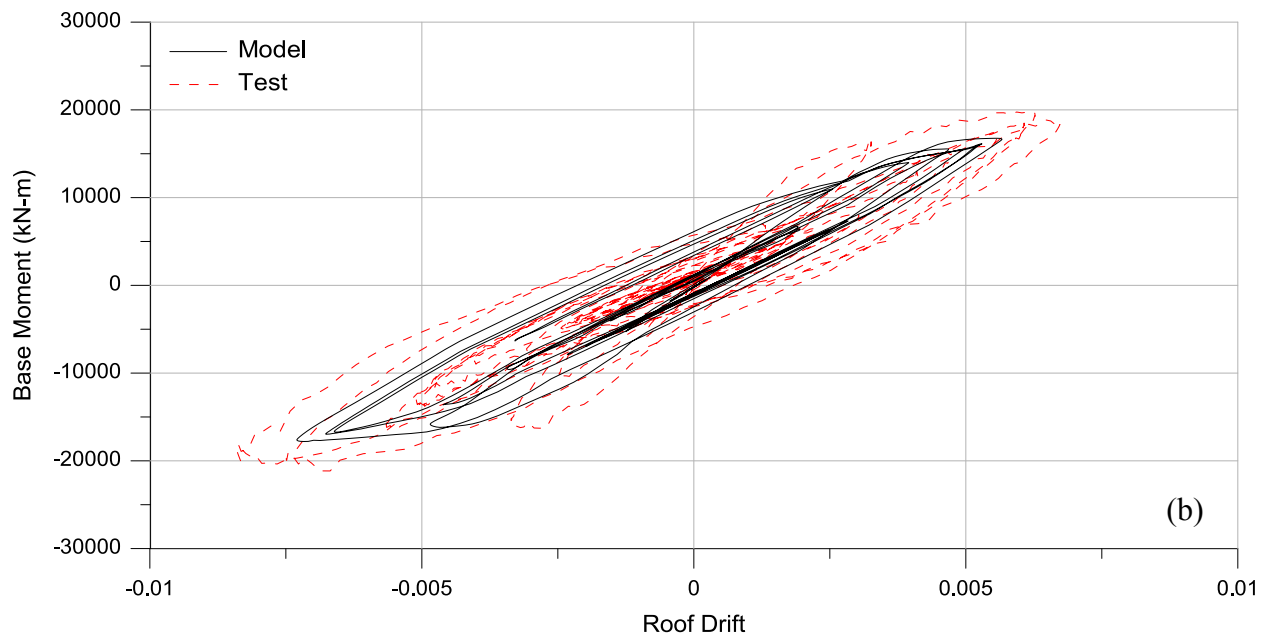
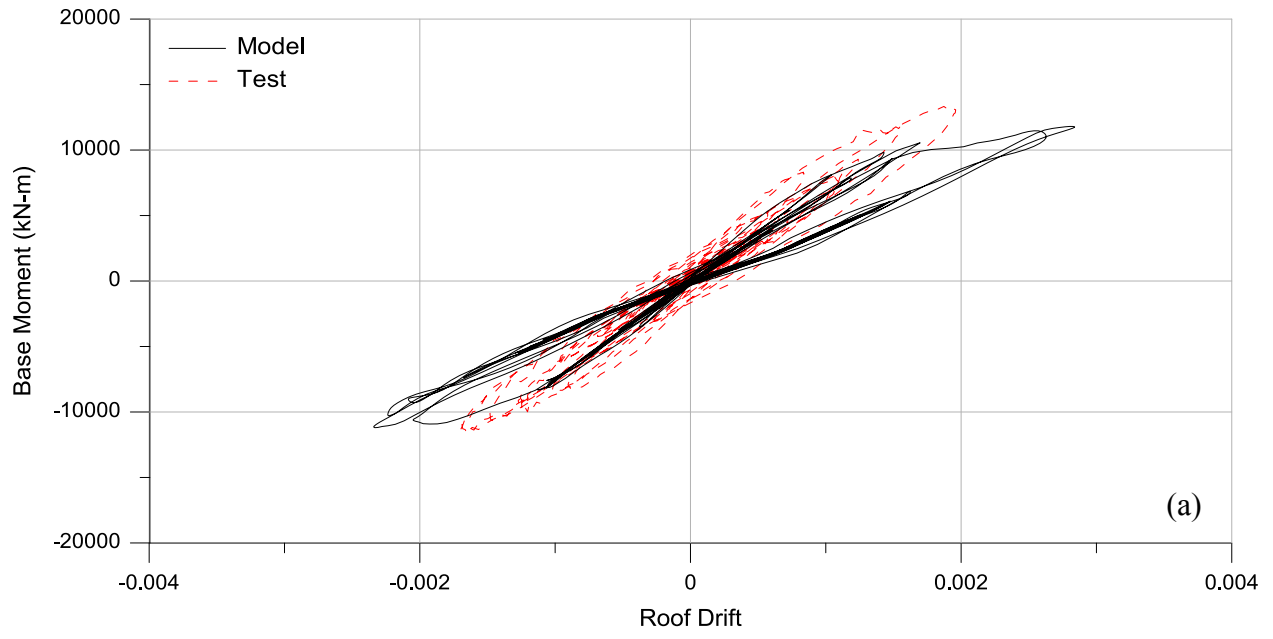


Figure 5-27. Enhanced model at 25% Kobe record – effect of including concrete tension behavior

5.9.1.2. Slip/Extension

Potential impact of reinforcing bar slip/extension was modeled explicitly by adding nonlinear moment-rotation springs at the base and top of the columns, as well as at the beam-column interfaces. The contribution of slip/extension was estimated using the approach recommended by Alsiwat and Saatcioglu (1992), where cumulative displacements (bar extensions) were obtained by integrating the strains along the rebar development length (l_d), and then were divided by the neutral axis depth of the beam (or column) to achieve beam (or column) yield rotation (θ_y). Rotational springs were implemented in Perform 3D as elastic materials with moment-rotation stiffness values of M_y/θ_y . As recommended in ASCE 41-06 Supplement #1, a moment-curvature analysis was used to define the secant stiffness at the yield point in the enhanced model which includes a slip/extension spring. Slip/extension deformations in the walls were neglected because they generally do not contribute significantly and are typically more important for low-rise walls than for slender walls (ASCE 41-06).

As shown in Figure 5-28, explicit modeling of stiffness reduction due to slip/extension deformations improved overall stiffness of the structure at 50% Kobe, whereas the elastic stiffness (at 25% Kobe) was underestimated particularly after concrete lost its tensile capacity. The model was still not capable of capturing the global response or the stiffness reduction at 100% Kobe record.



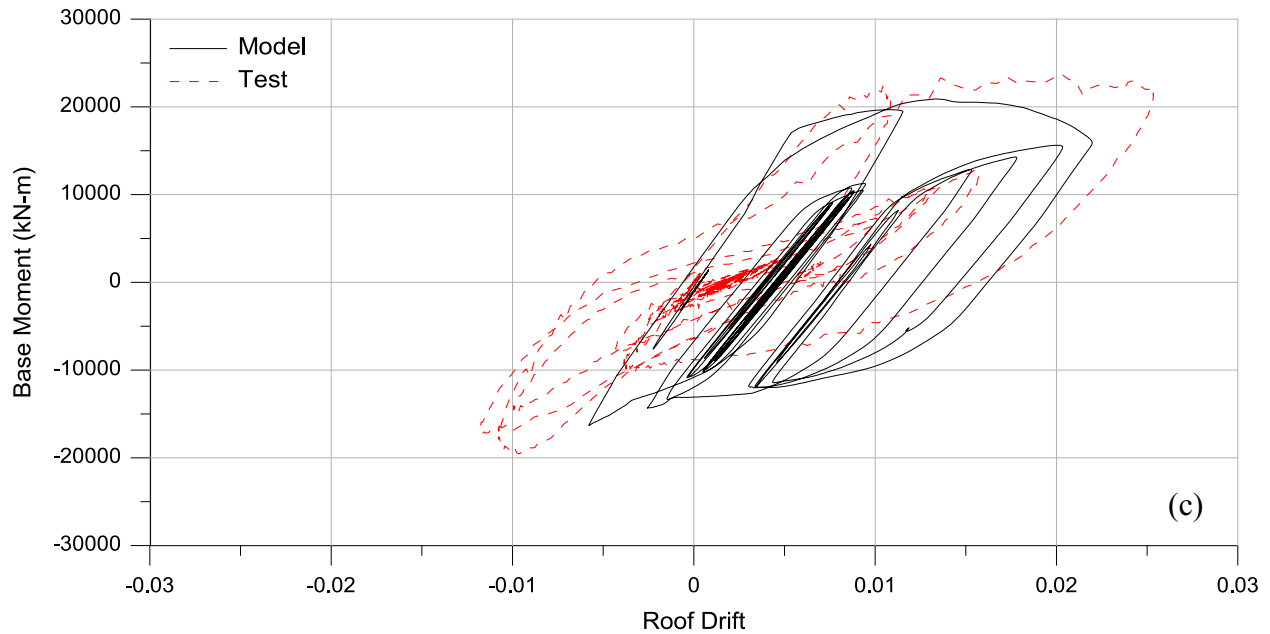
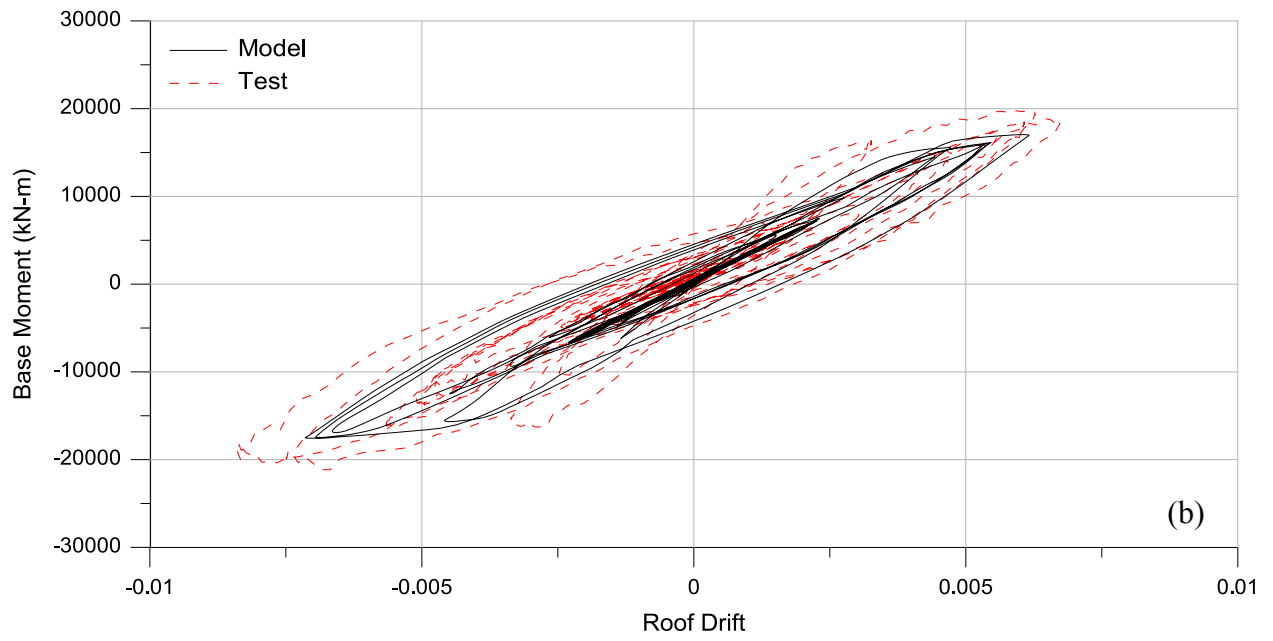
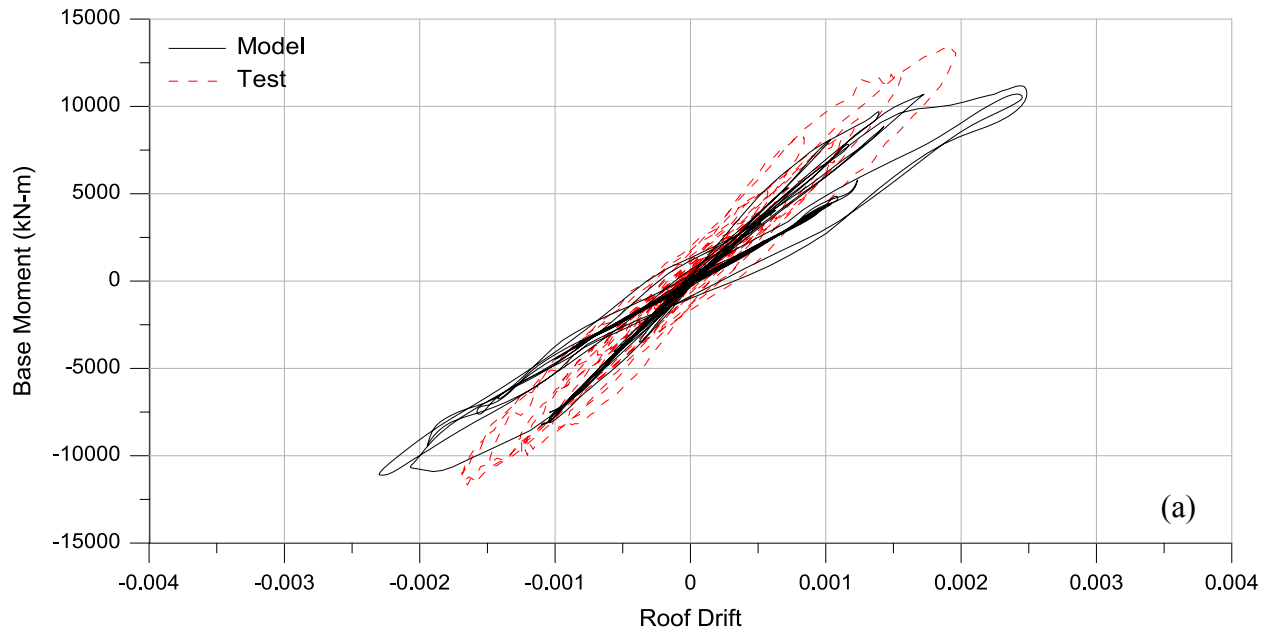


Figure 5-28. Enhanced model at (a) 25%, (b) 50%, (c) 100% Kobe records – effects of modeling slip/extension effects explicitly

5.9.1.3. Cyclic degradation

To include the effects of cyclic loading in stiffness reduction, which was a significant deficiency at the 100% Kobe responses (Figure 5-28(c)), cyclic degradation was modeled in the reinforcing steel behavior as well as in the beam moment-rotation hinges using the parameters presented in Chapter 2. Figure 5-29 shows that the responses were captured modestly better, particularly for 100% Kobe record, although test results show more degradation (pinching) than included in the model. A limited study was conducted to assess the sensitivity of model results to the assumed cyclic degradation parameters; these results are reported later.



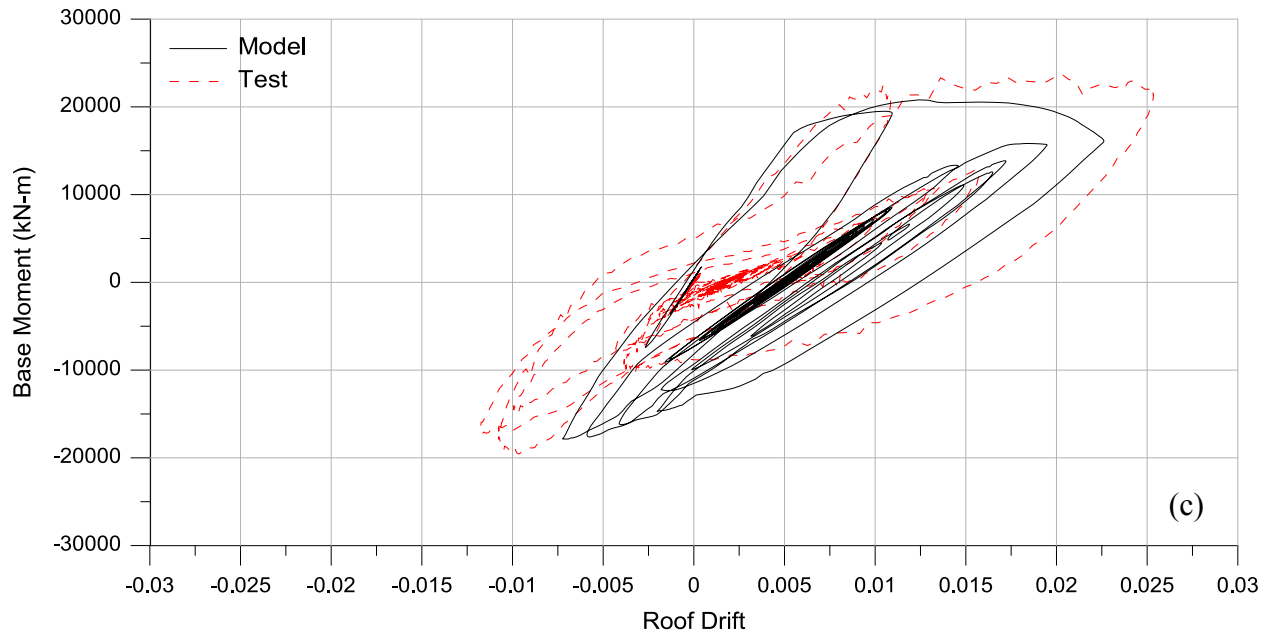


Figure 5-29. Enhanced model at (a) 25%, (b) 50%, (c) 100% Kobe records – effects of cyclic degradation

5.9.1.4. Strength degradation in beams and columns

Strength degradation in beams and columns were modeled based on the backbone parameters recommended by ASCE 41-06. Strength loss interaction was integrated to the model, that is, strength loss in positive direction also resulted in strength loss in negative direction, and vice versa. This feature allowed the model to better reflect the impacts of damage to the frame members (e.g. buckling of rebars and crushing of concrete) because once the damage happens, it affects both positive and negative moment capacities. Figure 5-30 shows that the global response, residual and peak displacements, and overall stiffness in 100% Kobe record were better captured; however, strength loss at larger drift levels was overestimated. Responses are not affected in the low level events (25% and 50% Kobe), as the responses were essentially elastic for 25% Kobe, and only minor yielding occurred for 50% Kobe records.

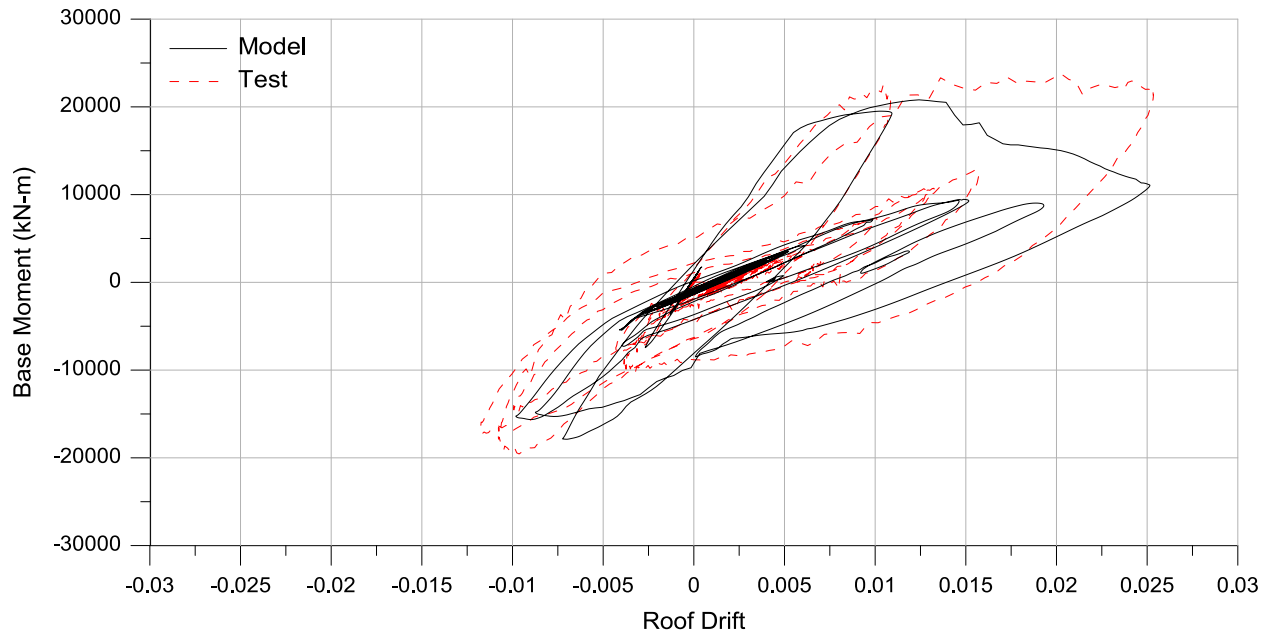
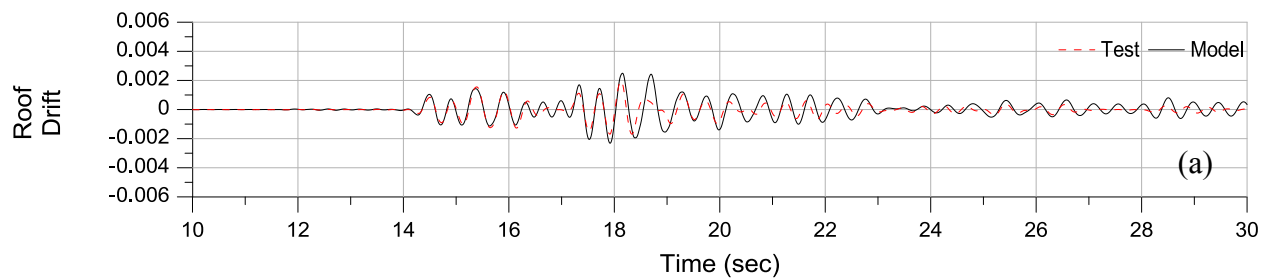


Figure 5-30. Enhanced model at 100% Kobe record – effects of strength degradation

5.9.2. Comparisons of the enhanced analytical results with test results

Results obtained using the enhanced model, which includes additional properties such as slip/extension of longitudinal reinforcement, tension behavior of the concrete material, and strength and stiffness degradation of the components, were compared to the test results. Comparisons (Figure 5-31 to Figure 5-36) indicate that including these modeling parameters significantly improved the correlation between model and test results.



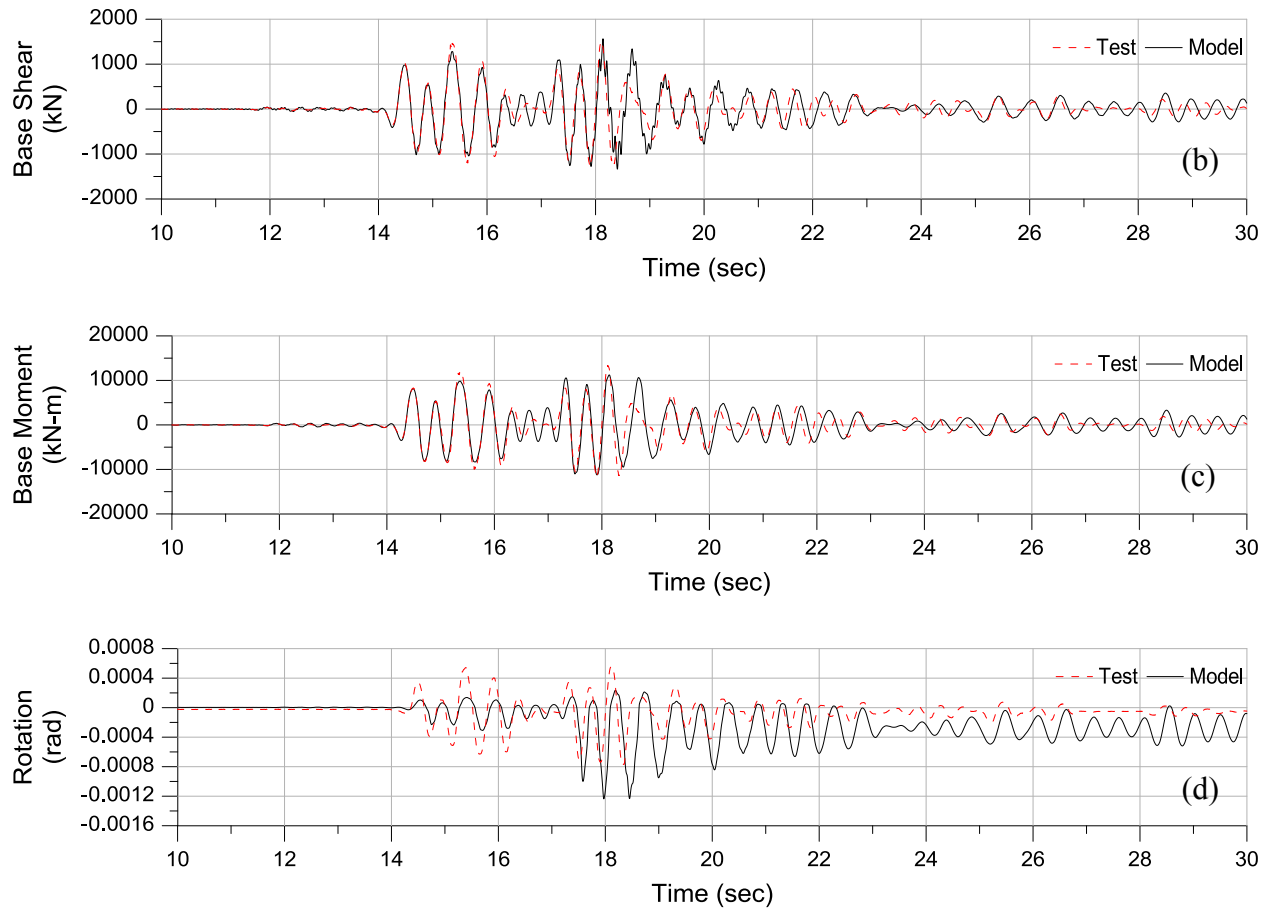


Figure 5-31. Comparisons at 25% Kobe: (a) roof drifts, (b) base shears, (c) base overturning moments, (d)

base rotations over 550 mm

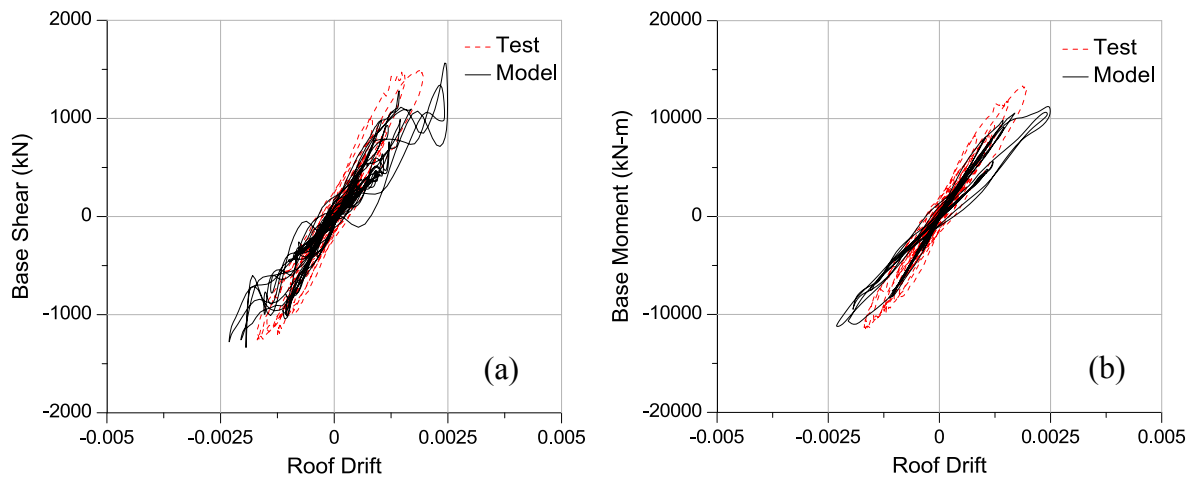


Figure 5-32. Comparisons at 25% Kobe: (a) Base shear vs roof drift, (b) Base moment vs roof drift

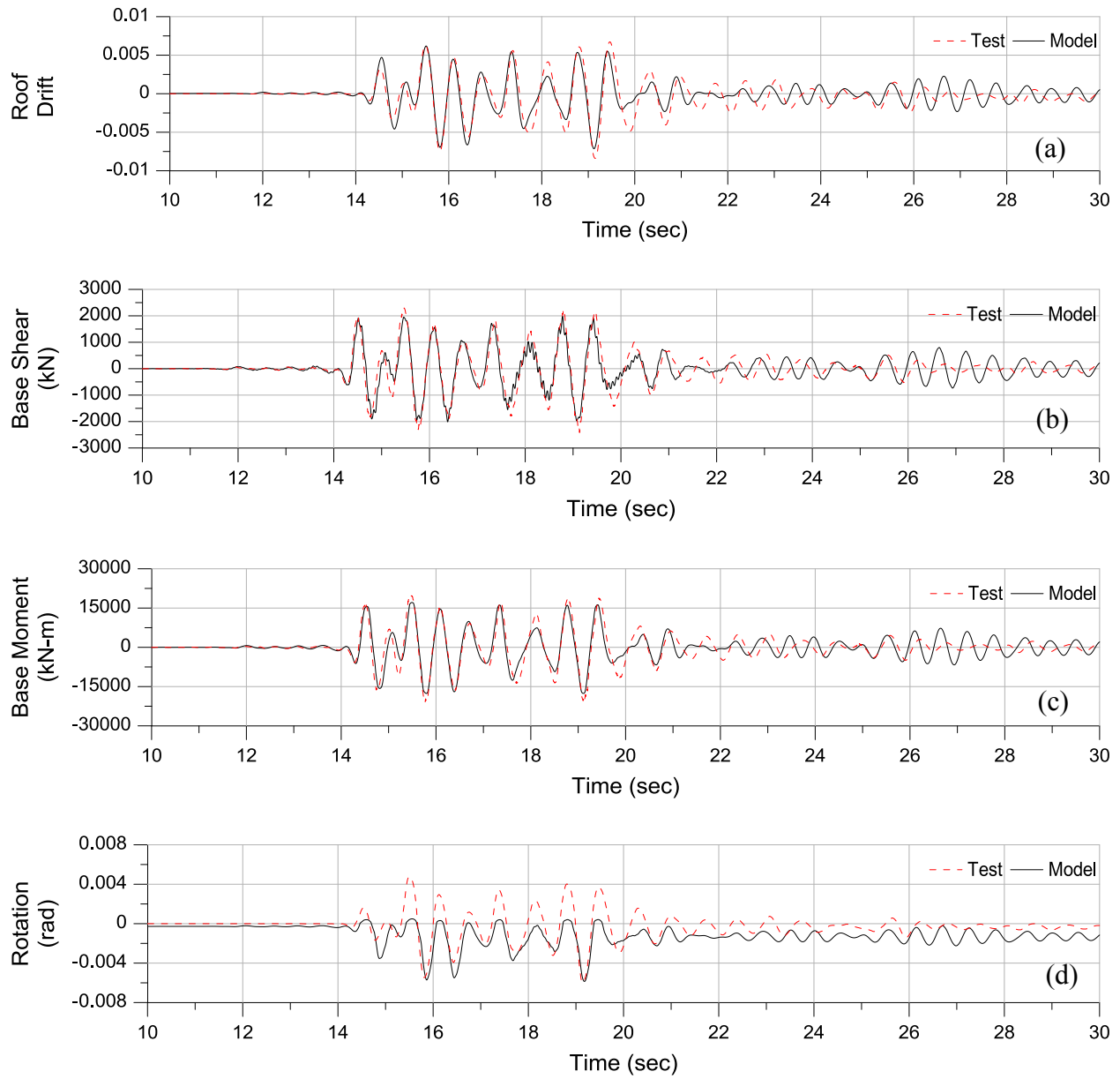


Figure 5-33. Comparisons at 50% Kobe: (a) roof drifts, (b) base shears, (c) base overturning moments, (d) base rotations over 550 mm

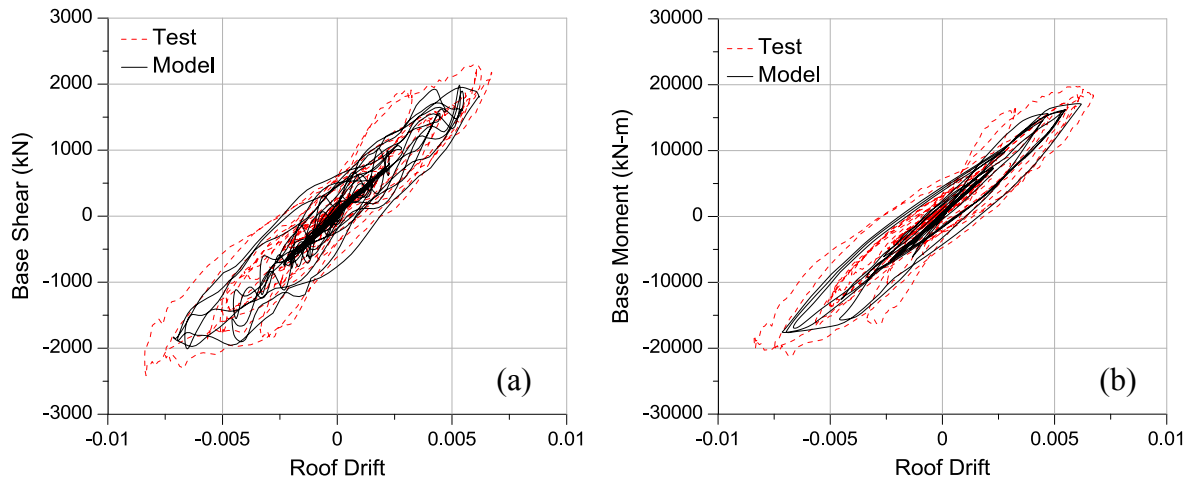
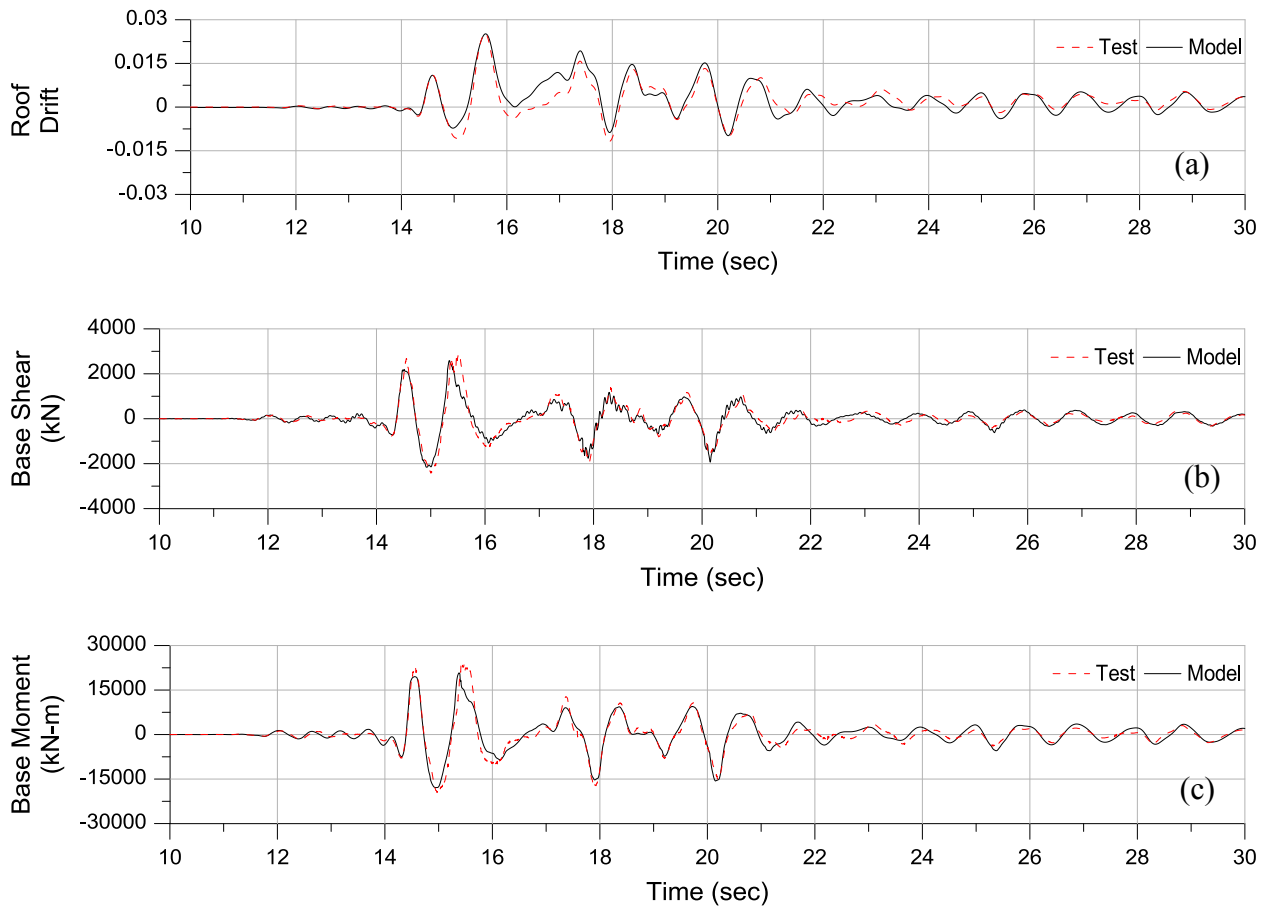


Figure 5-34. Comparisons at 50% Kobe: (a) Base shear vs roof drift, (b) Base moment vs roof drift



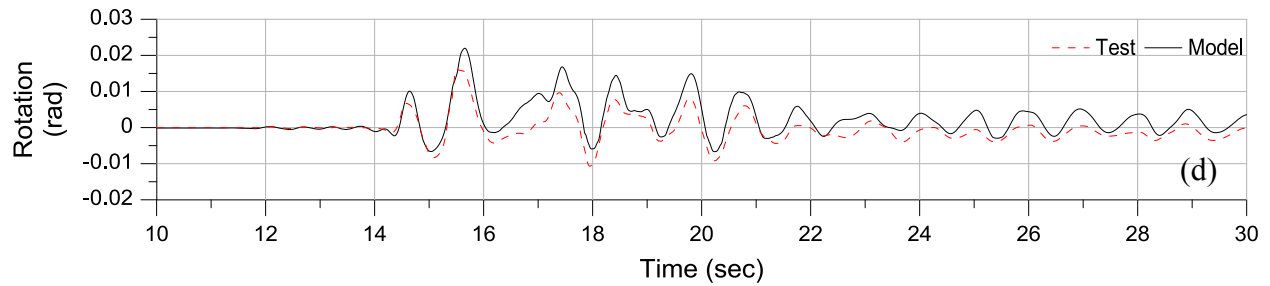


Figure 5-35. Comparisons at 100% Kobe: (a) roof drifts, (b) base overturning moments, (c) base shears, (d) base rotations

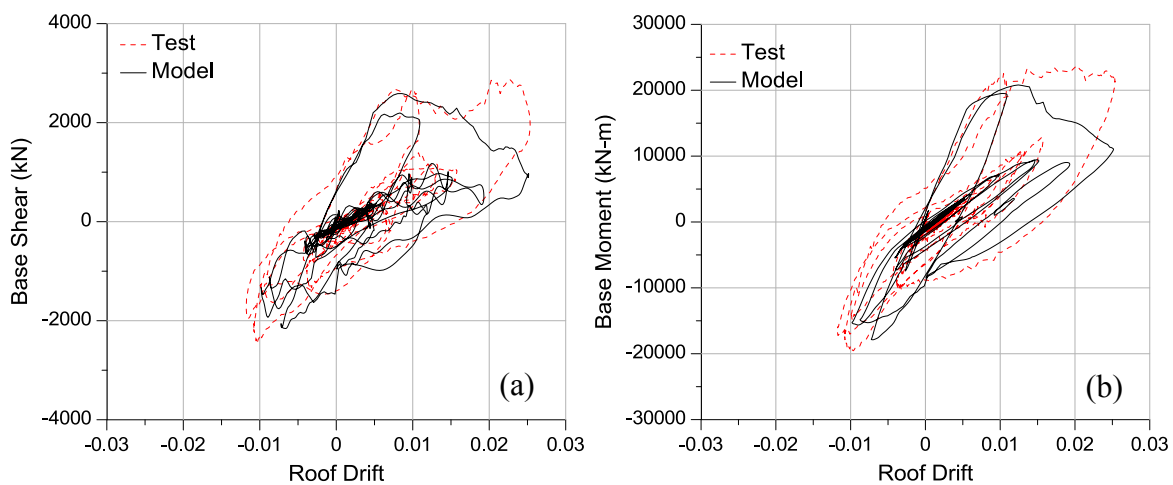


Figure 5-36. Comparisons at 100% Kobe: (a) Base moment vs roof drifts, (b) Base shear vs roof drifts

5.10. Sensitivity Studies

Sensitivity of computed results to modeling parameters for slip/extension hinges, degradation of reinforcing steel, and cyclic degradation parameters for beams and reinforcing steel were investigated. Note that sensitivity for each modeling parameter was examined individually, that is, model results for changes in each modeling parameter are compared to the “base” model results presented in Section 5.8.4, as well as the test results. Comparisons and recommendations are discussed in the following subsections.

5.10.1. Slip/extension behavior

Slip/extension hinges were originally implemented as elastic materials with moment-rotation stiffness of M_y/θ_y . However, using a single stiffness value resulted in underestimating the initial stiffness of the structure. To better reflect the real behavior, the slip/extension hinges were defined to have a bilinear relationship (with two slopes), as presented in Figure 5-37. The slope was changed at a moment of $M = 2/3M_y$; where the initial slope was defined as twice the slope of the elastic material (M_y/θ_y), whereas the second slope was obtained by connecting to the two points between (A) $M = 2/3M_y$ and (B) $M = M_y$.

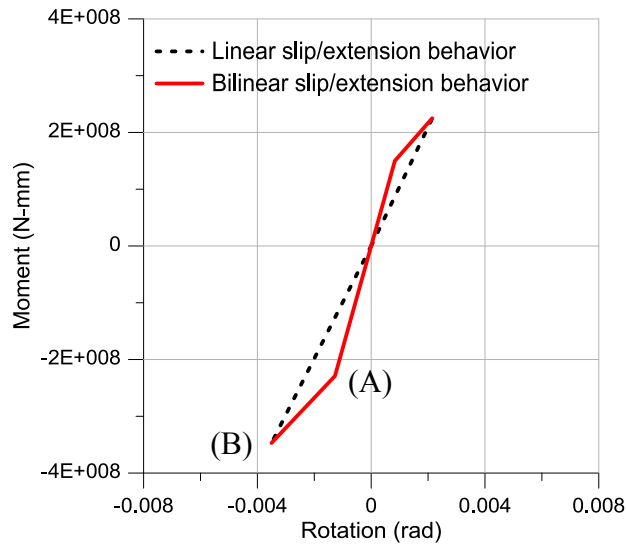
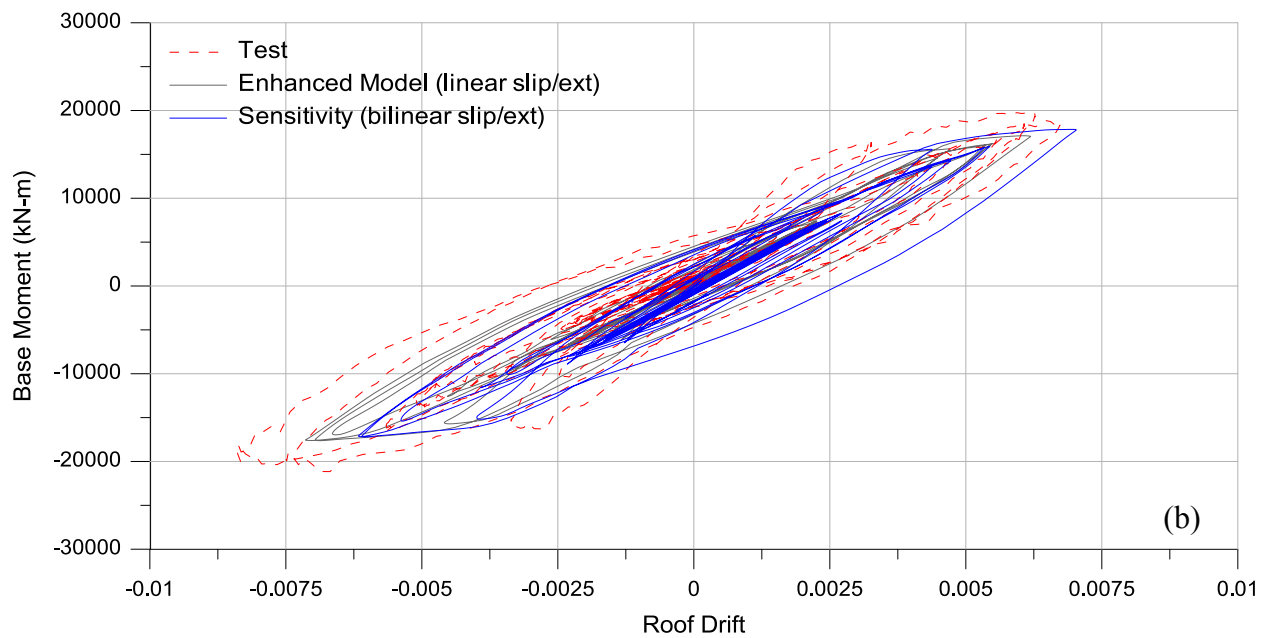
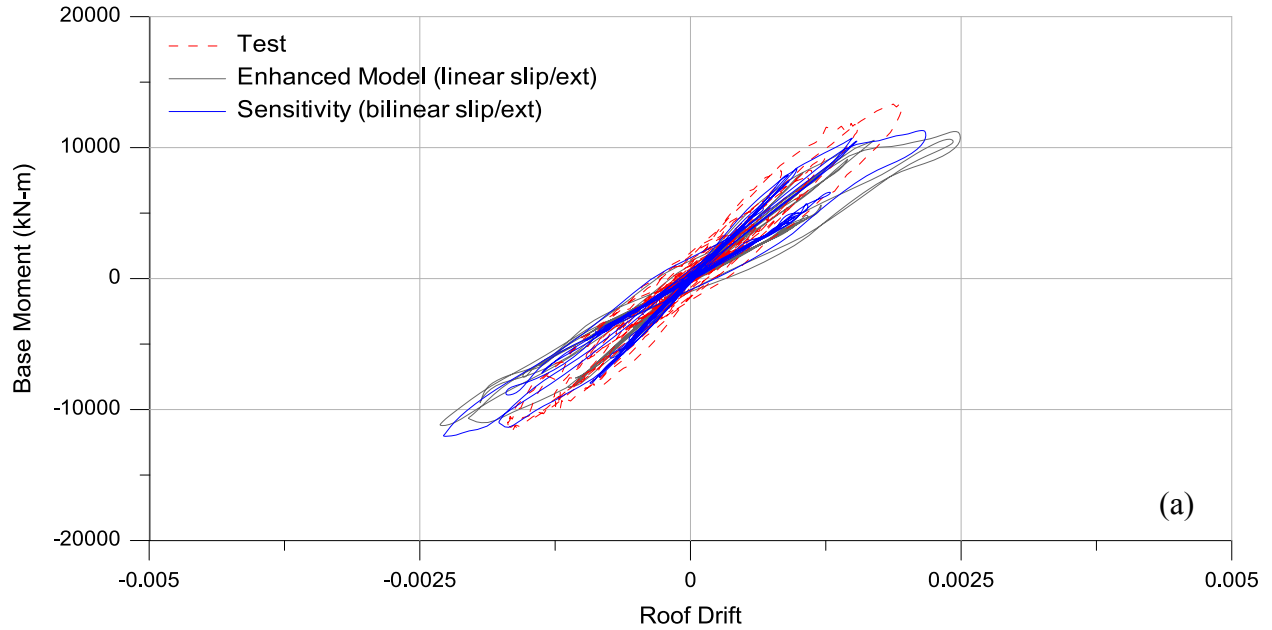


Figure 5-37. Slip/extension moment-rotation hinge properties

Figure 5-38 compares the new model with bilinear slip/extension hinges to the “base” model as well as the test results for each of the records. The blue solid line represents the model with bilinear hinges, whereas the black solid line and red dashed line show the original model and test results, respectively. As shown in Figure 5-38(a), the overall stiffness and peak displacements modestly improved by having a bilinear model (which made the initial slope stiffer) for 25% Kobe record. For the 50% Kobe, global response and the overall stiffness remained very similar,

while drifts were underestimated in the negative direction. Effects of including bilinear slip/extension hinges were more obvious for the 100% Kobe record, where peak displacements were underestimated about 20% compared to the base model.



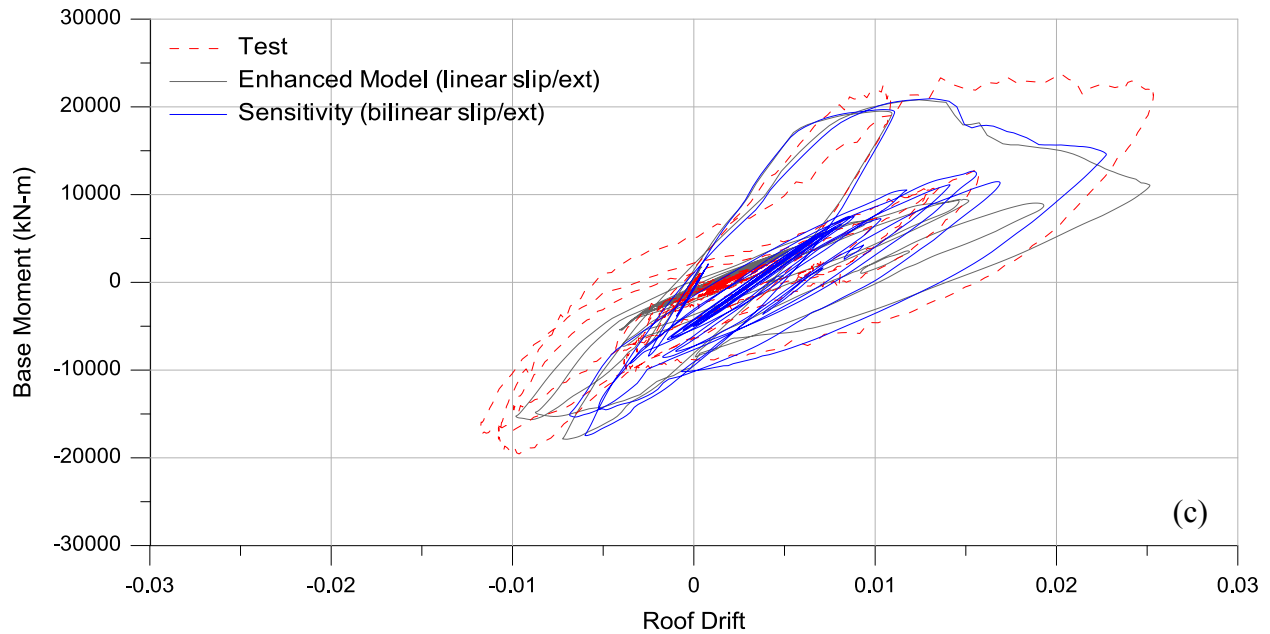


Figure 5-38. Enhanced model at (a) 25%, (b) 50%, (c) 100% Kobe records – sensitivity of the slip/extension behavior

5.10.2. Reinforcing steel behavior

Sensitivity of the results to the slope of the degrading portion of the reinforcing steel was investigated. In the original model, the reinforcing steel was modeled with a stress drop to zero at a strain of 0.05 with a degrading slope of 21400 MPa. Figure 5-39 shows additional two different steel behaviors considered in the sensitivity studies: steel types II and III with a degrading slope of 9290 and 5570 MPa, respectively.

Results presented in Figure 5-40 indicate that descending portion of the steel material only modestly changes the global response at 100% Kobe record. Because strength degradation did not occur in the lower intensity records, comparisons for the 25% and 50% Kobe records are not presented here.

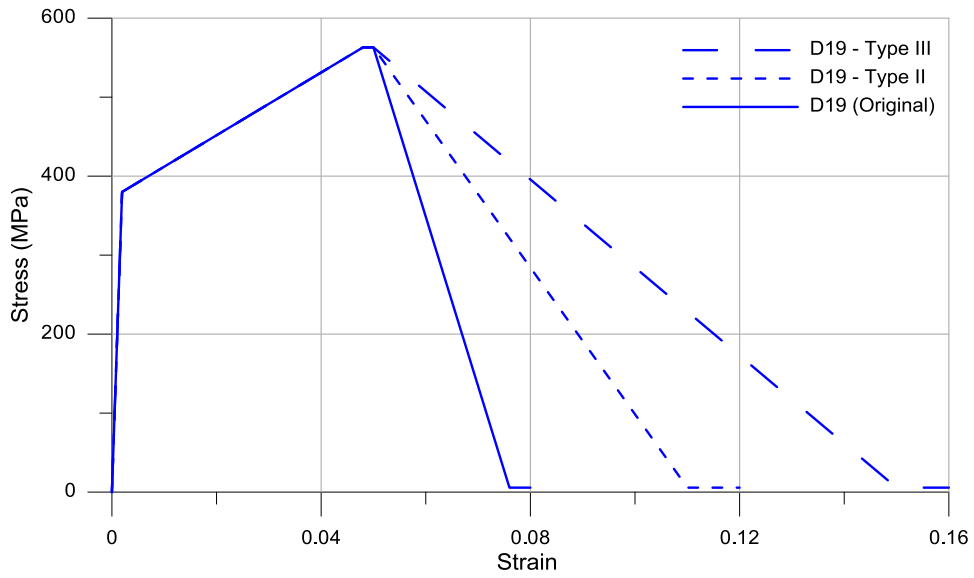


Figure 5-39. Alternative steel behaviors for sensitivity studies (example for D19 bars)

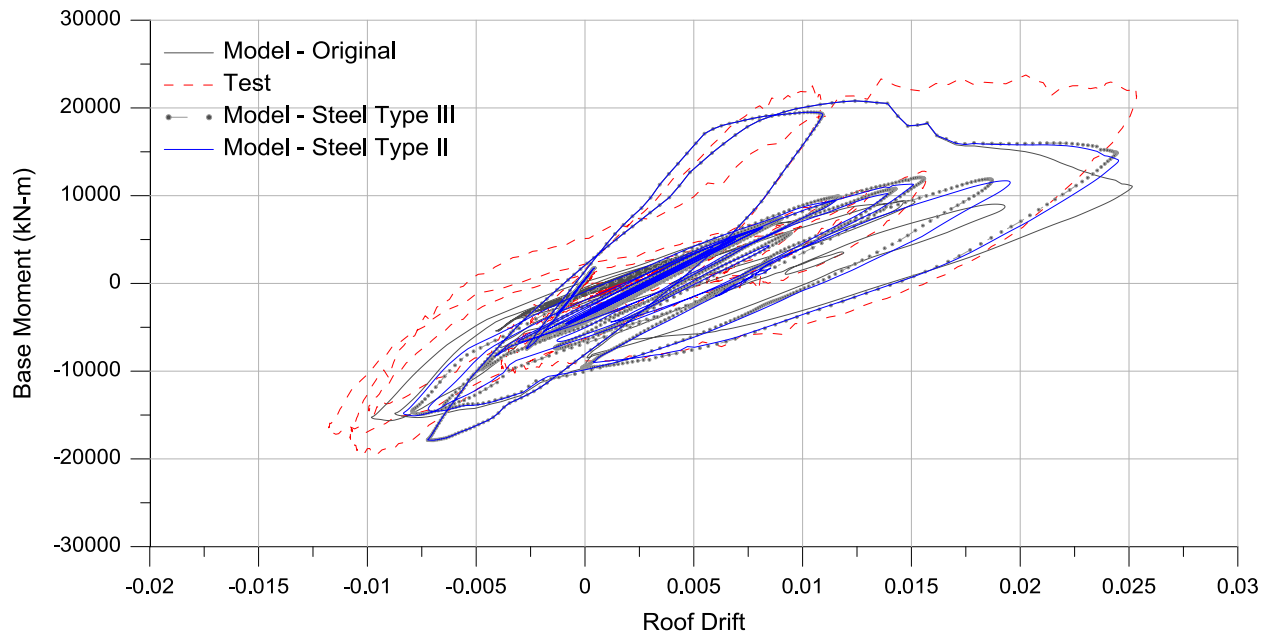


Figure 5-40. Enhanced model at 100% Kobe record – sensitivity of the descending portion of the steel material

5.10.3. Cyclic degradation parameters

Sensitivity of model results to changes in the parameters used to model stiffness degradation due to cyclic actions (cyclic degradation) also was investigated. In the original model, cyclic degradation was included in the reinforcing steel behavior, as well as in the beam moment-rotation hinges. Table 2-8 and Table 5-7 show the original cyclic degradation parameters used in reinforcing steel behavior and in beam moment-rotation hinges, respectively; as well as alternative values that were used in the sensitivity studies.

Table 5-6. Cyclic degradation parameters for the reinforcing steel

| Deformation | Energy Factor | | |
|-------------|---------------|--------|-------|
| | Original | Higher | Lower |
| DY = 0.002 | 0.7 | 0.9 | 0.5 |
| 0.0025 | 0.68 | 0.88 | 0.48 |
| 0.004 | 0.64 | 0.84 | 0.44 |
| 0.006 | 0.62 | 0.82 | 0.42 |
| DX = 0.08 | 0.6 | 0.8 | 0.4 |

Table 5-7. Cyclic degradation parameters for the beam moment-rotation hinges

| Deformation | Energy Factor | | |
|-------------|---------------|--------|-------|
| | Original | Higher | Lower |
| DY | 0.5 | 0.7 | 0.3 |
| DL | 0.4 | 0.6 | 0.2 |
| DR | 0.35 | 0.55 | 0.15 |
| DX | 0.35 | 0.55 | 0.15 |

Results presented in Figure 5-41 and Figure 5-42 indicate that selection of cyclic degradation parameters has only a modest influence on global responses. Use of larger values for cyclic degradation overestimates the stiffness reduction as well as roof drift, particularly in the

positive direction. Smaller values for cyclic degradation (less degradation) energy factors result in lower drift responses in both directions.

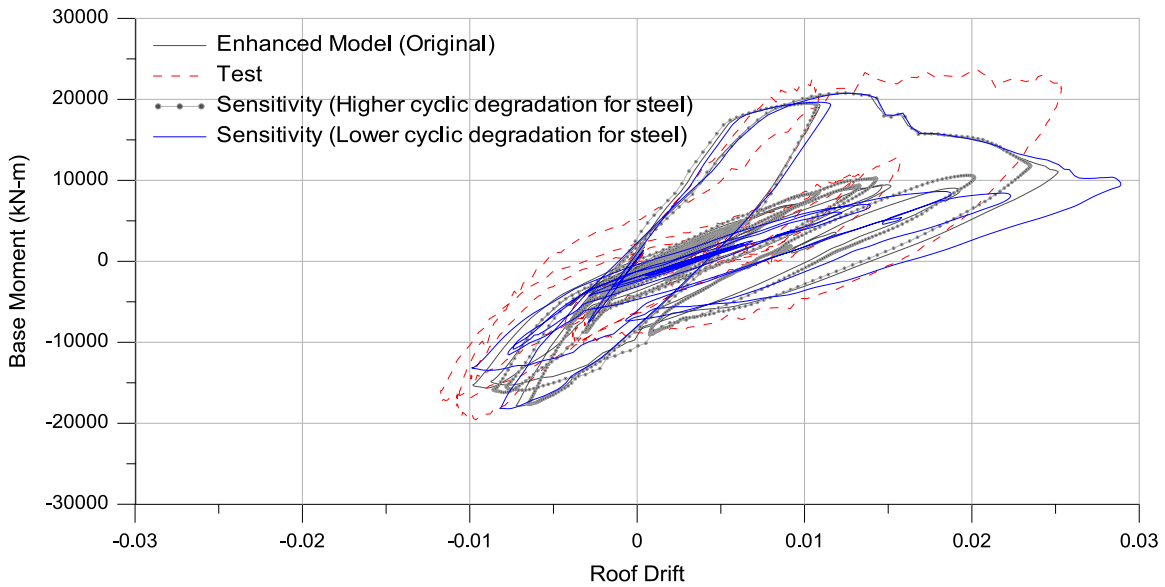


Figure 5-41. Enhanced model at 100% Kobe record – sensitivity of the cyclic degradation parameters used in the steel material

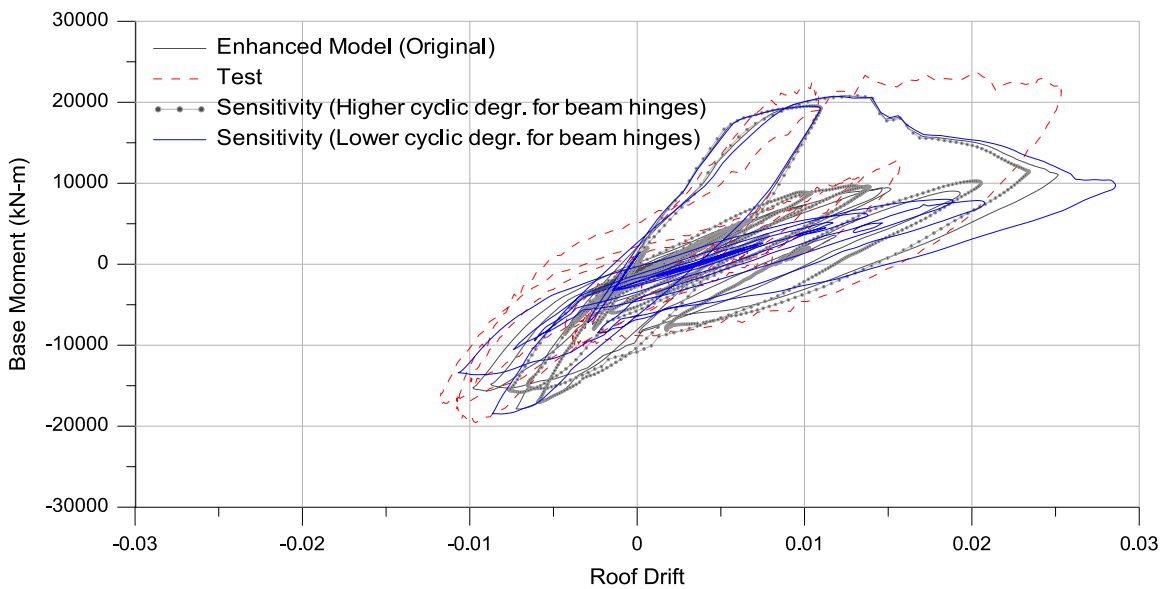


Figure 5-42. Enhanced model at 100% Kobe record – sensitivity of the cyclic degradation parameters used in the steel material

5.11. Summary and Conclusions

Detailed modeling studies related to the December 2010 tests of two, full-scale, four-story buildings that were tested on the NIED E-Defense shake table are presented along with a brief summary of the tests. Ability of current nonlinear modeling techniques to capture the lateral load versus roof displacement relations were assessed by comparing experimental and analytical results. Analytical results for the RC building revealed that the preliminary (blind) model was capable of adequately capturing the responses at the service-level event. However, additional features such as slip/extension of longitudinal reinforcement, and stiffness and strength degradation were included in the model to better capture responses at collapse-level events where significant strength loss and stiffness degradation were observed. Although the enhanced model substantially improved the responses, some discrepancies (such as overestimation of strength degradation as well as failing to capture the responses in the negative direction) were still observed for the 100% Kobe record.

Sensitivity of computed results to modeling parameters for slip/extension hinges, degradation of reinforcing steel, and cyclic degradation parameters for beams and reinforcing steel were investigated. The results indicated that the overall stiffness and peak displacements were improved by having a bilinear model (which made the initial slope stiffer) for the slip/extension hinge behavior. Descending portion of the steel material only modestly changes the global response at 100% Kobe record, whereas it does not affect the results at 25% and 50% Kobe records. Use of larger values for cyclic degradation overestimates the stiffness reduction as well as roof drift, particularly in the positive direction. Smaller values for cyclic degradation energy factors (less degradation) result in lower drift responses in both directions.

Future studies will focus on including sliding-shear behavior at the wall-foundation interface. A bilinear model could be used to account for the near rigid behavior prior to initiation of shear sliding (e.g. in 25% Kobe record). In addition, interpretation of the actual test data indicated that sliding stiffness significantly dropped once the concrete crushed and reinforcement buckled at the wall boundaries; however, Perform 3D is not capable of modeling sliding behavior that is coupled with wall bending behavior. An alternative computational platform might be used to overcome this issue.

Future studies will also include investigating effects of biaxial responses and torsion using three-dimensional analysis (current modeling involves two-dimensional analysis for the shear wall direction), as well as analyzing the building under the Takatori ground motions which were applied following the Kobe motions. It is noted that the building was already significantly damaged, particularly at the base of walls and columns, after 100% Kobe record. Whether the current modeling techniques are sufficient to capture responses of severe damage will be investigated, modeling deficiencies will be identified, and recommendations will be provided for collapse-level events.

Nonlinear modeling and analysis of this building was helpful to assess the modeling techniques used in the previous chapters. Modeling of the Alto Rio building (Chapter 4) was intended to be revised based on the recommendations given in this study to achieve a more reliable model. However, analysis results and comparisons suggest that most of the discrepancies between analytical and test results that were observed using the preliminary model (same modeling approach as in the Alto Rio) at the collapse-level event were related to the beam and column components. Given that the Alto Rio building was a shear wall building (no frame members), the recommendations given for the collapse-level event were not applicable.

Revisions to Chapter 2 were not considered necessary because the study involved comparative analysis and the results of the comparisons would not be significantly impacted by any of the modeling enhancements investigated in Chapter 5.

Chapter 6 Summary and Conclusions

6.1. Summary

Seismic performance, modeling, and failure assessment of reinforced concrete shear wall buildings was investigated using information presented in four chapters. The brief introduction provided in Chapter 1 was followed by a case study of 42-story reinforced concrete dual system building in Chapter 2. This chapter included detailed information about the prototype building and different design methodologies (e.g. code-based design, performance-based design). Seismic performance of the code-designed and performance-based designed buildings was assessed and compared at various levels of ground shaking intensity. Performance differences between different design approaches were investigated and presented for various response quantities. A summary of cost analysis (conducted by a professional cost estimator) also was provided. Chapter 2 also included an assessment of the collapse potential due to shear failures observed in some wall sections. A wall shear failure criterion was defined based on previous tests, and potential wall shear failures were investigated by post-processing response history analysis results. The study identified a need to establish improved wall shear failure criteria.

Chapter 3 summarized a detailed study conducted to assess and potentially improve on the wall shear failure criterion was used in the study presented in Chapter 2. A basis for classifying shear wall behavior based on expected failure mode was identified, by which shear walls were categorized into three bins: shear-controlled walls, transition walls, and flexure-controlled walls. For each bin, alternative relations for wall shear strength and normalized deformation capacity were proposed using a wall test database. Statistics (median, dispersion) on wall shear strength and normalized wall deformation capacity were assessed for the entire wall

database as well as for walls meeting minimum web reinforcement ratios as specified in ACI 318-11. These statistics provide information that is essential for the application of performance-based design approaches. Capacity of the walls was assessed in terms of shear strength and deformation capacity, separately; whereas failure criteria with an interaction between shear strength and deformation capacity will be assessed in the future studies.

Chapter 4 presented a study that assessed possible reasons for the collapse of the Alto Rio building in the 2010 Chile Earthquake. Overall information about the earthquake was provided followed by a brief overview of building code provisions used in design of reinforced concrete buildings in Chile. A description of the building along with the schematics of building damage were presented. This chapter includes preliminary analyses (based on post-earthquake observed damage, structural drawings, and section analyses) and detailed nonlinear static and dynamic response history analyses that were conducted for a representative slice of the building (Axes 11 and 13) using the ground motions recorded in Concepcion. Details of the analytical model (in Perform 3D) and analysis results for various response quantities were presented. The chapter concluded with a possible collapse scenario, which was generally consistent with reported damage.

Chapter 5 provided a comparative study of experimental and analytical results for the four-story reinforced concrete building (RC Building) that was tested on the NIED E-Defense shake table in December 2010. Background information was provided, followed by a description of the RC Building, details of the test program, and an overview of the test results. A detailed review of the building design was conducted to assess whether the design of the building satisfied U.S. code provisions (i.e., strength requirements, drift requirements, and detailing requirements). The modeling studies focused on providing comparisons between measured and

predicted (analytical) responses for the shear wall direction of the RC Building. Two analytical models developed in Perform 3D: (i) preliminary (blind) model, which was based on current modeling techniques, i.e. without taking advantage of information gleaned from test data; (ii) enhanced model, which included additional modeling features to better capture the results. Nonlinear modeling and analysis of this building was helpful to assess the current modeling techniques.

6.2. Conclusions

Primary conclusions that were drawn from the case study of a 42-story reinforced concrete dual system building (Chapter 2) include:

1. Both code-based designed and performance-based designed buildings are expected to satisfy performance objectives - excellent performance is expected. The performance-based designed building achieved slightly better performance than the code-designed building, due to the lower wall shear stresses and lower wall compressive strains observed at the shear walls of this building, although the difference was modest.
2. Axial load demands on the corner columns were more critical in the code-designed building, although precise impact on collapse potential is unknown, given our lack of understanding related to the behavior of well-detailed, large columns subjected to high axial loads. The beams and column plastic rotation demands were limited for both designs.
3. Construction costs were estimated to be about 20% higher in Building 2B (performance-based design), whereas lifetime maintenance costs were about 20% lower in the same building.

The following conclusions were derived from the statistical study conducted to assess shear strength and deformation capacity of reinforced concrete shear walls (Chapter 3):

1. ACI 318-11 underestimates the shear strength by 20% for the shear-controlled (squat) walls (i.e., ratio of $v_{test}/v_{n,ACI} = 1.2$), whereas the peak shear stress for flexure-controlled (slender) walls is only 70% of the ACI 318-11 nominal shear strength. It is noted $v_{test}/v_{n,ACI}$ ratio of 1.2 seems very low compared to the previous findings (Wallace, 1998; Orakcal, et al., 2009) which indicated that the ratio was 1.5, potentially because there were some walls in the shear-controlled bin that actually did not fail in pure shear; therefore, wall classification criteria needs to be carefully reassessed.
2. The mean shear strength (v_n) obtained using the proposed (best-fitted) equation for shear-controlled walls was $8.2\sqrt{f'_c}$ with a standard deviation of $3\sqrt{f'_c}$.
3. The normalized deformation capacity was defined as curvature ductility for all types of walls, whereas for shear-controlled walls displacement ductility also was considered because by definition shear-controlled walls are not expected to have inelastic curvature. The mean normalized deformation capacity, in terms of curvature ductility (μ_ϕ), increased from about 3 to 7 as the wall category switched from shear-controlled to flexure-controlled. For the shear-controlled walls, the displacement ductility was about the same as curvature ductility, although dispersion was reduced.
4. The derived equations can be used by engineers for the application of performance-based design approaches, and to improve reliability of their designs. Demand-to-

Capacity (DCR) ratios/distributions can be obtained and used to adjust the design variables to improve safety. Demand distributions would be obtained from nonlinear response history analysis results, whereas capacity distributions would be determined using the proposed equations. The overlapping area of the two distributions would define the probability of failure.

Collapse assessment of the Alto Rio building in the 2010 Chile Earthquake (Chapter 4) led to the following conclusions:

1. The analysis results were generally consistent with the observed damage that was reported after the earthquake. A variety of factors likely led to the building collapse including discontinuities (both in cross section and in vertical reinforcement), filled-in walls that were placed across the corridor at the first story at some axes, wall openings within the first story and the first subterranean level, and splices of wall vertical boundary and web reinforcement.
2. Post-processing of the nonlinear response history analysis results indicated that compressive concrete and rebar strains rapidly reached very large values (greater than 0.03) at the web boundary of the T- and L-shaped wall cross sections at the east side of the building. The dramatic increase in the compression demands would likely have initiated the damage relatively early in the response history ($t= 20$ seconds), and eventually led to collapse of the building.
3. Results of a strut-and-tie model indicated that very large Demand-to-Capacity (DCR) ratios were likely below in these first story walls across the corridors, likely due to tensile yielding of wall web reinforcement followed by buckling of reinforcement

upon load reversal in the long duration earthquake. This damage would likely occur prior to flexural-compression damage (concrete crushing and rebar buckling) at wall edges along the east side of the building due to large cyclic tension and compression demands. Reduced overturning resistance of the building would result due to the wall damage, and significant discontinuities, such as walls across the corridor at the first story, vertical discontinuities and setbacks, and large openings in the basement walls produced stress concentrations likely to produce wall damage. The damage in the first story corridor walls, combined with damage at wall boundaries, poor splice details, especially in some west transverse walls at ground line, and the long duration ground motions, were likely sufficient to produce a building that was susceptible to overturning.

Conclusions drawn from the comparative study of experimental and analytical results on the four-story reinforced concrete building tested on the E-Defense shake table (Chapter 5) are summarized below:

1. The preliminary (blind) model was capable of adequately capturing the responses at the service-level event, although significant discrepancies were observed at collapse-level events where significant strength loss and stiffness degradation were observed.
2. The enhanced model which included additional features such as tension behavior of concrete, slip/extension behavior of longitudinal reinforcement, strength degradation in beams and columns, and stiffness degradation due to cyclic actions led to improved correlation between computed and measured responses for the collapse-

level events. However, strength degradation was overestimated in the model, and the model failed to capture the asymmetric responses observed in the tests.

3. For nonlinear modeling of shear wall buildings at the service-level events, including tension behavior of concrete and use of a bilinear model (versus a linear model) for the slip/extension hinge behavior significantly improved the correlation between computed and measured responses for global response parameters (such as base shear versus roof drift). For collapse-level events, it is important to consider including strength and stiffness degradation in beams and columns.

Appendix A

Ground Motion Selection Methodology

A.1 Ground Motion Selection and Scaling Assumptions

- T_{\min} & T_{\max} at 0.5sec & 10.0 sec.
- Maximum acceptable scale factor = 4.0
- No restriction on magnitude
- R_{\min} & R_{\max} at 0.0 and 70.0 Km
- Min and max shear wave velocity = 200.0 and 700.0 m/s
- Low pass filter frequency lower than 0.1 Hz
- Used a subset of NGA database (no aftershocks & etc.)
- Diversify motions from various events as much as possible

A.2 Procedure

1. Target spectrum obtained from Marshal for 5% damping
2. A subset of NGA database is used to identify motion.
3. Records are ranked according to the error between target spectrum and geometric mean of ground motion pairs.
4. A weight function of 10% for periods between 0.5 to 3 seconds, 60% from 3 seconds to 7 seconds, and 30% from 7 seconds to 10 seconds is used.
5. From each earthquake not more than 2 records were selected.
6. The records are filtered using 8-node filter and down-sampled with $dt=0.04$ sec.

Appendix B

DETAILS OF THE DATABASE

Table B-1. Specimen Geometry Data

| Specimen | | Loading type | Shape | Dimensions (mm) | | | Aspect ratio | Shear span ratio | Axial load ratio |
|----------------------|---------------|--------------|-----------|-----------------|-------|-------|--------------|------------------|------------------|
| | | | | H_w | L_w | t_w | | | |
| Tran (2011) | RW-A20-P10-S4 | Cyclic | Rectangle | 2438 | 1219 | 152 | 2.0 | 2.0 | 0.07 |
| | RW-A20-P10-S7 | Cyclic | Rectangle | 2438 | 1219 | 152 | 2.0 | 2.0 | 0.07 |
| | RW-A15-P10-S5 | Cyclic | Rectangle | 1829 | 1219 | 152 | 1.5 | 1.5 | 0.07 |
| Salonikios (1999) | LSW1 | Cyclic | Rectangle | 1200 | 1200 | 100 | 1.0 | 1.0 | 0.00 |
| | LSW2 | Cyclic | Rectangle | 1200 | 1200 | 100 | 1.0 | 1.0 | 0.00 |
| | LSW3 | Cyclic | Rectangle | 1200 | 1200 | 100 | 1.0 | 1.0 | 0.07 |
| | LSW4 | Cyclic | Rectangle | 1200 | 1200 | 100 | 1.0 | 1.0 | 0.00 |
| | LSW5 | Cyclic | Rectangle | 1200 | 1200 | 100 | 1.0 | 1.0 | 0.00 |
| | MSW1 | Cyclic | Rectangle | 1800 | 1200 | 100 | 1.5 | 1.5 | 0.00 |
| | MSW2 | Cyclic | Rectangle | 1800 | 1200 | 100 | 1.5 | 1.5 | 0.00 |
| | MSW3 | Cyclic | Rectangle | 1800 | 1200 | 100 | 1.5 | 1.5 | 0.07 |
| | MSW4 | Cyclic | Rectangle | 1800 | 1200 | 100 | 1.5 | 1.5 | 0.00 |
| | MSW5 | Cyclic | Rectangle | 1800 | 1200 | 100 | 1.5 | 1.5 | 0.00 |
| | MSW6 | Cyclic | Rectangle | 1800 | 1200 | 100 | 1.5 | 1.5 | 0.00 |
| Wang (2000) | SW7 | Cyclic | Rectangle | 1500 | 700 | 100 | 2.1 | 2.1 | 0.24 |
| | SW8 | Cyclic | Rectangle | 1500 | 700 | 100 | 2.1 | 2.1 | 0.35 |
| | SW9 | Cyclic | Rectangle | 1500 | 700 | 100 | 2.1 | 2.1 | 0.24 |
| Corley (1982) | B1 | Cyclic | Barbell | 4570 | 1910 | 102 | 2.4 | 2.4 | 0.00 |
| | B2 | Cyclic | Barbell | 4570 | 1910 | 102 | 2.4 | 2.4 | 0.00 |
| | B3 | Cyclic | Barbell | 4570 | 1910 | 102 | 2.4 | 2.4 | 0.00 |
| | B4 | Monotonic | Barbell | 4570 | 1910 | 102 | 2.4 | 2.4 | 0.00 |
| | B5 | Cyclic | Barbell | 4570 | 1910 | 102 | 2.4 | 2.4 | 0.00 |
| | B6 | Cyclic | Barbell | 4570 | 1910 | 102 | 2.4 | 2.4 | 0.13 |
| | B7 | Cyclic | Barbell | 4570 | 1910 | 102 | 2.4 | 2.4 | 0.08 |
| | B8 | Cyclic | Barbell | 4570 | 1910 | 102 | 2.4 | 2.4 | 0.09 |

continued on next page

continued from previous page

| Specimen | | Loading type | Shape | Dimensions (mm) | | | Aspect ratio | Shear span ratio | Axial load ratio | |
|-------------------|----------------|--------------|-----------|-----------------|-------|-------|--------------|------------------|------------------|------|
| | | | | H_w | L_w | t_w | | | | |
| Corley | B9 | Cyclic | Barbell | 4570 | 1910 | 102 | 2.4 | 2.4 | 0.09 | |
| Massone (2006) | Test 1 | Cyclic | Barbell | 1520 | 1520 | 152 | 1.0 | 0.5 | 0.00 | |
| | Test 2 | Cyclic | Barbell | 1520 | 1520 | 152 | 1.0 | 0.5 | 0.00 | |
| | Test 3 | Cyclic | Barbell | 1520 | 1520 | 152 | 1.0 | 0.5 | 0.00 | |
| | Test 6 | Cyclic | Rectangle | 1220 | 1370 | 152 | 0.9 | 0.4 | 0.10 | |
| | Test 7 | Cyclic | Rectangle | 1220 | 1370 | 152 | 0.9 | 0.4 | 0.05 | |
| | Test 8 | Cyclic | Rectangle | 1220 | 1370 | 152 | 0.9 | 0.4 | 0.05 | |
| | Test 10 | Cyclic | Rectangle | 1220 | 1370 | 152 | 0.9 | 0.4 | 0.00 | |
| | Test 11 | Cyclic | Rectangle | 1520 | 1520 | 152 | 1.0 | 0.5 | 0.00 | |
| | Test 12 | Cyclic | Rectangle | 1520 | 1520 | 152 | 1.0 | 0.5 | 0.00 | |
| | Test 13 | Cyclic | Rectangle | 1520 | 1520 | 152 | 1.0 | 0.4 | 0.00 | |
| | Test 14 | Cyclic | Rectangle | 1520 | 1520 | 152 | 1.0 | 0.5 | 0.00 | |
| | Hidalgo (2002) | Specimen 1 | Cyclic | Rectangle | 2000 | 1000 | 120 | 2.0 | 1.0 | 0.00 |
| | | Specimen 2 | Cyclic | Rectangle | 2000 | 1000 | 120 | 2.0 | 1.0 | 0.00 |
| | | Specimen 4 | Cyclic | Rectangle | 2000 | 1000 | 120 | 2.0 | 1.0 | 0.00 |
| Specimen 6 | | Cyclic | Rectangle | 1800 | 1300 | 120 | 1.4 | 0.7 | 0.00 | |
| Specimen 7 | | Cyclic | Rectangle | 1800 | 1300 | 120 | 1.4 | 0.7 | 0.00 | |
| Specimen 8 | | Cyclic | Rectangle | 1800 | 1300 | 120 | 1.4 | 0.7 | 0.00 | |
| Specimen 9 | | Cyclic | Rectangle | 1800 | 1300 | 100 | 1.4 | 0.7 | 0.00 | |
| Specimen 10 | | Cyclic | Rectangle | 1800 | 1300 | 80 | 1.4 | 0.7 | 0.00 | |
| Specimen 13 | | Cyclic | Rectangle | 1400 | 1400 | 100 | 1.0 | 0.5 | 0.00 | |
| Specimen 14 | | Cyclic | Rectangle | 1200 | 1700 | 80 | 0.7 | 0.4 | 0.00 | |
| Specimen 24 | | Cyclic | Rectangle | 1800 | 1300 | 100 | 1.4 | 0.7 | 0.00 | |
| Specimen 28 | | Cyclic | Rectangle | 1400 | 1400 | 100 | 1.0 | 0.5 | 0.00 | |
| Dazio (2009) | | WSH1 | Cyclic | Rectangle | 4560 | 2000 | 150 | 2.3 | 2.3 | 0.05 |
| | WSH2 | Cyclic | Rectangle | 4560 | 2000 | 150 | 2.3 | 2.3 | 0.06 | |
| | WSH3 | Cyclic | Rectangle | 4560 | 2000 | 150 | 2.3 | 2.3 | 0.06 | |
| | WSH4 | Cyclic | Rectangle | 4560 | 2000 | 150 | 2.3 | 2.3 | 0.06 | |
| Kabeyasawa (1993) | NW-1 | Cyclic | Barbell | 3000 | 1700 | 80 | 1.8 | 2.0 | 0.14 | |
| | NW-2 | Cyclic | Barbell | 2000 | 1700 | 80 | 1.2 | 1.3 | 0.13 | |
| | NW-3 | Cyclic | Barbell | 3000 | 1700 | 80 | 1.8 | 2.0 | 0.17 | |
| | NW-4 | Cyclic | Barbell | 3000 | 1700 | 80 | 1.8 | 2.0 | 0.20 | |

continued on next page

continued from previous page

| Specimen | Loading type | Shape | Dimensions (mm) | | | Aspect ratio | Shear span ratio | Axial load ratio | |
|----------------------|--------------|---------|-----------------|-------|-------|--------------|------------------|------------------|------|
| | | | H_w | L_w | t_w | | | | |
| Kabeyasawa (1993) | NW-5 | Cyclic | Barbell | 3000 | 1700 | 80 | 1.8 | 2.0 | 0.16 |
| | NW-6 | Cyclic | Barbell | 3000 | 1700 | 80 | 1.8 | 2.0 | 0.17 |
| | W-08 | Cyclic | Barbell | 2000 | 1700 | 80 | 1.2 | 0.7 | 0.12 |
| | W-12 | Cyclic | Barbell | 2000 | 1700 | 80 | 1.2 | 0.7 | 0.12 |
| | NO.1 | Cyclic | Barbell | 2000 | 1700 | 80 | 1.2 | 1.3 | 0.17 |
| | NO.2 | Cyclic | Barbell | 2000 | 1700 | 80 | 1.2 | 1.3 | 0.15 |
| | NO.3 | Cyclic | Barbell | 2000 | 1700 | 80 | 1.2 | 1.3 | 0.15 |
| | NO.4 | Cyclic | Barbell | 2000 | 1700 | 80 | 1.2 | 1.3 | 0.18 |
| | NO.5 | Cyclic | Barbell | 3000 | 1700 | 80 | 1.8 | 2.0 | 0.14 |
| | NO.7 | Cyclic | Barbell | 2000 | 1700 | 80 | 1.2 | 1.3 | 0.15 |
| | NO.8 | Cyclic | Barbell | 2000 | 1700 | 80 | 1.2 | 1.3 | 0.14 |
| | M35X | Cyclic | Barbell | 2000 | 1700 | 80 | 1.2 | 2.0 | 0.35 |
| | M35H | Cyclic | Barbell | 2000 | 1700 | 80 | 1.2 | 2.0 | 0.35 |
| | P35H | Cyclic | Barbell | 2000 | 1700 | 80 | 1.2 | 2.0 | 0.35 |
| | M30H | Cyclic | Barbell | 2000 | 1700 | 80 | 1.2 | 2.0 | 0.30 |
| | MW35H | Cyclic | Barbell | 2000 | 1700 | 80 | 1.2 | 2.0 | 0.35 |
| | MAE03 | Cyclic | Barbell | 1100 | 2180 | 80 | 0.5 | 0.6 | 0.04 |
| | MAE07 | Cyclic | Barbell | 1100 | 2180 | 80 | 0.5 | 0.6 | 0.04 |
| | SMZ01 | Cyclic | Barbell | 1400 | 2700 | 75 | 0.5 | 0.7 | 0.00 |
| | SMZ03 | Cyclic | Barbell | 1400 | 2700 | 75 | 0.5 | 0.7 | 0.00 |
| | W8N18 | Cyclic | Barbell | 1700 | 1400 | 80 | 1.2 | 2.0 | 0.20 |
| | W8N13 | Cyclic | Barbell | 1700 | 1400 | 80 | 1.2 | 2.0 | 0.13 |
| | W8N8H | Cyclic | Barbell | 1700 | 1400 | 80 | 1.2 | 2.0 | 0.08 |
| W72M6 | Cyclic | Barbell | 1080 | 3080 | 120 | 0.4 | 0.8 | 0.03 | |
| TAK01 | Cyclic | Barbell | 2700 | 1900 | 85 | 1.4 | 1.8 | 0.14 | |
| TAK02 | Cyclic | Barbell | 2700 | 1900 | 85 | 1.4 | 1.8 | 0.14 | |
| TAK03 | Cyclic | Barbell | 2700 | 1900 | 85 | 1.4 | 1.8 | 0.14 | |
| Thomsen (1995) | RW1 | Cyclic | Rectangle | 3658 | 1220 | 102 | 3.0 | 3.0 | 0.10 |
| | RW2 | Cyclic | Rectangle | 3658 | 1220 | 102 | 3.0 | 3.0 | 0.07 |
| | TW2 | Cyclic | T-shaped | 3658 | 1220 | 102 | 3.0 | 3.0 | 0.08 |
| Jiang (1999) | SSW-T | Cyclic | Rectangle | 2800 | 1000 | 75 | 2.8 | 2.8 | 0.10 |
| | DSW-T | Cyclic | Rectangle | 2800 | 1000 | 75 | 2.8 | 2.8 | 0.10 |

continued on next page

continued from previous page

| <i>Specimen</i> | | <i>Loading type</i> | <i>Shape</i> | <i>Dimensions (mm)</i> | | | <i>Aspect ratio</i> | <i>Shear span ratio</i> | <i>Axial load ratio</i> |
|----------------------|--------|---------------------|--------------|------------------------|-------|-------|---------------------|-------------------------|-------------------------|
| | | | | H_w | L_w | t_w | | | |
| Ji (2002) | SW-1 | Cyclic | Rectangle | 3000 | 1000 | 60 | 3.0 | 3.0 | 0.25 |
| | SW-2 | Cyclic | Barbell | 3000 | 1000 | 60 | 3.0 | 3.0 | 0.20 |
| Zhou (2004) | SW-1 | Cyclic | Rectangle | 2250 | 900 | 75 | 2.5 | 2.5 | 0.10 |
| | SW-2 | Cyclic | Rectangle | 2250 | 900 | 75 | 2.5 | 2.5 | 0.20 |
| | SW-3 | Cyclic | Rectangle | 2250 | 900 | 75 | 2.5 | 2.5 | 0.10 |
| | SW-4 | Cyclic | Rectangle | 2250 | 900 | 75 | 2.5 | 2.5 | 0.20 |
| Zhang (2007) | SW1-1 | Cyclic | Rectangle | 2000 | 1000 | 125 | 2.0 | 2.0 | 0.10 |
| | SW1-2 | Cyclic | Rectangle | 2000 | 1000 | 125 | 2.0 | 2.0 | 0.20 |
| | SW1-3 | Cyclic | Rectangle | 2000 | 1000 | 125 | 2.0 | 2.0 | 0.30 |
| | SW1-4 | Cyclic | Rectangle | 2000 | 1000 | 125 | 2.0 | 2.0 | 0.40 |
| | SW2-1 | Cyclic | Rectangle | 1000 | 1000 | 125 | 1.0 | 1.0 | 0.30 |
| | SW2-2 | Cyclic | Rectangle | 1500 | 1000 | 125 | 1.5 | 1.5 | 0.30 |
| | SW2-3 | Cyclic | Rectangle | 2000 | 1000 | 125 | 2.0 | 2.0 | 0.30 |
| | SW2-4 | Cyclic | Rectangle | 2500 | 1000 | 125 | 2.5 | 2.5 | 0.30 |
| | SW4-1 | Cyclic | Rectangle | 2000 | 1000 | 125 | 2.0 | 2.0 | 0.30 |
| | SW4-2 | Cyclic | Rectangle | 2000 | 1000 | 125 | 2.0 | 2.0 | 0.30 |
| | SW4-4 | Cyclic | Rectangle | 2000 | 1000 | 125 | 2.0 | 2.0 | 0.30 |
| | SW5-1 | Cyclic | Rectangle | 2000 | 1000 | 125 | 2.0 | 2.0 | 0.30 |
| | SW5-3 | Cyclic | Rectangle | 2000 | 1000 | 125 | 2.0 | 2.0 | 0.30 |
| | SW6-1 | Cyclic | Rectangle | 2000 | 1000 | 125 | 2.0 | 2.0 | 0.30 |
| SW6-3 | Cyclic | Rectangle | 2000 | 1000 | 125 | 2.0 | 2.0 | 0.30 | |
| Paulay (1982) | Wall 1 | Cyclic | Rectangle | 1500 | 3000 | 100 | 0.5 | 0.5 | 0.00 |
| | Wall 2 | Cyclic | Rectangle | 1500 | 3000 | 100 | 0.5 | 0.5 | 0.00 |
| | Wall 4 | Cyclic | I-Shaped | 1500 | 3000 | 100 | 0.5 | 0.5 | 0.00 |
| Adebar (2007) | Adebar | Cyclic | Barbell | 11700 | 1625 | 127 | 7.2 | 7.2 | 0.10 |
| Pilakoutas (1995) | SW4 | Cyclic | Rectangle | 1200 | 600 | 60 | 2.0 | 2.0 | 0.00 |
| | SW5 | Cyclic | Rectangle | 1200 | 600 | 60 | 2.0 | 2.0 | 0.00 |
| | SW6 | Cyclic | Rectangle | 1200 | 600 | 60 | 2.0 | 2.0 | 0.00 |
| | SW7 | Cyclic | Rectangle | 1200 | 600 | 60 | 2.0 | 2.0 | 0.00 |
| | SW8 | Cyclic | Rectangle | 1200 | 600 | 60 | 2.0 | 2.0 | 0.00 |
| | SW9 | Cyclic | Rectangle | 1200 | 600 | 60 | 2.0 | 2.0 | 0.00 |
| Ali (1991) | W1 | Cyclic | Barbell | 3556 | 1219 | 125 | 2.9 | 2.9 | 0.05 |

continued on next page

continued from previous page

| Specimen | | Loading type | Shape | Dimensions (mm) | | | Aspect ratio | Shear span ratio | Axial load ratio |
|------------------|-----|--------------|-----------|-----------------|-------|-------|--------------|------------------|------------------|
| | | | | H_w | L_w | t_w | | | |
| Ali | W3 | Cyclic | Barbell | 3556 | 1219 | 125 | 2.9 | 2.9 | 0.05 |
| Sittipunt (1995) | W1 | Cyclic | Barbell | 2150 | 1500 | 100 | 1.4 | 1.4 | 0.10 |
| | W2 | Cyclic | Barbell | 2150 | 1500 | 100 | 1.4 | 1.4 | 0.10 |
| Carvajal (1983) | M-2 | Cyclic | Rectangle | 1550 | 500 | 100 | 3.1 | 3.1 | 0.08 |
| | M-3 | Cyclic | Rectangle | 1550 | 500 | 100 | 3.1 | 3.1 | 0.08 |
| | M-4 | Cyclic | Rectangle | 1550 | 500 | 100 | 3.1 | 3.1 | 0.09 |
| | M-5 | Cyclic | Rectangle | 1550 | 500 | 100 | 3.1 | 3.1 | 0.08 |
| | M-6 | Cyclic | Rectangle | 1550 | 500 | 100 | 3.1 | 3.1 | 0.11 |

where H_w , L_w , and t_w are height, length and thickness of the wall, respectively, *Aspect ratio* is height to length ratio (H_w/L_w), *Shear span ratio* (M/VL_w) is normalized moment (M) to shear (V) ratio, and *Axial load ratio* is $P/A_g f'_c$, where P is the axial load, A_g is the gross section of the wall, and f'_c is the compressive strength of concrete.

Table B-2. Specimen Concrete and Web Reinforcement Details

| Specimen | | Concrete f_c (MPa) | Web Reinforcement | | | | | | | | |
|------------|---------------|-------------------------|-------------------|--------------|-----------|---------------|------------------|--------------|-----------|---------------|------------------|
| | | | # of curtains | Φ mm | s mm | ρ_l % | f_{y_l} MPa | Φ mm | s mm | ρ_l % | f_{y_l} MPa |
| Tran | RW-A20-P10-S4 | 47.1 | 2 | 6 | 140 | 0.27 | 400 | 6 | 140 | 0.27 | 517 |
| | RW-A20-P10-S7 | 48.4 | 2 | 10 | 152 | 0.61 | 448 | 10 | 152 | 0.61 | 448 |
| | RW-A15-P10-S5 | 48.7 | 2 | 6 | 114 | 0.32 | 400 | 6 | 114 | 0.32 | 517 |
| Salonikios | LSW1 | 22.2 | 2 | 4 | 100 | 0.56 | 610 | 4 | 100 | 0.56 | 610 |
| | LSW2 | 21.6 | 2 | 4 | 100 | 0.28 | 610 | 4 | 100 | 0.28 | 610 |
| | LSW3 | 23.9 | 2 | 4 | 100 | 0.28 | 610 | 4 | 100 | 0.28 | 610 |
| | LSW4 | 23.2 | 2 | 4 | 100 | 0.28 | 610 | 4 | 100 | 0.28 | 610 |
| | LSW5 | 24.9 | 2 | 4 | 100 | 0.28 | 610 | 4 | 100 | 0.28 | 610 |
| | MSW1 | 26.1 | 2 | 4 | 100 | 0.56 | 610 | 4 | 100 | 0.56 | 610 |
| | MSW2 | 26.2 | 2 | 4 | 100 | 0.28 | 610 | 4 | 100 | 0.28 | 610 |
| | MSW3 | 24.1 | 2 | 4 | 100 | 0.28 | 610 | 4 | 100 | 0.28 | 610 |
| | MSW4 | 24.6 | 2 | 4 | 100 | 0.28 | 610 | 4 | 100 | 0.28 | 610 |
| | MSW5 | 22.0 | 2 | 4 | 100 | 0.28 | 610 | 4 | 100 | 0.28 | 610 |
| | MSW6 | 27.5 | 2 | 4 | 100 | 0.28 | 610 | 4 | 100 | 0.56 | 610 |
| Wang | SW7 | 36.8 | 2 | 8 | 150 | 0.67 | 305 | 8 | 100 | 1.01 | 305 |
| | SW8 | 40.2 | 2 | 8 | 150 | 0.67 | 305 | 8 | 100 | 1.01 | 305 |
| | SW9 | 43.1 | 2 | 8 | 150 | 0.67 | 305 | 8 | 75 | 1.34 | 305 |
| Corley | B1 | 53.0 | 2 | 6 | 228.6 | 0.24 | 521 | 6 | 203 | 0.27 | 521 |
| | B2 | 53.6 | 2 | 6 | 228.6 | 0.24 | 532 | 6 | 102 | 0.55 | 532 |
| | B3 | 47.3 | 2 | 6 | 228.6 | 0.24 | 478 | 6 | 203 | 0.27 | 478 |
| | B4 | 45.0 | 2 | 6 | 228.6 | 0.24 | 505 | 6 | 203 | 0.27 | 505 |
| | B5 | 45.3 | 2 | 6 | 228.6 | 0.24 | 502 | 6 | 102 | 0.55 | 502 |
| | B6 | 21.9 | 2 | 6 | 228.6 | 0.24 | 512 | 6 | 102 | 0.55 | 512 |
| | B7 | 49.4 | 2 | 6 | 228.6 | 0.24 | 490 | 6 | 102 | 0.55 | 490 |
| | B8 | 42.0 | 2 | 6 | 228.6 | 0.24 | 454 | 10 | 102 | 1.38 | 482 |

continued on next page

continued from previous page

| Specimen | | Concrete f_c (MPa) | Web Reinforcement | | | | | | | | | |
|-------------|---------|-------------------------|-------------------|--------------|-----------|---------------|------------------|--------------|-----------|---------------|------------------|-----|
| | | | # of curtains | Φ mm | s mm | ρ_l % | f_{y_l} MPa | Φ mm | s mm | ρ_t % | f_{y_t} MPa | |
| Corley | B9 | 44.1 | 2 | 6 | 228.6 | 0.24 | 461 | 6 | 102 | 0.55 | 461 | |
| Massone | Test 1 | 25.5 | 1 | 13 | 230 | 0.38 | 424 | 13 | 330 | 0.26 | 424 | |
| | Test 2 | 31.4 | 1 | 13 | 230 | 0.38 | 424 | 13 | 330 | 0.26 | 424 | |
| | Test 3 | 31.0 | 1 | 13 | 230 | 0.38 | 424 | 13 | 330 | 0.26 | 424 | |
| | Test 6 | 31.4 | 1 | 13 | 330 | 0.26 | 424 | 13 | 305 | 0.29 | 424 | |
| | Test 7 | 31.9 | 1 | 13 | 330 | 0.26 | 424 | 13 | 305 | 0.29 | 424 | |
| | Test 8 | 32.0 | 1 | 13 | 330 | 0.26 | 424 | 13 | 305 | 0.29 | 424 | |
| | Test 10 | 31.0 | 1 | 13 | 330 | 0.26 | 424 | 13 | 305 | 0.29 | 424 | |
| | Test 11 | 31.7 | 1 | 13 | 280 | 0.31 | 352 | 13 | 280 | 0.31 | 352 | |
| | Test 12 | 31.9 | 1 | 13 | 280 | 0.31 | 352 | 13 | 280 | 0.31 | 352 | |
| | Test 13 | 33.0 | 1 | 13 | 280 | 0.31 | 352 | 13 | 280 | 0.31 | 352 | |
| | Test 14 | 33.6 | 1 | 13 | 280 | 0.31 | 352 | 13 | 280 | 0.31 | 352 | |
| | Hidalgo | Specimen 1 | 19.4 | 0 | 0 | 0 | 0.25 | 392 | 0 | 0 | 0.13 | 392 |
| | | Specimen 2 | 19.6 | 0 | 0 | 0 | 0.25 | 402 | 0 | 0 | 0.25 | 402 |
| | | Specimen 4 | 19.5 | 0 | 0 | 0 | 0.25 | 402 | 0 | 0 | 0.38 | 402 |
| Specimen 6 | | 17.6 | 0 | 0 | 0 | 0.26 | 314 | 0 | 0 | 0.13 | 314 | |
| Specimen 7 | | 18.1 | 0 | 0 | 0 | 0.13 | 471 | 0 | 0 | 0.25 | 471 | |
| Specimen 8 | | 15.7 | 0 | 0 | 0 | 0.26 | 471 | 0 | 0 | 0.25 | 471 | |
| Specimen 9 | | 17.6 | 0 | 0 | 0 | 0.26 | 366 | 0 | 0 | 0.26 | 366 | |
| Specimen 10 | | 16.4 | 0 | 0 | 0 | 0.25 | 367 | 0 | 0 | 0.25 | 367 | |
| Specimen 13 | | 18.1 | 0 | 0 | 0 | 0.26 | 370 | 0 | 0 | 0.26 | 370 | |
| Specimen 14 | | 17.1 | 0 | 0 | 0 | 0.25 | 366 | 0 | 0 | 0.13 | 366 | |
| Specimen 24 | | 23.9 | 0 | 0 | 0 | 0.25 | 431 | 0 | 0 | 0.00 | 431 | |
| Specimen 28 | | 23.3 | 0 | 0 | 0 | 0.25 | 431 | 0 | 0 | 0.00 | 431 | |
| Dazio | WSH1 | 45.0 | 2 | 6 | 125 | 0.30 | 601 | 6 | 150 | 0.25 | 601 | |
| | WSH2 | 40.5 | 2 | 6 | 125 | 0.30 | 535 | 6 | 150 | 0.25 | 535 | |
| | WSH3 | 39.2 | 2 | 8 | 125 | 0.54 | 700 | 6 | 150 | 0.25 | 552 | |
| | WSH4 | 40.9 | 2 | 8 | 125 | 0.54 | 714 | 6 | 150 | 0.25 | 559 | |
| Kabeyasawa | NW-1 | 87.6 | 2 | 6 | 150 | 0.47 | 1001 | 6 | 150 | 0.47 | 1001 | |
| | NW-2 | 93.6 | 2 | 6 | 150 | 0.47 | 1001 | 6 | 150 | 0.47 | 1001 | |

continued on next page

continued from previous page

| Specimen | | Concrete f_c (MPa) | Web Reinforcement | | | | | | | | |
|------------|-------|-------------------------|-------------------|--------|------|----------|----------|--------|------|----------|----------|
| | | | # of curtains | Φ | s | ρ_l | f_{yl} | Φ | s | ρ_l | f_{yl} |
| | | | | mm | mm | % | MPa | mm | mm | % | MPa |
| Kabeyasawa | NW-3 | 55.5 | 1 | 6 | 150 | 0.24 | 753 | 6 | 150 | 0.24 | 753 |
| | NW-4 | 54.6 | 1 | 6 | 150 | 0.24 | 753 | 6 | 150 | 0.24 | 753 |
| | NW-5 | 60.3 | 2 | 6 | 150 | 0.47 | 753 | 6 | 150 | 0.47 | 753 |
| | NW-6 | 65.2 | 2 | 6 | 150 | 0.47 | 753 | 6 | 150 | 0.47 | 753 |
| | W-08 | 103.3 | 2 | 6 | 150 | 0.47 | 1079 | 6 | 150 | 0.47 | 1079 |
| | W-12 | 137.5 | 2 | 6 | 150 | 0.47 | 1079 | 6 | 150 | 0.47 | 1079 |
| | NO.1 | 65.1 | 2 | 6 | 400 | 0.18 | 792 | 6 | 400 | 0.18 | 792 |
| | NO.2 | 70.8 | 2 | 6 | 230 | 0.31 | 792 | 6 | 230 | 0.31 | 792 |
| | NO.3 | 71.8 | 2 | 6 | 150 | 0.47 | 792 | 6 | 150 | 0.47 | 792 |
| | NO.4 | 103.4 | 2 | 6 | 150 | 0.47 | 792 | 6 | 150 | 0.47 | 792 |
| | NO.5 | 76.7 | 2 | 6 | 150 | 0.47 | 792 | 6 | 150 | 0.47 | 792 |
| | NO.7 | 71.5 | 2 | 6 | 80 | 0.88 | 792 | 6 | 80 | 0.88 | 792 |
| | NO.8 | 76.1 | 2 | 6 | 55 | 1.29 | 792 | 6 | 55 | 1.29 | 792 |
| | M35X | 62.6 | 2 | 6 | 100 | 0.71 | 810 | 6 | 100 | 0.71 | 810 |
| | M35H | 68.6 | 2 | 6 | 100 | 0.71 | 810 | 6 | 100 | 0.71 | 810 |
| | P35H | 66.5 | 2 | 6 | 100 | 0.71 | 810 | 6 | 100 | 0.71 | 810 |
| | M30H | 61.4 | 2 | 6 | 100 | 0.71 | 810 | 6 | 100 | 0.71 | 810 |
| | MW35H | 59.7 | 2 | 6 | 100 | 0.71 | 810 | 6 | 100 | 0.71 | 810 |
| | MAE03 | 58.3 | 2 | 6 | 67 | 1.06 | 321 | 6 | 67 | 1.06 | 321 |
| | MAE07 | 58.1 | 2 | 6 | 40 | 1.77 | 321 | 6 | 40 | 1.77 | 321 |
| | SMZ01 | 83.6 | 1 | 6 | 75 | 0.50 | 369 | 6 | 75 | 0.50 | 369 |
| | SMZ03 | 83.6 | 1 | 6 | 75 | 0.50 | 369 | 6 | 75 | 0.50 | 369 |
| | W8N18 | 72.7 | 2 | 6 | 60 | 1.18 | 848 | 6 | 60 | 1.18 | 848 |
| | W8N13 | 79.0 | 2 | 6 | 60 | 1.18 | 848 | 6 | 60 | 1.18 | 848 |
| | W8N8H | 79.4 | 2 | 6 | 60 | 1.18 | 848 | 6 | 60 | 1.18 | 848 |
| | W72M6 | 82.3 | 2 | 10 | 100 | 1.31 | 560 | 10 | 100 | 1.31 | 560 |
| | TAK01 | 62.3 | 2 | 6 | 65 | 1.02 | 413 | 6 | 65 | 1.02 | 413 |
| | TAK02 | 62.3 | 2 | 6 | 45 | 1.48 | 413 | 6 | 45 | 1.48 | 413 |
| TAK03 | 62.3 | 2 | 6 | 65 | 1.02 | 413 | 6 | 65 | 1.02 | 413 | |
| Thomsen | RW1 | 31.6 | 2 | 6 | 191 | 0.33 | 448 | 6 | 191 | 0.33 | 448 |

continued on next page

continued from previous page

| Specimen | | Concrete f_c (MPa) | Web Reinforcement | | | | | | | | |
|------------|--------|-------------------------|-------------------|--------|------|----------|-----------|--------|------|----------|-----------|
| | | | # of curtains | Φ | s | ρ_l | f_{y_l} | Φ | s | ρ_t | f_{y_t} |
| | | | | mm | mm | % | MPa | mm | mm | % | MPa |
| Thomsen | RW2 | 43.7 | 2 | 6 | 191 | 0.33 | 448 | 6 | 191 | 0.33 | 448 |
| | TW2 | 41.7 | 2 | 6 | 140 | 0.45 | 448 | 6 | 140 | 0.45 | 448 |
| Jiang | SSW-T | 24.1 | 2 | 7 | 80 | 1.11 | 289 | 7 | 80 | 1.11 | 289 |
| | DSW-T | 24.9 | 2 | 7 | 80 | 1.11 | 289 | 7 | 80 | 1.11 | 289 |
| Ji | SW-1 | 17.7 | 2 | 4 | 100 | 0.42 | 452 | 4 | 100 | 0.42 | 452 |
| | SW-2 | 17.7 | 2 | 4 | 100 | 0.42 | 452 | 4 | 100 | 0.42 | 452 |
| Zhou | SW-1 | 37.3 | 2 | 6 | 90 | 0.84 | 345 | 6 | 90 | 0.84 | 345 |
| | SW-2 | 37.3 | 2 | 6 | 90 | 0.84 | 345 | 6 | 90 | 0.84 | 345 |
| | SW-3 | 37.3 | 2 | 6 | 90 | 0.84 | 345 | 6 | 90 | 0.84 | 345 |
| | SW-4 | 37.3 | 2 | 6 | 90 | 0.84 | 345 | 6 | 90 | 0.84 | 345 |
| Zhang | SW1-1 | 19.7 | 2 | 6 | 125 | 0.36 | 392 | 6 | 125 | 0.36 | 392 |
| | SW1-2 | 19.7 | 2 | 6 | 125 | 0.36 | 392 | 6 | 125 | 0.36 | 392 |
| | SW1-3 | 19.7 | 2 | 6 | 125 | 0.36 | 392 | 6 | 125 | 0.36 | 392 |
| | SW1-4 | 19.7 | 2 | 6 | 125 | 0.36 | 392 | 6 | 125 | 0.36 | 392 |
| | SW2-1 | 37.7 | 2 | 6 | 125 | 0.36 | 392 | 6 | 125 | 0.36 | 392 |
| | SW2-2 | 37.7 | 2 | 6 | 125 | 0.36 | 392 | 6 | 125 | 0.36 | 392 |
| | SW2-3 | 37.7 | 2 | 6 | 125 | 0.36 | 392 | 6 | 125 | 0.36 | 392 |
| | SW2-4 | 37.7 | 2 | 6 | 125 | 0.36 | 392 | 6 | 125 | 0.36 | 392 |
| | SW4-1 | 37.7 | 2 | 6 | 125 | 0.36 | 392 | 6 | 125 | 0.36 | 392 |
| | SW4-2 | 37.7 | 2 | 6 | 125 | 0.36 | 392 | 6 | 125 | 0.36 | 392 |
| | SW4-4 | 37.7 | 2 | 6 | 125 | 0.36 | 392 | 6 | 125 | 0.36 | 392 |
| | SW5-1 | 37.7 | 2 | 6 | 125 | 0.36 | 392 | 6 | 125 | 0.36 | 392 |
| | SW5-3 | 37.7 | 2 | 6 | 125 | 0.36 | 392 | 6 | 125 | 0.36 | 392 |
| | SW6-1 | 37.7 | 2 | 6 | 125 | 0.36 | 392 | 6 | 125 | 0.36 | 392 |
| SW6-3 | 37.7 | 2 | 6 | 125 | 0.36 | 392 | 6 | 125 | 0.36 | 392 | |
| Paulay | Wall 1 | 27.2 | 1 | 12 | 140 | 0.81 | 300 | 16 | 120 | 1.68 | 380 |
| | Wall 2 | 28.0 | 1 | 12 | 175 | 0.65 | 300 | 16 | 135 | 1.49 | 380 |
| | Wall 4 | 30.2 | 1 | 10 | 200 | 0.39 | 315 | 16 | 300 | 0.67 | 380 |
| Adebar | Adebar | 49.0 | 1 | 12 | 305 | 0.27 | 455 | 12 | 305 | 0.27 | 455 |
| Pilakoutas | SW4 | 36.9 | 2 | 6 | 300 | 0.31 | 550 | 6 | 240 | 0.39 | 550 |

continued on next page

continued from previous page

| Specimen | | Concrete f_c (MPa) | Web Reinforcement | | | | | | | | |
|------------|-----|-------------------------|-------------------|--------|-----|----------|----------|--------|-----|----------|----------|
| | | | # of curtains | Φ | s | ρ_l | f_{yl} | Φ | s | ρ_t | f_{yt} |
| | | | | mm | mm | % | MPa | mm | mm | % | MPa |
| Pilakoutas | SW5 | 31.8 | 2 | 6 | 200 | 0.47 | 550 | 4 | 120 | 0.35 | 400 |
| | SW6 | 38.6 | 2 | 6 | 300 | 0.31 | 550 | 4 | 120 | 0.35 | 400 |
| | SW7 | 32.0 | 2 | 6 | 200 | 0.47 | 550 | 6 | 240 | 0.39 | 550 |
| | SW8 | 45.8 | 2 | 6 | 300 | 0.31 | 550 | 4 | 100 | 0.42 | 400 |
| | SW9 | 38.9 | 2 | 6 | 300 | 0.31 | 550 | 4 | 70 | 0.60 | 400 |
| Ali | W1 | 34.5 | 1 | 6 | 152 | 0.17 | 562 | 6 | 152 | 0.17 | 562 |
| | W3 | 34.5 | 1 | 6 | 152 | 0.17 | 562 | 6 | 152 | 0.17 | 562 |
| Sittipunt | W1 | 36.6 | 1 | 10 | 200 | 0.39 | 450 | 10 | 150 | 0.52 | 450 |
| | W2 | 35.8 | 1 | 10 | 150 | 0.52 | 450 | 10 | 100 | 0.79 | 450 |
| Carvajal | M-2 | 28.1 | 2 | 4 | 100 | 0.25 | 588 | 4 | 100 | 0.25 | 588 |
| | M-3 | 28.2 | 2 | 4 | 100 | 0.25 | 588 | 4 | 100 | 0.25 | 588 |
| | M-4 | 25.6 | 2 | 4 | 100 | 0.25 | 588 | 4 | 100 | 0.25 | 588 |
| | M-5 | 28.7 | 2 | 4 | 100 | 0.25 | 588 | 4 | 100 | 0.25 | 588 |
| | M-6 | 20.8 | 2 | 4 | 100 | 0.25 | 588 | 4 | 100 | 0.25 | 588 |

where f_c is the concrete strength, s is the spacing between rebars, Φ is the rebar diameter, ρ_l and f_{yl} are ratio and yield strength of the vertical web reinforcement, respectively, and ρ_t and f_{yt} are ratio and yield strength of the transverse web reinforcement, respectively.

Table B-3. Specimen Boundary Reinforcement Details

| Specimen | | Boundary width | | Vertical bound. reinf. | | | | Transverse bound. reinf. | | | | |
|------------|---------------|----------------|----------------|------------------------|--------------|------------------|------------------|--------------------------|-----------|---------------|-----------------|--------|
| | | bc_x (mm) | bc_y (mm) | # of bars | Φ mm | ρ_{bl} % | f_{ybl} MPa | Φ mm | s mm | ρ_s % | f_{ys} MPa | s/db |
| Tran | RW-A20-P10-S4 | 210 | 152 | 8 | 13 | 3.17 | 472 | 6 | 50 | 1.55 | 472 | 3.9 |
| | RW-A20-P10-S7 | 210 | 152 | 8 | 19 | 7.14 | 477 | 6 | 50 | 1.55 | 477 | 2.6 |
| | RW-A15-P10-S5 | 210 | 152 | 8 | 13 | 3.17 | 472 | 6 | 50 | 1.55 | 472 | 3.9 |
| Salonikios | LSW1 | 240 | 100 | 8 | 8 | 1.68 | 585 | 4 | 26 | 1.95 | 610 | 3.3 |
| | LSW2 | 240 | 100 | 6 | 8 | 1.26 | 585 | 4 | 26 | 1.73 | 610 | 3.3 |
| | LSW3 | 240 | 100 | 6 | 8 | 1.26 | 585 | 4 | 26 | 1.73 | 610 | 3.3 |
| | LSW4 | 240 | 100 | 6 | 8 | 1.26 | 585 | 4 | 26 | 1.73 | 610 | 3.3 |
| | LSW5 | 240 | 100 | 8 | 8 | 1.68 | 585 | 4 | 26 | 1.73 | 610 | 3.3 |
| | MSW1 | 240 | 100 | 8 | 8 | 1.68 | 585 | 4 | 42 | 1.21 | 610 | 5.3 |
| | MSW2 | 240 | 100 | 6 | 8 | 1.26 | 585 | 4 | 42 | 1.07 | 610 | 5.3 |
| | MSW3 | 240 | 100 | 6 | 8 | 1.26 | 585 | 4 | 42 | 1.07 | 610 | 5.3 |
| | MSW4 | 240 | 100 | 6 | 8 | 1.26 | 585 | 4 | 27 | 1.67 | 610 | 3.4 |
| | MSW5 | 240 | 100 | 6 | 8 | 1.26 | 585 | 4 | 27 | 1.67 | 610 | 3.4 |
| | MSW6 | 240 | 100 | 6 | 8 | 1.26 | 585 | 4 | 27 | 1.88 | 610 | 3.4 |
| Wang | SW7 | 100 | 100 | 4 | 14 | 6.16 | 405 | 6 | 50 | 2.26 | 366 | 3.6 |
| | SW8 | 100 | 100 | 4 | 12 | 4.52 | 432 | 6 | 50 | 2.26 | 366 | 4.2 |
| | SW9 | 100 | 100 | 4 | 20 | 12.57 | 375 | 6 | 75 | 1.51 | 366 | 3.8 |
| Corley | B1 | 305 | 305 | 8 | 12.7 | 1.09 | 450 | 0 | 0 | 0.00 | 0 | 0.0 |
| | B2 | 305 | 305 | 12 | 19.05 | 3.68 | 410 | 0 | 0 | 0.00 | 0 | 0.0 |
| | B3 | 305 | 305 | 8 | 12.7 | 1.09 | 438 | 6 | 34 | 1.64 | 478 | 2.7 |
| | B4 | 305 | 305 | 8 | 12.7 | 1.09 | 450 | 6 | 34 | 1.64 | 505 | 2.7 |
| | B5 | 305 | 305 | 12 | 19.05 | 3.68 | 444 | 6 | 34 | 2.19 | 502 | 1.8 |
| | B6 | 305 | 305 | 12 | 19.05 | 3.68 | 441 | 3 | 34 | 0.55 | 487 | 1.8 |
| | B7 | 305 | 305 | 12 | 19.05 | 3.68 | 458 | 6 | 34 | 2.19 | 490 | 1.8 |
| | B8 | 305 | 305 | 12 | 19.05 | 3.68 | 447 | 6 | 34 | 2.19 | 454 | 1.8 |
| | B9 | 305 | 305 | 12 | 19.05 | 3.68 | 430 | 6 | 34 | 2.19 | 461 | 1.8 |

continued on next page

continued from previous page

| Specimen | | Boundary width | | Vertical bound. reinf. | | | | Transverse bound. reinf. | | | | s/db | |
|-------------|---------|----------------|----------------|------------------------|--------------|------------------|------------------|--------------------------|-----------|---------------|------------------|------|-----|
| | | bc_x (mm) | bc_y (mm) | # of bars | Φ mm | ρ_{bl} % | f_{ybl} MPa | Φ mm | s mm | ρ_s % | f_{y_s} MPa | | |
| Massone | Test 1 | 170 | 152 | 4 | 16 | 3.11 | 448 | 0 | 0 | 0.00 | 0 | 0.0 | |
| | Test 2 | 128 | 152 | 1 | 13 | 1.72 | 424 | 0 | 0 | 0.00 | 0 | 0.0 | |
| | Test 3 | 128 | 152 | 1 | 13 | 1.72 | 424 | 0 | 0 | 0.00 | 0 | 0.0 | |
| | Test 6 | 128 | 152 | 2 | 13 | 1.36 | 424 | 0 | 0 | 0.00 | 0 | 0.0 | |
| | Test 7 | 128 | 152 | 2 | 13 | 1.36 | 424 | 0 | 0 | 0.00 | 0 | 0.0 | |
| | Test 8 | 128 | 152 | 2 | 13 | 1.36 | 424 | 0 | 0 | 0.00 | 0 | 0.0 | |
| | Test 10 | 128 | 152 | 2 | 13 | 1.36 | 424 | 0 | 0 | 0.00 | 0 | 0.0 | |
| | Test 11 | 128 | 152 | 2 | 13 | 1.36 | 352 | 0 | 0 | 0.00 | 0 | 0.0 | |
| | Test 12 | 128 | 152 | 2 | 13 | 1.36 | 352 | 0 | 0 | 0.00 | 0 | 0.0 | |
| | Test 13 | 128 | 152 | 2 | 13 | 1.36 | 352 | 0 | 0 | 0.00 | 0 | 0.0 | |
| | Test 14 | 128 | 152 | 2 | 13 | 1.36 | 352 | 0 | 0 | 0.00 | 0 | 0.0 | |
| | Hidalgo | Specimen 1 | 0 | 0 | 0 | 0 | 0.00 | 0 | 0 | 0 | 0.00 | 0 | 0.0 |
| | | Specimen 2 | 0 | 0 | 0 | 0 | 0.00 | 0 | 0 | 0 | 0.00 | 0 | 0.0 |
| | | Specimen 4 | 0 | 0 | 0 | 0 | 0.00 | 0 | 0 | 0 | 0.00 | 0 | 0.0 |
| Specimen 6 | | 0 | 0 | 0 | 0 | 0.00 | 0 | 0 | 0 | 0.00 | 0 | 0.0 | |
| Specimen 7 | | 0 | 0 | 0 | 0 | 0.00 | 0 | 0 | 0 | 0.00 | 0 | 0.0 | |
| Specimen 8 | | 0 | 0 | 0 | 0 | 0.00 | 0 | 0 | 0 | 0.00 | 0 | 0.0 | |
| Specimen 9 | | 0 | 0 | 0 | 0 | 0.00 | 0 | 0 | 0 | 0.00 | 0 | 0.0 | |
| Specimen 10 | | 0 | 0 | 0 | 0 | 0.00 | 0 | 0 | 0 | 0.00 | 0 | 0.0 | |
| Specimen 13 | | 0 | 0 | 0 | 0 | 0.00 | 0 | 0 | 0 | 0.00 | 0 | 0.0 | |
| Specimen 14 | | 0 | 0 | 0 | 0 | 0.00 | 0 | 0 | 0 | 0.00 | 0 | 0.0 | |
| Specimen 24 | | 0 | 0 | 0 | 0 | 0.00 | 0 | 0 | 0 | 0.00 | 0 | 0.0 | |
| Specimen 28 | 0 | 0 | 0 | 0 | 0.00 | 0 | 0 | 0 | 0.00 | 0 | 0.0 | | |
| Dazio | WSH1 | 200 | 150 | 6 | 10 | 1.57 | 620 | 6 | 75 | 1.43 | 662 | 7.5 | |
| | WSH2 | 200 | 150 | 6 | 10 | 1.57 | 747 | 6 | 75 | 1.59 | 583 | 7.5 | |
| | WSH3 | 260 | 200 | 6 | 12 | 1.30 | 726 | 6 | 75 | 1.21 | 615 | 6.3 | |
| | WSH4 | 0 | 0 | 6 | 12 | 0.00 | 675 | 6 | 150 | 0.00 | 0 | 12.5 | |
| Kabeyasawa | NW-1 | 200 | 200 | 12 | 10 | 2.36 | 776 | 6 | 40 | 2.83 | 1262 | 4.0 | |
| | NW-2 | 200 | 200 | 12 | 10 | 2.36 | 776 | 6 | 40 | 2.83 | 1262 | 4.0 | |
| | NW-3 | 200 | 200 | 12 | 10 | 2.36 | 840 | 5 | 40 | 1.96 | 1233 | 4.0 | |
| | NW-4 | 200 | 200 | 16 | 10 | 3.14 | 840 | 5 | 40 | 1.96 | 1233 | 4.0 | |

continued on next page

continued from previous page

| Specimen | | Boundary width | | Vertical bound. reinf. | | | | Transverse bound. reinf. | | | | |
|------------|-------|----------------|--------|------------------------|--------|-------------|-----------|--------------------------|------|----------|-----------|--------|
| | | bc_x | bc_y | # of bars | Φ | ρ_{bl} | f_{ybl} | Φ | s | ρ_s | f_{y_s} | s/db |
| | | (mm) | (mm) | | mm | % | MPa | mm | mm | % | MPa | |
| Kabeyasawa | NW-5 | 200 | 200 | 16 | 10 | 3.14 | 840 | 5 | 40 | 1.96 | 1233 | 4.0 |
| | NW-6 | 200 | 200 | 12 | 13 | 3.98 | 776 | 5 | 40 | 1.96 | 1233 | 3.1 |
| | W-08 | 200 | 200 | 12 | 10 | 2.36 | 761 | 6 | 40 | 2.83 | 1372 | 4.0 |
| | W-12 | 170 | 170 | 12 | 10 | 3.26 | 761 | 6 | 40 | 3.33 | 1372 | 4.0 |
| | NO.1 | 200 | 200 | 16 | 13 | 5.31 | 1009 | 6 | 40 | 2.54 | 1395 | 3.1 |
| | NO.2 | 200 | 200 | 16 | 13 | 5.31 | 1009 | 6 | 40 | 2.54 | 1395 | 3.1 |
| | NO.3 | 200 | 200 | 16 | 13 | 5.31 | 1009 | 6 | 40 | 2.54 | 1395 | 3.1 |
| | NO.4 | 200 | 200 | 16 | 13 | 5.31 | 1009 | 6 | 40 | 2.54 | 1395 | 3.1 |
| | NO.5 | 200 | 200 | 16 | 13 | 5.31 | 1009 | 6 | 40 | 2.54 | 1395 | 3.1 |
| | NO.7 | 200 | 200 | 16 | 13 | 5.31 | 1009 | 6 | 40 | 2.54 | 1395 | 3.1 |
| | NO.8 | 200 | 200 | 16 | 13 | 5.31 | 1009 | 6 | 40 | 2.54 | 1395 | 3.1 |
| | M35X | 200 | 200 | 16 | 13 | 5.31 | 848 | 6 | 60 | 1.88 | 810 | 4.6 |
| | M35H | 200 | 200 | 12 | 10 | 2.36 | 848 | 6 | 60 | 1.88 | 810 | 6.0 |
| | P35H | 200 | 200 | 12 | 10 | 2.36 | 848 | 6 | 60 | 0.94 | 810 | 6.0 |
| | M30H | 200 | 200 | 12 | 10 | 2.36 | 848 | 6 | 60 | 1.88 | 810 | 6.0 |
| | MW35H | 200 | 200 | 12 | 10 | 2.36 | 848 | 6 | 60 | 1.88 | 810 | 6.0 |
| | MAE03 | 180 | 180 | 12 | 16 | 7.93 | 389 | 5 | 67 | 0.65 | 321 | 4.2 |
| | MAE07 | 180 | 180 | 12 | 16 | 7.93 | 389 | 5 | 67 | 0.65 | 321 | 4.2 |
| | SMZ01 | 250 | 250 | 12 | 13 | 2.55 | 377 | 6 | 50 | 0.90 | 369 | 3.8 |
| | SMZ03 | 250 | 250 | 12 | 19 | 5.44 | 393 | 6 | 50 | 0.90 | 369 | 2.6 |
| | W8N18 | 200 | 200 | 12 | 10 | 2.36 | 385 | 6 | 50 | 2.26 | 851 | 5.0 |
| | W8N13 | 200 | 200 | 12 | 10 | 2.36 | 385 | 6 | 50 | 2.26 | 851 | 5.0 |
| | W8N8H | 200 | 200 | 12 | 10 | 2.36 | 579 | 6 | 50 | 2.26 | 851 | 5.0 |
| W72M6 | 800 | 120 | 16 | 10 | 1.31 | 792 | 10 | 100 | 1.51 | 792 | 10.0 | |
| TAK01 | 200 | 200 | 12 | 13 | 3.98 | 360 | 5 | 65 | 1.21 | 923 | 5.0 | |
| TAK02 | 200 | 200 | 12 | 13 | 3.98 | 360 | 5 | 65 | 1.21 | 923 | 5.0 | |
| TAK03 | 200 | 200 | 12 | 13 | 3.98 | 360 | 5 | 65 | 1.21 | 923 | 5.0 | |
| Thomsen | RW1 | 152 | 64 | 8 | 9.5 | 5.86 | 434 | 5 | 76 | 1.34 | 434 | 8.0 |
| | RW2 | 152 | 64 | 8 | 9.5 | 5.86 | 434 | 5 | 51 | 2.01 | 434 | 5.4 |
| | TW2 | 408 | 64 | 8 | 9.5 | 2.19 | 434 | 5 | 32 | 2.42 | 434 | 3.4 |

continued on next page

continued from previous page

| Specimen | | Boundary width | | Vertical bound. reinf. | | | | Transverse bound. reinf. | | | | s/db |
|------------|--------|----------------|----------------|------------------------|--------|-------------|-----------|--------------------------|------|----------|----------|------|
| | | bc_x (mm) | bc_y (mm) | # of bars | Φ | ρ_{bl} | f_{ybl} | Φ | s | ρ_s | f_{ys} | |
| | | | | | mm | % | MPa | mm | mm | % | MPa | |
| Jiang | SSW-T | 140 | 75 | 8 | 6.5 | 2.53 | 289 | 7 | 90 | 1.51 | 289 | 13.8 |
| | DSW-T | 140 | 75 | 8 | 6.5 | 2.53 | 289 | 7 | 90 | 1.51 | 289 | 13.8 |
| Ji | SW-1 | 120 | 60 | 6 | 12 | 9.42 | 365 | 4 | 30 | 2.09 | 452 | 2.5 |
| | SW-2 | 120 | 120 | 6 | 12 | 4.71 | 365 | 6 | 30 | 3.14 | 452 | 2.5 |
| Zhou | SW-1 | 180 | 75 | 10 | 8 | 3.72 | 527 | 4 | 30 | 1.82 | 300 | 3.8 |
| | SW-2 | 180 | 75 | 10 | 8 | 3.72 | 527 | 4 | 30 | 1.82 | 300 | 3.8 |
| | SW-3 | 180 | 75 | 10 | 8 | 3.72 | 526.7 | 4 | 30 | 1.82 | 300 | 3.8 |
| | SW-4 | 180 | 75 | 10 | 8 | 3.72 | 526.7 | 4 | 30 | 1.82 | 300 | 3.8 |
| Zhang | SW1-1 | 200 | 125 | 6 | 10 | 1.88 | 379 | 6 | 80 | 1.10 | 392 | 8.0 |
| | SW1-2 | 200 | 125 | 6 | 10 | 1.88 | 379 | 6 | 80 | 1.10 | 392 | 8.0 |
| | SW1-3 | 200 | 125 | 6 | 10 | 1.88 | 379 | 6 | 80 | 1.10 | 392 | 8.0 |
| | SW1-4 | 200 | 125 | 6 | 10 | 1.88 | 379 | 6 | 80 | 1.10 | 392 | 8.0 |
| | SW2-1 | 200 | 125 | 6 | 10 | 1.88 | 379 | 6 | 80 | 1.10 | 392 | 8.0 |
| | SW2-2 | 200 | 125 | 6 | 10 | 1.88 | 379 | 6 | 80 | 1.10 | 392 | 8.0 |
| | SW2-3 | 200 | 125 | 6 | 10 | 1.88 | 379 | 6 | 80 | 1.10 | 392 | 8.0 |
| | SW2-4 | 200 | 125 | 6 | 10 | 1.88 | 379 | 6 | 80 | 1.10 | 392 | 8.0 |
| | SW4-1 | 200 | 125 | 6 | 8 | 1.21 | 343 | 6 | 80 | 1.10 | 392 | 10.0 |
| | SW4-2 | 200 | 125 | 6 | 10 | 1.88 | 352 | 6 | 80 | 1.10 | 392 | 8.0 |
| | SW4-4 | 200 | 125 | 6 | 12 | 2.71 | 325 | 6 | 80 | 1.10 | 392 | 6.7 |
| | SW5-1 | 250 | 125 | 6 | 10 | 1.51 | 379 | 6 | 80 | 0.99 | 392 | 8.0 |
| | SW5-3 | 150 | 125 | 6 | 10 | 2.51 | 379 | 6 | 80 | 1.27 | 392 | 8.0 |
| | SW6-1 | 200 | 125 | 6 | 10 | 1.88 | 379 | 4 | 80 | 0.49 | 348 | 8.0 |
| SW6-3 | 200 | 125 | 6 | 10 | 1.88 | 379 | 6 | 60 | 1.46 | 392 | 6.0 | |
| Paulay | Wall 1 | 200 | 100 | 4 | 12 | 2.26 | 300 | 12 | 50 | 6.79 | 300 | 4.2 |
| | Wall 2 | 200 | 100 | 4 | 12 | 2.26 | 300 | 12 | 50 | 6.79 | 300 | 4.2 |
| | Wall 4 | 100 | 500 | 6 | 12 | 1.36 | 300 | 12 | 50 | 5.43 | 300 | 4.2 |
| Adebar | Adebar | 203 | 380 | 5 | 11.5 | 0.67 | 455 | 10 | 64 | 1.67 | 455 | 5.6 |
| Pilakoutas | SW4 | 266 | 60 | 4 | 12 | 2.83 | 500 | 0 | 0 | 0.00 | 0 | 0.0 |
| | SW5 | 253 | 60 | 2 | 16 | 2.65 | 530 | 0 | 0 | 0.00 | 0 | 0.0 |
| | SW6 | 266 | 60 | 4 | 12 | 2.83 | 500 | 0 | 0 | 0.00 | 0 | 0.0 |

continued on next page

continued from previous page

| Specimen | | Boundary width | | Vertical bound. reinf. | | | | Transverse bound. reinf. | | | | |
|------------|-----|----------------|--------|------------------------|--------|-------------|-----------|--------------------------|-----|----------|----------|--------|
| | | bc_x | bc_y | # of bars | Φ | ρ_{bl} | f_{ybl} | Φ | s | ρ_s | f_{ys} | s/db |
| | | (mm) | (mm) | | mm | % | MPa | mm | mm | % | MPa | |
| Pilakoutas | SW7 | 253 | 60 | 2 | 16 | 2.65 | 530 | 0 | 0 | 0.00 | 0 | 0.0 |
| | SW8 | 268 | 60 | 6 | 10 | 2.93 | 530 | 0 | 0 | 0.00 | 0 | 0.0 |
| | SW9 | 268 | 60 | 6 | 10 | 2.93 | 530 | 0 | 0 | 0.00 | 0 | 0.0 |
| Ali | W1 | 127 | 127 | 4 | 12.7 | 3.14 | 540 | 5 | 65 | 0.95 | 540 | 5.1 |
| | W3 | 127 | 127 | 4 | 12.7 | 3.14 | 540 | 5 | 65 | 0.95 | 540 | 5.1 |
| Sittipunt | W1 | 250 | 250 | 6 | 16 | 2.29 | 473 | 0 | 0 | 0.00 | 0 | 0.0 |
| | W2 | 250 | 250 | 6 | 16 | 2.29 | 473 | 0 | 0 | 0.00 | 0 | 0.0 |
| Carvajal | M-2 | 100 | 100 | 1 | 12.7 | 1.27 | 412 | 0 | 0 | 0.00 | 0 | 0.0 |
| | M-3 | 100 | 100 | 1 | 12.7 | 1.27 | 412 | 0 | 0 | 0.00 | 0 | 0.0 |
| | M-4 | 100 | 100 | 1 | 9.5 | 0.71 | 451 | 0 | 0 | 0.00 | 0 | 0.0 |
| | M-5 | 100 | 100 | 1 | 9.5 | 0.71 | 451 | 0 | 0 | 0.00 | 0 | 0.0 |
| | M-6 | 100 | 100 | 1 | 9.5 | 0.71 | 451 | 0 | 0 | 0.00 | 0 | 0.0 |

where bc_x and bc_y are the boundary widths in longitudinal and transverse directions, respectively. Φ is rebar diameter, ρ_{bl} and f_{ybl} are ratio and yield strength of the vertical reinforcement in the boundaries, respectively, and ρ_s and f_{ys} are ratio and yield strength of the transverse reinforcement in the boundaries, respectively.

Table B-4. Specimen Load and Displacement Data

| Specimen | | Displacement (mm) | | | | Shear Force (kN) | | | | @ Failure (80%Vmax) | |
|------------|---------------|-------------------|------|-------|-------|------------------|------|------|-----|---------------------|-----------|
| | | D1 | D2 | D3 | D4 | F1 | F2 | F3 | F4 | Displacement (mm) | Drift (%) |
| Tran | RW-A20-P10-S4 | 0.0 | 15.0 | 53.0 | 70.0 | 0 | 480 | 480 | 445 | 99.6 | 4.1 |
| | RW-A20-P10-S7 | 0.0 | 18.0 | 74.0 | 74.0 | 0 | 720 | 720 | 286 | 74.0 | 3.0 |
| | RW-A15-P10-S5 | 0.0 | 9.0 | 56.0 | 72.0 | 0 | 600 | 600 | 355 | 63.8 | 3.5 |
| Salonikios | LSW1 | 0.0 | 2.0 | 8.0 | 10.0 | 0 | 262 | 262 | 200 | 9.7 | 0.8 |
| | LSW2 | 0.0 | 2.6 | 4.8 | 10.5 | 0 | 191 | 191 | 128 | 8.3 | 0.7 |
| | LSW3 | 0.0 | 2.9 | 6.6 | 15.5 | 0 | 268 | 268 | 236 | 21.4 | 1.8 |
| | LSW4 | 0.0 | 3.2 | 5.0 | 10.0 | 0 | 232 | 232 | 171 | 8.8 | 0.7 |
| | LSW5 | 0.0 | 4.0 | 9.0 | 16.0 | 0 | 240 | 240 | 160 | 13.2 | 1.1 |
| | MSW1 | 0.0 | 8.1 | 12.6 | 27.5 | 0 | 197 | 197 | 142 | 23.3 | 1.3 |
| | MSW2 | 0.0 | 8.0 | 20.0 | 36.0 | 0 | 120 | 120 | 82 | 30.1 | 1.7 |
| | MSW3 | 0.0 | 5.0 | 16.0 | 26.0 | 0 | 170 | 170 | 110 | 21.7 | 1.2 |
| | MSW4 | 0.0 | 8.0 | 18.0 | 27.0 | 0 | 158 | 158 | 125 | 26.6 | 1.5 |
| | MSW5 | 0.0 | 7.3 | 14.5 | 25.0 | 0 | 187 | 187 | 146 | 24.0 | 1.3 |
| | MSW6 | 0.0 | 12.0 | 19.0 | 27.0 | 0 | 200 | 200 | 140 | 24.3 | 1.4 |
| Wang | SW7 | 0.0 | 5.9 | 25.0 | 31.3 | 0 | 201 | 201 | 155 | 30.5 | 1.7 |
| | SW8 | 0.0 | 5.6 | 21.0 | 24.0 | 0 | 224 | 224 | 175 | 23.7 | 1.4 |
| | SW9 | 0.0 | 8.4 | 27.0 | 31.5 | 0 | 300 | 300 | 245 | 31.9 | 1.8 |
| Corley | B1 | 0.0 | 25.4 | 101.6 | 152.4 | 0 | 271 | 271 | 133 | 121.6 | 2.7 |
| | B2 | 0.0 | 31.8 | 127.0 | 132.1 | 0 | 658 | 658 | 249 | 128.6 | 2.8 |
| | B3 | 0.0 | 25.4 | 177.8 | 203.2 | 0 | 276 | 276 | 187 | 193.5 | 4.2 |
| | B4 | 0.0 | 40.6 | 304.8 | 347.2 | 0 | 343 | 343 | 117 | 317.7 | 7.0 |
| | B5 | 0.0 | 36.3 | 125.2 | 132.3 | 0 | 712 | 712 | 463 | 129.3 | 2.8 |
| | B6 | 0.0 | 33.0 | 77.5 | 81.3 | 0 | 845 | 845 | 467 | 79.2 | 1.7 |
| | B7 | 0.0 | 32.5 | 125.2 | 129.5 | 0 | 970 | 970 | 627 | 127.7 | 2.8 |
| | B8 | 0.0 | 27.9 | 152.4 | 177.8 | 0 | 947 | 947 | 311 | 160.0 | 3.5 |
| | B9 | 0.0 | 30.5 | 139.7 | 152.4 | 0 | 1001 | 1001 | 350 | 143.6 | 3.1 |

continued on next page

continued from previous page

| Specimen | | Displacement (mm) | | | | Shear Force (kN) | | | | @ Failure (80%Vmax) | | |
|-------------|---------|-------------------|------|------|------|------------------|------|------|-----|---------------------|-----------|-----|
| | | D1 | D2 | D3 | D4 | F1 | F2 | F3 | F4 | Displacement (mm) | Drift (%) | |
| Massone | Test 1 | 0.0 | 2.5 | 8.8 | 22.7 | 0 | 633 | 633 | 267 | 13.6 | 0.9 | |
| | Test 2 | 0.0 | 4.1 | 19.8 | 27.7 | 0 | 453 | 453 | 179 | 22.4 | 1.5 | |
| | Test 3 | 0.0 | 6.1 | 20.1 | 33.5 | 0 | 491 | 491 | 163 | 24.1 | 1.6 | |
| | Test 6 | 0.0 | 3.0 | 10.7 | 15.2 | 0 | 819 | 819 | 285 | 12.1 | 1.0 | |
| | Test 7 | 0.0 | 2.5 | 9.7 | 15.3 | 0 | 648 | 648 | 45 | 10.9 | 0.9 | |
| | Test 8 | 0.0 | 2.8 | 10.7 | 15.5 | 0 | 690 | 690 | 267 | 12.3 | 1.0 | |
| | Test 10 | 0.0 | 3.0 | 10.7 | 15.2 | 0 | 819 | 819 | 285 | 12.1 | 1.0 | |
| | Test 11 | 0.0 | 3.0 | 10.7 | 15.2 | 0 | 819 | 819 | 285 | 12.1 | 0.8 | |
| | Test 12 | 0.0 | 3.0 | 10.7 | 15.2 | 0 | 819 | 819 | 285 | 12.1 | 0.8 | |
| | Test 13 | 0.0 | 3.0 | 10.7 | 15.2 | 0 | 819 | 819 | 285 | 12.1 | 0.8 | |
| | Test 14 | 0.0 | 3.0 | 10.7 | 15.2 | 0 | 819 | 819 | 285 | 12.1 | 0.8 | |
| | Hidalgo | Specimen 1 | 0.0 | 4.5 | 18.6 | 19.1 | 0 | 210 | 210 | 155 | 19.0 | 0.9 |
| | | Specimen 2 | 0.0 | 7.5 | 25.0 | 30.0 | 0 | 269 | 269 | 160 | 27.5 | 1.4 |
| | | Specimen 4 | 0.0 | 7.5 | 18.8 | 36.3 | 0 | 324 | 324 | 165 | 25.9 | 1.3 |
| Specimen 6 | | 0.0 | 3.9 | 13.5 | 20.8 | 0 | 350 | 350 | 240 | 18.1 | 1.0 | |
| Specimen 7 | | 0.0 | 3.8 | 15.8 | 20.8 | 0 | 373 | 373 | 273 | 19.6 | 1.1 | |
| Specimen 8 | | 0.0 | 5.0 | 20.4 | 21.4 | 0 | 344 | 344 | 267 | 21.3 | 1.2 | |
| Specimen 9 | | 0.0 | 3.6 | 14.3 | 17.5 | 0 | 257 | 257 | 200 | 17.2 | 1.0 | |
| Specimen 10 | | 0.0 | 3.6 | 8.9 | 15.0 | 0 | 187 | 187 | 135 | 13.3 | 0.7 | |
| Specimen 13 | | 0.0 | 2.6 | 9.6 | 11.6 | 0 | 288 | 288 | 239 | 11.6 | 0.8 | |
| Specimen 14 | | 0.0 | 1.0 | 4.4 | 8.5 | 0 | 255 | 255 | 140 | 6.2 | 0.5 | |
| Specimen 24 | | 0.0 | 2.1 | 4.6 | 8.4 | 0 | 232 | 232 | 94 | 5.8 | 0.3 | |
| Specimen 28 | | 0.0 | 2.0 | 6.2 | 11.9 | 0 | 258 | 258 | 163 | 9.3 | 0.7 | |
| Dazio | WSH1 | 0.0 | 12.3 | 32.0 | 51.3 | 0 | 344 | 344 | 278 | 51.3 | 1.1 | |
| | WSH2 | 0.0 | 14.0 | 51.0 | 64.6 | 0 | 362 | 362 | 297 | 66.1 | 1.5 | |
| | WSH3 | 0.0 | 18.2 | 93.4 | 93.4 | 0 | 454 | 454 | 400 | 93.4 | 2.0 | |
| | WSH4 | 0.0 | 15.9 | 62.0 | 77.9 | 0 | 442 | 442 | 322 | 73.7 | 1.6 | |
| Kabeyasawa | NW-1 | 0.0 | 18.0 | 59.1 | 90.0 | 0 | 1062 | 1062 | 500 | 70.8 | 2.4 | |
| | NW-2 | 0.0 | 14.0 | 30.0 | 42.0 | 0 | 1468 | 1468 | 800 | 35.3 | 1.8 | |
| | NW-3 | 0.0 | 11.3 | 29.7 | 39.0 | 0 | 717 | 717 | 300 | 32.9 | 1.1 | |
| | NW-4 | 0.0 | 15.0 | 27.9 | 43.5 | 0 | 784 | 784 | 625 | 43.3 | 1.4 | |

continued on next page

continued from previous page

| <i>Specimen</i> | | <i>Displacement (mm)</i> | | | | <i>Shear Force (kN)</i> | | | | <i>@ Failure (80%Vmax)</i> | |
|-----------------|-------|--------------------------|-----------|-----------|-----------|-------------------------|-----------|-----------|-----------|----------------------------|------------------|
| | | <i>D1</i> | <i>D2</i> | <i>D3</i> | <i>D4</i> | <i>F1</i> | <i>F2</i> | <i>F3</i> | <i>F4</i> | <i>Displacement (mm)</i> | <i>Drift (%)</i> |
| Kabeyasawa | NW-5 | 0.0 | 14.4 | 45.6 | 60.0 | 0 | 900 | 900 | 500 | 52.1 | 1.7 |
| | NW-6 | 0.0 | 18.8 | 40.2 | 51.0 | 0 | 1056 | 1056 | 500 | 44.3 | 1.5 |
| | W-08 | 0.0 | 5.6 | 14.6 | 26.0 | 0 | 1670 | 1670 | 1000 | 20.3 | 1.0 |
| | W-12 | 0.0 | 6.6 | 15.6 | 23.6 | 0 | 1719 | 1719 | 1100 | 20.0 | 1.0 |
| | NO.1 | 0.0 | 5.8 | 15.3 | 17.1 | 0 | 1101 | 1101 | 850 | 16.9 | 0.8 |
| | NO.2 | 0.0 | 7.7 | 15.0 | 17.0 | 0 | 1255 | 1255 | 1000 | 17.0 | 0.8 |
| | NO.3 | 0.0 | 7.6 | 15.0 | 17.0 | 0 | 1379 | 1379 | 1250 | 19.3 | 1.0 |
| | NO.4 | 0.0 | 6.0 | 12.0 | 15.0 | 0 | 1697 | 1697 | 1500 | 17.2 | 0.9 |
| | NO.5 | 0.0 | 17.0 | 30.0 | 32.0 | 0 | 1159 | 1159 | 1000 | 32.9 | 1.1 |
| | NO.7 | 0.0 | 7.0 | 16.0 | 17.0 | 0 | 1499 | 1499 | 1250 | 17.2 | 0.9 |
| | NO.8 | 0.0 | 8.0 | 14.1 | 16.5 | 0 | 1639 | 1639 | 1250 | 16.1 | 0.8 |
| | M35X | 0.0 | 10.0 | 37.0 | 40.0 | 0 | 1049 | 1049 | 700 | 38.8 | 1.9 |
| | M35H | 0.0 | 9.0 | 30.0 | 34.0 | 0 | 1055 | 1055 | 550 | 31.7 | 1.6 |
| | P35H | 0.0 | 8.3 | 29.0 | 35.0 | 0 | 1020 | 1020 | 600 | 31.9 | 1.6 |
| | M30H | 0.0 | 8.3 | 29.0 | 35.0 | 0 | 959 | 959 | 320 | 30.8 | 1.5 |
| | MW35H | 0.0 | 7.9 | 30.0 | 34.0 | 0 | 1012 | 1012 | 500 | 31.6 | 1.6 |
| | MAE03 | 0.0 | 2.6 | 7.0 | 10.0 | 0 | 1460 | 1460 | 1200 | 10.4 | 0.9 |
| | MAE07 | 0.0 | 2.7 | 7.0 | 9.0 | 0 | 1676 | 1676 | 60 | 7.4 | 0.7 |
| | SMZ01 | 0.0 | 2.8 | 12.1 | 29.4 | 0 | 1154 | 1154 | 680 | 20.5 | 1.5 |
| | SMZ03 | 0.0 | 4.2 | 11.3 | 16.8 | 0 | 2081 | 2081 | 1000 | 13.4 | 1.0 |
| | W8N18 | 0.0 | 8.5 | 25.5 | 28.9 | 0 | 882 | 882 | 440 | 26.9 | 1.6 |
| | W8N13 | 0.0 | 6.8 | 45.9 | 51.0 | 0 | 762 | 762 | 500 | 48.9 | 2.9 |
| | W8N8H | 0.0 | 6.8 | 32.3 | 49.3 | 0 | 689 | 689 | 417 | 40.9 | 2.4 |
| | W72M6 | 0.0 | 4.4 | 20.4 | 22.9 | 0 | 3695 | 3695 | 2970 | 22.9 | 2.1 |
| TAK01 | 0.0 | 10.1 | 35.1 | 54.0 | 0 | 999 | 999 | 560 | 43.7 | 1.6 | |
| TAK02 | 0.0 | 8.1 | 35.1 | 40.5 | 0 | 1007 | 1007 | 850 | 42.0 | 1.6 | |
| TAK03 | 0.0 | 8.9 | 27.0 | 33.8 | 0 | 1288 | 1288 | 750 | 30.2 | 1.1 | |
| Thomsen | RW1 | 0.0 | 17.0 | 77.5 | 92.0 | 0 | 107 | 107 | 29 | 81.5 | 2.2 |
| | RW2 | 0.0 | 22.5 | 84.0 | 86.0 | 0 | 154 | 154 | 135 | 87.2 | 2.4 |
| | TW2 | 0.0 | 38.0 | 80.0 | 80.0 | 0 | 362 | 362 | 290 | 80.0 | 2.2 |

continued on next page

continued from previous page

| Specimen | | Displacement (mm) | | | | Shear Force (kN) | | | | @ Failure (80%Vmax) | |
|------------|--------|-------------------|------|-------|-------|------------------|-----|-----|------|---------------------|-----------|
| | | D1 | D2 | D3 | D4 | F1 | F2 | F3 | F4 | Displacement (mm) | Drift (%) |
| Jiang | SSW-T | 0.0 | 11.0 | 38.0 | 57.0 | 0 | 128 | 128 | 95 | 52.7 | 1.9 |
| | DSW-T | 0.0 | 13.0 | 55.0 | 87.0 | 0 | 89 | 89 | 73 | 90.6 | 3.2 |
| Ji | SW-1 | 0.0 | 14.0 | 22.0 | 24.0 | 0 | 83 | 83 | 61 | 23.5 | 0.8 |
| | SW-2 | 0.0 | 22.0 | 50.5 | 55.0 | 0 | 115 | 115 | 103 | 59.1 | 2.0 |
| Zhou | SW-1 | 0.0 | 14.4 | 46.7 | 53.0 | 0 | 128 | 128 | 60 | 49.1 | 2.2 |
| | SW-2 | 0.0 | 17.8 | 44.4 | 48.9 | 0 | 152 | 152 | 53 | 45.8 | 2.0 |
| | SW-3 | 0.0 | 13.8 | 37.5 | 42.5 | 0 | 128 | 128 | 70 | 39.7 | 1.8 |
| | SW-4 | 0.0 | 18.0 | 40.0 | 42.5 | 0 | 167 | 167 | 67 | 40.8 | 1.8 |
| Zhang | SW1-1 | 0.0 | 6.0 | 20.0 | 21.0 | 0 | 196 | 196 | 110 | 20.5 | 1.0 |
| | SW1-2 | 0.0 | 7.0 | 22.0 | 23.0 | 0 | 238 | 238 | 175 | 22.8 | 1.1 |
| | SW1-3 | 0.0 | 7.0 | 21.0 | 23.0 | 0 | 240 | 240 | 150 | 22.1 | 1.1 |
| | SW1-4 | 0.0 | 5.5 | 12.0 | 13.0 | 0 | 200 | 200 | 150 | 12.8 | 0.6 |
| | SW2-1 | 0.0 | 2.7 | 8.9 | 9.8 | 0 | 540 | 540 | 200 | 9.2 | 0.9 |
| | SW2-2 | 0.0 | 3.0 | 11.5 | 13.8 | 0 | 275 | 275 | 50 | 12.1 | 0.8 |
| | SW2-3 | 0.0 | 5.0 | 13.5 | 14.2 | 0 | 225 | 225 | 55 | 13.7 | 0.7 |
| | SW2-4 | 0.0 | 9.8 | 17.7 | 22.0 | 0 | 226 | 226 | 200 | 25.2 | 1.0 |
| | SW4-1 | 0.0 | 4.0 | 12.0 | 12.5 | 0 | 225 | 225 | 155 | 12.3 | 0.6 |
| | SW4-2 | 0.0 | 5.0 | 10.0 | 11.0 | 0 | 217 | 217 | 161 | 10.8 | 0.5 |
| | SW4-4 | 0.0 | 6.7 | 16.0 | 17.3 | 0 | 225 | 225 | 214 | 21.1 | 1.1 |
| | SW5-1 | 0.0 | 5.0 | 12.0 | 12.5 | 0 | 220 | 220 | 155 | 12.3 | 0.6 |
| | SW5-3 | 0.0 | 6.0 | 16.0 | 18.0 | 0 | 280 | 280 | 150 | 16.9 | 0.8 |
| | SW6-1 | 0.0 | 6.5 | 15.0 | 18.5 | 0 | 245 | 245 | 175 | 17.5 | 0.9 |
| SW6-3 | 0.0 | 4.0 | 19.0 | 20.0 | 0 | 264 | 264 | 200 | 19.8 | 1.0 | |
| Paulay | Wall 1 | 0.0 | 4.5 | 14.0 | 20.0 | 0 | 800 | 800 | 480 | 17.0 | 1.1 |
| | Wall 2 | 0.0 | 3.8 | 13.8 | 19.8 | 0 | 875 | 875 | 655 | 18.6 | 1.2 |
| | Wall 4 | 0.0 | 3.5 | 18.0 | 26.0 | 0 | 880 | 880 | 640 | 23.9 | 1.6 |
| Adebar | Adebar | 0.0 | 52.0 | 278.0 | 288.0 | 0 | 160 | 160 | 140 | 294.0 | 2.5 |
| Pilakoutas | SW4 | 0.0 | 6.6 | 19.5 | 22.1 | 0 | 107 | 107 | 100 | 27.4 | 2.3 |
| | SW5 | 0.0 | 55.2 | 110.0 | 270.0 | 0 | 102 | 102 | 24 | 151.8 | 12.7 |
| | SW6 | 0.0 | 7.0 | 17.3 | 22.7 | 0 | 107 | 107 | 79 | 21.4 | 1.8 |

continued on next page

continued from previous page

| Specimen | | Displacement (mm) | | | | Shear Force (kN) | | | | @ Failure (80%Vmax) | |
|------------|-----|-------------------|------|------|-------|------------------|-----|-----|-----|---------------------|-----------|
| | | D1 | D2 | D3 | D4 | F1 | F2 | F3 | F4 | Displacement (mm) | Drift (%) |
| Pilakoutas | SW7 | 0.0 | 7.8 | 20.5 | 22.6 | 0 | 125 | 125 | 99 | 22.5 | 1.9 |
| | SW8 | 0.0 | 6.3 | 24.0 | 26.5 | 0 | 91 | 91 | 77 | 27.4 | 2.3 |
| | SW9 | 0.0 | 6.1 | 23.6 | 25.7 | 0 | 100 | 100 | 77 | 25.4 | 2.1 |
| Ali | W1 | 0.0 | 23.0 | 90.4 | 104.1 | 0 | 153 | 153 | 144 | 137.0 | 3.9 |
| | W3 | 0.0 | 23.0 | 55.0 | 58.0 | 0 | 161 | 161 | 41 | 55.8 | 1.6 |
| Sittipunt | W1 | 0.0 | 6.8 | 36.0 | 54.7 | 0 | 483 | 483 | 247 | 43.7 | 2.0 |
| | W2 | 0.0 | 20.6 | 33.8 | 55.3 | 0 | 533 | 533 | 400 | 51.0 | 2.4 |
| Carvajal | M-2 | 0.0 | 6.0 | 35.0 | 66.7 | 0 | 34 | 34 | 30 | 88.9 | 5.7 |
| | M-3 | 0.0 | 8.3 | 70.0 | 75.0 | 0 | 36 | 36 | 31 | 77.6 | 5.0 |
| | M-4 | 0.0 | 4.3 | 57.1 | 75.7 | 0 | 29 | 29 | 25 | 83.8 | 5.4 |
| | M-5 | 0.0 | 5.7 | 14.3 | 48.6 | 0 | 28 | 28 | 23 | 53.8 | 3.5 |
| | M-6 | 0.0 | 3.1 | 10.0 | 45.4 | 0 | 29 | 29 | 20 | 34.4 | 2.2 |

where $D1$, $D2$, $D3$, and $D4$ are lateral displacements, and $F1$, $F2$, $F3$, and $F4$ are lateral loads defined at four points of the backbone curves: origin, yield, strength degradation, and residual, respectively (Figure B-1).

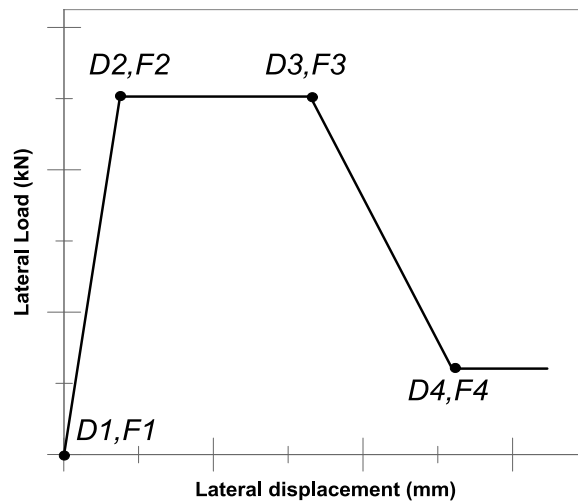


Figure B-1. Four points defined to obtain backbone curves

Summary of the range of parameters

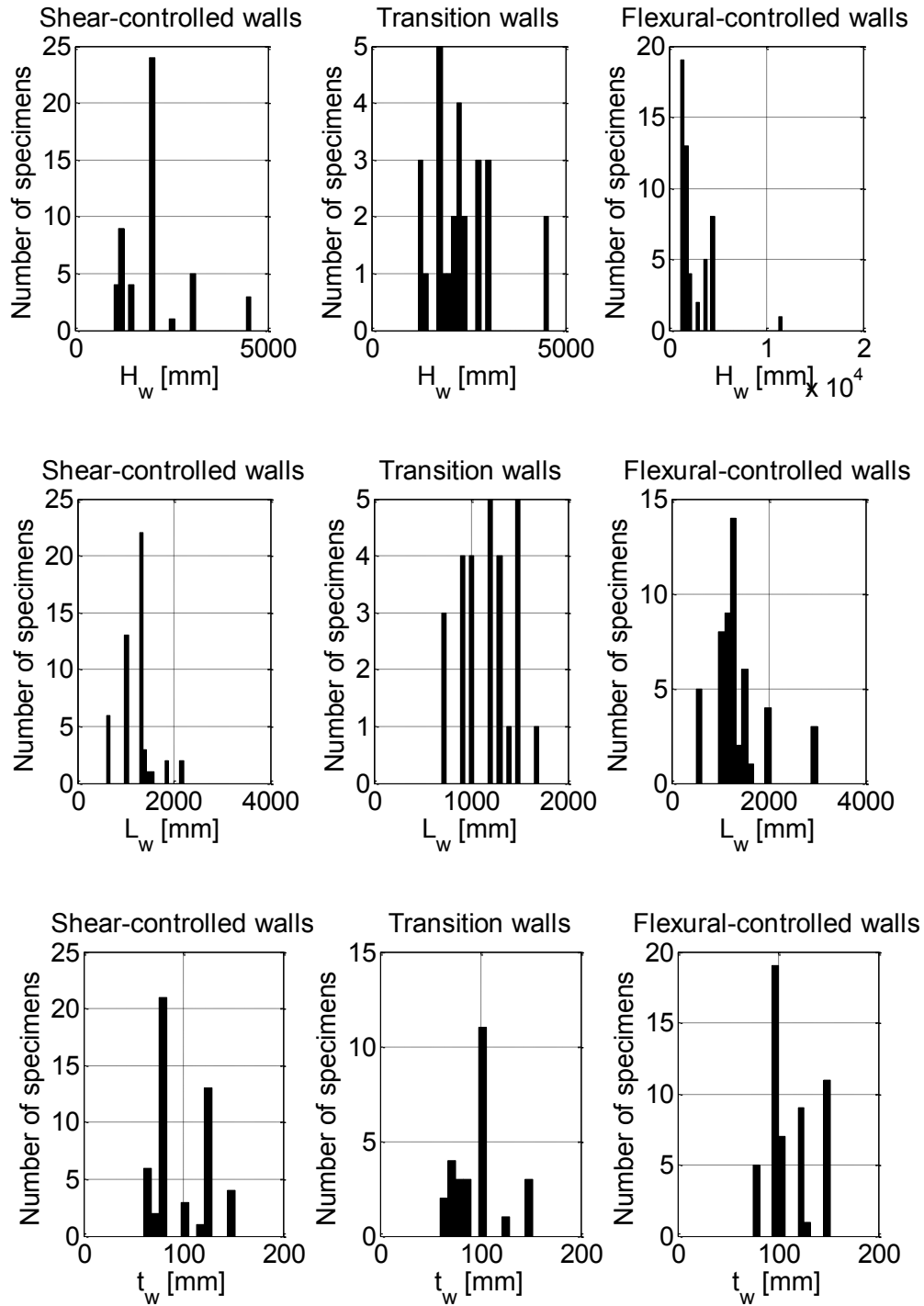


Figure B-2. Range of height, length, thickness in three failure regions

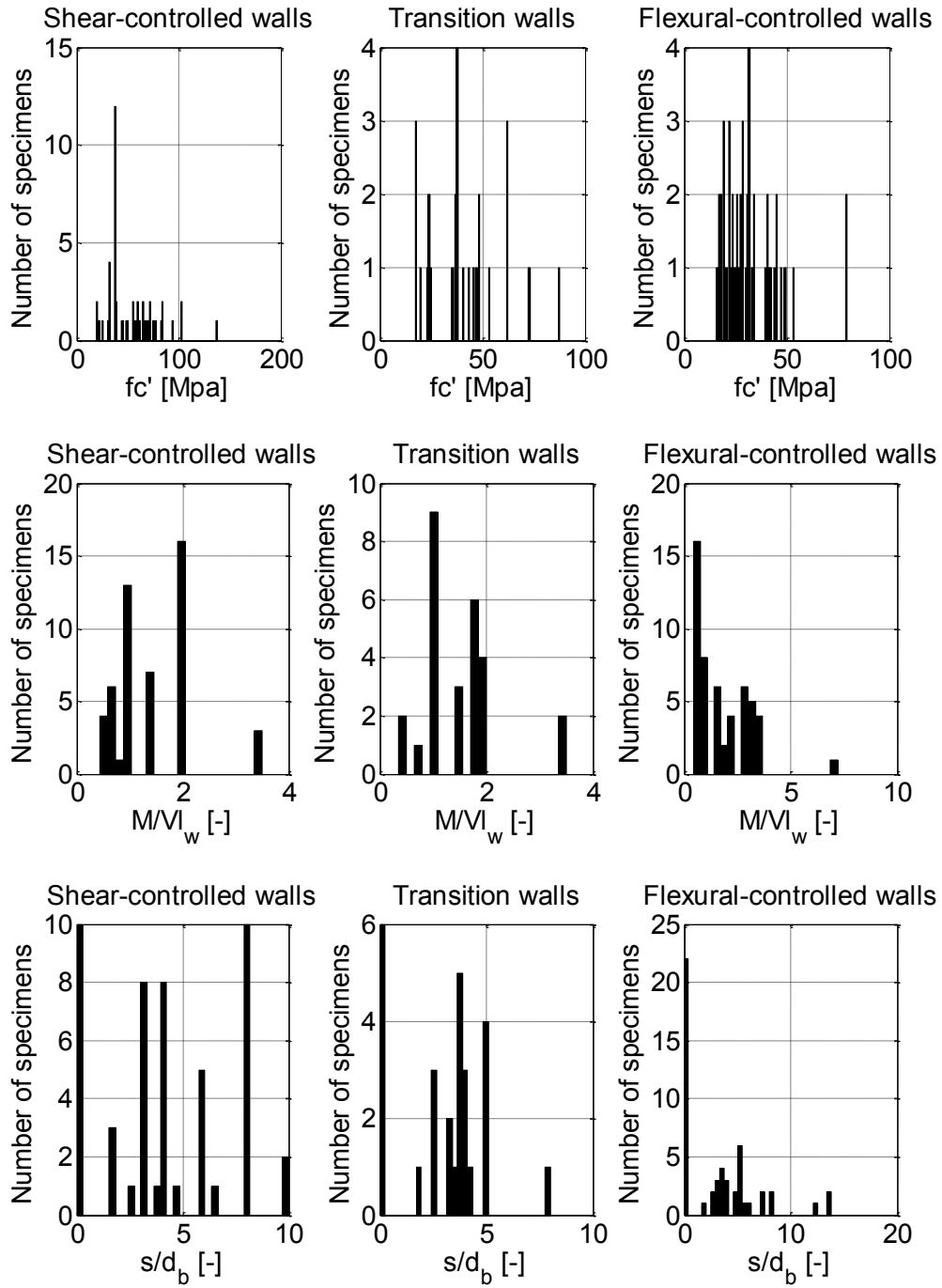


Figure B-3. Range of concrete strength, shear span ratio, spacing to boundary bar diameter ratio in three failure regions

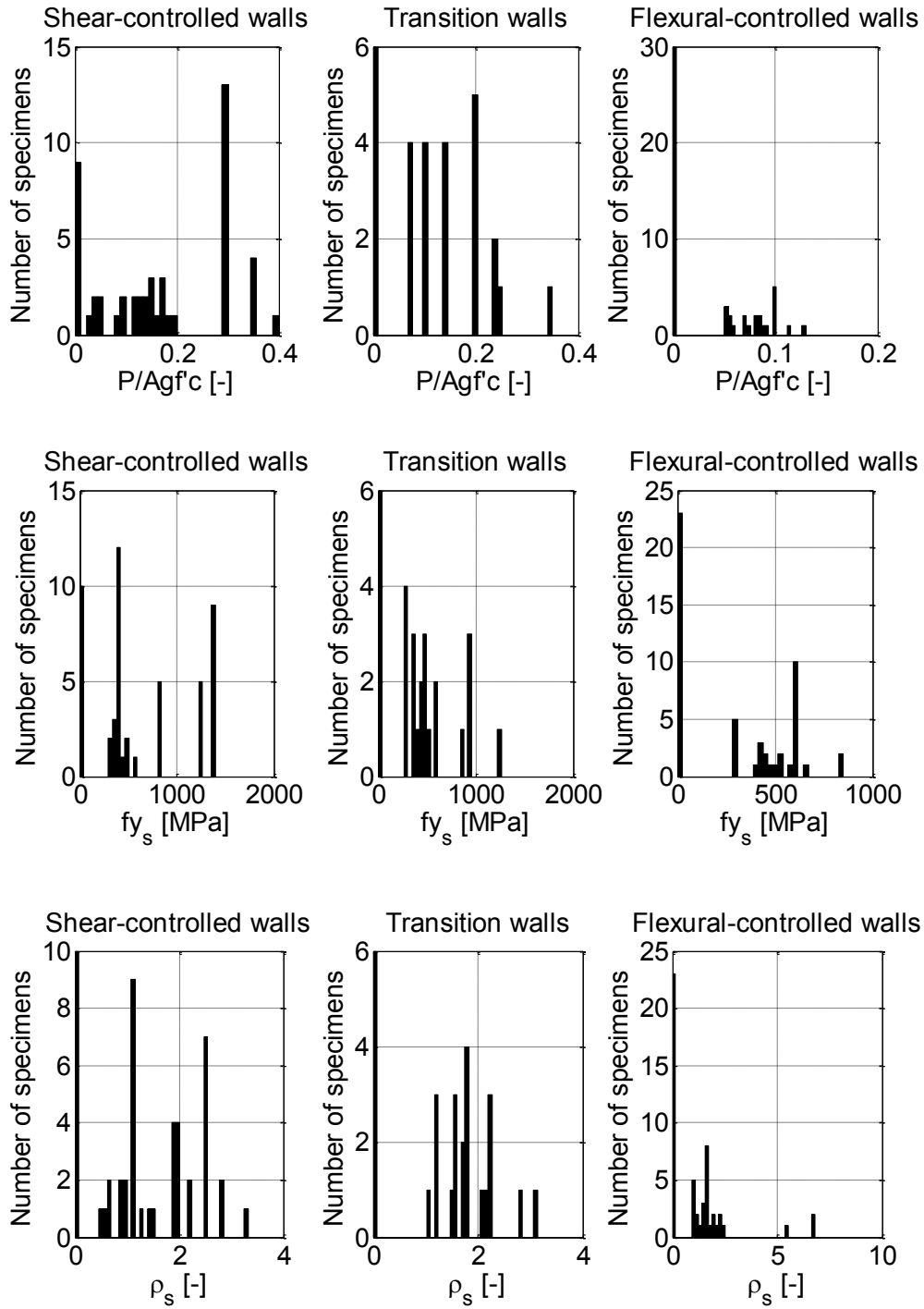


Figure B-4. Range of axial load ratio, yield strength of transverse boundary reinforcement, transverse boundary reinforcement ratio in three failure regions

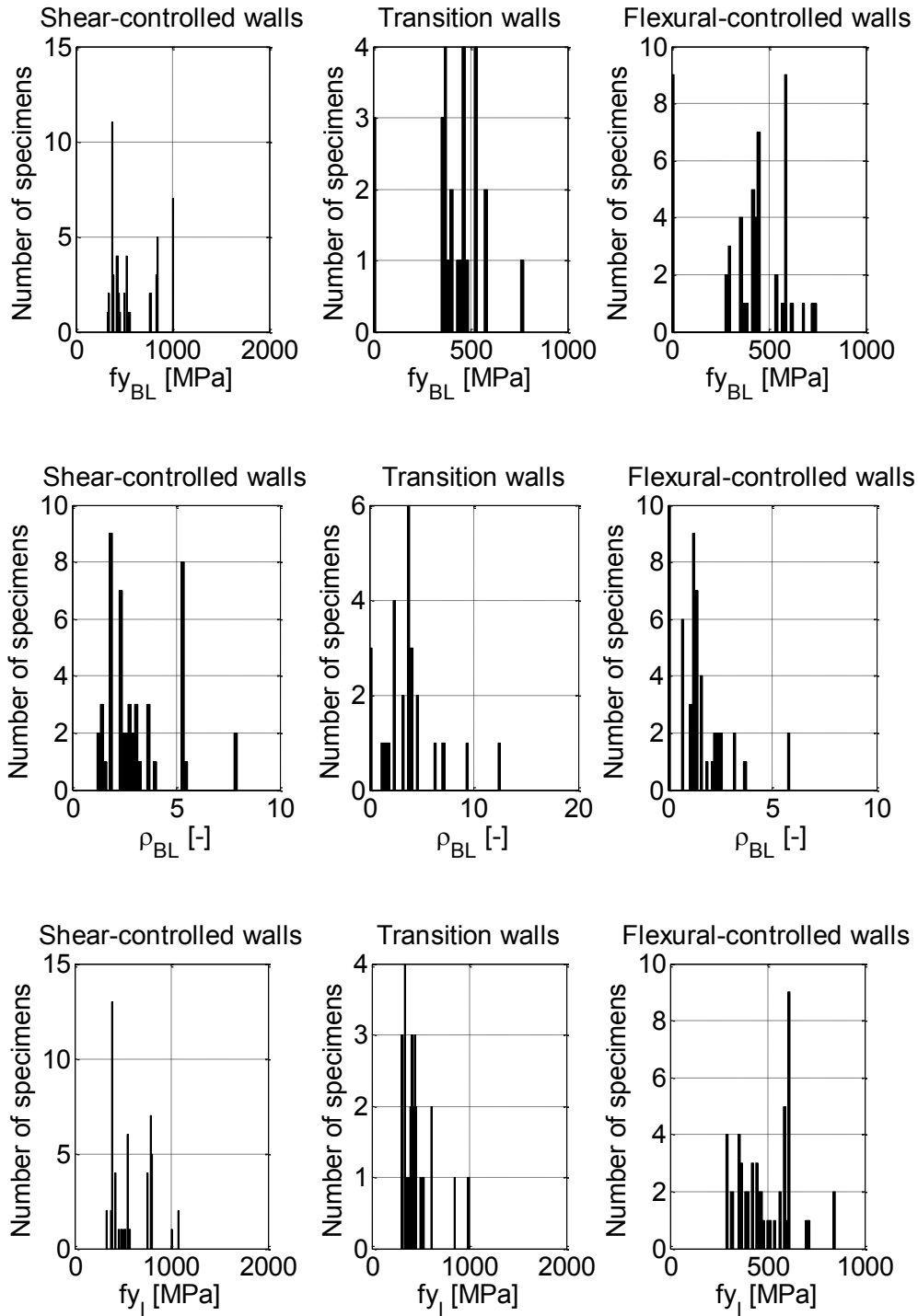


Figure B-5. Range of yield strength of longitudinal boundary reinforcement, longitudinal boundary reinforcement ratio, yield strength of longitudinal web reinforcement in three failure regions

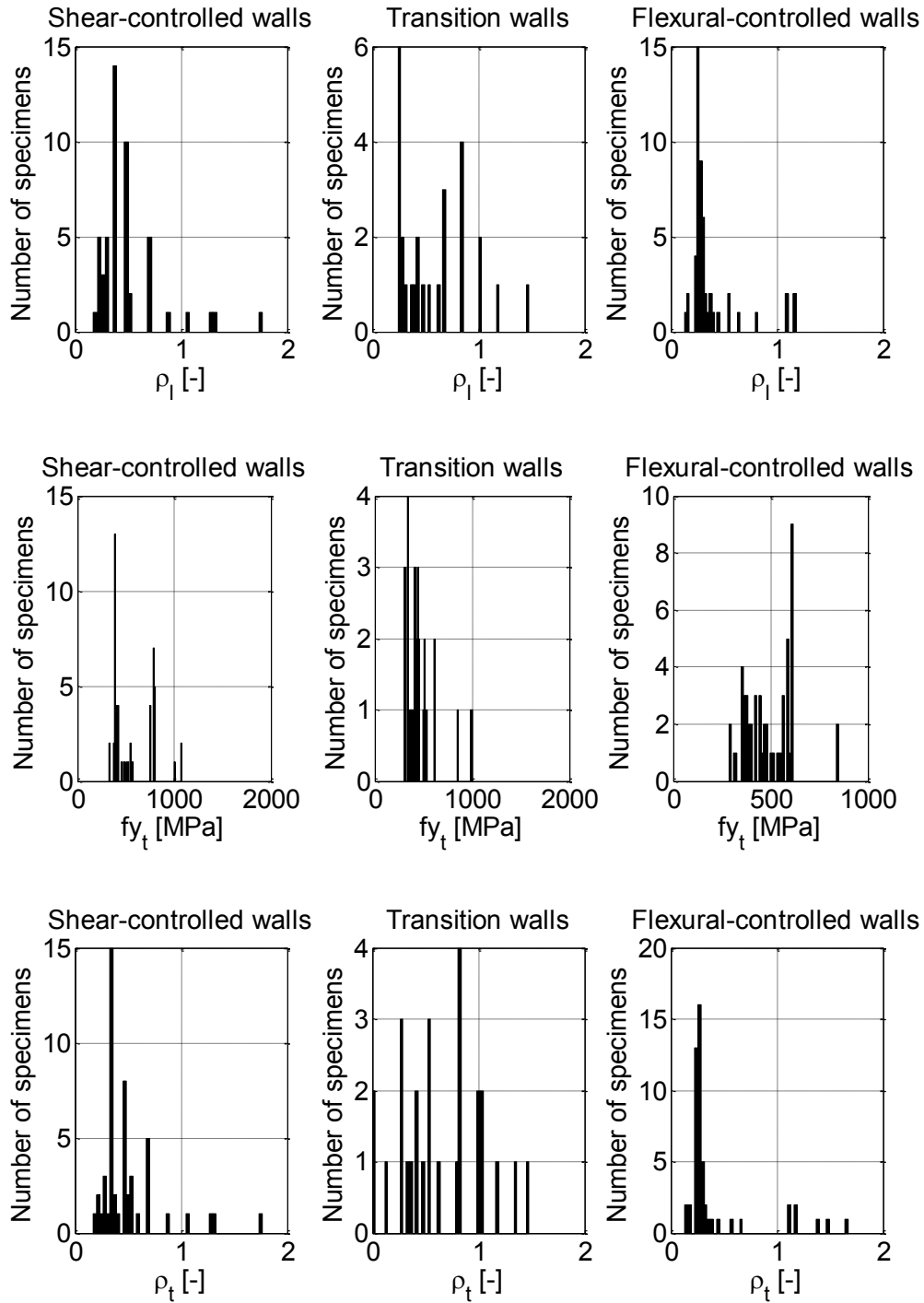
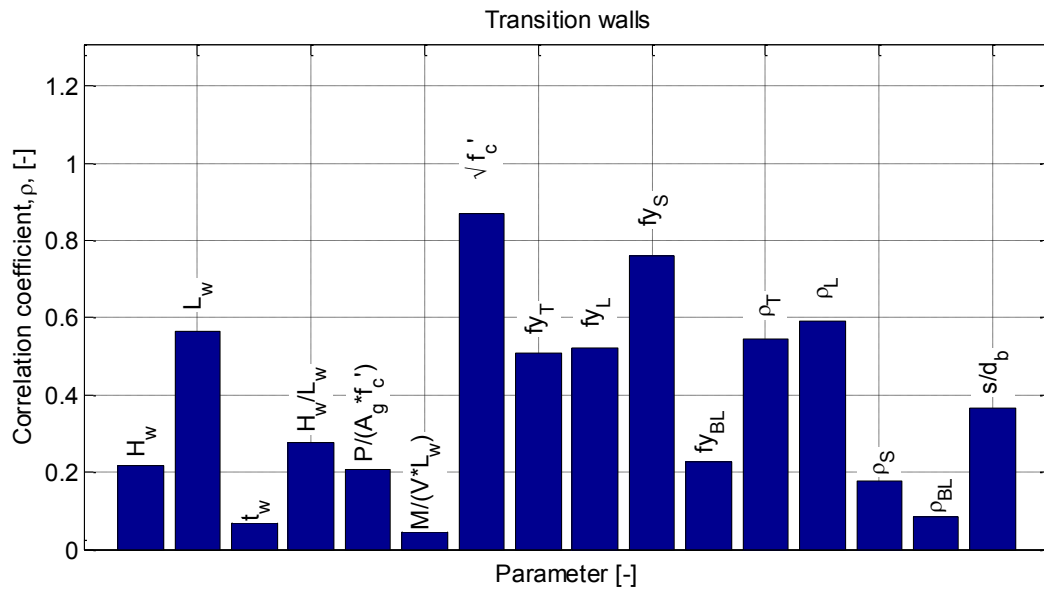
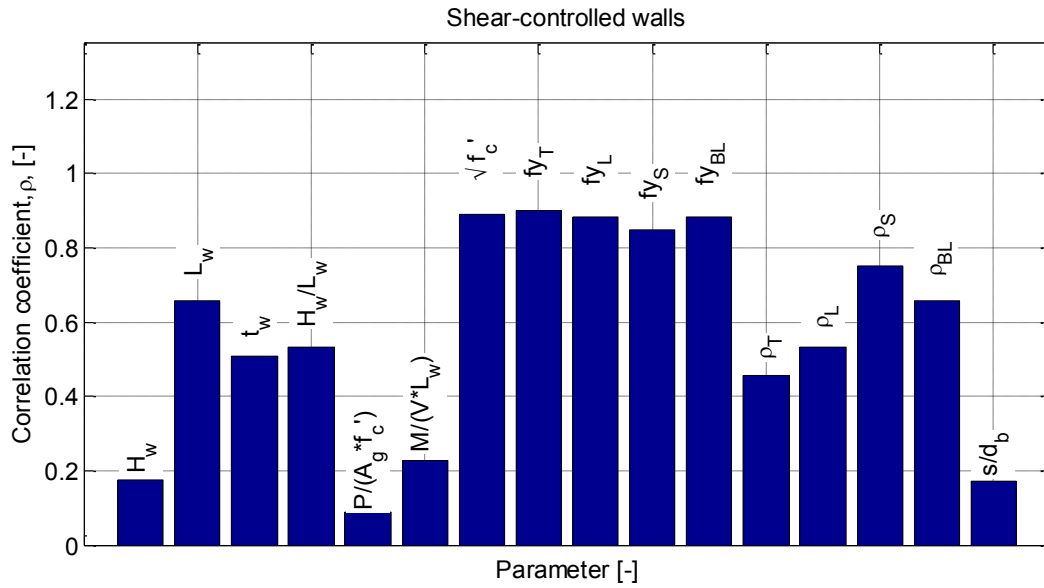


Figure B-6. Range of yield strength of longitudinal web reinforcement ratio, yield strength of transverse web reinforcement, transverse web reinforcement ratio in three failure regions

Regression Analysis Results



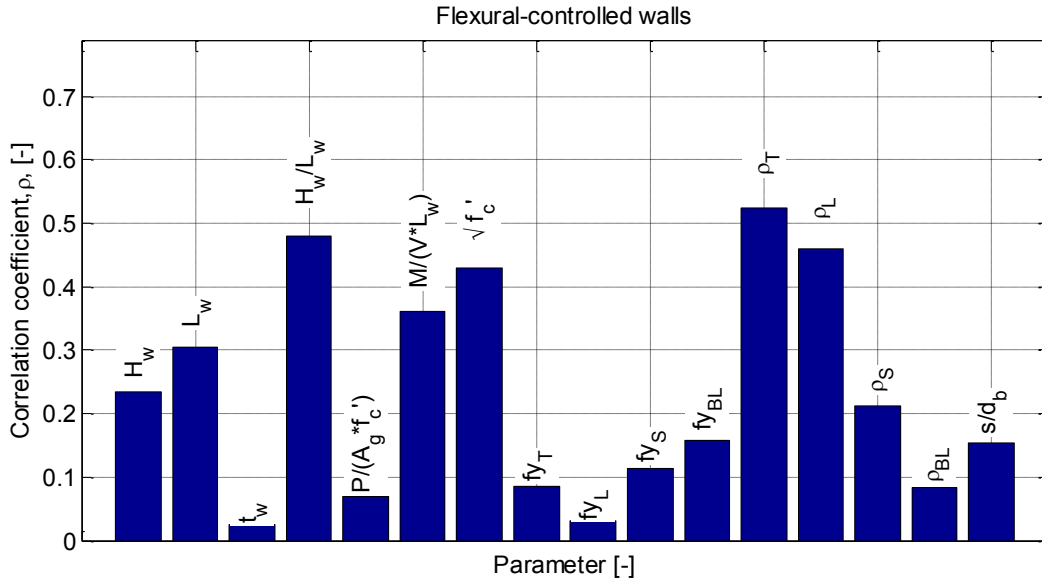
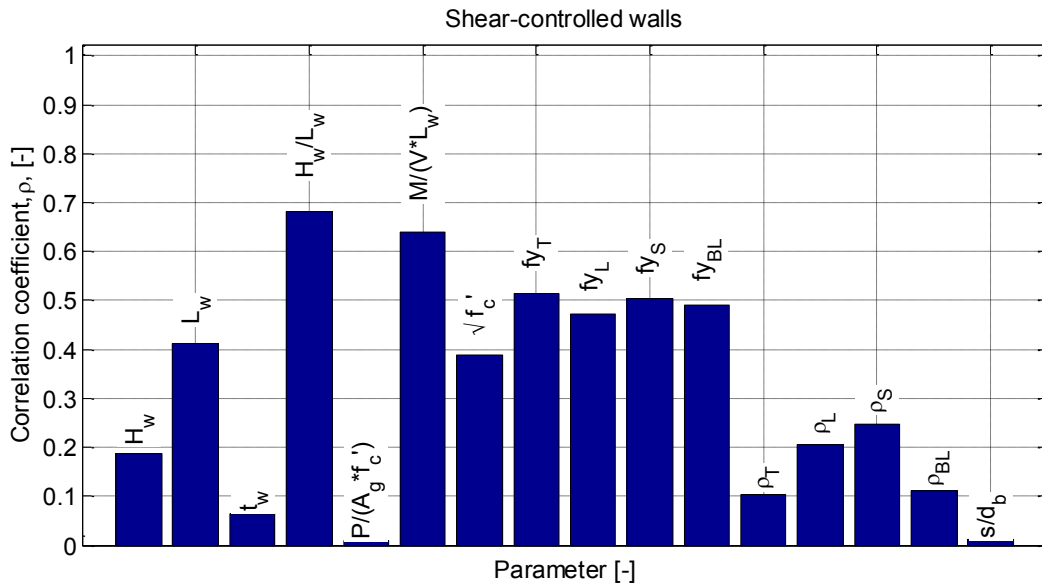


Figure B-7. Distribution of correlation coefficient of key parameters with respect to the shear strength



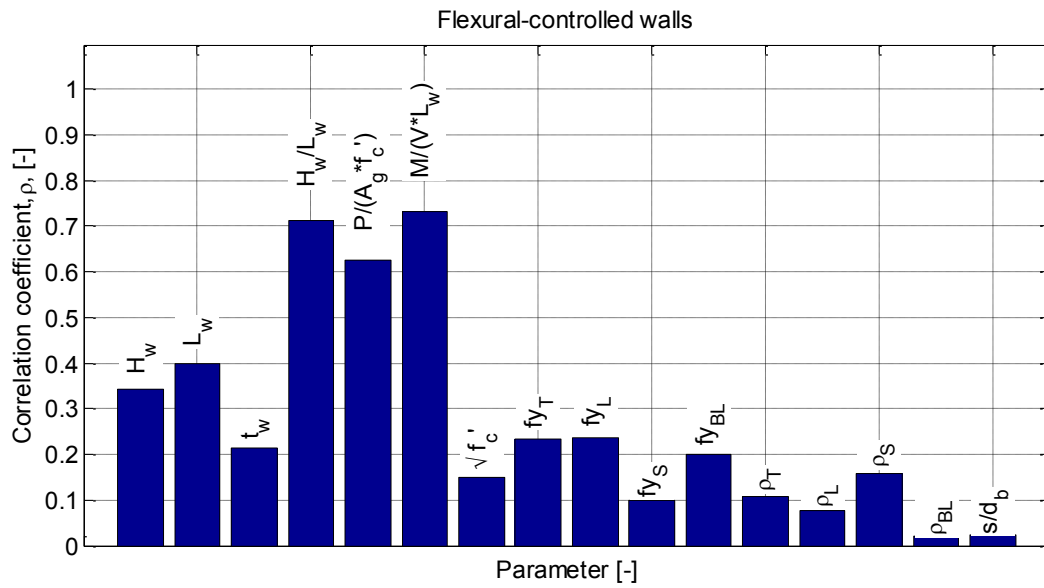
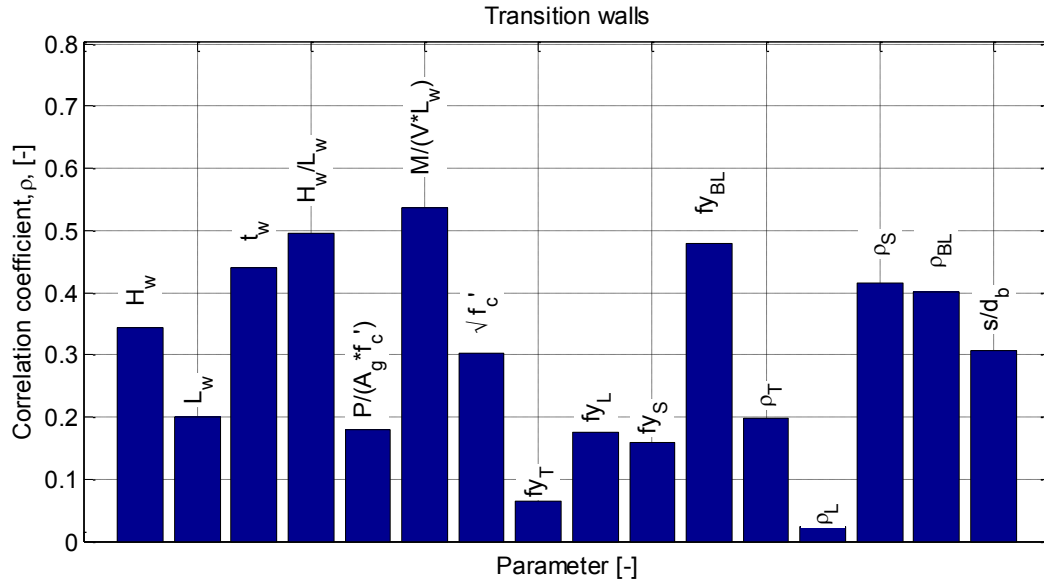


Figure B-8. Distribution of correlation coefficient of key parameters with respect to the normalized deformation capacity (curvature ductility)

Appendix C

Modeling Details

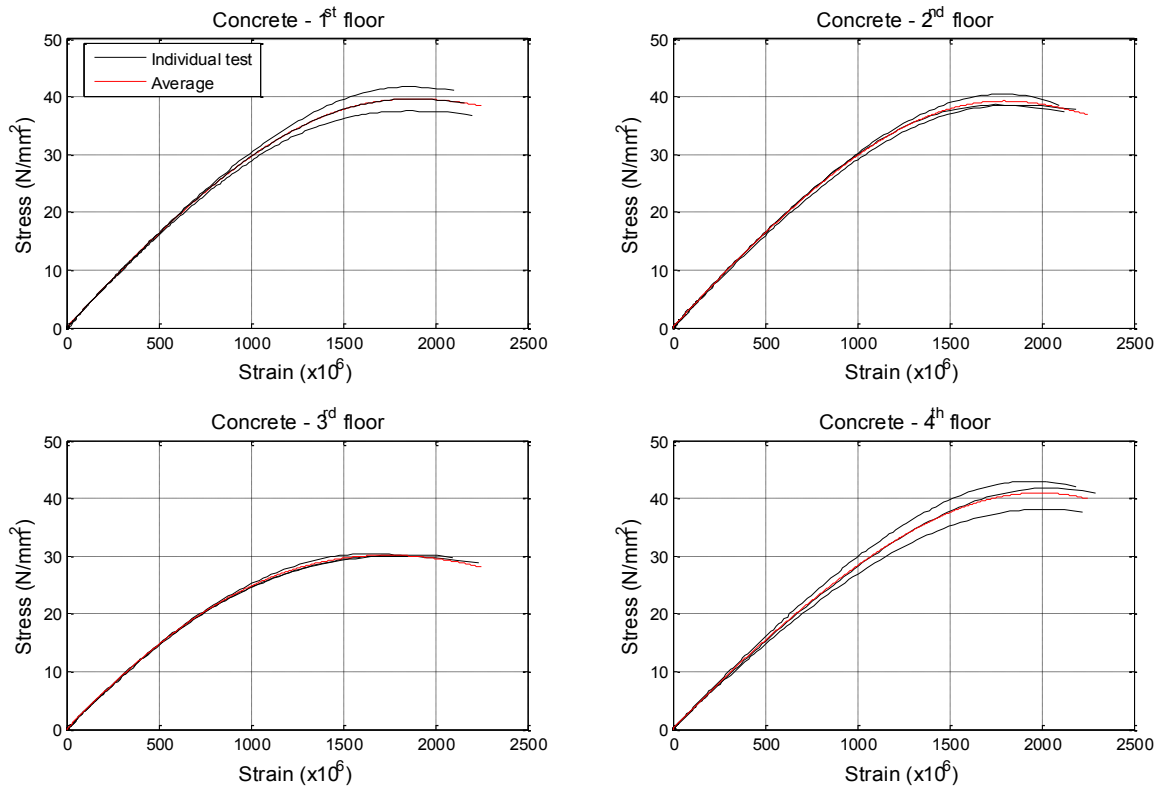


Figure C-1. Concrete properties from the test results

References

1. ACI 318-95. (1995). "Building Code Requirements for Structural Concrete and Commentary," American Concrete Institute Committee 318.
2. ACI 318-08. (2008). "Building Code Requirements for Structural Concrete and Commentary," American Concrete Institute Committee 318.
3. ACI 318-11. (2011). "Building Code Requirements for Structural Concrete and Commentary," American Concrete Institute Committee 318.
4. ACI Committee 363. (1992). "State-of-the-Art Report on High-Strength Concrete (ACI 363-92)," ACI Manual of Concrete Practice, American Concrete Institute, Detroit, 2005.
5. Adebar, P., Ibrahim A.M.M., Bryson M., (2007). "Test of High-Rise Core Wall: Effective Stiffness for Seismic Analysis," ACI Journal of Structural Engineering, Vol. 104, No. 5, September-October 2007, pp. 549-559.
6. Ali, A., Wight, J.K., (1991). "RC Structural Walls with Staggered Door Openings," Journal of Structural Engineering, ASCE, V. 117, No. 5, pp. 1514-1531.
7. Alsiwat J. M., and Saatcioglu M. (1992). "Reinforcement Anchorage Slip under Monotonic Loading," Journal of Structural Engineering, ASCE, Vol.118, No.9, Sept. 1992. pp. 2421-2438.
8. American Society of Civil Engineers (2010). "ASCE/SEI 7-10: Minimum Design Loads for Buildings and Other Structures," Reston, VA, 650 pp.
9. Applied Technology Council. (2009). Guidelines for Seismic Performance Assessment of Buildings (50% Draft), ATC-58, Redwood City, CA.

10. Applied Technology Council. (2010). ATC-72: Modeling and Acceptance Criteria for Seismic Design and Analysis of Tall Buildings. ATC, Redwood City, CA.
11. ASCE/SEI 7. (2005). Minimum Design Loads for Buildings and Other Structures, Structural Engineering Institute of the American Society of Civil Engineers.
12. ASCE/SEI Seismic Rehabilitation Standards Committee. (2007). Seismic Rehabilitation of Existing Buildings (ASCE/SEI 41-06), American Society of Civil Engineers, Reston, VA, US.
13. ASCE/SEI 7. (2010). Minimum Design Loads for Buildings and Other Structures, Structural Engineering Institute of the American Society of Civil Engineers.
14. Bae, S., Miseses, A., Bayrak, O., (2005). "Inelastic buckling of reinforcing bars," Journal of Structural Engineering, ASCE, 1996:131(2): 314-321.
15. Bonelli, P. (2010), Personal Communication.
16. Carvajal, O. and Pollner, E., (1983). "Muros de Concreto Reforzados con Armadura Minima," Boletin Tecnico, Universidad Central de Venezuela, Facultad de Ingenieria, Ano 21 (72-73), Enero-Diciembre, 5-36 (in Spanish).
17. Computer and Structures, Inc. (2006). *Perform-3D V4: Nonlinear Analysis and Performance Assessment for 3D Structures*, Berkeley, CA.
18. Computer and Structures, Inc. (2011). *Perform-3D V5: Nonlinear Analysis and Performance Assessment for 3D Structures*, Berkeley, CA.
19. Cosenza, E. and Prota, A., (2006). "Experimental Behavior and Numerical Modeling of Smooth Steel Bars under Compression," Journal of Earthquake Engineering, 10:3, pp. 313-329.

20. Dazio A., Beyer K., Bachmann H., (2009). "Quasi-static cyclic tests and plastic hinge analysis of RC structural walls," *Engineering Structures*, Volume 31, Issue 7, July 2009, pp. 1556-1571.
21. Earthquake Engineering Research Institute, (2010). "EERI Special Earthquake Report- June 2010: The Mw 8.8 Chile Earthquake of February 27, 2010," Oakland, CA.
22. Elwood, K. J., Matamoros, A. B., Wallace, J. W., Lehman, D. E., Heintz, J. A., Mitchell, A. D., Moore, M. A., Valley, M. T., Lowes, L. N., Comartin, C. D., and Moehle, J. P., (2007). Update to ASCE/SEI 41 Concrete Provisions. *Earthquake Spectra*, Vol. 23, No. 3, pp. 493~523.
23. ETABS Nonlinear Version 9.2.0 (2008). *Extended 3D Analysis of Building Structures*, Computers and Structures, Inc. Berkeley, CA.
24. Fry, J.A, Hooper, J.D., Klemencic, R. (2010). Core wall case study design for Pacific Earthquake Engineering Research/ California seismic safety commission, *The Structural Design of Tall and Special Buildings*, 19(1-2):61-75.
25. Ghodsi, T., Ruiz, J.F., Massie, C., Chen, Y. (2010). PEER/ SSC tall building design case history no. 2, *The Structural Design of Tall and Special Buildings*, 19(1-2):197-256.
26. Gogus, A., (2010). "Structural wall systems - nonlinear modeling and collapse assessment of shear walls and slab-column frames," *Doctoral dissertation*, University of California, Los Angeles, CA.
27. Hidalgo, P.A., Ledezma, C.A., Jordan, R.M., (2002). "Seismic Behavior of Squat Reinforced Concrete Shear Walls," *Earthquake Spectra*, EERI, Vol. 18, No.2, May 2002, pp.287-308.

28. Hognestad, E., (1951). "A study of combined bending and axial load in RC members," University of Illinois Eng. Exp. Stat. Bull. 399(2): pp. 36-57.
29. International Code Council (2006). "International Building Code," Falls Church, VA.
30. Jiang, H., (1999). "Research on seismic behavior of shear walls dissipating energy along vertical direction with application", Doctoral Dissertation, Tongji University, China. (In Chinese).
31. Ji, S., (2002). "Dynamic Analysis of the Elastic-plastic Response of High-rise Reinforced Concrete Frame-wall Structures Subjected to Ground Motion", Doctoral Dissertation, Tongji University, China. (In Chinese).
32. Kabeyasawa, T.; and Hiraishi, H., (1993). "Test and Analyses of High-Strength Reinforced Concrete Shear Walls in Japan," ACI SP 176-13, pp. 281-310.
33. Lagos, R., Kupfer, M., (2012). "Performance of High Rise Buildings under the February 27th 2010 Chilean Earthquake," Proceedings, One Year after the 2011 Great East Japan Earthquake, March 1-4, 2012, Tokyo, Japan, Paper , 1754-1765 (Paper 15).
34. Langdon (2010). Cost Model for PEER Tall Buildings Study: Concrete Dual System Structural Option. Final Report, <http://peer.berkeley.edu/tbi/publications-reports/>
35. LATBSDC. (2008). An Alternative Procedure For Seismic Analysis and Design of Tall Buildings Located in the Los Angeles Region, Los Angeles Tall Buildings Structural Design Council.
36. Lowes, L.N., Mitra, N., and Altoontash, A., (2004). A Beam-Column Joint Model for Simulating the Earthquake Response of Reinforced Concrete Frames. PEER Report, PEER 2003/10. Feb. 2004, UC Berkeley.

37. Mander, J.B., Priestley, M.J.N. and Park, R., (1988). "Theoretical Stress-Strain Model for Confined Concrete", ASCE Journal of Structural Engineering, 114(8), 1804-1826
38. Massone, L.M., (2006). "RC Wall Shear – Flexure Interaction: Analytical and Experimental Responses," Doctoral Dissertation, University of California, Los Angeles.
39. Massone, L.M., Orakcal, K., Wallace, J.W., (2004). "Flexural and shear responses in slender RC shear walls," 13WCEE Secretariat, Vancouver, B.C., 13th World Conference on Earthquake Engineering: Conference Proceedings, Vancouver, B.C., Aug. 1-6, 2004. Paper No. 1067.
40. Massone, L.M., Beltran J.F, Lacaze, C., Rojas P.A., (2010). "Modelacion del Pandeo de Refuerzo Longitudinal de Elementos de Hormigon Armado," Congreso Chileno de Sismologia e Ingenieria Antisismica. X Jornadas, Chile. (in Spanish).
41. Massone, L.M., Bonelli, P., Lagos, R., Lüder, C., Moehle, J.P., Wallace, J.W., (2012). "Seismic Design and Construction Practices for Reinforced Concrete Buildings," EERI Spectra, Special Issue, 2010 Chile Earthquake, accepted for publication January 2012.
42. Moehle, J.P., Bozorgnia, Y., Jayaram, N., Jones,P., Rahnama, M., Shome, N., Tuna, Z., Wallace, J.W., Yang, T.Y., Zareian, F., (2011). "Case studies of the seismic performance of tall buildings designed by alternative means," Task 12 Report for the Tall Buildings Initiative, PEER 2011/05, Pacific Earthquake Engineering Research Center, College of Engineering, University of California, Berkeley.
43. Nagae, T.; Wallace, J. W., (2011). "Design and instrumentation of the 2010 E-Defense four-story reinforced concrete and post-tensioned concrete buildings," PEER Report, PEER-2011/104. June 2011, UC Berkeley.

44. Nagae T., Tahara, K., Fukuyama K., Matsumori T., Shiohara H., Kabeyasawa T., Kono, S., Nishiyama, M., Moehle, J., Wallace, J., Sause, R., Ghannoum, W., (2012). "Test results of Four-Story Reinforced Concrete and Post-Tensioned Concrete Buildings: The 2010 E-Defense Shaking Table Test," Submitted to be published in Proceedings of Fifteenth World Conference on Earthquake Engineering (15WCEE), September 24-28, 2012, Lisbon, Portugal.
45. Naish, D., Fry, A., Klemencic, R. and Wallace, J.W., (2009). Testing and Reinforced Concrete Coupling Beams. Paper submitted to ACI structural journal, Los Angeles, CA.
46. Naish, D., (2010). "Testing and Modeling of Reinforced Concrete Coupling Beams," Doctoral Dissertation, University of California, Los Angeles, pp. 125
47. Oesterle, R. G., Fiorato, A. E., Corley, W. G., (1981). "Reinforcement details for earthquake-resistant structural walls," Portland Cement Association, Research and Development bulletin, 12p.
48. Official Chilean Code NCh 433.of.96. (1996). "Seismic Design of Buildings", Instituto Nacional de Normalizacion, Santiago, Chile.
49. Orakcal, K., Wallace, J. W., (2006). "Flexural Modeling of reinforced Concrete Walls- Experimental Verification," ACI Structural Journal, V. 103, No. 2, March-April 2006.
50. Orakcal, K., Massone, L.M., Wallace, J. W., (2009). "Shear strength of lightly reinforced wall piers and spandrels," ACI Structural Journal, 106(4): 455-465.
51. Pacific Earthquake Engineering Research Center (2010). Guidelines for performance-based seismic design of tall buildings, Report PEER-2010/05, Pacific Earthquake Engineering Research Center, University of California, Berkeley, CA.

52. Panagiotou, M., (2008). Seismic design, testing and analysis of reinforced concrete wall buildings, PhD Dissertation, Dept. of Civil Engineering, University of California, San Diego, CA.
53. Park R., (1988). "State-of-the Art Report – Ductility Evaluation From Laboratory and Analytical Testing," Proceedings of Ninth World Conference on Earthquake Engineering, August 2-9, 1988, Tokyo-Kyoto, Japan, Vol. VIII, pp. 605-616.
54. Paulay, T., Priestley, M.J.N., and Syngge, A.J., (1982). "Ductility in Earthquake Resisting Squat Shearwalls," ACI Journal, 79(4). pp.257-269.
55. Pilakoutas, K., Elnashai A., (1995). "Cyclic behavior of reinforced concrete cantilever walls, Part I: Experimental Results," ACI Journal of Structural Engineering, Vol. 92, No. 3, May-June issue, pp. 271-281.
56. Popov, E.P., Bertero, V. V., and Krawinkler, H., (1972). Cyclic Behavior of Three R.C. Flexural Members with High Shear, Report No. EERC 72-5, Earthquake Engineering Research Center, University of California, Berkeley, CA.
57. Powell, G.H., (2007). "Detailed Example of a Tall Shear Wall Building Using CSI's Perform 3D Nonlinear Dynamic Analysis," Computers and Structures Inc., Berkeley, CA.
58. Priestley, M. J. N., Verma R., and Xiao Y., (1994). "Seismic shear strength of reinforced concrete columns," ASCE Journal of Structural Engineering, Vol. 120, No. 8, pp. 2310-2329.
59. Razvi, S., and Saatcioglu, M., (1992). "Strength and ductility of confined concrete," Journal of Structural Engineering, ASCE, Vol.118, No.6, pp. 1590-1606.

60. Rodriguez, M.E., Botero, J.C. and Villa, J., (1999). "Cyclic Stress-strain Behavior of Reinforcing Steel Including Effect of Buckling," *Journal of Structural Engineering*, 125:6, pp. 605-612.
61. Roy, H.E.H, Sozen, M.A., (1965). "Ductility of Concrete in Flexural Mechanics of Reinforced Concrete," SP12, American Concrete Institute/American Society of Civil Engineers, Detroit, pp. 213–235.
62. Salas M.C., (2008). "Modeling of Tall Reinforced Concrete Wall Buildings," MS Thesis, University of California, Los Angeles.
63. Salonikios, T. N., Kappos A. J., Tegos I. A., Penelis G. G., (1999). "Cyclic Load Behavior of Low-Slenderness Reinforced Concrete Walls: Design Basis and Test Results," *ACI Journal of Structural Engineering*, Vol. 96, No.4, pp. 649-660.
64. Sittipunt, C., Wood, S.L., Lukkunaprasit P., and Pattararattanakul, P., (2001). "Cyclic Behavior of Reinforced Concrete Structural Walls with Diagonal Web Reinforcement," *ACI Journal of Structural Engineering*, Vol. 98, No. 4, July-August 2001, pp. 554-562.
65. Thomsen, J.H., and Wallace, J.W., (1995). "Displacement-Based Design of Reinforced Concrete Structural Walls: An Experimental Investigation of Walls with Rectangular and T-Shaped Cross-Sections," Report No. CU/CEE-95/06, Department of Civil Engineering Clarkson University, Postdam, N.Y., 353 pp.
66. Thomsen, J.H., and Wallace, J.W., (2004). "Experimental Verification of Displacement-Based Design Procedures for Slender Reinforced Concrete Structural Walls," *Journal of Structural Engineering*, ASCE, V. 130, No. 4, pp. 618-630.
67. Tran, T. A., (2010). "Lateral Load Behavior and Modeling of Low-Rise RC Walls for Performance-Based Design," Ph.D. Seminar, University of California, Los Angeles.

68. Tuna, Z., (2009). "Quantification of Seismic Performance Levels of Tall Buildings," M.S. Thesis. University of California, Los Angeles.
69. Tuna, Z., Wallace, J.W., (2011). "Preliminary Collapse Assessment of the Torre Alto Rio Building in The Mw = 8.8 February 27, 2010 Chile Earthquake," Proceedings, 8th International Conference on Urban Earthquake Engineering, Tokyo Institute of Technology, March 7-8, 2011, Tokyo, Japan.
70. Wallace, J.W., Moehle, J.P., (1989). "The 1985 Chile Earthquake: An Evaluation of Structural Requirements for Bearing Wall Buildings," Report N° UCB/EERC-89-05.
71. Wallace, J.W., Moehle, J.P., (1993). "An Evaluation of Ductility and Detailing Requirements of Bearing Wall Buildings Using Structural Walls," Journal of Structural Engineering, pp. 121(1).
72. Wallace, J. W., (1996). "Evaluation of UBC-94 Provisions for Seismic Design of RC Structural Walls," Earthquake Spectra, Vol. 12, No. 2, pp. 327 – 348.
73. Wallace, J.W., (1998). "Behavior and Design of High-Strength RC Walls," SP176-12, American Concrete Institute/High-Strength Concrete in Seismic Regions, pp. 259–279.
74. Wallace, J. W., Elwood, K. J., Massone, L. M., (2008). "Investigation of the Axial Load Capacity for Lightly Reinforced Wall Piers," Journal of Structural Engineering/ASCE, Vol. 134, No.9. pp. 1548-1557.
75. Wallace, J. W., (2011). "February 27, 2010 Chile Earthquake: Preliminary Observations on Structural Performance and Implications for U.S. Building Codes and Standards," ASCE Structures Congress, Las Vegas, April 14-16, 2011, Paper 1159.

76. Wallace, J.W., Massone, L.M., Bonelli, P., Dragovich, J., Lagos, R, Lüder, C., Moehle, J.P., (2012). "RC Building Damage and Implications for U.S. Codes" EERI Spectra, Special Issue, 2010 Chile Earthquake, accepted for publication January 2012.
77. Wallace, J.W. (2010), Personal Communication.
78. Wood, S.L., Moehle, J.P., Wight, J.K., (1987). "A Report to the National Science Foundation Research Grants ECE 86-03789, ECE 86-03624, and ECE 06089," University of Illinois Engineering Experiment Station, College of Engineering, University of Illinois at Urbana-Champaign.
79. Wood, S. L., (1990). "Shear strength of low-rise reinforced concrete walls," ACI Journal of Structural Engineering, Vol. 87, No. 1, January 1990, pp. 99-107.
80. Wood, S., (1991). "Performance of Reinforced Concrete Buildings During the 1985 Chile Earthquake: Implications for the Design of Structural Walls" Earthquake Spectra 7, 607.
81. Yang, T.Y., Moehle J.P., Hurtato, G., (2010). "Seismic modeling and behavior of gravity frames in high-rise building," Proceedings, 9th National Conference on Earthquake Engineering, Toronto, Canada, July 25-29, 2010.
82. Zhang, Y., Wang, Z., (2000). "Seismic Behavior of Reinforced Concrete Shear Walls Subjected to High Axial Loading," ACI Journal of Structural Engineering, Vol. 97, No. 5, pp. 739-750.
83. Zhang, H., (2007). "Study on the Performance-based Seismic Design Method for Shear Wall Structures," Doctoral Dissertation, Tongji University, China. (In Chinese).
84. Zhou, G., (2004). "Research on the hysteric behavior of high-rise reinforced concrete shear walls," Master's Thesis, Tongji University, China. (In Chinese).